

Spectro-microscopic investigation of Fe-oxide based model catalysts and instrumental development

Dissertation

zur Erlangung des akademischen Grades

doctor rerum naturalium (Dr. rer. nat.)

im Fach Physik eingereicht an der

Mathematisch-Naturwissenschaftlichen Fakultät

der Humboldt-Universität zu Berlin

von Frau M.S. Francesca Genuzio

Präsident: Prof. Dr. Jan-Hendrik Olbertz

Dekan: Prof. Dr. Elmar Kulke

Gutachter: Prof. Dr. H.-J. Freund

Prof. Dr. N. Koch

Prof. Dr. C. Koch

Tag der mündlichen Prüfung: 11.02.2016

Abstract

This work presents the investigation of Fe-oxide systems, combining microscopy (LEEM, X-PEEM), diffraction (LEED) and spectroscopy (XPS), and the electron-optical development of adaptive optics and aberration corrections for an electrostatic imaging energy analyzer.

Experimentally, we studied magnetite (Fe_3O_4) and hematite ($\alpha\text{-Fe}_2\text{O}_3$) thin films, the most stable iron oxides phases, widely used as catalysts and as a support for catalytically active systems. Their crystal structure, stoichiometry as well as their surface termination can be tuned by special preparation procedures. Taking advantage of real time observation with microscopy, diffraction and spectroscopy, we investigated (a) the surface modifications of Fe_3O_4 and $\alpha\text{-Fe}_2\text{O}_3$ thin films by Fe deposition; (b) the reversible phase transformation $\text{Fe}_3\text{O}_4 \leftrightarrow \alpha\text{-Fe}_2\text{O}_3$ under different oxidation conditions; (c) the formation of the metastable $\gamma\text{-Fe}_2\text{O}_3$ phase and (d) the interaction of Fe_3O_4 and $\alpha\text{-Fe}_2\text{O}_3$ surfaces with supported Pt nanoparticles .

An algorithm was developed to simulate the LEEM image contrast for inhomogeneous 2D surfaces. The possible application to experimental data and the limitation will be discussed.

Finally, the design of an energy filtering system is presented, which will be implemented in a new generation PEEM/LEEM microscope. The system bases on the same imaging principle as the magnetic Ω -filter, successfully implemented in the actual SMART microscope. The new instrument aims for the improvement of lateral and energy resolution in X-PEEM (5 nm and 70 meV, respectively) and a routine operation with easy handling. The majority of the possible second order aberrations are self-compensated by intrinsic symmetry. The effect of the other aberrations is reduced by an adequate design for the deceleration-acceleration optics in combination with optimized pass energy. Furthermore, additional hexapole multipoles compensate for the residual dominating aberrations, yielding in the lateral resolution and energy resolution better than 2 nm and 75 meV, respectively.

Zusammenfassung

Diese Arbeit untersucht Fe-Oxid-Systeme mit Hilfe einer Kombination aus Mikroskopie (LEEM, Röntgen PEEMs), Beugung (LEED) und Spektroskopie (XPS) und berichtet über die elektronenoptische Entwicklung adaptiver Optiken und Aberrationskorrekturen für einen elektrostatischen abbildenden Energieanalysator.

Experimentell untersuchten wir Magnetit (Fe_3O_4) und Hämatit ($\alpha\text{-Fe}_2\text{O}_3$) Dünnschichten, die stabilsten Eisenoxid-Phasen, die weithin als Katalysatoren und als Träger für katalytisch aktive Systeme eingesetzt werden. Ihre Kristallstruktur, Stöchiometrie sowie deren Oberflächenterminierung können durch spezielle Herstellungsverfahren eingestellt werden. Unter Ausnutzung der Echtzeit-Beobachtung mit Mikroskopie, Beugung und Spektroskopie untersuchten wir (a) die Oberflächenmodifikationen von Fe_3O_4 und $\alpha\text{-Fe}_2\text{O}_3$ -Dünnschichten durch Fe Ablagerung; (b) die reversible Phasenumwandlung $\text{Fe}_3\text{O}_4 \leftrightarrow \alpha\text{-Fe}_2\text{O}_3$ unter verschiedenen Oxidationsbedingungen; (c) die Bildung der metastabilen $\gamma\text{-Fe}_2\text{O}_3$ -Phase und (d) die Wechselwirkung von Fe_3O_4 und $\alpha\text{-Fe}_2\text{O}_3$ Oberflächen mit unterstützten Pt-Nanopartikeln.

Es wurde ein Algorithmus entwickelt, um den LEEM Bildkontrast für inhomogene 2D Oberflächen zu simulieren. Die mögliche Anwendung auf experimentelle Daten und die Einschränkungen werden diskutiert werden.

Abschließend wird das Design eines Energiefilter-System vorgestellt, das in ein PEEM/LEEM Mikroskop der neuen Generation eingebaut werden wird. Das System basiert auf dem gleichen Abbildungsprinzip wie der magnetische Ω -Filter, der erfolgreich im aktuellen SMART Mikroskop eingesetzt wird. Das neue Instrument zielt auf die Verbesserung der Orts- und Energieauflösung im XPEEM (5 nm und 70 meV) und einen routinemäßigen Betrieb mit einfacher Handhabung. Die Mehrzahl der möglichen Aberrationen zweiter Ordnung wird durch die intrinsische Symmetrie selbstkompensiert. Die Wirkung der anderen Aberrationen wird durch ein geeignetes Design der Verzögerungs- und Beschleunigungsoptiken kombiniert mit einer optimierten Passenergie reduziert. Darüber hinaus kompensieren zusätzliche Hexapole die restlichen dominierenden Aberrationen, wodurch eine Orts- und Energieauflösung besser als 2 nm bzw. 75 meV erreicht wird.

Publications

„Interconversion of α -Fe₂O₃ and Fe₃O₄ Thin Films: Mechanisms, Morphology, and Evidence for Unexpected Substrate Participation“ F. Genuzio, A. Sala, T. Schmidt, D. Menzel, and H.-J. Freund, The Journal of Physical Chemistry C, 2014, 118 (50), pp 29068–29076

“Phase transformations in thin iron oxide films: Spectromicroscopic study of velocity and shape of the reaction fronts“ F. Genuzio, A. Sala, Th. Schmidt, D. Menzel, H.-J. Freund, Submitted to Surface Science

Selbstständigkeitserklärung

Hiermit erkläre ich, dass ich die vorliegende Dissertation selbstständig und nur unter Verwendung der angegebenen Literatur und Hilfsmittel angefertigt habe.

Francesca Genuzio

Contents

Introduction	1
1. Experimental overview.....	4
1.1 Experimental Techniques	4
1.1.1 LEED	4
1.1.2 LEEM	5
1.1.3 X-PEEM	6
1.2 Experimental Setup	7
1.2.1 SMART Microscope.....	9
1.2.2 Main Chamber	10
1.3 Thin films	11
1.4 Iron Oxide.....	13
1.4.1 Fe oxide crystal structure.....	13
1.4.2 Fe oxide in thin film	16
1.5 Evaporator calibration	18
1.5.1 Fe evaporator	18
1.5.2 Pt evaporator.....	18
1.6 Solid State Transformation.....	20
1.7 Supported Nanoparticles on reducible oxide: SMSI	21
2. Supported α-Fe₂O₃(0001) thin films: growth and preparation Surface modification induced by Fe deposition on Fe₃O₄(111) and α-Fe₂O₃(0001)	24
2.1 Ordered α -Fe ₂ O ₃ (0001) thin film preparation: influence of the oxidation parameters and the substrates morphology.	24
2.1.1 α -Fe ₂ O ₃ /Pt(111): investigation of preparation parameters	25
2.1.2 α -Fe ₂ O ₃ nucleation: role of the substrate defects	29
2.1.3 α -Fe ₂ O ₃ : crystallographic defects	33
2.1.4 α -Fe ₂ O ₃ thin films supported on Ag(111) and Ru(0001)	38
2.1.5 Mixed films.....	40
2.2 Effect of Fe deposition on Fe-oxide surfaces: biphasic termination	41
2.2.1 α -Fe ₂ O ₃ biphasic termination: structural models	43
2.2.2 Fe deposition on α -Fe ₂ O ₃ / Fe ₃ O ₄ Mixed film	47
2.2.3 Modification of Fe ₃ O ₄ (111) surface termination by Fe deposition and UHV annealing.....	53
2.3 Summary and conclusions	59
3. Phase transformation in thin iron oxide films: mechanism, velocity and shape of the reaction front.....	61

3.1	Phase identification	62
3.1.1	Phase transformation mechanism	63
3.2	Experimental observation of the phase transformation	65
3.2.1	$\text{Fe}_3\text{O}_4 + \text{O}_2 \rightarrow \gamma\text{-Fe}_2\text{O}_3$	65
3.2.2	$\gamma\text{-Fe}_2\text{O}_3 \rightarrow \alpha\text{-Fe}_2\text{O}_3$	69
3.2.3	$\text{Fe}_3\text{O}_4 + \text{O}_2 \rightarrow \alpha\text{-Fe}_2\text{O}_3$	72
3.2.4	$\text{Fe}_2\text{O}_3 \rightarrow \text{Fe}_3\text{O}_4 + \text{O}_2$ (thin films supported on Ag(111))	74
3.2.5	$\text{Fe}_3\text{O}_4 \rightarrow \text{Fe}_2\text{O}_3 + \text{Fe}$ (thin films supported on Pt(111))	75
3.2.6	Fe deposition $\alpha\text{-Fe}_2\text{O}_3/\text{Pt}(111)$: $\alpha\text{-Fe}_2\text{O}_3 \rightarrow \text{Fe}_3\text{O}_4$	80
3.3	Average and local speed of the reaction front	86
3.3.1	Methods: measurement of the reaction front velocity	86
3.3.2	Temperature dependency of average front motion	89
3.3.3	Reaction front morphology: local kinetics.....	94
3.4	Conclusions	101
4.	Pt Nanoparticles Supported on Fe-oxides thin films: $\text{Fe}_3\text{O}_4/\text{Pt}(111)$ and biphasic terminated $\alpha\text{-Fe}_2\text{O}_3/\text{Pt}(111)$	104
4.1	Pt NPs on Fe_3O_4	107
4.1.1	Pt NPs formation and encapsulation: X-PEEM and real time LEED X-PEEM.	107
	X-PEEM data.....	108
4.1.2	Encapsulation in $p_{\text{O}_2}=1.5 \cdot 10^{-7}$ mbar.....	115
4.1.3	Influence of deposition temperature on NPs shape and size	118
4.2	Investigation on the Pt NPs supported on biphasic terminated $\alpha\text{-Fe}_2\text{O}_3$	123
4.2.1	Results	124
4.2.2	Discussion.....	132
4.3	Summary.....	134
5.	Simulation of LEEM-image contrast.....	136
5.1	Electron waves treatment	137
5.1.1	The specific case of LEEM.....	140
5.2	The 2D algorithm	141
5.2.1	Definition of the Object function.....	143
5.3	Results and Discussion	145
5.3.1	Simple Phase object.....	145
5.3.2	Pure Amplitude and mixed Amplitude-phase object.....	148
5.3.3	Discussion.....	151
5.4	Conclusions	154
6.	Optical development of an energy filter for LEEM/PEEM application	155

6.1 Electrostatic Ω -filter	157
6.1.1 First order optical properties (energy dispersion).....	161
6.1.2 Second order optical properties (aberration coefficient)	162
6.2 Adaptive optics	163
6.2.1 Introduction and definitions.....	164
6.2.2 Retarding System.....	167
6.2.3 Accelerating System	172
6.2.4 Projective Optics.....	177
6.3 Hexapole Correction.....	177
6.3.1 Hexapole deflection	178
6.3.2 Simulation of hexapole field and deflection.	180
6.3.3 Hexapole Deflection in the Ω -filter	182
6.3.4 Symmetries of the system	185
6.4 Strategies for aberration correction	191
6.4.1 Entrance conditions	192
6.4.2 Energy Resolution	192
6.4.3 Lateral resolution	195
6.4.4 Hexapoles arrangement	198
6.5 Conclusions	201
7. Summary and Outlooks	203
Appendix 1:.....	i
Appendix 2	viii
Appendix 3	xvi
Appendix 4	xxvi
Appendix 5	xxviii
Appendix 6	xxx
Appendix 7	xxxii
References	xliii

Introduction

In this work an aberration corrected and energy filtered Low Energy and Photo-Emitted Electron Microscope (LEEM/PEEM) was used to investigate catalytically relevant systems. Additionally, an instrumental development to improve the performance of the energy filter is presented. The experiments were performed at the SMART spectro-microscope [1, 2], operating at the HZB synchrotron facility in Berlin.

The invention and the application of Electron Microscopy have been a breakthrough in many scientific fields, opening the door to the direct visualization of sub-nanometric phenomena. Since the first prototypes, developed in the 30s of the last century, enormous technological and instrumental progress in this field has been done. One of the most significant technical improvements was the introduction of aberrations correction, leading to the enhancement of the lateral resolution. Still today, however, the instrumental resolution is far from the theoretical diffraction limit, opening possibilities for further technical improvements. The SMART microscope is the first prototype of LEEM/PEEM microscope fully corrected up to the second aberration order, by simultaneous correction of spherical and chromatic aberrations. It is also the first LEEM/PEEM instrument achieving 2.6 nm in LEEM [1, 2] and 18 nm in energy filtered XPEEM [3], providing chemical and structural information with high lateral resolution in-situ and in real time. The main innovative aspects introduced in the SMART design have been the electrostatic mirror and the magnetic Ω -shaped energy filter.

The first part of my thesis presents the experimental application of LEEM, LEED and XPEEM to supported iron-oxide thin films as model catalysts. The focus is addressed on magnetite (Fe_3O_4), maghemite ($\gamma\text{-Fe}_2\text{O}_3$) and hematite ($\alpha\text{-Fe}_2\text{O}_3$) crystals, widely used in industrial catalysis, environmental application (e.g. photo-chemistry, filtering systems), medicine (e.g. contrast agent in medical imaging, and drug delivery) and technology (e.g. recording devices, field sensors) [4-7].

Over the years, the structural properties, the transition between the different phases, the surface termination and the interaction with supported metal nanoparticles have been intensively studied with various techniques, either in natural crystals or in thin films. Despite the considerable progress in the characterization of these systems, many questions still remain open, because of the complex interplay between structural, elastic, magnetic and chemical properties. Indeed, it has been largely demonstrated in thin film systems, that the structural

and catalytic properties can be modified and controlled by choice of the supporting crystal, preparation conditions [8] and/or additional metal deposition [9-13]. Similarly, the inter-conversion between Fe oxide phases depends in a complex way on ambient conditions (e.g. oxygen pressure, temperature) [14-17], supporting substrate [18] and the internal structure and orientation of the oxide film [19-21].

Within this wide research topic, the investigations in this work addressed to the comprehensive characterization of the iron-oxide film preparation and the effects of additional Fe deposition (chapter 2), the crystal phase transition under well defined experimental conditions (chapter 3), as well as the interaction with supported Pt nanoparticles (chapter 4). The samples were about 10 nm thin oxide films grown in situ and epitaxial on various single crystal supports (Pt(111), Ag(111) or Ru(0001)) by iterations of Fe vapor-deposition and oxidation under controlled conditions. This leads to well defined structures and crystalline orientation of the surface, controlled by the choice of preparation parameters [12, 22]. Moreover, it is possible to quantitatively correlate the preparation parameters to the formation of surface features and defects (e.g. film morphology, step edges, kinks and/or shape and size of nano-particles), which are crucial factors affecting the catalytic activity. Thanks to the high acquisition rate of LEEM and LEED, the sample modifications can be observed under reaction conditions, both in image and diffraction mode. The final film composition (X-PEEM), structure (LEED) and morphology (LEEM) can be directly related to specific treatments of the sample.

Chapter 5 presents an algorithm, developed within our research group, for the simulation of the LEEM contrast of various surfaces features at variable focus conditions. In fact, it was shown recently that the refractive nature of the phase contrast in LEEM can be used quantitatively to extract information on the height of superficial features [23-25]. While such methods have already been successfully applied to experimental data on homogenous surfaces (i.e. uniform composition) [24], it is not yet extended to the study of complex surfaces, i.e. composed by more than one material. This work aims for the characterization of the contrast of complex surface morphologies and provides suggestions for experimental applications.

The final chapter is dedicated to the theoretical development of an electrostatic imaging Ω -filter to be implemented in a commercial LEEM instrument (the so-called SMART II). The filtering system uses the same working principle of the magnetic Ω -filter already successfully operating in the SMART microscope. Energy filtering of the electron beam allows obtaining a

final image with a narrow energy window, e.g. selecting electrons from a photoemission energy spectrum for element specific imaging (in X-PEEM) or separating elastically from inelastically diffracted electrons to improve the image contrast (in LEEM). Furthermore, narrowing the energy spread reduces sensibly the effect of chromatic aberrations in standard LEEM microscopes and therefore improves the lateral resolution. However, the optical elements like energy filters introduce additional aberrations and consequently might deteriorate the image quality. This can be avoided by optimizing the optical system design, as discussed in chapter 6.

1. Experimental overview

This chapter introduces the experimental part of work. It presents the experimental techniques used in the following experimental work (section 1.1) and the experimental setup (section 1.2). The thin film growth, the structure of the investigated Fe oxides and the calibration of the evaporators are presented in 1.3, 1.4 and 1.5 respectively. Finally, section 1.6 gives a little overview on solid-solid phase transformations, and section 1.7 introduces the so-called SMSI (Strong Metal Support Interaction), i.e. interaction between supported metal nanoparticles and the oxides support.

1.1 Experimental Techniques

The experiments were carried out at the spectro-microscope SMART (*Spectro-Microscope with Aberration correction for many Relevant Techniques*), operating at the synchrotron facility of the HZB in Berlin. The SMART is capable to probe the sample with different surface science probing tools like LEED, LEEM, X-PEEM and XPS.

1.1.1 LEED

LEED (Low Energy Electron Diffraction) is a well-known surface sensitive technique, which visualizes the diffraction pattern of elastically backscattered electrons from a well-ordered structure. The incoming plane electron waves are scattered by surface atoms (see Fig 1.1a). If the atomic structure is periodic and the periodic length is comparable with the wavelength of the electrons, the interference between the partial waves of backscattered electron occurs according to the Bragg condition:

$$d_{atoms} \sin\theta = n \lambda$$

Where d_{atoms} is the distance between the atoms (i.e. the scattering centers), θ is the angle between the incident ray and the scattering planes, λ is the wavelength of incident electron wave and n is the diffraction order.

The intensity distribution of the LEED pattern can be written as the product of two contributions:

$$I(\vec{k}, \vec{K}) = F(\vec{k}, \vec{K})G(\vec{K});$$

where $F(\vec{k}, \vec{K})$ is the **intensity structure factor**, the absolute scattering amplitude of a single unit, and $G(\vec{K})$ is the **intensity form factor** (or **lattice factor**), representing the interference effect from the periodic rearrangement of single units. The **structure factor** contains the information on the composition and arrangement of the atoms inside the single unit, while the **lattice factor** gives the position of the diffraction spots and the shape of the spot profile.

In the ideal case (infinite and completely ordered crystal):

$$G_{\text{ideal}} = \sum_{\vec{G}} \delta(\vec{K}_{\parallel} - \vec{G}_{\parallel})$$

All variations from the ideal profile contain statistical information related to the statistical distribution of defects (islands, terrace, steps,...) at the surface. For example, Lorentzian and Gaussian spot profiles are characteristic of continuous and peaked size distribution, respectively. Henzler rings, generally observed during epitaxy, are a particular case of a peaked island size distribution with random orientations.

Different levels of insight can be derived from the LEED pattern [26, 27]:

- From the qualitative observation of the spots position, relative distances and symmetries one can easily determine the cell unit dimensions and symmetries of the system, the existence of rotational domains and the presence of long-range periodicities in the system.
- The analysis of the lattice factor $G(\vec{K})$ (SPA-LEED) and its deviation from the ideal case (due to broadening, splitting,...), gives the quantitative determinations of size distribution and topology of the surface defects (Kinematic approximation) [28].
- The analysis of the form factor $F(\vec{k}, \vec{K})$ (LEED-IV) provides the atomic models within the unit cell, by simulating the multiple electron scattering events between neighboring scattering centers (Dynamical approximation) [29].

1.1.2 LEEM

LEEM (Low Energy Electron Microscopy) is an electron microscopic technique originally developed by E. Bauer in 1962 as imaging counterpart of LEED [30, 31]. The lens system image the sample surface on the projector, using one of the elastically reflected electron beams (selected in one of intermediate diffraction planes by a contrast aperture, or CA, see Fig 1.1b).

The most natural application of LEEM is the imaging of specimen surfaces, because of the high backscattering cross-section and the only a few nanometer small penetration depth of slow electrons with a typical kinetic energy of 0-500 eV.

In the so-called "**brightfield mode**", the image is formed using the normally backscattered electron beam (i.e. the (0,0) spot in LEED, see Fig 1.1c). In this mode, the image contrast (discussed in more detail in chapter 6) is a direct consequence of the interaction of electron waves, arising from the local variation in diffraction conditions (amplitude contrast) or from the interference between electrons with different optical paths (phase contrasts). In the first case different materials or facets can be visualized, while in the second atomic steps, dislocations and defects. A third contrast mechanism ("**darkfield mode**") can be achieved by imaging a non-specular reflected beam (see Fig 1.1c). In this way, rotational domains and coexisting phase contributions can be separated.

Compared to other electron-microscopic techniques (such as TEM, SEM, etc.) the spatial resolution is limited to about 2 - 20 nm, but the high signal-to-noise ratio, combined with the "parallel acquisition" determines the possibility of high acquisition rates; consequently, samples can be observed **in-situ** and **in real time** with nanometric resolution.

Thanks to all characteristics and its surface sensitivity, LEEM is specifically indicated to study clean surfaces and thin films. In particular one can study: the local crystal structure and topography, rotational and superstructure domains, structural phase transitions, such as growth) and reaction mechanisms. Further details on LEEM can be found in [30, 31].

1.1.3 X-PEEM

X-PEEM (X-ray Photo-Emitted Electron Microscopy) can be easily implemented in a LEEM microscope, as the electron optics column is in principle the same. Different to LEEM, electrons used for imaging are emitted at the specimen surface after a primary photon excitation [32]. The image contrast is given by the local variation in electron emission, arising from local variation in the chemical composition, chemical state (chemical shifts), electronic state (valence band, work function), magnetism (XMCD) and molecular orientation (NEXAFS).

The SMART system can be used as spatially resolved XPS, thanks to the combination of synchrotron monochromatic light and electron energy filtering [1-3].

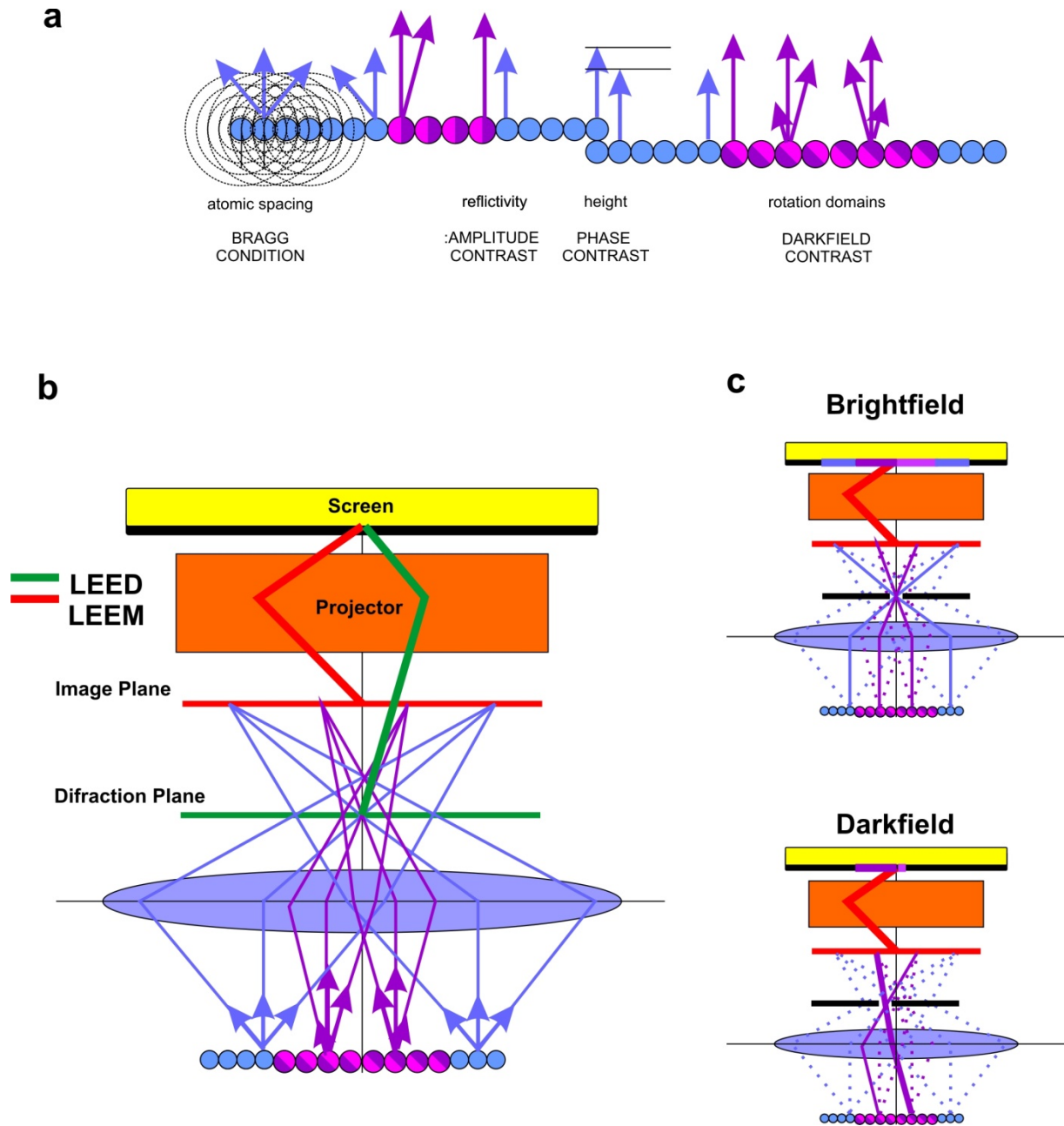


Fig. 1.1: a) Schematic view of interference processes involved in the different contrast mechanisms in LEEM and LEED. b) LEED and LEEM images can be produced in the same experimental setup: according to the set-up of the projector system (given by the focal length of the lenses), either the diffraction pattern or real space image can be projected on the detector system. Depending on the position of the CA (contrast aperture) either brightfield or darkfield image can be obtained (Fig 1.1c).

1.2 Experimental Setup

The experimental setup consists of two main parts: the microscope itself and the main chamber. Fig. 1.2 shows a photo of the operating microscope, while the optical scheme is presented in Fig. 1.3.

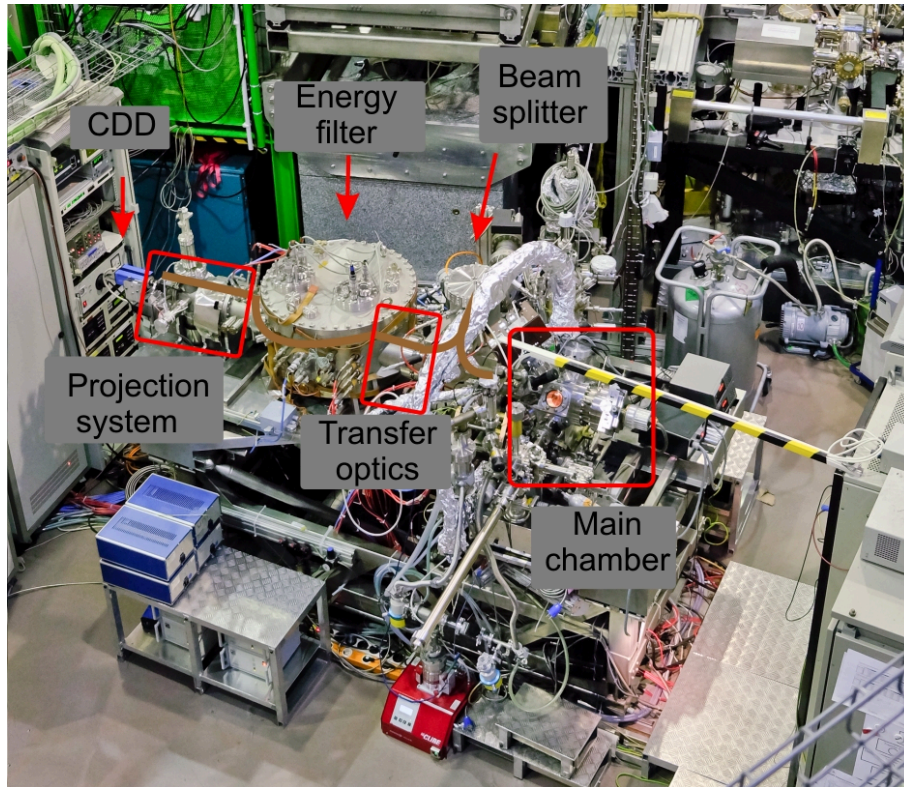


Fig. 1.2: SMART microscope.

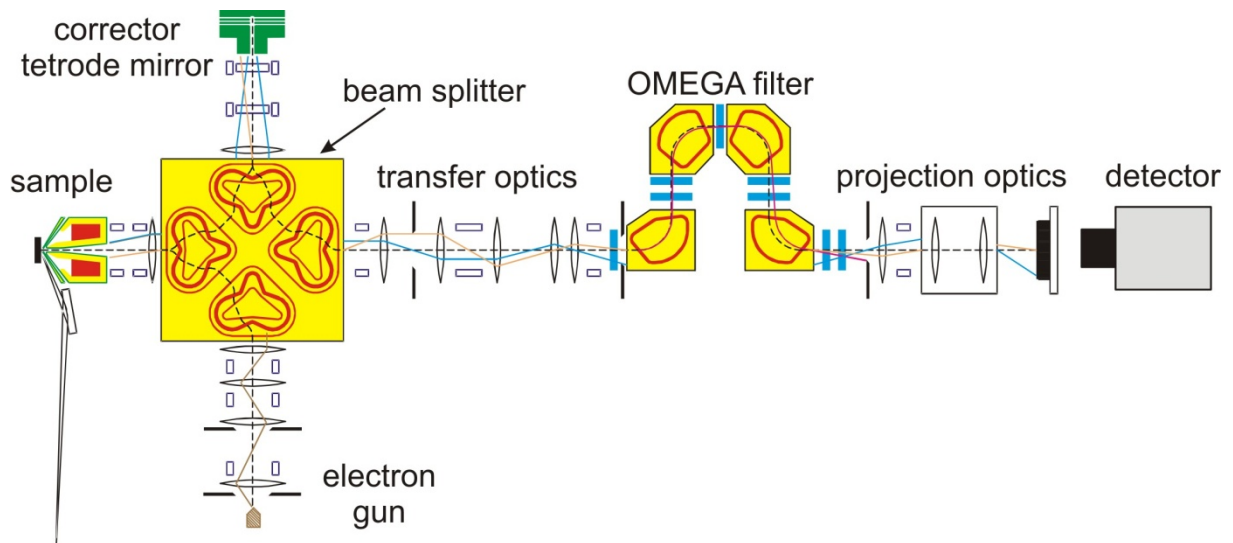


Fig. 1.3: SMART microscope, optical scheme. The sample is located in the main chamber. The electrons are accelerated from the low energy at the sample to the passing energy in the microscope (15 keV) by the electric field between the sample and the objective lens. The beam splitter separates the optical path of the incoming and the reflected beam. The tetrode mirror corrects the aberration introduced by the objective lens, while the electron energy is filtered by the exit slit introduced after the magnetic Ω -filter. The filtered beam is magnified and projected on the detector.

1.2.1 SMART Microscope

The SMART microscope [1, 2, 33, 34] comprises:

- the electron gun (emission gun working at 15 kV) for electron beam formation
- beam splitter, which allows the separation of incoming and outgoing electron beams
- the immersion objective lens, which reduces the incoming electron energy from 15keV to the energy wanted at the sample, and reaccelerates outgoing electrons
- an electrostatic mirror, which corrects the aberrations induced by the objective lens
- the transfer optics, which defines pre-magnification and allows the switch between image and diffraction mode
- the omega filter for energy filtering
- the projection system

The whole system works at the operating voltage of 15 kV.

The resolution obtained in LEEM is 2.6 nm [35]; in X-PEEM space charge effect limits to 18 nm [36]. Typically, fields of view range from 30 μm down to 1 μm .

1.2.2 Main Chamber

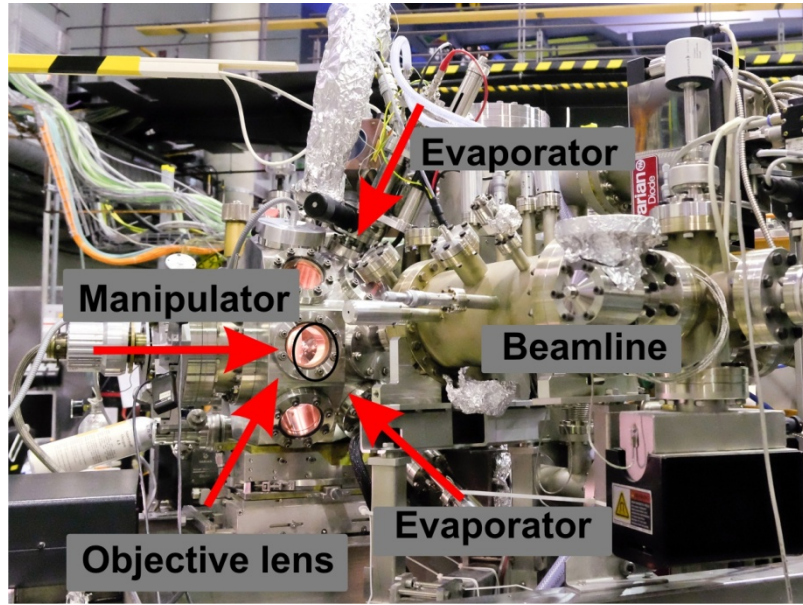


Fig. 1.4: Main chamber of the SMART

The main UHV chamber is designed for direct sample preparation. The base pressure is in the range of 1×10^{-10} mbar maintained by an ionic pump and a titanium sublimation pump.

The manipulator and the objective lens are placed on the principal axis of the microscope. On the perpendicular axis there are the linear drives to the preparation chamber, the gas line to fill the chamber with pure gases and the pumps in the bottom. Finally, the evaporators, the beamline and the Hg-lamp ($h\nu = 4.9$ eV) are placed sideways, pointing to the sample at grazing incidence of 20° .

Pt(111), Ru(0001) and Ag(111) crystals have been mounted on a commercial Elmitec sample holder with a Mo cap. The sample holder allows the annealing of the sample from its back side; $T < 700$ K can be reached by radiation from a filament while $T > 700$ K require electron bombardment up to a maximum temperature of 2000 K. The temperature is measured with an accuracy superior to 10 K by a W26%Re/W5%Re thermocouple spot-welded to the crystal support. The single crystals are cleaned by repeated cycles of argon sputtering and high temperature UHV annealing (Ru(0001): $T = 1300$ K; Pt(111): $T = 1100$ K; Ag(111): $T = 830$ K), until a sharp LEED pattern without a structured background is obtained. Additional O_2 treatment (1×10^{-6} mbar, 700 K) followed by UHV annealing removes carbon contamination.

Fe and Pt are deposited by Omicron EFM3 evaporators, using an iron rod or a graphite crucible containing Pt, respectively. Both metals are 99.995% pure. The evaporators, heated by electron bombardment using a 0.125 mm W99%Th1% filament, are mounted on a side port, separated from the main chamber by a VAT valve for their detachment. It can be approached to the sample down to a minimum distance of 20 cm, pointing under a grazing incidence angle of 20 deg (the calibration procedures are described later in section 1.5).

Oxygen (99.999% purity) can be dosed by a leak valve directly into the main chamber of the microscope.

1.3 Thin films

Thin films supported on conducting metal substrates are typically used as samples in the surface science approach [12, 37]. Thin oxide films can be grown either by the direct oxidation of the corresponding metal surface (single crystal) or by hetero-epitaxy, i.e. metal atoms are deposited on a single crystal, generally of a different material [22, 38].

The correct choice of the substrate plays a primary role for the hetero-epitaxial growth of a well-ordered oxide layer. A small lattice mismatch between the substrate and supported film is required to reduce the strain at the oxide/crystal interface. In addition, the support should be inert, in order to prevent metal alloying or oxygen diffusion to the underneath layers. Metal atoms can be deposited either in O₂ atmosphere (MBE), leading to the direct formation of the oxide, or in UHV, and oxidized in a second step.

The possible growth modes for a thin film have been classified and identified in three categories [39]:

- 3D island (Volmer-Weber)
- Layer by layer (Frank-van der Merwe)
- layer-plus-island growth (Stranski-Krastanov)

The resulting growth mechanism is strongly influenced by the surface free energies (also called surface tension) of both the metal support and the oxide.

The *Surface free energy for unit of area* γ may be defined as:

$$\gamma = \frac{(E_{surf} - E_{Bulk})}{A} = \frac{W}{2A}$$

where A is the area of the surface, $(E_{surf} - E_{Bulk})$ is the excess of energy of the surface with respect to the bulk due to the broken bonds at the interface, or more simply, the work W necessary to create two (one for each volumes created) surfaces cutting the bulk along a crystal plane per unit of area formed.

The Young equation, valid for rigid support, expresses the equilibrium condition:

$$\gamma_{sub} = \gamma_{ads} - \gamma_{inter} \cdot \cos \theta_{conct}$$

where γ_{sub} , γ_{ads} and γ_{inter} are the surface free energy of the substrate, the adsorbate and of their interface; θ_{conct} is the contact angle.

The *spreading parameter* S is defined as:

$$S = \gamma_{sub} - (\gamma_{ads} - \gamma_{inter})$$

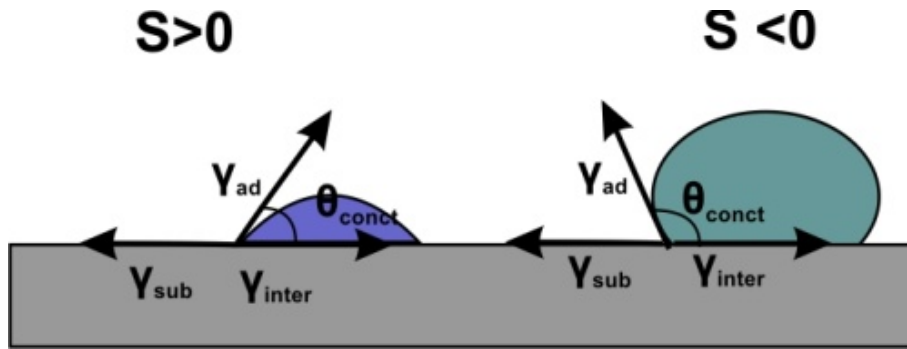


Fig. 1.5: relation between surface tension and spreading parameter

Based on the value of S :

- $S > 0$, Frank-van der Merwe growth. In case of a strong bonding between the deposited atoms and the support, the support surface is completely wetted (layer-by-layer) (Fig 1.6a).
- $S < 0$, Volmer-Weber growth: if the interaction between deposited atoms is stronger than the bonding with the support atoms, the deposits nucleate on the surface (3D islands), minimizing the contact area with the substrate (Fig 1.6b)

The Stranski-Krastanov type of growth is a specific case: first, a full layer is formed and then, when a critical thickness is reached, further growth is controlled by the nucleation of particles or islands (Fig 1.6c).

Even though at the thermodynamic equilibrium a system has only one possible growing mode, kinetic effects can lead to the observation of "meta-stable" growth modes, which can also be observed (for instance as consequence of limited atom diffusion). In the Fe oxide system supported on Pt(111), for instance, quasi layer-by-layer or Stranski-Krastanov growth can be observed by direct oxidation of Fe during deposition, depending on the thickness of the underneath Fe-oxide (see Fig 1.6b).

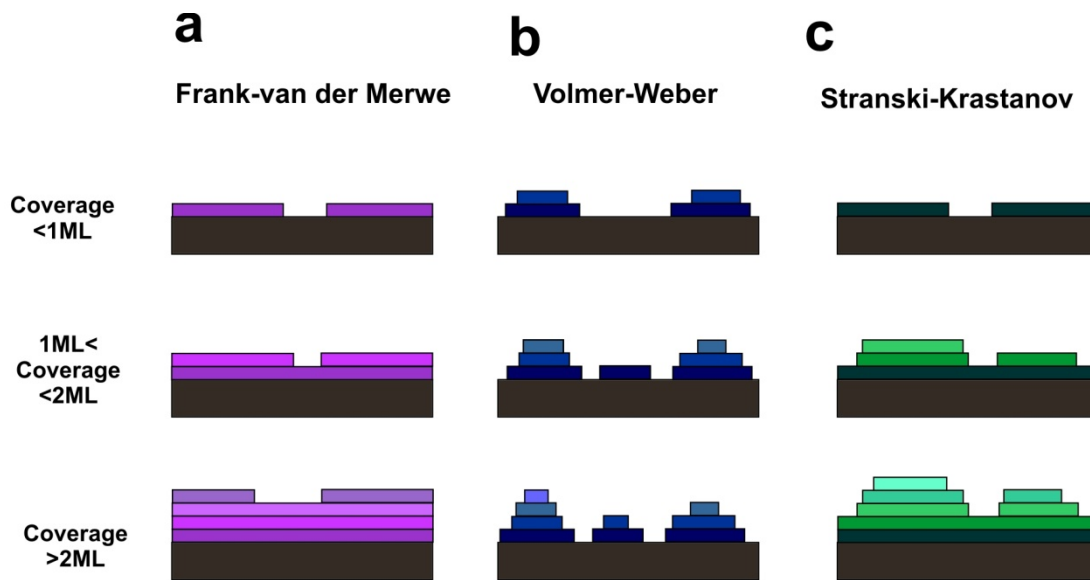


Fig. 1.6: Growth modes in hetero-epitaxy: Fig 1.6a) layer-by-layer. Fig 1.6b) 3D island nucleation (Volmer-Weber growth mode). Fig 1.6c) 3D islands nucleate after the formation of the first complete layers (SK).

1.4 Iron Oxide

1.4.1 Fe oxide crystal structure

According to the phase diagram for the Fe-O system as function of temperature and oxygen pressure (Fig. 1.7) [22, 40], FeO, Fe₃O₄ and α -Fe₂O₃ are the stable phases under thermodynamic equilibrium; the resulting bulk oxide stoichiometries depend on O₂ pressure and temperature [41].

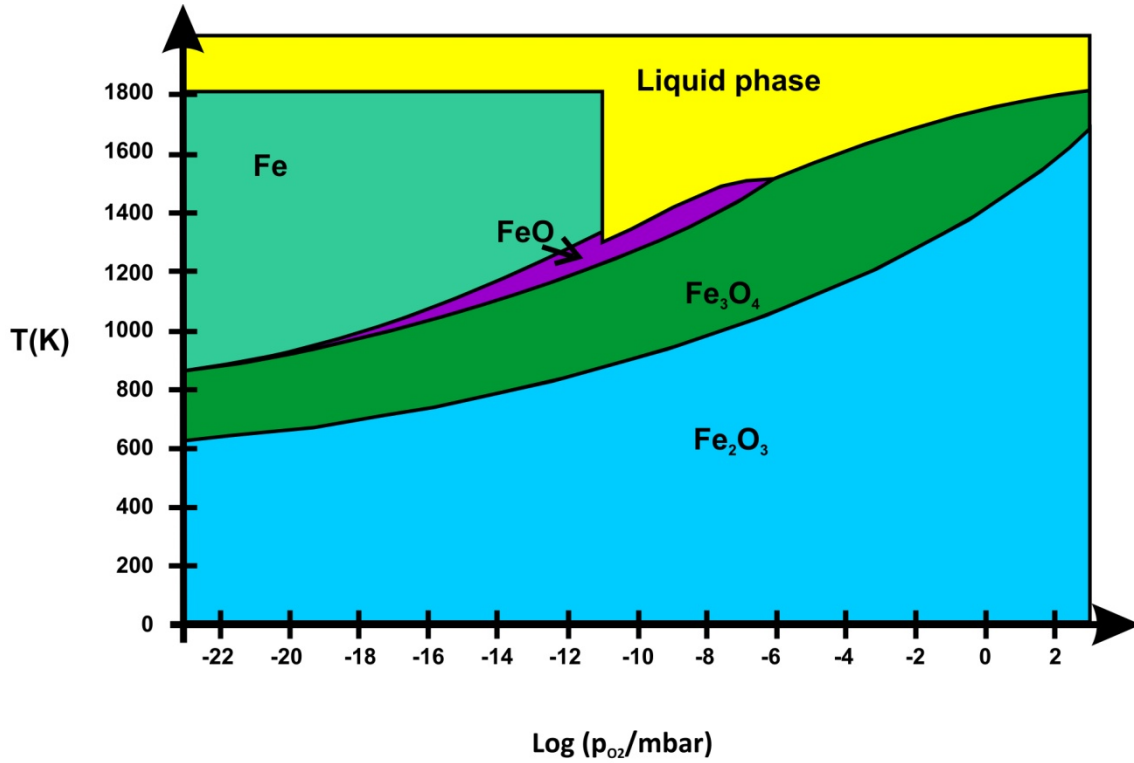


Fig. 1.7: phase diagram for bulk Fe oxides calculated in [40]

All these three phases will be thoroughly discussed in this thesis; their crystal structures under are shown in Fig 1.8.

Wüstite

FeO [22, 42] crystallizes in the rock-salt structure. A cubic unit cell includes four formula units and has a lattice constant of 4.3 Å. Oxygen O anions form a close-packed fcc sublattice while Fe^{2+} cations are located underneath in the interstitial sites. All iron atoms are octahedrally coordinated to oxygen. This phase is stable for $T > 843\text{K}$. Therefore, stable FeO can be prepared above this T and then quenched in O_2 pressure.

Magnetite

Fe_3O_4 crystallizes in the inverse spinel structure [42]. The cubic unit cell includes eight formula units $(\text{Fe}^{3+})_{\text{tet}}[\text{Fe}^{2+}\text{Fe}^{3+}]_{\text{oct}}\text{O}^{2-}_4$ and has a lattice constant of 8.396 Å. Oxygen O^{2-} anions form hexagonal close-packed fcc sublattice with ABC stacking, while iron cations are located in the interstitial sites forming either **Kagomé** or **Mix-Trigonal** layers, alternating in the structure. The Kagomé layers consist of octahedrally coordinated Fe^{2+} and Fe^{3+} ions while the Mix-Trigonal layers consist of tetrahedrally (Fe^{3+}) and octahedrally coordinated (Fe^{2+} and

Fe^{3+}) ions. The fraction of unoccupied sites in both Fe layers ($1/4$) form a hexagonal lattice with a periodicity of $a=5.94 \text{ \AA}$.

Fe_3O_4 is rarely perfectly stoichiometrical; Fe vacancies are the most favorable defect. In the so-called “non-stoichiometric magnetite” $\text{Fe}_{3-\delta}\text{O}_4$ (with $0 < \delta < 1/3$), arbitrarily distributed cations vacancies are mainly located at the octahedral interstitials. The case $\delta = 1/3$ corresponds the "maghemite" phase, i.e. $\gamma\text{-Fe}_2\text{O}_3$ (see description below).

Hematite

$\alpha\text{-Fe}_2\text{O}_3$ is the only iron oxide phase that is stable at room temperature in ambient conditions. It crystallizes in the corundum structure [42]. Hematite can be described in both hexagonal and in the rhombohedral system, with lattice constants of $a_{\text{hex}} = 5.035 \text{ \AA}$ and $c_{\text{hex}} = 13.72 \text{ \AA}$ (six formula units per unit cell) and $a_{\text{rh}} = 5.427 \text{ \AA}$ and $\alpha_{\text{rh}}=55.3^\circ$ (two formula units per unit cell). Along the (0001) plane, oxygen anions form hcp sub-lattices in ABAB stacking; Fe^{3+} cations occupy $2/3$ of the possible interstitial sites. The O-O distance in oxygen sub-lattices is 2.91 \AA . Iron ions form two sub-layers with inter-atomic distances of 5.03 \AA .

Maghemite

Natural maghemite ($\gamma\text{-Fe}_2\text{O}_3$) occurs in soils as a weathering product of magnetite (Fe_3O_4), to which it is structurally related. Both oxides exhibit an inverse spinel crystal structure [42, 43]. The maghemite structure can be obtained by creating $8/3$ vacancies out of the 24 Fe octahedral sites in the cubic unit cell of magnetite: differently from Fe_3O_4 and “non-stoichiometric” Fe_3O_4 all the iron cations in $\gamma\text{-Fe}_2\text{O}_3$ are in the Fe^{3+} trivalent state.

The nature and the degree of ordering of the iron vacancies in the octahedral sites has been the subject of investigations for several decades; nevertheless, it is not clear under which conditions, if any, vacancy disorder occurs [44-46].

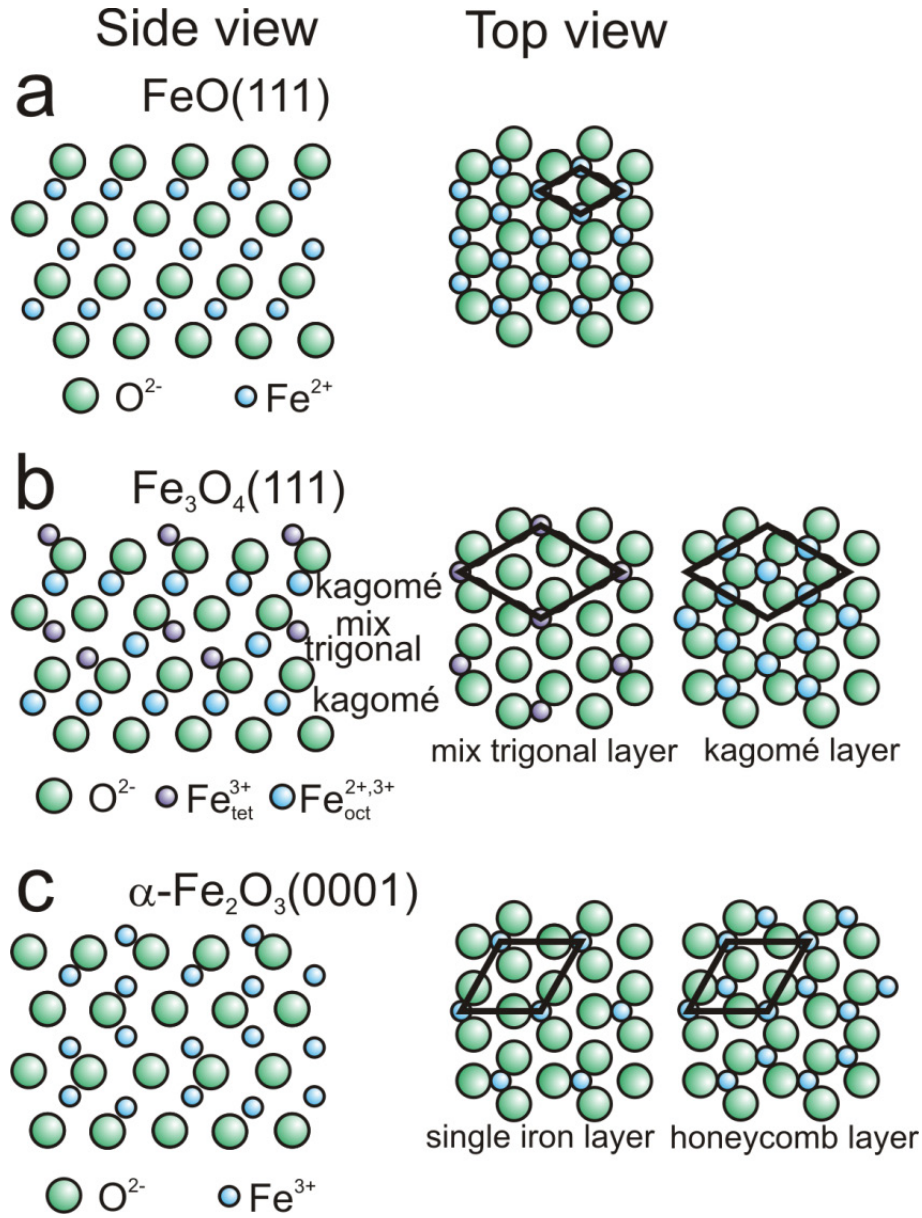


Fig. 1.8: summarizes the Fe terminated buck truncated (111) and (0001) surfaces for FeO(111) (a) Fe_3O_4 (111) (b) and $\alpha\text{-Fe}_2\text{O}_3$ (0001) (c), which are the terminations involved in our experiments.

1.4.2 Fe oxide in thin film

FeO , Fe_3O_4 and $\alpha\text{-Fe}_2\text{O}_3$ thin films, exposing (111) or (0001) surfaces, have been successfully grown in a large range of ambient conditions on Pt(111), Ag(111) and Ru(0001) single crystals [8, 9, 18, 20, 22, 47]. The Pt(111) Ru(0001) and Ag(111) surfaces have a similar close packed structure with inter-atomic distance of 2.77 Å, 2.704 Å and 2.89 Å, respectively.

The $\text{FeO}(111)$ phase, can be grown up to 2.5 ML; the lattice constant is close to those of the substrates, originating a typical Moiré pattern as a fingerprint (Fig.1.9a).

The Fe_3O_4 (111) surface forms a (2×2) reconstruction (Fig 1.9b) with respect to substrate periodicity, while $\alpha\text{-Fe}_2\text{O}_3$ (0001) is characterized by the $(\sqrt{3} \times \sqrt{3})\text{R}30^\circ$ geometry (Fig 1.9c).

All these three oxides can grow as two rotational domains [22]. Both $\alpha\text{-Fe}_2\text{O}_3$ and Fe_3O_4 thin films can exhibit two kinds of surface termination depending on the preparation conditions: the **unreconstructed** or the **"biphase"** terminations [22, 48-50]. This last termination is largely discussed in section 2.2, and it is characterized by the presence of hexagonal extra spots in the LEED pattern, indicating an additional long range periodicity occurring at the surface.

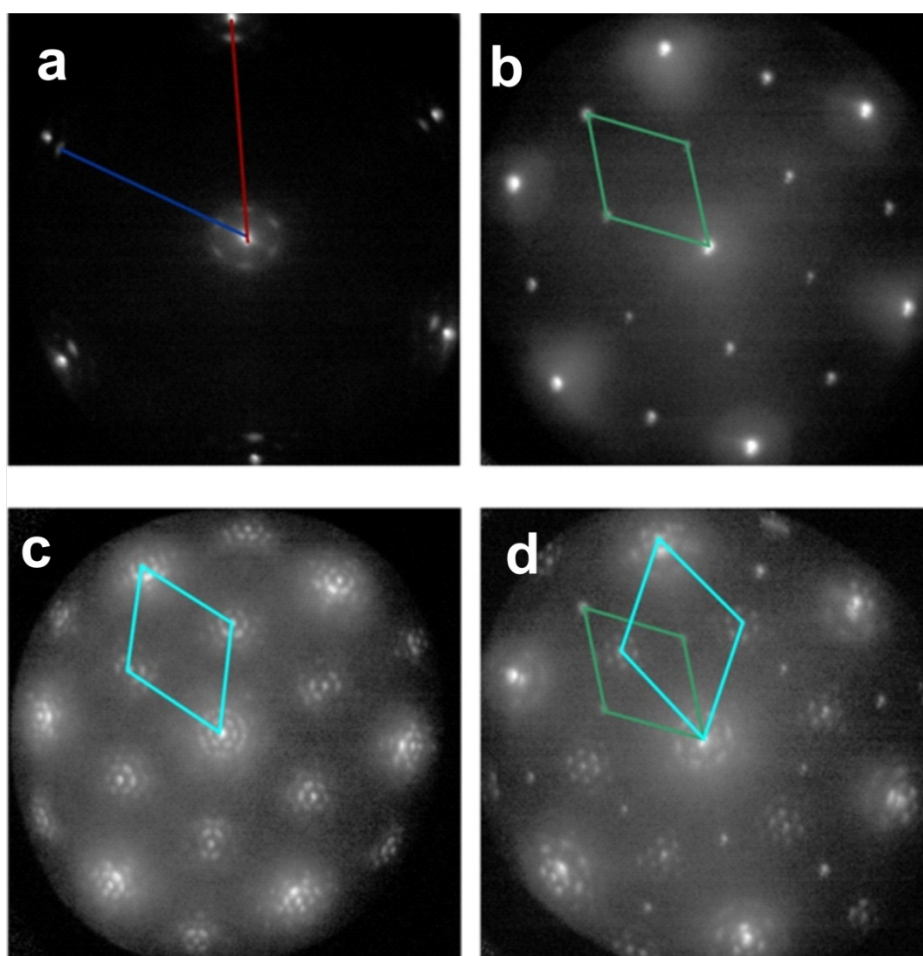


Fig. 1.9: Typical LEED patterns for: a) $\text{FeO}(111)/\text{Pt}(111)$; b) $\text{Fe}_3\text{O}_4/\text{Pt}(111)$ unreconstructed (2×2) ; c) Biphase terminated $\alpha\text{-Fe}_2\text{O}_3$ with the $(\sqrt{3} \times \sqrt{3})\text{R}30^\circ$ reconstruction; d) mixed $\text{Fe}_3\text{O}_4/\alpha\text{-Fe}_2\text{O}_3$ film on $\text{Pt}(111)$. $E_k = 38 \text{ eV}$

1.5 Evaporator calibration

1.5.1 Fe evaporator

The calibration of the Fe evaporation takes advantage of the Stranski-Krastanow growth mode of FeO(111)/Pt(111) (RT Fe deposition and oxidation performed at $p_{O_2}=1 \times 10^{-6}$ mbar, $T=1000$ K) [51]. For a coverage < 1 ML, FeO(111) forms 1 ML thick islands on the Pt(111); the islands coverage, after deposition at constant flux (deposition time ≈ 1 min) can be estimated in LEEM. In the following, 1 ML of Fe is defined as the amount of material necessary to form a closed layer of FeO(111) on Pt(111). Further details concerning this procedure are reported in [52]. The deposition rate used in the experiments is ≈ 0.3 ML/min.

1.5.2 Pt evaporator

The Pt evaporator has been calibrated by the direct observation of homo-epitaxy of Pt on Pt(111).

The sequence in Fig 1.10, shows the real time LEEM acquisitions of the Pt deposition as performed at 623 K, 720 K and 800 K respectively. It is well-known that homo-epitaxial Pt/Pt(111) exhibits three different regimes according to the deposition rate and the temperature [53, 54]: at a high temperature growth occurs following the layer-by-layer mode, either by the nucleation of 2D island (Fig 1.10b, $T \approx 720$ K) or by massive step flow ($T \approx 800$ K) (Fig 1.10c). 3D random growth is observed for lower T (Fig. 1.10a). From the observation of the growth of 2D islands in the layer-by-layer regime, one can estimate exactly the amount of Pt necessary to complete 1 ML (i.e. when no island is visible anymore).

Besides calibration purposes, the direct observation of three homo-epitaxial growth regimes is also useful to understand the influence of deposition temperature on the shape of the supported NP studied in chapter 4.

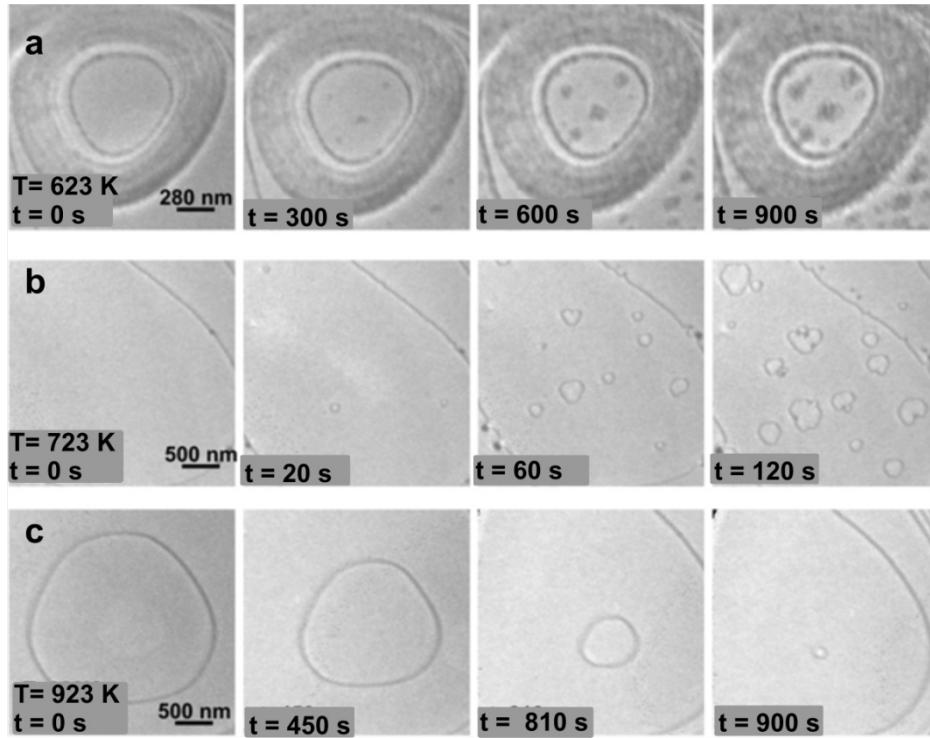


Fig. 1.10: LEEM. Homo-epitaxy of Pt/Pt(111) at different temperatures; a) disorder island; b) 2D island nucleation; c) step flow. $E_k=21$ eV; FoV 400 nm

In order to gain reasonable flux in our set-up, we used a graphite crucible instead of a Pt rod. Carbon from the crucible can be emitted and attached to the surface; anyway, this contamination can be sensitively reduced by dosing O_2 during annealing or quenching the surface in oxygen: in this way, carbon atoms interact with O, forming CO or CO_2 , which are desorbed from the surface (see Fig 1.11)

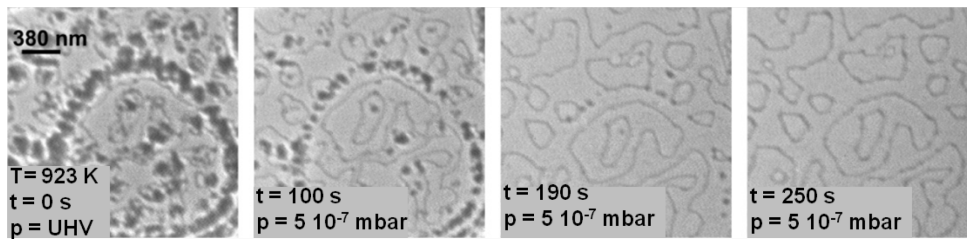


Fig. 1.11: LEEM. Effect of O_2 annealing on the C contamination on Pt(111). $E_k=21$ eV; FoV 400 nm

In the experiment presented in chapter 4, the presence of residual carbon at the surface has been excluded by XPS; the deposition flux is 0.067 ML/min.

1.6 Solid State Transformation

The experimental investigation of the phase transformations between iron-oxides is the topic of chapter 3.

As for the other type of reactions, the driving force in solid-solid phase transformations is the decrease of the total free energy of the system [55-59]. However, as the reacting phases (both parent and product phase) are solids, the kinetic of the system is influenced by factors, which are negligible in gas or liquid reactions (such as: strain, misfit, internal and external stress, interfacial energy, ...) [59-62].

Solid-solid reactions can occur *with* (for instance the transformations $\text{Fe}_3\text{O}_4 \rightarrow \gamma\text{-Fe}_2\text{O}_3$ and $\text{Fe}_3\text{O}_4 \rightarrow \alpha\text{-Fe}_2\text{O}_3$) or *without compositional change* (for instance $\gamma\text{-Fe}_2\text{O}_3 \rightarrow \alpha\text{-Fe}_2\text{O}_3$). As a consequence of the minimization of the interfacial energy between the crystalline phases, the product phase forms with specific crystallographic orientation, closely related to those of the parent phase (so-called topotactic relationships) [55, 59].

One classification of the solid-state reaction is based on its limiting step. The reaction is **diffusion limited** if the kinetic is controlled by long-range diffusion of chemical component through the film [58]; the growth follows the parabolic rate law. Alternatively, the transformation can also proceed through single thermally activated atomic jumps across the interface between parent and product phases. In this case, the reaction is called **interface limited**; no long range diffusion is required and single atoms move less than unit cell distances (linear rate law) [58].

Except for **martensitic** transformations (which are diffusionless transformations), diffusion and transport are always necessary to enable the solid-state reaction [58, 59]. Diffusion (via vacancies or interstitial mechanism) can be described as a thermally activated Arrhenius type process, following the equation:

$$D = D_0 e^{-\left(\frac{E_A}{k_B T}\right)}$$

Where E_A is the energy barrier for the defect movement (vacancies or interstitial atoms) [63].

During **self-diffusion** point defects (vacancies, interstitial atoms) need to be formed, i.e. atomic bonds need to be broken; as consequence E_A is in the order of the atomic bond in the solids. However, at dislocation lines and grain boundaries, point defects are already

present: in this case, the energy barrier is lower than in bulk diffusion; the barrier height depends on the geometry of the dislocation/boundary [64-68].

In **homogeneous** reactions, the product nuclei develop uniformly in the parent phase [55, 56, 58, 59]. On the contrary, **heterogeneous** reactions proceed through the continuous movement of the reaction front (or phase boundary), whose morphology rarely resembles the equilibrium shape of the growing crystal. Generally, the boundary motion is strongly influenced by the relative orientation (i.e. conformation of the interface) [61, 69, 70] and the internal structure of the crystals (dislocation, cracks, grain boundary distribution,...), as well as the strength of the driving force (“quasi at” or “far from” equilibrium). For all these reasons, it has been suggested, that the structure of the reacting front itself might influence the transformation mechanism at the microscopic level, which should be investigated in detail in each single case [59].

Solid state reactions in thin films systems differ substantially from their bulk (thick film) counterpart due to the limited size and the interaction with the underneath substrate [38, 71]. For instance, the abundance of grain boundaries and dislocations is higher than in bulk materials, due to the misfit between the film and the substrate; as a consequence low temperature diffusion is favored [64-66]. It has been shown that differently from bulk reactions, which are generally diffusion controlled, in thin films the same reaction is generally interface controlled, showing a linear growth rate [60, 62].

1.7 Supported Nanoparticles on reducible oxide: SMSI

Nano-sized metal catalysts, such as metal nanoparticles (NPs), are a topic of great interest in catalysis (chapter 5). In fact, enhancing the surface/volume ratio, the active catalyst surface increases and the amount of required material is reduced. Moreover, nanometric structures have size-dependent properties, which may differ strongly from those of the bulk material (for instance, Au clusters) [10, 37, 72, 73].

Oxides surfaces are often used as a support for NPs. Depending on the metal/oxide system four main classes of chemical interactions at the metal-oxide interface can occur (see Fig 1.12) [74]:

- Redox reaction: the metal overlayer oxidizes and the oxide is reduced, generally by oxygen diffusion from the supporting oxide

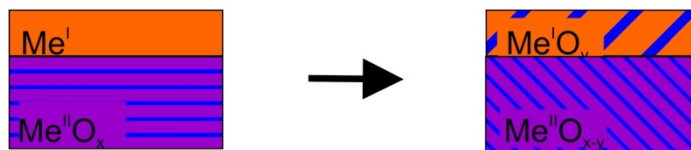
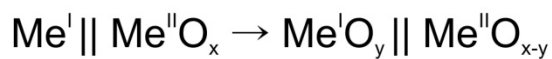
- Alloy formation: metal from the nanostructure and metal from the oxides interact forming stable bimetallic compounds at the interface. The process occurs thanks to the incorporation of oxide cations in the metal overlayer
- Interdiffusion: metal atoms and/or cations from the oxide can diffuse at the interface leading to the formation of a mixed oxide layer or of an "inter-diffusion zone" near the interface
- Encapsulation: the metal overlayer is covered by a thin oxide film. During the reaction, cations diffuse from the oxide over the metal surface

The driving force behind all these processes, which have been addressed in the literature as strong-support interaction (SMSI), is the electrochemical potential gradient across the metal/oxide interface [74]. However, the nature of the metal/substrate interaction is not always fully understood.

The encapsulation process was first found on the TiO_2 system, supporting noble metal NPs (Pt, Pd, Ir, Rh, Fe,...) [75-79], and subsequently on other systems, treated in reducing conditions [80-83]. In the context of heterogeneous catalysis, the interest on this phenomenon arises from the fact that in many cases the chemisorption of gases on the encapsulated particles is strongly altered. Generally, encapsulation have been observed for metal NPs with high surface energies (such as Pt, Pd) supported on oxides with relatively lower surface energy (the driving force is represented by the minimization of the surface energy of the system), and the “reducibility” of the oxide has been identified as one of the key factors. Recently, encapsulation of Pt NPs have been observed also on Fe_3O_4 oxide [9, 52, 84-86].

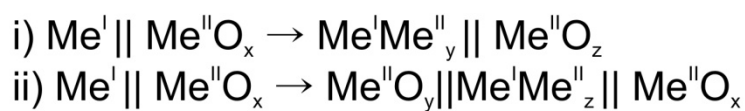
a

Redox Reaction

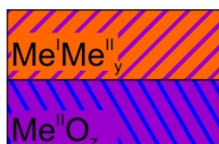
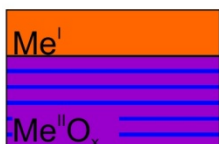


b

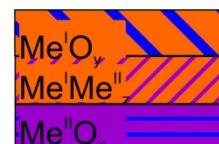
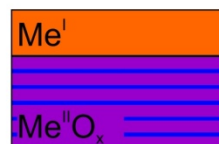
Alloy formation



i)

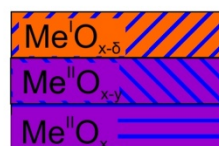
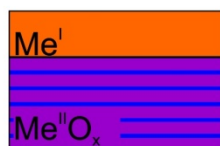


ii)



c

Encapsulation



d

Interdiffusion

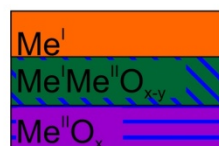
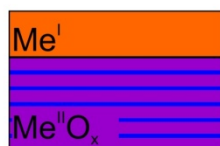


Fig. 1.12: Schematic representation of the four typologies of processes enabled by SMSI: a) Redox Reaction; b) Alloy formation, c) Encapsulation, d) Interdiffusion.

2. Supported α -Fe₂O₃(0001) thin films: growth and preparation

Surface modification induced by Fe deposition on Fe₃O₄(111) and α -Fe₂O₃(0001)

This chapter is divided in two parts. First, I describe the preparation procedure of α -Fe₂O₃ thin films in the low oxygen pressure regime (10^{-6} - 10^{-4} mbar) supported by Pt(111), Ag(111), and Ru(0001). The second part of the chapter focuses on the effects of Fe deposition on the Fe₃O₄ and α -Fe₂O₃ biphasic terminated surfaces. Our experiments show that Fe deposition induces reversible structural modifications of the film termination. As will be discussed, these modifications occur in a well-controlled manner and therefore can tune the surface structure of the Fe-oxide thin film.

2.1 Ordered α -Fe₂O₃(0001) thin film preparation: influence of the oxidation parameters and the substrates morphology.

Preparation procedures and the resulting termination of α -Fe₂O₃ thin films on Pt(111), Ag(111), and Ru(0001) substrates have been widely reported in the literature [18, 22, 47, 87, 88], showing that the termination of α -Fe₂O₃(0001) film strongly depends on the ambient O₂ pressure [88]. O-, Fe- and biphasic terminated surfaces can be produced by varying the oxidation parameters.

Two preparation procedures were mainly used: either oxidation of a precursor Fe₃O₄(111) thin film [22], or the direct oxidation of several ML of deposited Fe, similarly to the method used for Fe₃O₄ in references [8, 52, 86]. Both procedures have been investigated in this work. In this chapter, the second method is discussed; the first one, i.e. the oxidation of Fe₃O₄ film, will be considered in more detail in the next chapter. Films were grown directly in the main chamber of the SMART microscope: in this way, the preparation of the film is followed *in situ* and in real time. As a result we can (i) identify under which conditions the α -Fe₂O₃ phase nucleates, (ii) correlate the preparation conditions to the crystalline quality of the film and (iii) study the influence of the supporting substrate.

All α -Fe₂O₃ films discussed in this work were prepared in a low oxygen pressure regime and are always biphasic terminated. In fact the preparation of the stoichiometric unreconstructed α -Fe₂O₃ termination requires high oxygen pressure ($p_{O_2} > 10^{-1}$ mbar), which is not compatible with UHV systems [22, 89].

2.1.1 α -Fe₂O₃ /Pt(111): investigation of preparation parameters

The preparation of the α -Fe₂O₃(0001) thin films consists in: (i) preparation of a complete FeO monolayer on the clean substrate surface; (ii) repeated cycles of Fe deposition (7-9 ML) at RT; and (iii) oxidation. The procedure is similar to that used for Fe₃O₄(111) [8]. The deposition of Fe is performed at $T < 350$ K: in fact, at higher deposition temperature stable 3D Fe nanoparticles form, which do not change shape during oxidation at higher temperatures (Fig. 2.1).

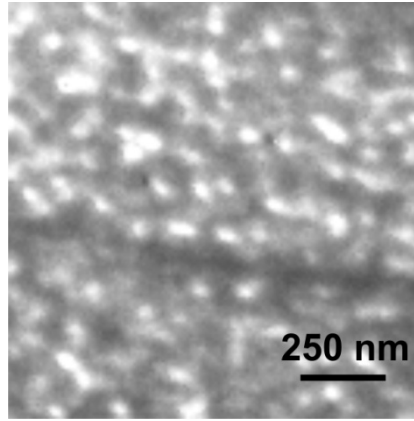


Fig. 2.1: LEEM. Fe NPs on Pt(111) formed by Fe deposition at $T = 370$ K. $E_k = 38$ eV

During the oxidation, the sample is exposed to molecular oxygen and kept for 5-10 minutes at the "oxidation" temperature. The output of this "prolonged" oxidation under specific temperature and pressure conditions is summarized in an experimental "phase diagram" (Fig. 2.2). The final composition was checked moving the sample by ± 1 mm in the x and y direction and the phase identification was based on LEEM and LEED. For pressures higher than 1×10^{-5} mbar, α -Fe₂O₃(0001) single phase thin films were obtained, i.e. without Fe₃O₄ areas, while for lower pressures ($10^{-5} < p_{O_2}$ mbar) the film consisted of coexisting α -Fe₂O₃(0001) and Fe₃O₄(111) areas, separated by well defined boundaries. In thin films oxidized at $p_{O_2} = 1 \times 10^{-6}$ mbar, single phase Fe₃O₄ films are expected [8, 22, 49]. The present investigation shows that α -Fe₂O₃(0001) islands are present as minority defects in an almost homogeneous Fe₃O₄ phase; the nucleation of these defects is discussed in paragraph 2.1.2.

For oxidation temperatures higher than 680-700 K the α -Fe₂O₃ surface shows a sharp diffraction pattern with low background intensity; at lower temperature the LEED pattern is characterized by high background intensity, and unsharp diffraction spots. At oxidation

temperature below 500 K the LEED did not show any clear diffraction spots (α -Fe₂O₃ (0001) or Fe₃O₄ (111)).

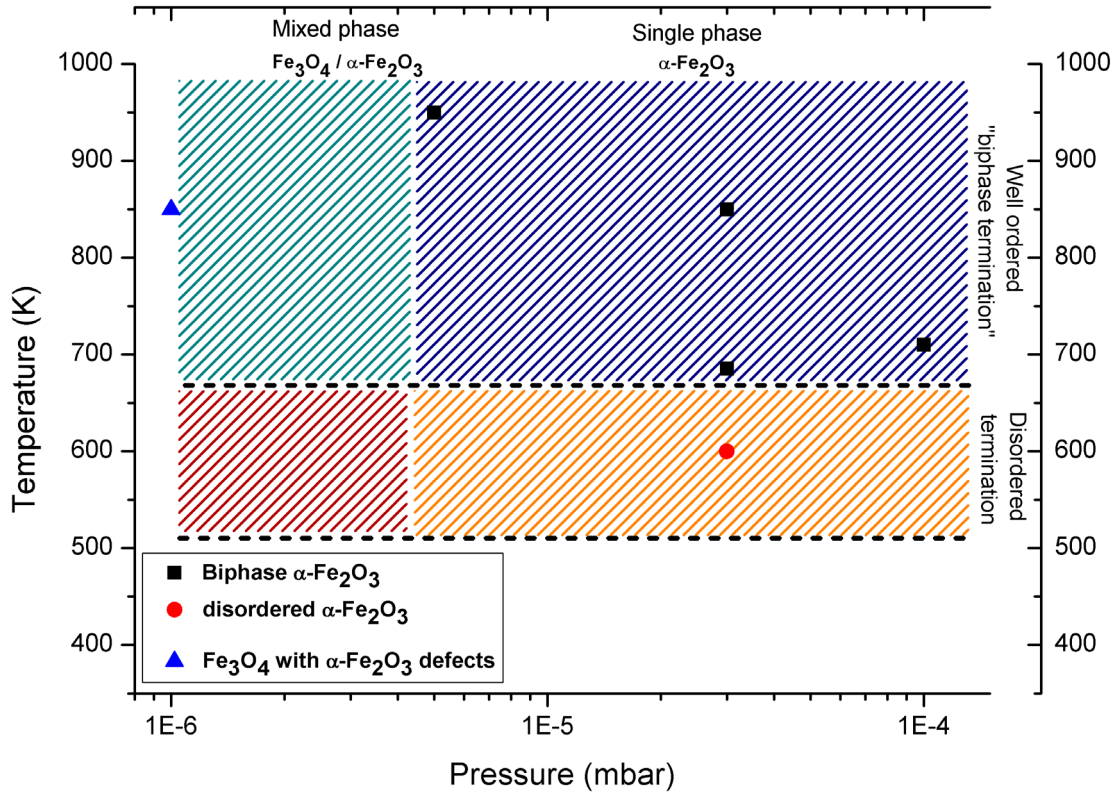


Fig. 2.2: P-T oxidation ranges investigated experimentally. The oxidation time is 5-10 minutes. The resulting film compositions and terminations are indicated. The sample prepared at 1×10^{-6} mbar consists of almost homogenous Fe₃O₄, where α -Fe₂O₃ islands are present as minority defects.

Thanks to real time LEED acquisition, individual stages occurring during the formation of a single phase α -Fe₂O₃(0001) film (biphase terminated) can be isolated. To do so, I studied the real time changes of the LEED pattern during isobaric ($p_{O_2} = 3 \times 10^{-5}$ mbar) annealing of the sample from RT to $T = 850$ K. Prior to the annealing 5 ML of Fe were deposited on a ≈ 10 nm thick film of Fe₃O₄(111) /Pt(111). Even if the reported data refer to a single experiment, the oxidation of the film follows generally these steps. During oxidation, the unordered Fe layer (Fig. 2.3a) crystallizes to Fe₃O₄ first: the oxidation starts at $T \approx 500$ K, when the (2x2) reconstruction appears (Fig. 2.3b). The initial Fe₃O₄ film is further oxidized to α -Fe₂O₃ at $T \approx 650$ K; at this temperature, the $(\sqrt{3} \times \sqrt{3})R30^\circ$ spots are unsharp and surrounded by a broad shadow. Finally, the formation of a clear biphase ordering at the surface (indicated by the

presence of the hexagonal extra-spots) occurs for oxidation temperatures higher than $T \approx 700$ K (Fig 2.3d; $T=850$ K).

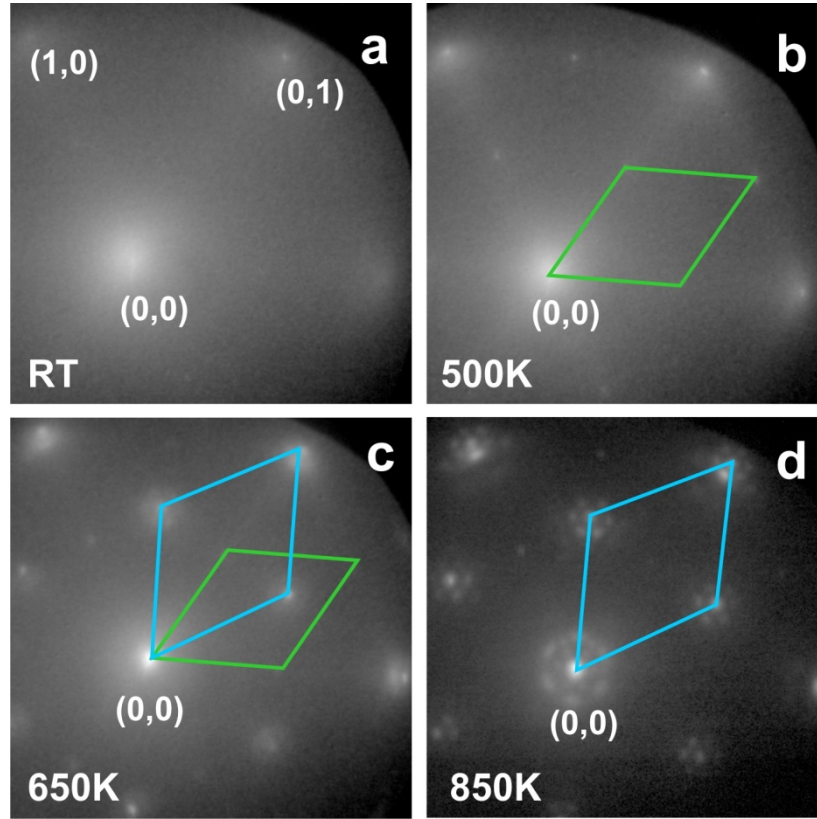


Fig. 2.3: LEED. Sequence during the isobaric annealing of the sample up to $T=850$ K; $p=3.0 \times 10^{-5}$ mbar; temperatures for each oxidation stage are indicated . Fig 2.3a) Fe layer as deposited at RT (5 ML). After deposition, the LEED pattern exhibits high non-crystalline background and the (2×2) diffraction spots from the $\text{Fe}_3\text{O}_4(111)$ substrate are absent, indicating the formation of an unordered Fe overlayer during deposition. Fig 2.3b) $\text{Fe}_3\text{O}_4(2 \times 2)$ reconstruction appears at ≈ 500 K; the background intensity is slightly decreased, due to the progressive ordering of the film. Fig 2.3c) developing $\alpha\text{-Fe}_2\text{O}_3$ phase spots appear at ≈ 650 K. The LEED pattern shows the co-existence of the (2×2) and $(\sqrt{3} \times \sqrt{3})R30^\circ$ diffraction spots, of the Fe_3O_4 and $\alpha\text{-Fe}_2\text{O}_3$ phase respectively. Fig 2.3d) biphasic terminated $\alpha\text{-Fe}_2\text{O}_3$ after oxidation at 850 K. The LEED image shows a sharp $(\sqrt{3} \times \sqrt{3})R30^\circ$ reconstruction; well defined hexagonal extra spots surround the $(0,0)$ and each second order spot. The (2×2) spots are absent. $E_k=38$ eV

$\alpha\text{-Fe}_2\text{O}_3(0001)$ films prepared at temperatures lower than $T \approx 700$ K, do not show clear hexagonal biphasic patterns, but diffuse intensity surrounding the main spots (Fig. 2.3c), meaning that the surface is not “long range ordered”. This can have two reasons: either the surface termination is structurally different from the biphasic, or the temperature is not high enough to establish perfect long range order. One method to probe (at least to some extent) the

surface structure is to measure the elastic backscattering reflectivity of the surface by varying the electron beam energy. This kind of measurements is called LEEM-IV analysis in brightfield mode (as only the (0,0) spot is used). The intensity modulations in the LEEM-IV curve relate to the crystal periodicity and to the band structure in the direction normal to the surface [30, 31]. The comparison of the LEEM-IV profiles of the "low" and "high" temperature terminations of the α -Fe₂O₃(0001) film is shown in Fig. 2.4. The surfaces were prepared by 5 min oxidation of Fe ($p_{\text{O}_2}=10^{-5}$ mbar) at 700 K and 850 K respectively; Fe was deposited at RT. Fig. 2.4 shows mainly qualitative differences between the absolute intensities between the two datasets. On the other hand, there is a clear correspondence of the maxima and minima in the energy dependence, indicating that the structures of these two terminations are similar.

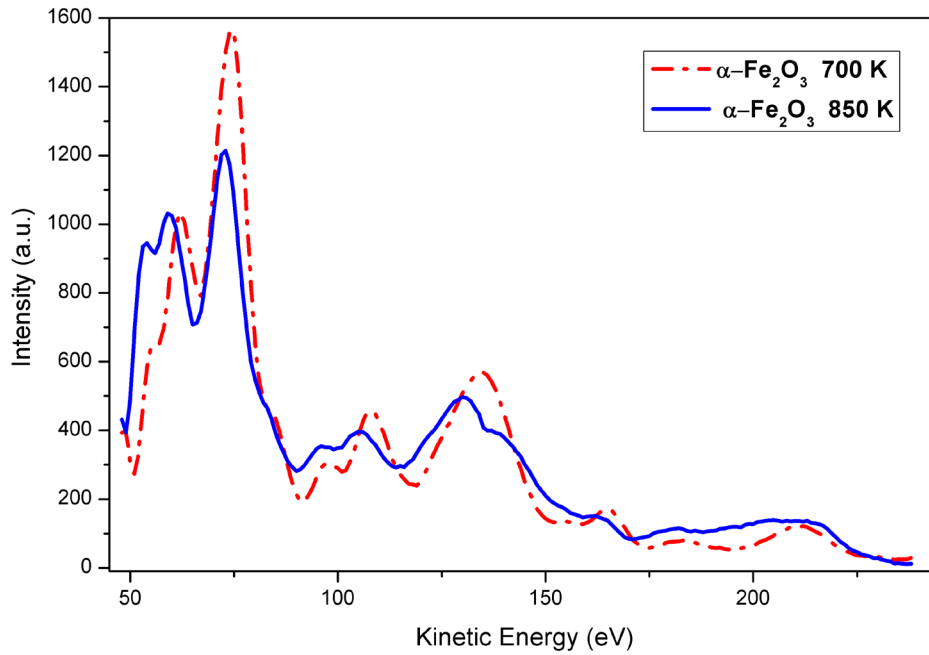


Fig. 2.4: LEEM-IV curves for α -Fe₂O₃ oxidized at T=700 K in blue (no clear biphas extra spots) and at T=850 K. The reflectivity of the surface in the normal direction depends on the band structure (the incoming electrons interact with the allowed electronic states of the crystals) and the crystal structure (scattering center periodicity) in the same direction. The two datasets show the same max-min modulation as a function of the incoming electron energy, which suggests that the two terminations have similar structures.

The reason for the absence of a clear hexagonal extra pattern in LEED is most likely the broadening of the diffraction spot size (which is inversely related to the domain size). After

low temperature oxidation, the surface consists of small and disordered biphas domains on the $\alpha\text{-Fe}_2\text{O}_3$ surface.

2.1.2 $\alpha\text{-Fe}_2\text{O}_3$ nucleation: role of the substrate defects

Real space recording (see for instance Fig. 2.5) of the sample oxidation shows that typically the $\alpha\text{-Fe}_2\text{O}_3$ phase (white contrast in the images) develops on the Fe_3O_4 phase (gray contrast) by the expansion of a clear growing front: homogenous nucleation was never observed in our experiments. The question addressed in this section is: where does the front originate?

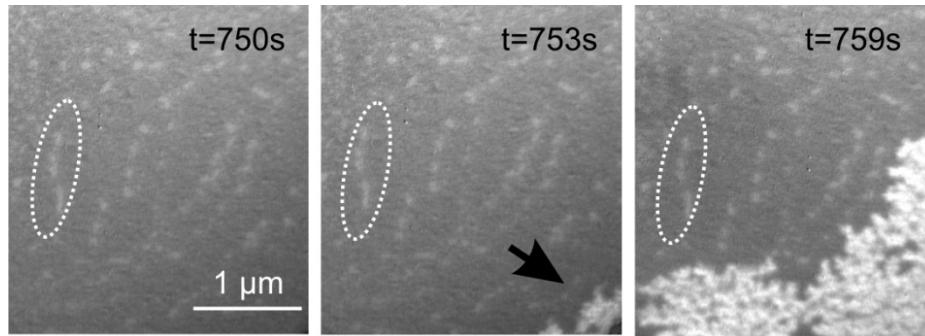


Fig. 2.5: LEEM. Typical growing front during $\alpha\text{-Fe}_2\text{O}_3$ (white) formation on Fe_3O_4 (gray); brighter islands in the Fe_3O_4 phase are FeO defects ($p=3\times 10^{-5}$ mbar, $T= 663$ K. $E_k= 23$ eV).

To answer this question, I have investigated a freshly prepared Fe_3O_4 film, oxidized at $T= 775$ K and $p_{\text{O}_2}=1\times 10^{-6}$ mbar, i.e. very close to the conditions generally used to prepare Fe_3O_4 films. Moving the sample by ± 1 mm in the x and y direction, $\alpha\text{-Fe}_2\text{O}_3$ nuclei were found dispersed in the homogenous Fe_3O_4 phase. The $\alpha\text{-Fe}_2\text{O}_3$ nuclei were spaced by ≈ 100 μm from each other and in all cases they were close to mesoscopic irregularities in the sample, as shown, for example in the series of images in Fig. 2.6. These objects are big defects, which affect the accelerating field between the sample and the objective lens. The identification of the co-existing Fe_3O_4 (black) and $\alpha\text{-Fe}_2\text{O}_3$ (white) phases is based on LEED and darkfield imaging.

To characterize the $\alpha\text{-Fe}_2\text{O}_3$ nucleation process in its initial stages, I focused the attention on a mesoscopic defect similar to the ones in Fig 2.6, where $\alpha\text{-Fe}_2\text{O}_3$ had not yet formed. The area was recorded during oxidation at $p_{\text{O}_2}=1\times 10^{-6}$ mbar, $T=773$ K after 5 ML Fe deposition at RT, i.e. reproducing the same condition used during the film preparation.

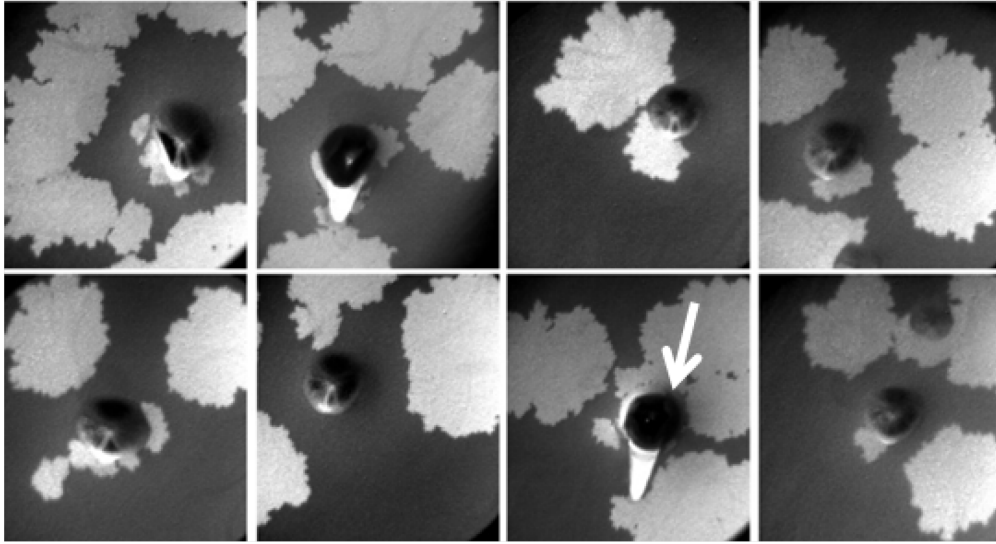


Fig. 2.6: LEEM. Example of α -Fe₂O₃ nuclei (white) on Fe₃O₄ film. Mesoscopic defects distorting the images are visible. In this case the film was prepared at $p_{O_2}=1 \times 10^{-6}$ mbar, $T=775$ K. The white arrow indicates the Fe deposition direction, which has been determined by the local XPS measurements described below. FoV=20 μ m, $E_K=38$ eV

The real time observation of the α -Fe₂O₃ formation is shown in the sequence Fig 2.7. After ≈ 160 s two small nuclei with white contrast appear. The number of nuclei increases with time; at the same time, they enlarge and merge. A closer look at the surface shows that phase boundaries expand along the line defects of the Fe₃O₄ phase.

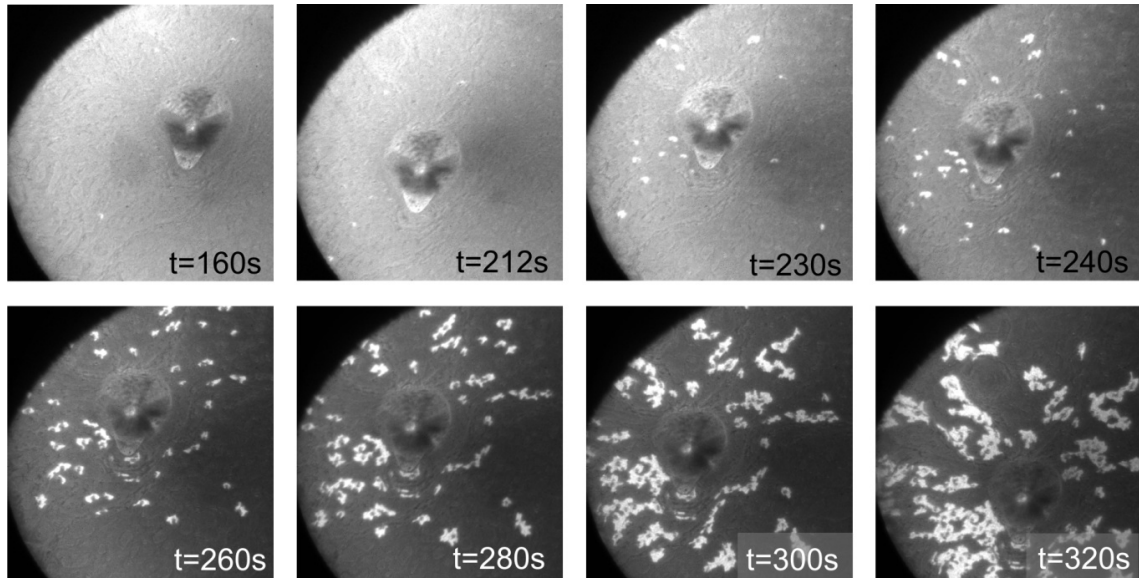


Fig. 2.7: LEEM. Real time observation of pristine α -Fe₂O₃ (white) on former Fe₃O₄ film ($p_{O_2}=1 \times 10^{-6}$ mbar, $T=773$ K). The change in the image contrast is associated with the progressive oxidation of the deposited Fe layer. FoV = 20 μ m; $E_K=24$ eV

The chemical composition of the area was characterized by spatially resolved XPS (spectra not shown) at the Pt4f and Fe3p peaks. LEEM (Fig 2.8a) and X-PEEM (Fig 2.8b-c) of the area are visible in Fig. 2.8. The black areas in the two PEEM images, absent in the LEEM image, are the light shadows produced by the mesa-like structure under the grazing incidence of the X-ray beam (20°): they are absent in the LEEM image, because of the normal incidence of the electron beam.

Fig 2.8b shows the X-PEEM image at the maximum of the Pt4f_{7/2} emission: the mesa-like structure and small islands in the film are bright, while the film is dark. Looking more carefully at the image, the “bottom” side of the mesa-structure appears brighter than the “top” one. Looking at the Fe3p emission peak, we observe the inversion of the contrast: the film is bright, as well as the top side of the protrusion, while its bottom side and the small island in the film are dark.

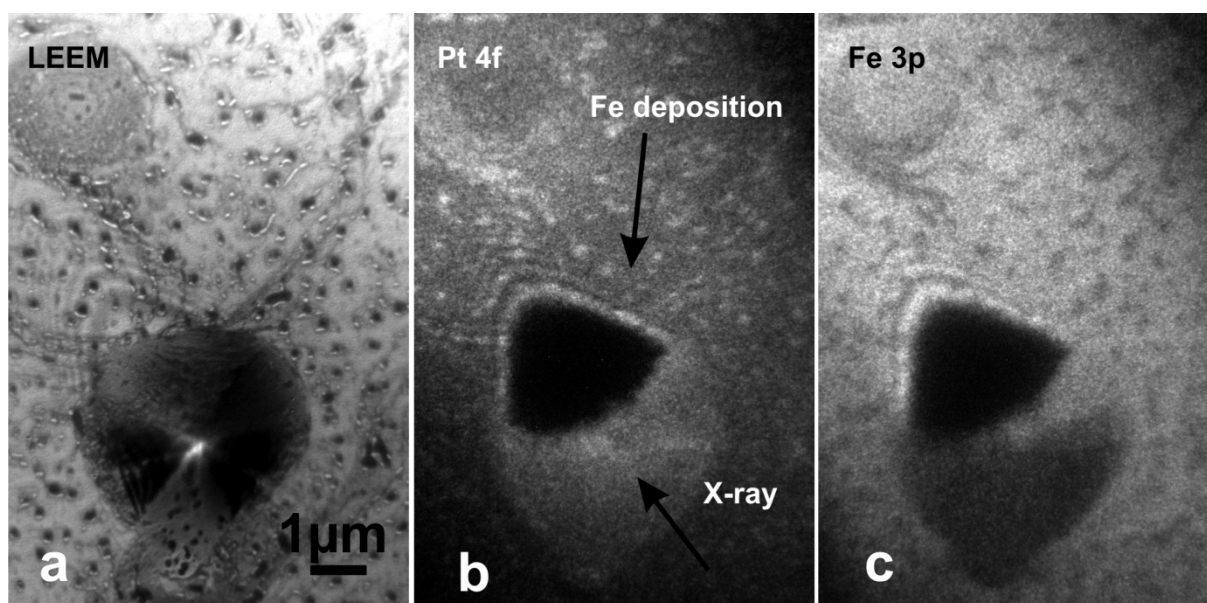


Fig. 2.8: LEEM (a) and X-PEEM (b-c) of the mesa-structure area. Fig. 2.8b) contrast obtained at the Pt4f line ($h\nu = 175$ eV, $E_k = 96.8$ eV). Fig. 2.8c) contrast obtained at the Fe3p line ($h\nu = 150$ eV, $E_k = 90.4$ eV) Fresnel diffraction fringes from the x-rays (at the mesa-like structure) are visible in the X-PEEM and LEEM image (in the latter case arising from beam damage).

This investigation shows that in the initial stages α -Fe₂O₃ domains nucleate in specific areas of the Fe₃O₄ films, close to big defects on the sample. The real time recording of the nucleation process shows that small nuclei form, initially scattered in the Fe₃O₄ phase, progressively enlarge and finally merge. The X-PEEM characterization outlines that the defect consists in a Pt protrusion, covered by iron oxide in the top part. The bottom side

consists of bare Pt, where Fe atoms were not deposited due to shadowing effect that the protrusion itself produces on the Fe flux. The small islands in the film are FeO(111) holes, ≈ 1 ML thick: the Pt signal is visible as the FeO layer is thinner than the escape depth of the electrons at this kinetic energy (≈ 0.6 nm). The protrusion height was inferred from the length of the mesa structure shadow illuminated with the X-ray beam (grazing incidence 20°) as shown in Fig 2.9b.

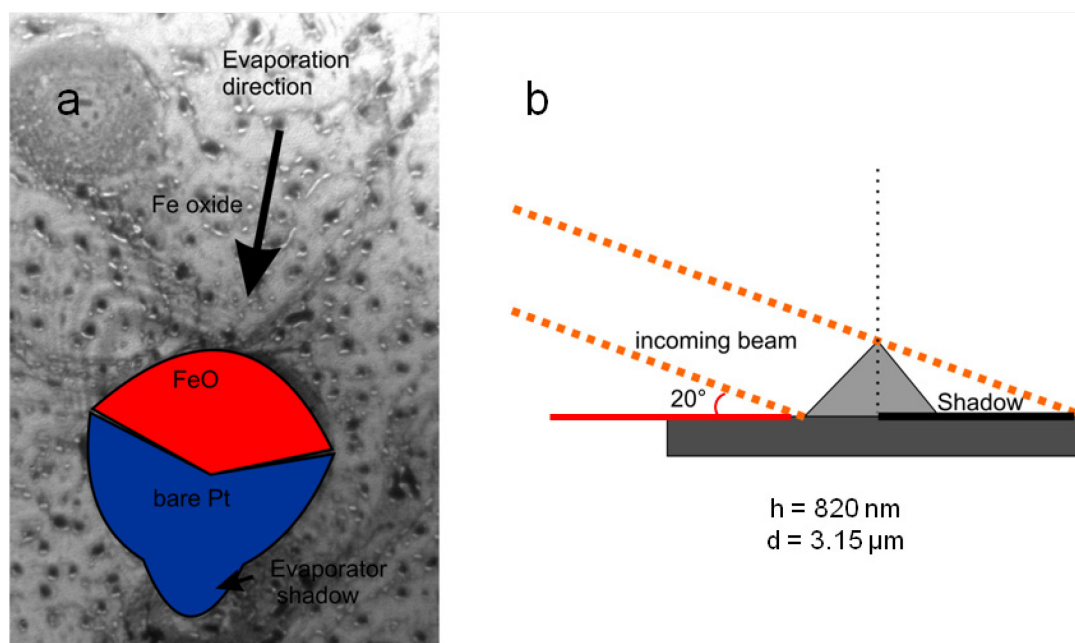


Fig. 2.9: a) LEEM. Composition of the area based on the local XPS spectra. Fig. 2.9b) Protrusion height determination was based on the shadow of the x-ray beam.

In the nucleation process of a new crystallographic phase in the parent (in this case $\alpha\text{-Fe}_2\text{O}_3$ and Fe_3O_4 , respectively) defects in the film are preferred nucleation sites because the stress contribution arising at the parent/product interface is lowered [59, 62]. For example, regions where there is a higher concentration of defects, step bunches, or other irregularities (grain boundaries, dislocations,...) are good candidates. Additionally, super-saturation is necessary to observe the process [58, 59]. Experimentally we observe the nucleation of $\alpha\text{-Fe}_2\text{O}_3$ only close to Pt mesa-structures. Therefore, we deduce that locally the system is super-saturated: most likely, the abundance of atomic oxygen is higher close to the protrusion than in other areas of the film. As the $\alpha\text{-Fe}_2\text{O}_3$ nuclei do not form in direct contact with the Pt protrusion, it might be that the Pt protrusion promotes the dissociation of O_2 (from the gas phase) to atomic oxygen, increasing locally the abundance of atomic oxygen at the oxide surface. However, the oxygen

atoms are not directly incorporated into the oxide, but diffuse on the surface to meet specific nucleation sites where they can be incorporated into the oxide.

2.1.3 α -Fe₂O₃: crystallographic defects

Rotational domains: α -Fe₂O₃

α -Fe₂O₃, like Fe₃O₄, can crystallize in two equivalent rotational domains. The distribution of the rotational domains can be visualized by darkfield imaging; in this mode, electrons from a selected LEED spot are used. Fig. 2.10a-b shows the darkfield images using the half order diffraction spots of α -Fe₂O₃, while Fig. 2.10c-d shows the darkfield images on an Fe₃O₄ thin film, using the ($\frac{1}{2}$;0) and the (0; $\frac{1}{2}$) diffraction spots. The inversion of the intensity between Fig. 2.10a and Fig. 2.10b means that the α -Fe₂O₃ film consists of two big rotational domains ($\approx 10\ \mu\text{m}$). On the other hand, the structure of the Fe₃O₄ film is much more “grainy” and the domains are much smaller ($< 1\ \mu\text{m}$) than those of α -Fe₂O₃.

These images reveal that, in the α -Fe₂O₃ phase, the rotational domains distribution differs substantially from that of its precursor Fe₃O₄, meaning that the crystalline domains of the Fe₃O₄ phase do not influence the domain orientation in the growing α -Fe₂O₃ phase. Most likely, during its growth, the α -Fe₂O₃ phase prefers to orient in one single domain (taking over the orientation of the initial defects) rather than forming many small rotational domains, separated by many anti-phase boundaries. As we have already discussed in the previous sections, the oxidation of the Fe₃O₄ film to α -Fe₂O₃ proceeds by the enlargement of α -Fe₂O₃ islands scattered in the Fe₃O₄ phase. Most likely, rotational domain boundaries are visible where two islands, differently oriented, merged together.

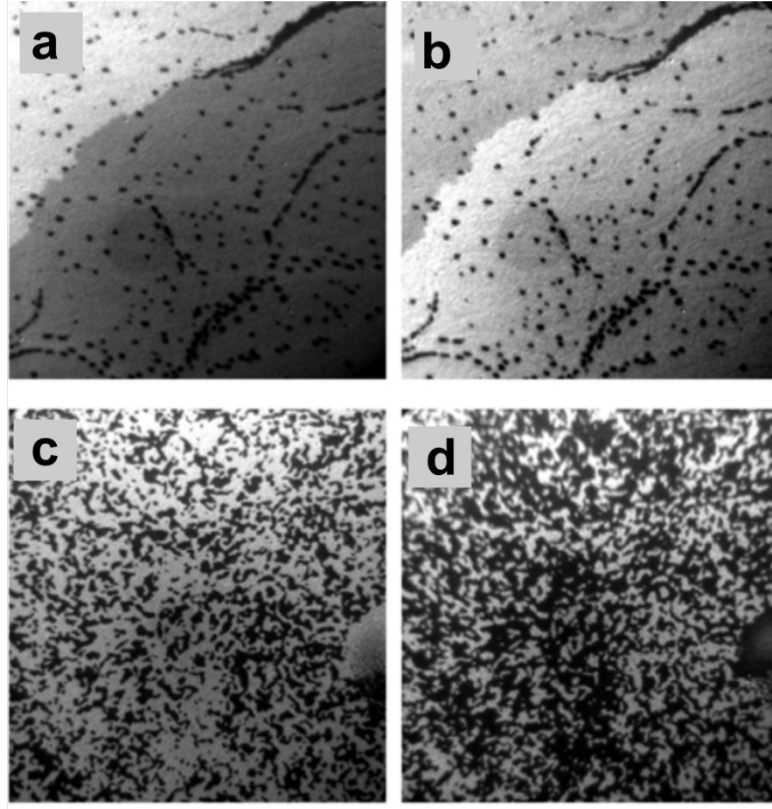


Fig. 2.10: LEEM. α -Fe₂O₃/Pt(111). Darkfield images reveal the presence of very big rotational domains (FoV = 12.4 μ m x 12.4 μ m, E_k = 24 eV). Fig 2.10 c-d) For comparison rotational domains of Fe₃O₄/Pt(111) at the same FoV are shown (E_k = 24 eV).

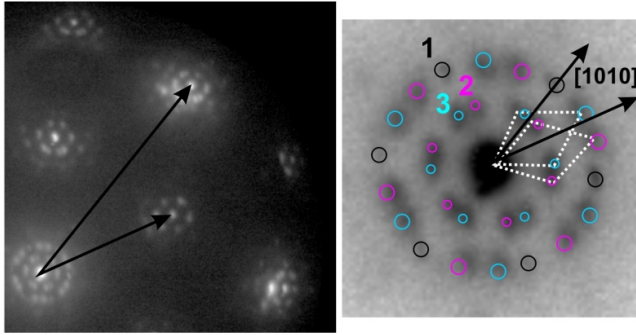
Rotational domains: Biphasic termination on α -Fe₂O₃

Fig 2.11a presents the LEED pattern of a single phase α -Fe₂O₃ thin film. The magnification around the (0,0) spots shows three kinds of spots associated with long range ordering. The spots are marked with three different colors. The black spots are the fingerprint of the FeO/Pt(111) Moiré pattern, having a periodicity of ≈ 20 Å, and being aligned along the [110]_{Pt} direction (which is equivalent to the [10-10] _{α -Fe₂O₃} direction). The second kinds of spots are indicated with magenta and light blue. They are the fingerprint of the biphasic superstructure. The innermost spots are the first order spots, with a lateral periodicity of ≈ 37.7 Å in real space. The blue and the magenta spots are tilted relative to the [1010] _{α -Fe₂O₃} direction by +10° and -10°, respectively. A similar rotation of superstructure spots was found and discussed in the case of FeO/Pt(111) [22, 51, 90]. Experimentally, the correlation between the biphasic and the α -Fe₂O₃ rotational domains (in the bulk of the film) could not be ruled out because darkfield imaging, in this case, cannot separate their contributions (both diffraction beams pass through the contrast aperture).

Fig 2.11b shows a simple geometrical model, reproducing the features of the LEED pattern discussed above. As will be discussed in detail in 2.2, the biphasic reconstruction is a consequence of the relaxation of the topmost oxygen layer compared to the $\alpha\text{-Fe}_2\text{O}_3$ bulk periodicity. The mismatch between the relaxed top-most oxygen layer and the un-relaxed underlying O layers in the $\alpha\text{-Fe}_2\text{O}_3$ bulk gives rise to a periodic modulation of the surface structure.

The model in Fig 2.11b displays only the O sub-lattices for the topmost and underlying layer. It should be kept in mind that this model is purely geometrical and both rotation angles and lattice expansion have been chosen arbitrarily. The light blue atoms represent the topmost layer, expanded relatively to the $\alpha\text{-Fe}_2\text{O}_3$ bulk value. The underlying oxygen layer of $\alpha\text{-Fe}_2\text{O}_3$ is colored orange. The topmost O lattice is rotated by -4.8° respect to the underlying O sublattice, leading to coincidence sites which are indicated by the green color. The unit cell of the coincidence overlayer structure ($\approx 36.6 \text{ \AA}$ lateral periodicity) is indicated in Fig 2.11b, being rotated by $+9^\circ$ respect to the $\alpha\text{-Fe}_2\text{O}_3$ unit cell. If the topmost O lattice is rotated by $+4.8^\circ$ respect to the $\alpha\text{-Fe}_2\text{O}_3$ orientation, the coincidence unit cell is rotated by -9° . The O-O interatomic distance is 3.15 \AA , which is extremely close to the value measured by STM on the biphasic terminated $\alpha\text{-Fe}_2\text{O}_3$ in [91].

a



b

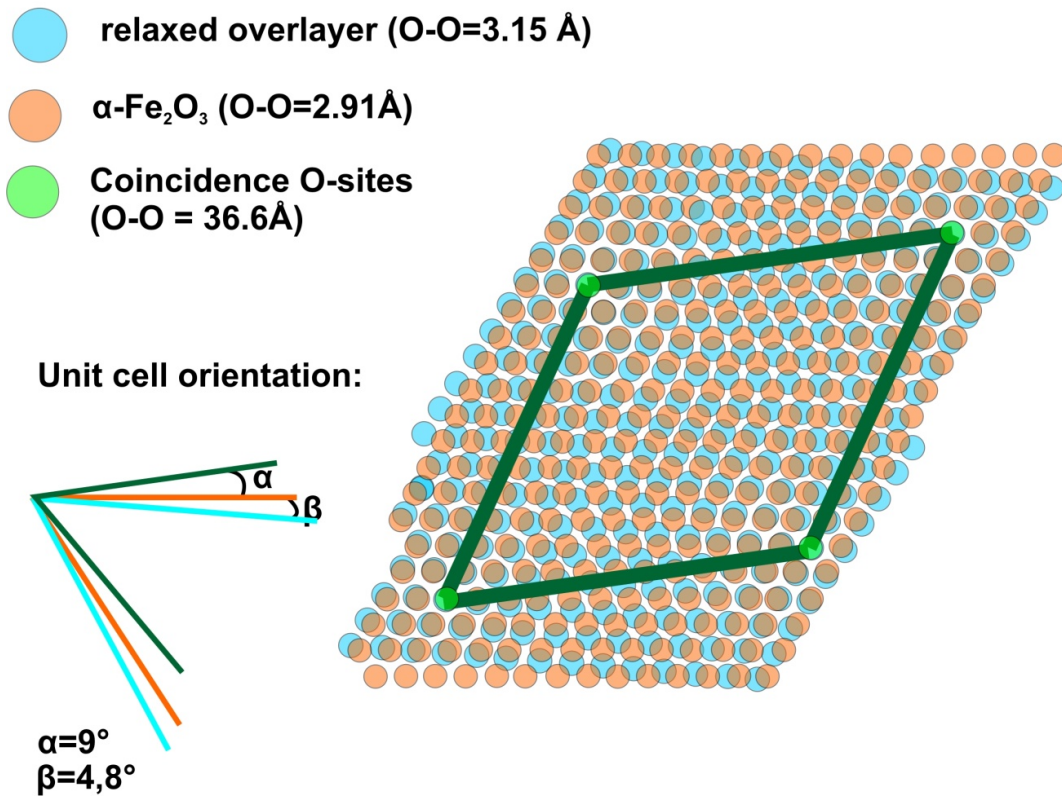


Fig. 2.11a) LEED pattern of the biphase in α -Fe₂O₃. The magnified image is shown on the right. Rotational domains of the biphase structure are indicated by magenta and blue circles; the FeO/Pt(111) superstructure is indicated in black ($E_k=40$ eV). Fig 2.11b displays a geometrical model for the system; only O sub-lattices have been considered. The light blue atoms represent the expanded topmost layer with respect to the α -Fe₂O₃ bulk value (orange). The topmost O lattice is rotated by -4.8° respect to the underlying O sublattice (both rotation angle and lattice expansion have been chosen arbitrarily). The coincidence sites are indicated by the green color. The unit cell of the coincidence overlayer structure (≈ 36.6 Å lateral periodicity) is indicated in Fig 2.11b, being rotated by $+9^\circ$ respect to the α -Fe₂O₃ unit cell.

Dewetted area of the α -Fe₂O₃ thin film: FeO phase

FeO areas are common defects in supported α -Fe₂O₃ and Fe₃O₄ thin films grown in our set-up [8, 52]. X-PEEM at the Pt4f peak (Fig 2.12c) confirms that these areas consist of a FeO layer, thinner than the escape depth of photo-emitted photons from the Pt substrate (1 ML). The formation of such “holes” in the Fe-oxide films grown on Pt indicates that Fe-oxides do not tend to wet the substrate, as already discussed in the literature [8, 22, 51]. FeO formation (dewetting of the film) is strongly enhanced by high temperature UHV annealing. In fact, high temperatures enable Fe diffusion (thermally activated), which is suppressed at lower temperatures. An example is given in Fig. 2.12a-b which shows the enlargement of the FeO area occurring during UHV annealing at $T = 920$ K (the annealing time was $t \approx 10$ min).

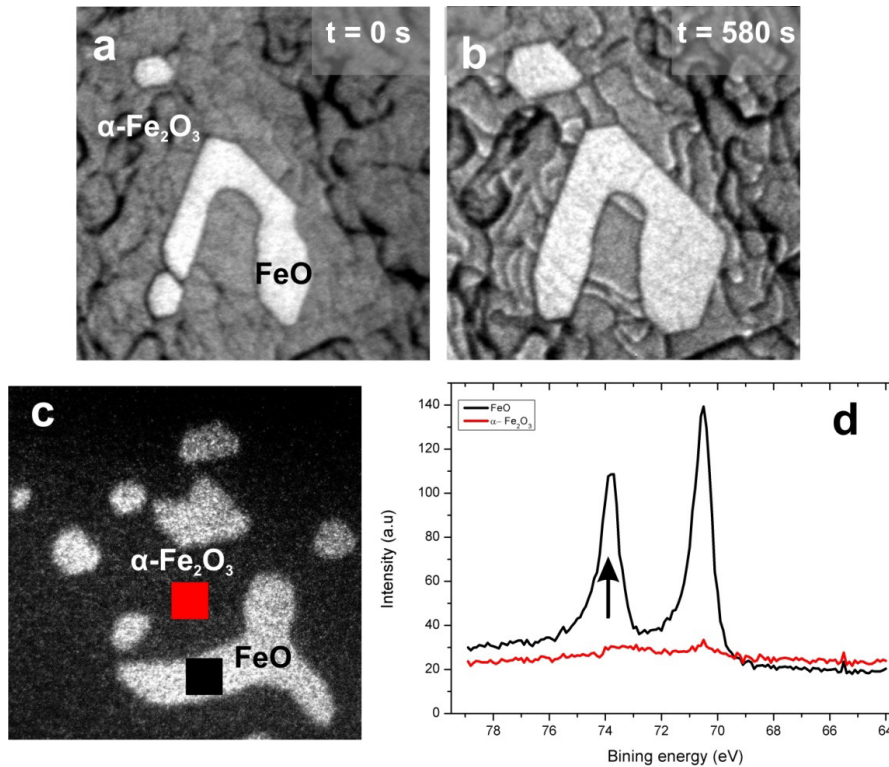


Fig. 2.12: α -Fe₂O₃/Pt(111). a-b) LEEM. FeO area in α -Fe₂O₃ before and after $t \approx 10$ min annealing in UHV at $T = 920$ K. The FeO area is enlarged because of the film dewetting. (FoV = $3.15 \times 3.15 \mu\text{m}$, $E_k = 38$ eV, FeO bright). X-PEEM at Pt4f (c) confirms that the FeO areas are holes in the film. (FoV = $4.90 \mu\text{m}$; $h\nu = 210$; $E_k = 136$ eV). Fig 2.12d) Integrated Pt4f spectra from the selected areas indicated in Fig 2.12c: the black and the red lines correspond to FeO and α -Fe₂O₃ phases, respectively.

Fig. 2.13 shows LEEM with electrons of $E_k = 5$ eV. Because the large electron escape depth (≈ 50 nm) in this energy range, the underlying morphology of the Pt substrate can be visualized. The wide darker lines in Fig. 2.13a correspond to the step bunches of the Pt(111)

crystal, and white areas are FeO holes. The shape of the FeO holes follow the substrate step bunches; in those regions the dewetting process is enhanced, which are unstable relative to thick Fe-oxide phases (Fig 2.13b) [8]. Dewetting can be partially reduced by lowering the oxidation temperature [52].

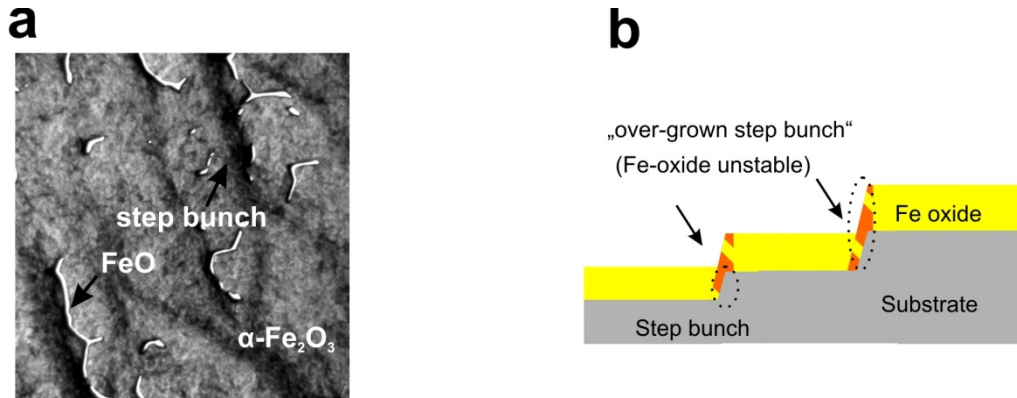


Fig. 2.13: a) LEEM. α -Fe₂O₃/Pt(111). FeO areas (with contrast) follow substrate steps bunches (wide dark lines) (FoV=8.27 μ m, E_k=5 eV). In this electron energy range, the LEEM image probes the deeper structure of the film: in fact, the escape depth of electrons in this energy range is \approx 50 nm, i.e. in the order of the film thickness. b) Schematic model of the sample structure.

2.1.4 α -Fe₂O₃ thin films supported on Ag(111) and Ru(0001)

α -Fe₂O₃ films were also successfully grown on Ag(111) and Ru(0001) surfaces, following the procedure adopted in [20, 47] and in [18], respectively. Also on these substrates, the preparation consists in cycles of Fe deposition and oxidation; however on Ag(111) we used lower oxidation temperature and longer oxidation times to prevent the segregation of Ag to the oxide surface and to ruin the substrate. In fact, the Ag(111) melting temperature (1240 K) is considerably lower than those of Pt (2050 K) and Ru (2610 K). The quality of the resulting film was checked in LEED, by evaluating the sharpness of the diffraction spots and the intensity of the background.

Table 2.1 summarizes standard pressure and temperature values used in our experiments for each substrate. Choosing these values lowers the annealing time, reduces dewetting and the necessary O₂ pressure (avoiding arc-overs inside the main chamber and decreasing the time required to pump the system down to UHV), and maintaining a good crystalline quality.

	Pt(111)	Ag(111)	Ru(0001)
Fe₃O₄	T=900K ;	T=670 K ;	T=900 K ;
	p=1.0x10 ⁻⁶ mbar	p=1.0x10 ⁻⁶ mbar	p=1.0x10 ⁻⁶ mbar
α-Fe₂O₃	T=870 K ;	T=820K ;	T=870 K ;
	p=3.0x10 ⁻⁵ mbar	p=3.0x10 ⁻⁵ mbar	p=3.0x10 ⁻⁵ mbar

Table 2.1: Optimized preparation parameters for Fe-oxides phase on Pt(111), Ag(111) and Ru(0001) substrates

As already pointed out, α -Fe₂O₃ grown in our set-up is always biphasic terminated. To rule out any influence of the lattice constant of the substrate on the structure of this termination, we have compared the superstructure spots for α -Fe₂O₃ films grown on these three different substrates, using SPA-LEED profile analysis. The α -Fe₂O₃ film was prepared in three different experiments on each of the substrates, i.e. α -Fe₂O₃/Pt(111), α -Fe₂O₃/Ag(111) and α -Fe₂O₃/Ru(0001). In the first step a FeO(111) layer was always prepared, i.e. FeO/Pt(111), FeO/Ag(111) and FeO/Ru(0001). The LEED patterns of the first FeO layer and for the final α -Fe₂O₃ film were acquired.

Thanks to the special optics of the SMART microscope (homogenous accelerating field and alignment of the optical axis), the diffraction spot position is independent on the electron energy. For each SPA-LEED profile, the calibration of the k-space position is referred to a fixed reference spot, whose corresponding real space distance is known. In this specific case, I have used the position of the $(\sqrt{3} \times \sqrt{3})R30^\circ$ spot of the α -Fe₂O₃ crystal, which is independent of the substrate periodicity unlike the FeO Moiré pattern or the substrate lattice constant. The same k-space calibration is valid for the FeO dataset, as within the experiment the optical alignment of the microscope was not changed.

Fig 2.14 shows the cross sections of the LEED intensity along the diagonal in the (1;0) direction for the first FeO(111) layer and the α -Fe₂O₃(0001) film growth on top of it. While we observe a change in the Moiré pattern periodicity for the FeO(111) layer grown on Pt(111), Ag(111) or Ru(0001) as a consequence of the different mismatches between substrate and

oxide overlayer (Fig 2.14a), the periodicity of the biphas superstructure on the α -Fe₂O₃ phase does not change (Fig 2.14b).

Consequently we conclude that the biphas termination on α -Fe₂O₃ is an intrinsic reconstruction of the surface, and its periodicity is independent of the film/substrate mismatch.

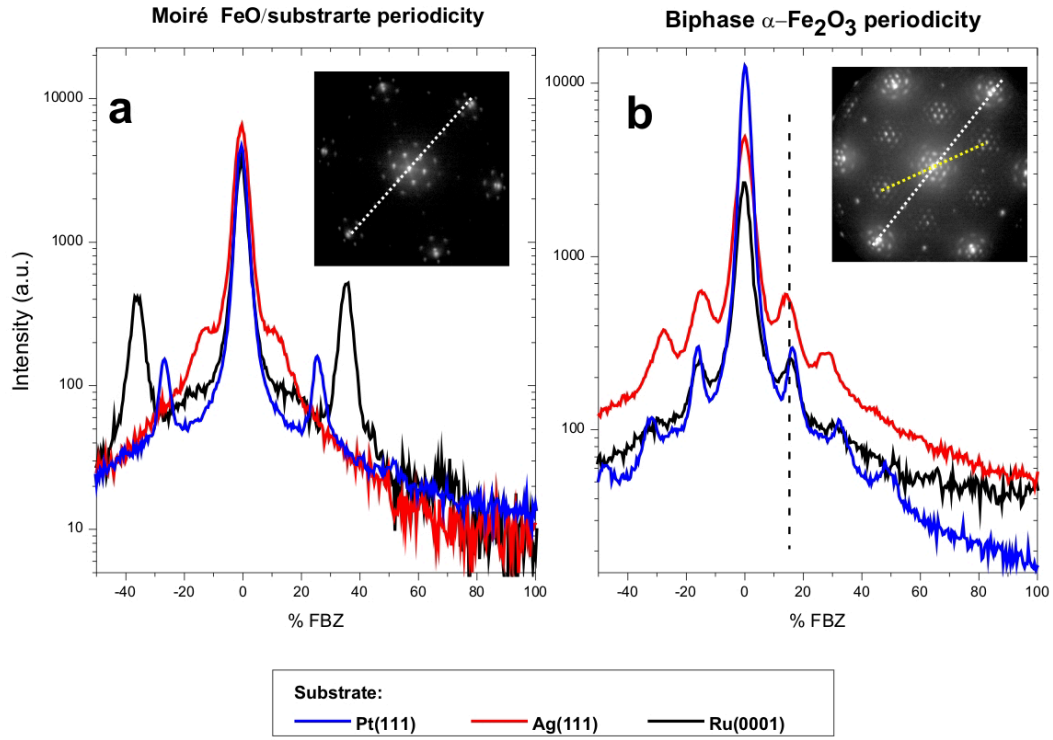


Fig. 2.14: SPA-LEED of the FeO(111) and biphas superstructure for thin films supported on Ag(111), Pt(111) and Ru(0001) substrates. The cross sections are taken along the (0,1) direction of the substrate (white lines). Both x-axes (also for the FeO layer) have been calibrated on the α -Fe₂O₃ Fe-sublattice unit cell (100% BZ) (yellow line in Fig 2.14b).

2.1.5 Mixed films

We have seen that α -Fe₂O₃ forms by the oxidation of deposited Fe to Fe₃O₄ and subsequently to α -Fe₂O₃. Stopping the oxidation before the complete conversion of the Fe₃O₄ phase leads to the co-existence of Fe₃O₄/ α -Fe₂O₃ phases in the same sample. The application of such Fe₃O₄/ α -Fe₂O₃ “mixed films” is very useful in experiments because the Fe₃O₄ and α -Fe₂O₃ can be studied under identical experimental conditions and can be directly compared.

In $\text{Fe}_3\text{O}_4/\alpha\text{-Fe}_2\text{O}_3$ mixed films, the two phases are univocally identified using the specific contrast in both LEEM and X-PEEM (Fig. 2.15).

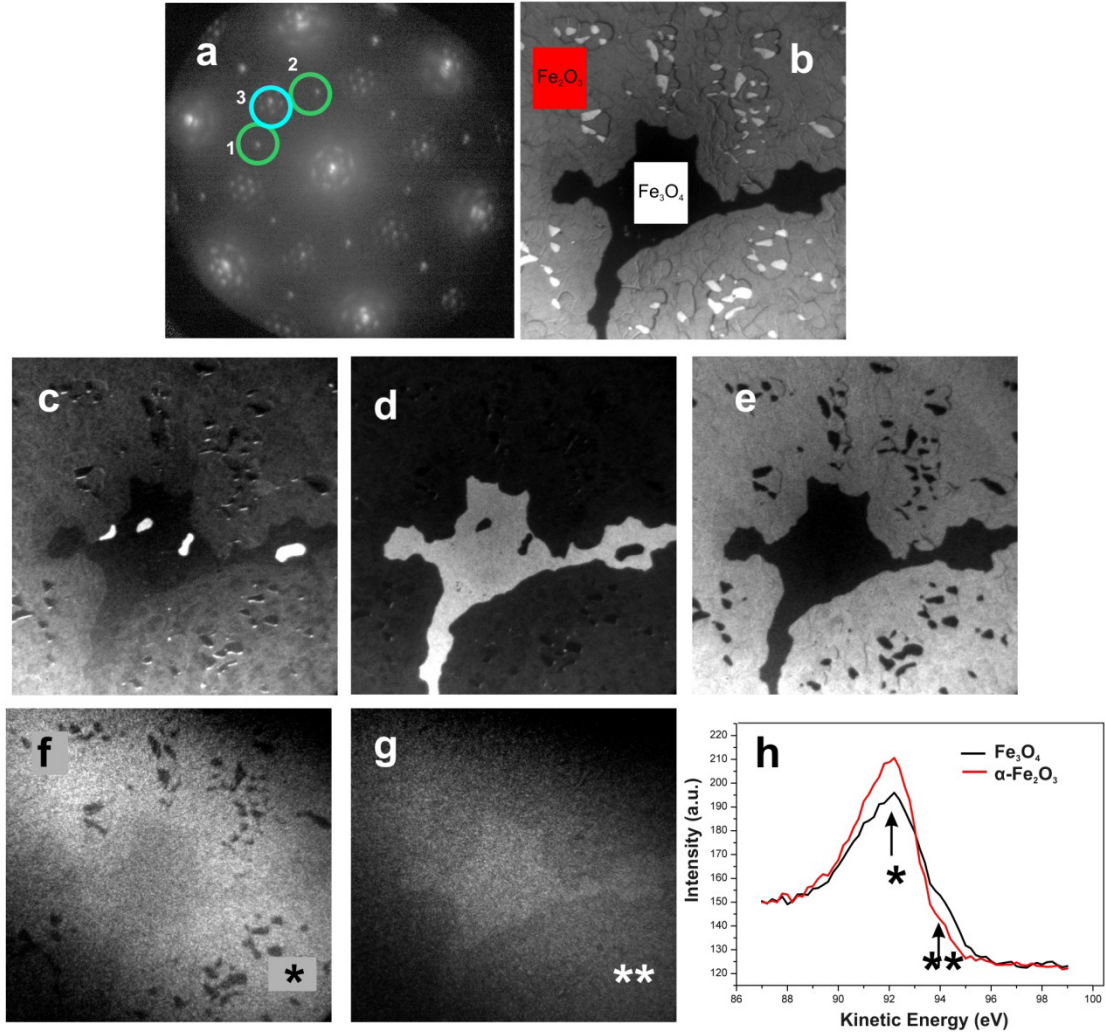


Fig. 2.15: Mixed film contrast. LEED (a) and LEEM-brightfield (b) of the surface: spots considered in the darkfield are indicated ($E_k=39$ eV). LEEM-darkfield on Fe_3O_4 two rotational domains (c-d) and $\alpha\text{-Fe}_2\text{O}_3$ (e); $E_k=24$ eV. X-PEEM (g-f) relative to different energy of the Fe3p peak, indicated in Fig 2.15h with “*” and “**” ($h\nu=150$ eV; $E_k=92,2$ eV and $E_k=94$ eV respectively). Area considered for the spectra 2.15h are indicated in 2.15b. FoV = $7.5\ \mu\text{m}$ (all images).

2.2 Effect of Fe deposition on Fe-oxide surfaces: biphasic termination

The next section focuses on the experiments addressing the effects of Fe deposition on top of $1/4$ Fe terminated Fe_3O_4 and biphasic terminated $\alpha\text{-Fe}_2\text{O}_3$. The interest on this topic is motivated by the evidence that the catalytic activity of Fe-oxide is related to the amount of Fe cations at the surface [22].

The present studies show that in controlled experimental conditions, the excess of deposited Fe, induces a reversible transformation in long range ordered terminations on top of the Fe-oxides. The controversial interpretation of the experimental results requires a discussion of the often contradictory models proposed in the literature for the biphasic termination [48, 50, 87, 92-94].

As anticipated in Chapter 1, the "biphasic termination" is a surface reconstruction found on Fe_3O_4 and $\alpha\text{-Fe}_2\text{O}_3$ crystals treated in extremely reducing conditions (i.e. Ar^+ sputtering and prolonged UHV annealing). The fingerprint of this termination is the specific long range periodicity (which varies in the range between 40 Å and 60 Å) which is visible as extra satellite spots in the corresponding LEED pattern [50] (see Fig 2.16) and/or intensity modulation (with the same periodicity) in STM measurements [48, 87, 94].

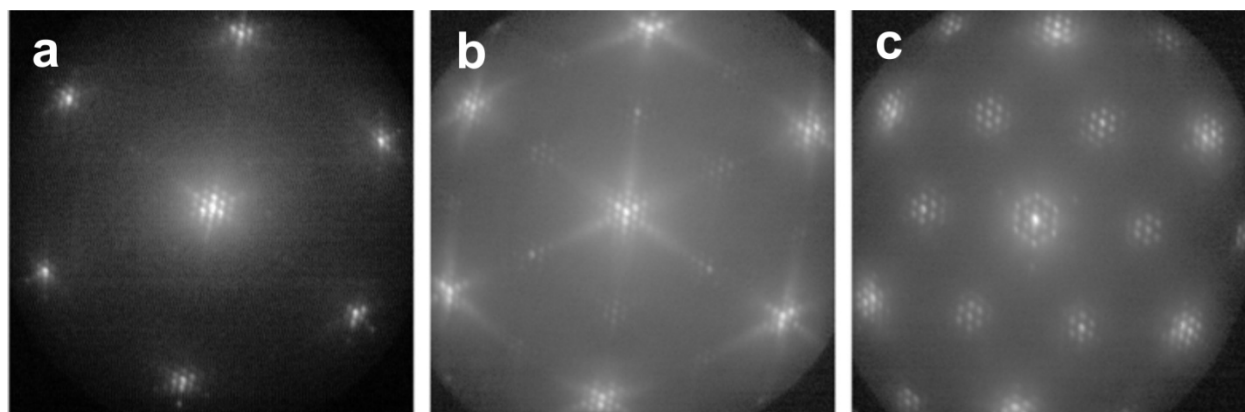


Fig. 2.16: LEED pattenr of Fe-oxide biphasic: a) on $\text{Fe}_3\text{O}_4/\text{Ru}(0001)$, $E_k=38$ eV. b) $\text{Fe}_3\text{O}_4/\text{Pt}(111)$; $E_k=40$ eV; c) on $\alpha\text{-Fe}_2\text{O}_3/\text{Pt}(111)$; $E_k=40$ eV

The origin of the long range ordering is still under debate, despite the extensive studies on $\text{Fe}_3\text{O}_4(111)$ and $\alpha\text{-Fe}_2\text{O}_3(0001)$ by several groups [22, 48, 50, 87, 91, 93, 94]. The main ambiguity is rising from the interpretation for the origin of the six-fold symmetric satellites in the LEED pattern and/or the long range modulations in the STM data. In fact, similar extra patterns are originated by multiple scattering across an interface (Moiré) as well as by co-existing island regularly rearranged. These two interpretations are at the basis of the two main models for the biphasic termination. Additionally, the formulation of an unambiguous model has been complicated by disparate typologies of samples used (single crystals, mineralogical, and thin films) and experimental conditions (Ar sputtering, UHV annealing, oxidation pressure,...) for the experiments [48, 50, 87, 92-94].

The most frequently used explanations for the biphasic termination on $\alpha\text{-Fe}_2\text{O}_3$ can be summarized as follow:

- Multiple scattering occurring at the interface between bulk termination, namely $\alpha\text{-Fe}_2\text{O}_3(0001)$ or $\text{Fe}_3\text{O}_4(111)$, and an $\text{Fe}_{1-x}\text{O}(111)$ overlayer was assumed by *Lad and Henrich* [50] and *Lanier et al.*[93];
- Long range ordered coexistence of $\alpha\text{-Fe}_2\text{O}_3$ and Fe_{1-x}O phases on bulk $\alpha\text{-Fe}_2\text{O}_3$ was suggested by *Condon et al.* [48] after their STM measurements on single crystal.

The biphasic structure on $\text{Fe}_3\text{O}_4(111)$ was studied in detail by STM in [49, 94]. Condon and coworkers [94] measured a termination similar to the one observed on top of $\alpha\text{-Fe}_2\text{O}_3$, suggesting an Fe_3O_4 -like/ Fe_{1-x}O rearrangement on bulk Fe_3O_4 [48, 94]. Samples treated in more strongly reducing conditions indicate the formation of a homogeneous Fe-terminated $\text{FeO}(111)$ overlayer. It has also been suggested that the biphasic ordering results as consequence of low temperature oxidation of the Fe_3O_4 film (870 K) [49]. Three different kinds of surface structure have been identified in the study: Fe- and O- terminated $\text{FeO}(111)$ as well as bulk truncated $\text{Fe}_3\text{O}_4(111)$, alternating with long range ordering.

2.2.1 $\alpha\text{-Fe}_2\text{O}_3$ biphasic termination: structural models

To simplify the discussion of the experimental data, we first present the two structural models for the $\alpha\text{-Fe}_2\text{O}_3$ termination mainly discussed in the literature [48, 50, 93].

In both models, the relaxation of the last oxygen layer is assumed to be a consequence of the reducing condition. The oxygen interatomic distance increases by $\approx 6\%$ from the $\alpha\text{-Fe}_2\text{O}_3$ bulk value to a value close to the O-O distance in FeO .

The mismatch between the relaxed O layer at the surface and the O layers in the $\alpha\text{-Fe}_2\text{O}_3$ bulk (bulk values: 3.04 Å and 2.91 Å respectively), gives rise to a superficial Moiré structure where areas with hcp and fcc vertical stacking alternate (see Fig 2.17). The Moiré pattern causes the observed long-range modulation at the surface (STM) or the hexagonal extra-spots (LEED).

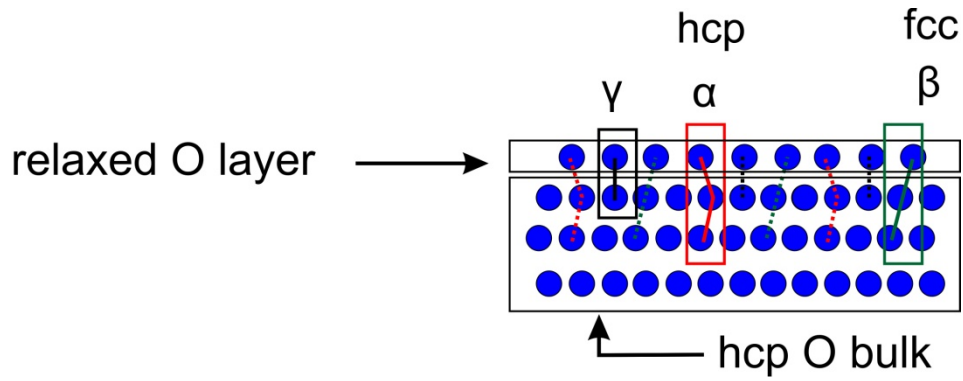


Fig. 2.17: Side view of the alternating hcp and fcc areas forming on top of the α -Fe₂O₃ bulk as consequence of the relaxation of the last oxygen layer.

The possible arrangements of the Fe atoms at the surface constitute the main difference among the structural models.

Condon et al. suggest that the Fe atoms are incorporated into the topmost layer following preferentially the underlying oxygen stacking: α -Fe₂O₃ in the hcp areas of the Moiré, or FeO(111) in the fcc ones [48].

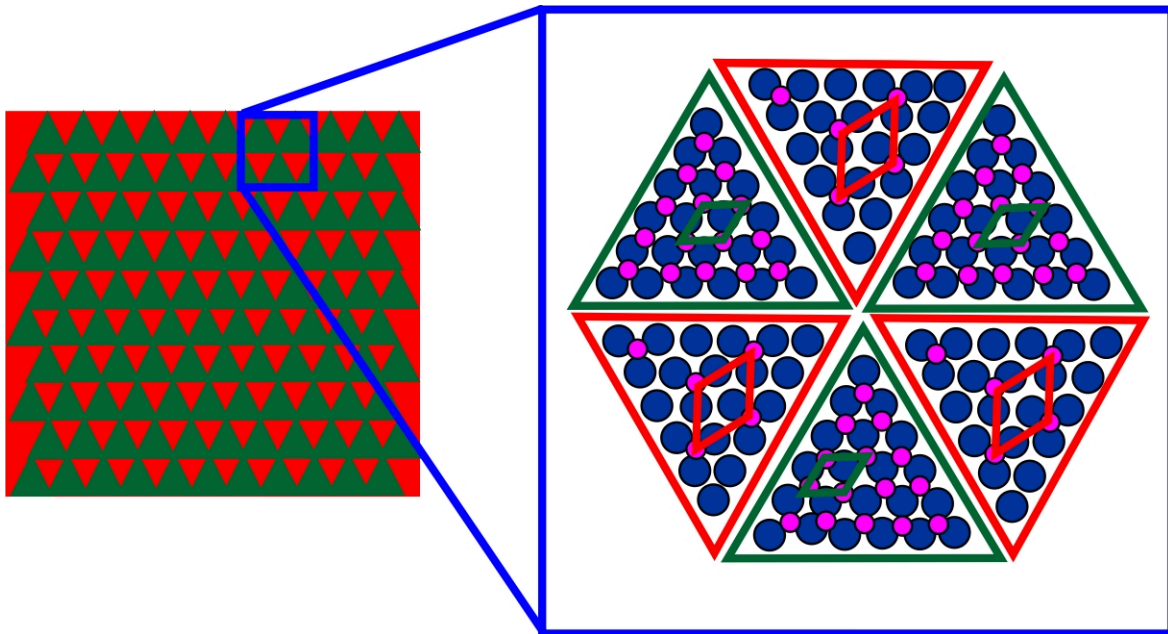


Fig. 2.18: Top view of the biphas model proposed by *Condon et al*[48]. Red and green triangles correspond to hcp and fcc areas of the vertical O stacking respectively. The Fe atoms arrange coherently into α -Fe₂O₃(0001) or FeO(111) geometry

The LEED pattern associated with this surface reconstruction is shown in Fig. 2.18. It derives from the superposition of two contributions:

- the $\alpha\text{-Fe}_2\text{O}_3$ $(\sqrt{3}\times\sqrt{3})\text{R}30^\circ$ surface reconstruction and the satellite spots due to the long range periodicity of the $\alpha\text{-Fe}_2\text{O}_3$ domains;
- FeO(111) main spots and their respective satellites, originating from the long range periodicity FeO domains.

The resulting LEED is henceforth simply called “ $(\sqrt{3}\times\sqrt{3})\text{R}30$ biphasse reconstruction” (see Fig 2.20).

If the Fe density is assumed to be the one of the oxygen atoms in the last layer ($\text{Fe}:\text{O}=1$) and each O is saturated by one Fe atoms, the resulting surface is a homogeneous FeO(111) overlayer as proposed in [50]. The surface model is shown in Fig. 2.19.

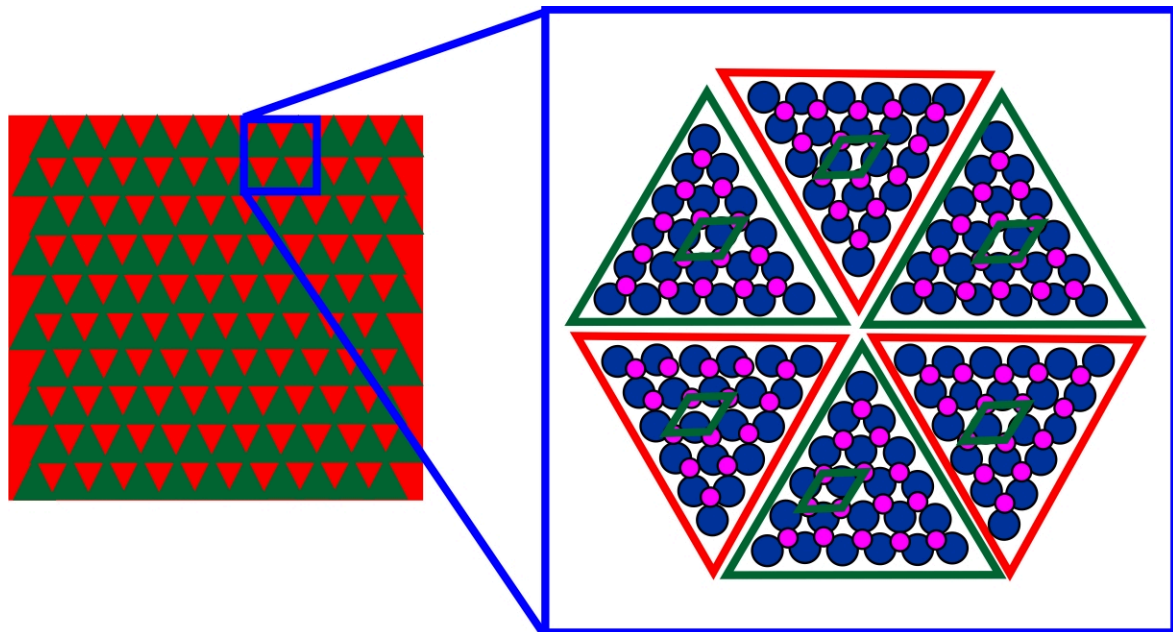


Fig. 2.19: Top view of the biphasse model proposed by *Lad et al.* [50]. As in the previous image, red and green triangles correspond to hcp and fcc areas of the vertical O stacking, leading to the same Moiré structure. However, differently from the previous model, each Fe atom saturates one O atom, leading to the formation of a homogeneous FeO(111) layer.

Probing this surface with LEED, the expected patterns consist of the superposition of the FeO(111) main spots and the Moiré pattern originating from the mismatch between the O-O interatomic distances in the surface and the bulk layers. The resulting LEED will be simply

called “(1x1) biphasic reconstruction”. It consists of a (1x1) reconstruction (see Fig 2.20), referred to the O periodicity, characterized by the extra spots. It is crucial that the LEED sensitivity is limited to the topmost layer, otherwise the $(\sqrt{3}\times\sqrt{3})R30^\circ$ spots originating from the $\alpha\text{-Fe}_2\text{O}_3$ bulk would be visible. This is the case in the following experiments, as the electron energy used (40 eV) LEED is very surface sensitive.

$(\sqrt{3}\times\sqrt{3})R30^\circ$ Reconstruction (1x1) Reconstruction

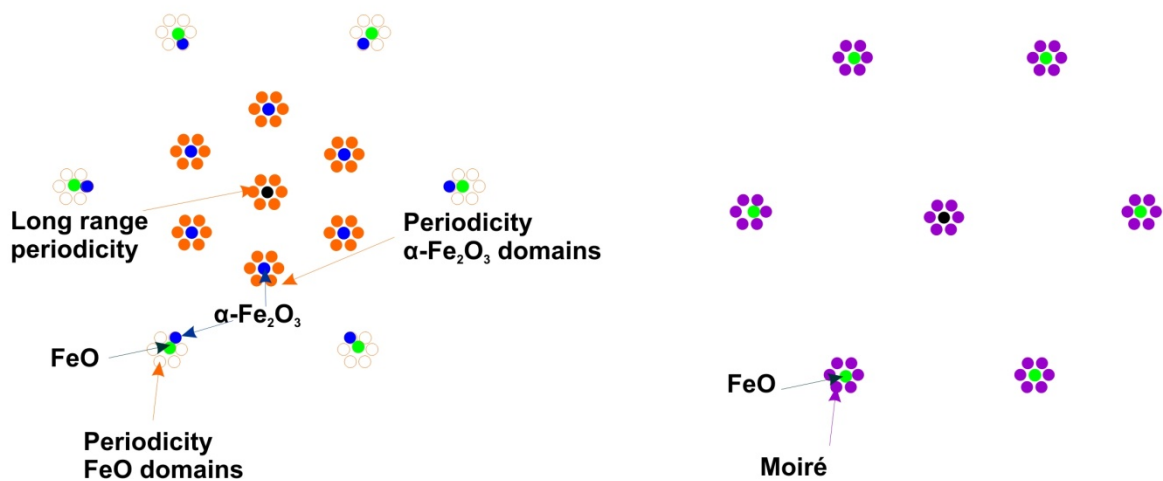


Fig. 2.20 Expected LEED pattern models for the two biphasic reconstructions discussed in Fig 2.18 and Fig.2.19

As the mismatch between the O layers in both models is the same, also the long range periodicity predicted for both structures is the same; consequently the position of the extra-spots should be the same. In principle, these two terminations differ only in the amount of Fe atoms at the surface. Therefore, it should be possible to discern which one is the "as prepared" termination of the $\alpha\text{-Fe}_2\text{O}_3$ film by studying the effects of Fe deposition in LEED.

It is important to remark that very recently another model for the biphasic termination has been suggested [95]. According to this model, the periodicity is given by two long range ordered $\alpha\text{-Fe}_2\text{O}_3$ domains, alternating the O- and the Fe-terminations. As the O layer in $\alpha\text{-Fe}_2\text{O}_3$ and the FeO(111) are both giving a (1x1) reconstruction (only with slightly different interatomic distances), then following the same arguments above, the LEED pattern associated to the this surface is a “ $(\sqrt{3}\times\sqrt{3})R30^\circ$ biphasic reconstruction”. A surface composed by alternating islands composed by O-terminated $\alpha\text{-Fe}_2\text{O}_3$ and FeO(111) would have the same LEED pattern as the “(1x1) biphasic reconstruction”.

2.2.2 Fe deposition on α -Fe₂O₃/ Fe₃O₄ Mixed film

A sub-monolayer coverage of Fe (0.4ML) was deposited at RT onto an α -Fe₂O₃ / Fe₃O₄ mixed film on Pt(111) in UHV. As the sample consists in a mixed film, the behaviors of Fe₃O₄ and α -Fe₂O₃ phases can be compared under the very same experimental conditions (namely coverage, temperature, pressure). Deposition was followed in real time in LEED (Fig. 2.21).

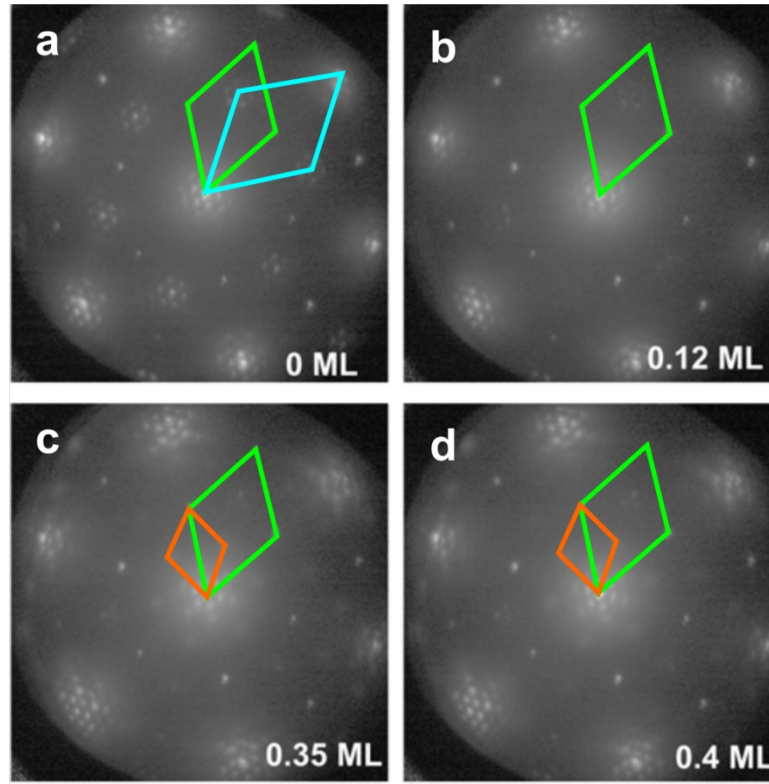


Fig. 2.21a-d): LEED recorded during the deposition of 0.4 ML Fe deposition on α -Fe₂O₃ / Fe₃O₄ mixed film at RT. $E_k = 39$ eV

The diffraction pattern of the starting surface (Fig 2.21a) exhibits the superposition of the (2x2) reconstruction of the Fe₃O₄ phase and the ($\sqrt{3} \times \sqrt{3}$)R30° reconstruction of the α -Fe₂O₃ termination, the spots of which are surrounded by the extra-satellite spots. Extra-satellites are also visible surrounding the (0,0) spot. After the deposition of 0.12 ML of Fe (Fig 2.21b) the ($\sqrt{3} \times \sqrt{3}$)R30° reconstruction has disappeared, while the (2x2) main spots are still visible; the extra-satellites surrounding the (0,0) and the (1,0) spots are also still visible. Increasing the Fe coverage (Fig 2.21c-d), an unknown pattern forms, characterized by weak and broad spots, arranged in a ($2\sqrt{3} \times 2\sqrt{3}$)R30° periodicity. This pattern coexists with the (2x2) reconstruction of the Fe₃O₄ and the extra-satellites surrounding the (0,0) and the (1,0) spots. ($\sqrt{3} \times \sqrt{3}$)R30° reconstruction from the α -Fe₂O₃ phase is absent. Single-phase areas LEED pattern were taken

after the Fe deposition (0.4 ML). Only the Fe_3O_4 area (Fig 2.22a), which is indicated by the (2×2) spots, shows the new $2(\sqrt{3} \times \sqrt{3})R30^\circ$ reconstruction, which will be discussed in the next paragraph. The $(0,0)$ spots do not exhibit the extra-satellite spots, characteristic of the long range ordering; however, we observe the formation of the Henzler ring [26], arising from disordered Fe clusters which have formed during deposition. Fig 2.22b shows the LEED pattern from the $\alpha\text{-Fe}_2\text{O}_3$ area. The $(\sqrt{3} \times \sqrt{3})R30^\circ$ periodicity is barely visible while the extra-satellites surrounding the $(0,0)$ spots are intense. This periodicity is associated to atomic positions of the Fe sublattice. As a result, we observe the formation of a (1×1) reconstruction characterized by long range ordering.

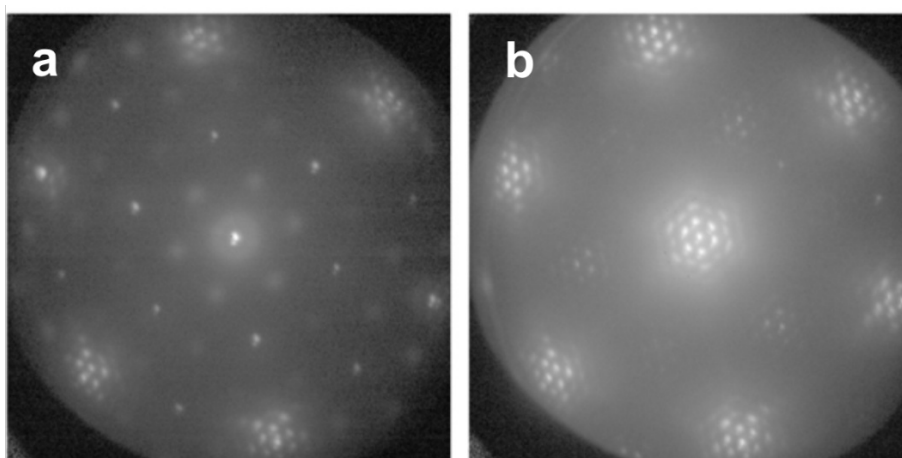


Fig. 2.22: LEED from selected area ($2.5 \mu\text{m} \times 2.5 \mu\text{m}$) after deposition: Fe_3O_4 (a), $\alpha\text{-Fe}_2\text{O}_3$ (b). In Fig 2.22a superstructure satellites are visible around the $(0,1)$ spots but absent on the others; in Fig 2.22b two spots belonging to the Fe_3O_4 phase are visible. This is an effect of aberration: electrons coming from areas neighboring the selected area used for LEED are deflected in such a way that they also contribute to the diffraction pattern. $E_k=39 \text{ eV}$

Using the linear correlation between deposition time and Fe coverage (the constant deposition flux is 0.3 ML/min), one can study the changes of the LEED intensity depending on the deposited Fe coverage. Fig 2.23 shows the coverage dependence of the intensity of the main diffraction spots during deposition. Focusing on the $\alpha\text{-Fe}_2\text{O}_3$ phase, the $\alpha\text{-Fe}_2\text{O}_3$ $(\sqrt{3} \times \sqrt{3})R30^\circ$ intensity (red curve) reaches a minimum at $\approx 0.14 \text{ ML}$. Moreover, the SPA-LEED analysis (Fig 2.24) confirms that the spatial periodicity of the biphasic superstructure has not changed during deposition. It should be noticed that the electron mean free path in solids is close to 0.5 nm at the energies used for LEED ($38\text{--}41 \text{ eV}$), i.e. practically only the first atomic layer contributes to the LEED.

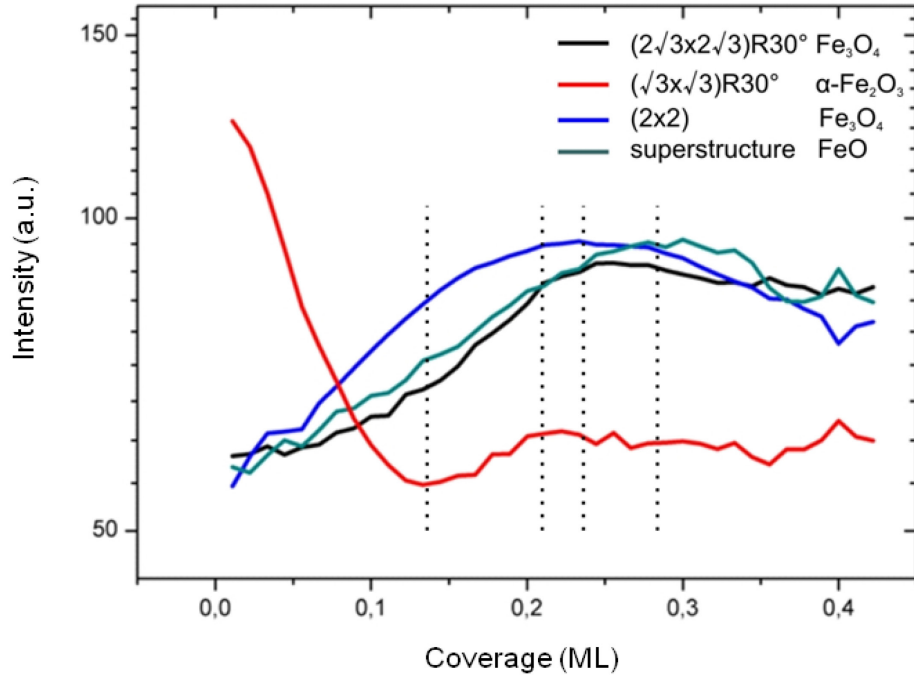


Fig. 2.23: Intensity dependence of the main LEED spots during 0.4 ML Fe deposition at RT on the mixed $\alpha\text{-Fe}_2\text{O}_3$ / Fe_3O_4 film. The $\alpha\text{-Fe}_2\text{O}_3$ ($\sqrt{3}\times\sqrt{3}$)R30° intensity (red curve) reaches a minimum at ≈ 0.14 ML ($\approx 1/7$ ML); Fe_3O_4 (2x2) (blue curve) increases up to ≈ 0.22 ML. $2(\sqrt{3}\times\sqrt{3})\text{R}30^\circ$ pattern rises up to 0.25 ML (black curve); FeO reaches its maximum at 0.3 ML (green curve).

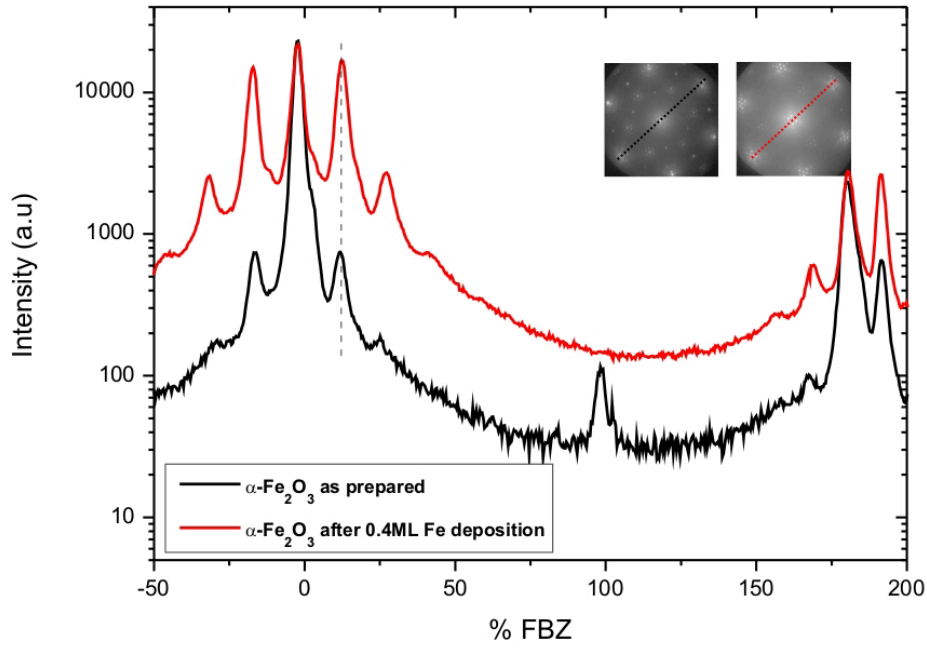


Fig. 2.24: SPA-LEED of the surface before and after Fe deposition (from Fig. 2.22a and Fig. 2.23b respectively). SPA-LEED profiles have been both acquired along the (1,0) direction, as shown in the image. The axis was calibrated on the (2x2) reconstruction of Fe_3O_4 ; absolute intensities have not been rescaled.

The disappearing of the Fe periodicity due to Fe deposition can be explained in two ways: (i) Fe deposition causes the disordering of the $(\sqrt{3}\times\sqrt{3})\text{R}30^\circ$ reconstruction; (ii) the deposited Fe atoms form an ordered (1x1) reconstruction. In the first case, the damping of the $(\sqrt{3}\times\sqrt{3})\text{R}30^\circ$ spot intensity is induced by the strong non-crystalline background. However, the formation of a fully disordered Fe over-layer is improbable, as the damping effect of the incoherent background intensity should affect all the diffraction spots in the same way. In fact, after deposition, the superstructure spots are still visible; moreover, the intensity of the Fe_3O_4 spots increases, instead of decreasing, and a new pattern becomes visible on the Fe_3O_4 area of the film. The second option, i.e. the formation of an ordered (1x1) reconstruction, might be explained as following. The $(\sqrt{3}\times\sqrt{3})\text{R}30^\circ$ periodicity arises from the Fe position (or vacancies) in the $\alpha\text{-Fe}_2\text{O}_3$ referred to the O-layer, the (1x1) reconstruction from the O periodicity. The transition from the first to the second reconstruction by Fe deposition might indicate that the deposited Fe atoms adsorb preferentially in the Fe vacancies present in the $\alpha\text{-Fe}_2\text{O}_3$ areas (which contribute to the $(\sqrt{3}\times\sqrt{3})\text{R}30^\circ$ periodicity). By filling these vacancies, all the oxygen atoms in this domain are saturated by one Fe atom (Fe:O=1 ratio), resulting in a FeO(111) structure.

If the starting $(\sqrt{3}\times\sqrt{3})R30^\circ$ reconstruction is composed by alternating FeO_x and $\alpha\text{-Fe}_2\text{O}_3$ domains, then during deposition the biphasic structure is transformed to a superficial $\text{FeO}(111)$ layer. On the other hand, the initial $(\sqrt{3}\times\sqrt{3})R30^\circ$ biphasic reconstruction might also arise from alternating O- and Fe- terminated regions of the $\alpha\text{-Fe}_2\text{O}_3$ surface, as discussed above. In this case, the final surface would be composed by alternating domains composed by O- terminated $\alpha\text{-Fe}_2\text{O}_3$ and $\text{FeO}(111)$. Based on the LEED data, both surface structures are possible.

The deposition experiment was repeated on a single phase $\alpha\text{-Fe}_2\text{O}_3$ thin film; in this case a higher Fe coverage has been deposited (3 ML) at RT (Fig. 2.25a). Again, the LEED pattern after deposition is characterized by the (1×1) biphasic reconstruction: the $(\sqrt{3}\times\sqrt{3})R30^\circ$ spots are invisible after deposition while the superstructure surrounding the (0,0) and the (1,0) spots is visible. After the deposition, the thermal stability of the (1×1) reconstruction was tested, by annealing the film under UHV condition up to 800 K in two steps. In the first annealing step the temperature was raised up to 675 K and then cooled down to RT to acquire LEED and a darkfield image of the surface; in the second up to 800 K. The process was followed in real time in LEEM. While the microscopic aspects will be discussed in detail in the next chapter (section 3.26, Fig 3.8), in the context of the reversible transformation $\text{Fe}_3\text{O}_4 \leftrightarrow \alpha\text{-Fe}_2\text{O}_3$, the LEED patterns and the related structure will be discussed in the following.

Fig 2.25 shows the LEED patterns of the surface before and after the two annealing steps. After annealing at 675 K, the LEED pattern is characterized by the superposition of the (2×2) reconstruction of the Fe_3O_4 and the extra-spots surrounding the (0,0). The (2×2) spots do not show extra-satellites; therefore the Fe_3O_4 phase is not characterized by long range ordering. After further annealing up to 800 K, the $(\sqrt{3}\times\sqrt{3})R30^\circ$ the biphasic reconstruction appears; the (2×2) spots of Fe_3O_4 are also visible.

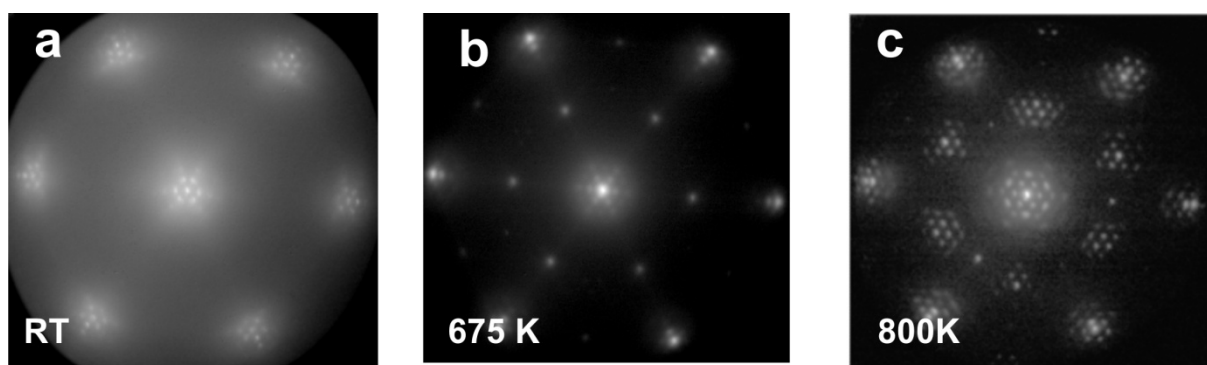


Fig. 2.25: a) LEED pattern of 3 ML deposited Fe on $\alpha\text{-Fe}_2\text{O}_3$ at RT; b-c) annealing of the surface in UHV.

$E_K=41$ eV

LEEM recordings (the sequence is reported in chapter 4) clarify that at $T \approx 715$ K the (1x1) biphasic terminated areas undergo a transformation to the $(\sqrt{3} \times \sqrt{3})R30^\circ$ biphasic reconstruction. The transition between the two terminations, which differ by the amount of Fe present at the surface, is most likely enabled by the segregation of part of Fe atoms forming the FeO(111) layer into the oxide bulk.

The outcome of these experiments can be summarized as following:

- As prepared, the films exhibit a $(\sqrt{3} \times \sqrt{3})R30^\circ$ biphasic termination, which might be constituted by (i) alternating domains with Fe_xO and $\alpha\text{-Fe}_2\text{O}_3$ structure or by (ii) alternating domains of O-terminated and Fe-terminated and $\alpha\text{-Fe}_2\text{O}_3$.
- The long range ordered (1x1) reconstruction can be induced on $\alpha\text{-Fe}_2\text{O}_3$ by RT Fe deposition. The LEED pattern is consistent with that of (i) a complete FeO(111) layer or (ii) alternating domains of O-terminated $\alpha\text{-Fe}_2\text{O}_3$ and FeO(111). In the first case the hexagonal satellite pattern is due to the 6% mismatch between FeO and $\alpha\text{-Fe}_2\text{O}_3$ oxygen lattice (3.04 Å and 2.91 Å respectively), while in the second from the domains periodicity.
- The starting termination (i.e. before Fe deposition) can be restored by annealing the film at $T > 710$ K.

If the proposed model is correct, then 0.142 ML ($\approx 1/7$ ML) of deposited Fe is sufficient to fill the Fe vacancies at the surface. The amount of Fe required for the transition between the two terminations might indicate that the coverage of the Fe- terminated domains is: (i) 25% of 1/3 Fe terminated surface (from bulk stacking: Fe-O-Fe-Fe); (ii) $\approx 50\%$ of 2/3 Fe terminated $\alpha\text{-Fe}_2\text{O}_3$ (from bulk stacking it would be Fe-Fe-O-Fe-Fe).

Even if the Fe-O-Fe-Fe surface should be the most stable termination according to theoretical calculations [89], STM on the $\alpha\text{-Fe}_2\text{O}_3$ biphasic performed by *Condon et al.* in [48] supports the last suggestion. Based on our data, we cannot exclude any of the two possibilities. In fact, on one hand there is still no theoretical calculation on the biphasic structure; on the other hand STM measurements are not directly correlated to the real geometry of the surface but strongly influenced by its electronic properties.

2.2.3 Modification of Fe₃O₄ (111) surface termination by Fe deposition and UHV annealing.

1.5 ML of Fe were deposited at RT on an approximately 10 nm thick Fe₃O₄ film, supported on Pt(111) (preparation procedure described elsewhere [8, 52]). The initial Fe₃O₄ surface is 1/4 Fe terminated, belonging to the Mix-Trigonal layer [8, 88], as confirmed by LEED-IV. During deposition, we observed the development of an unknown superstructure, as already mentioned in 2.2.2. Referred to the (1x1) structure due to the closed packed O lattice, the periodicity of the new structure is $(2\sqrt{3} \times 2\sqrt{3})R30^\circ$ (Fig. 2.26). The real time LEED intensity during deposition is correlated to the Fe coverage. As shown in Fig. 2.27, the (2x2) and the $(2\sqrt{3} \times 2\sqrt{3})R30^\circ$ intensities rise to a maximum at 0.25 ML of deposited Fe, which corresponds most likely to the maximum coverage of the reconstruction. The formation of the Henzler ring surrounding the (0,0) spots indicates the nucleation of randomly distributed Fe clusters during the deposition, which causes the damping of the spot intensity at higher deposition coverage.

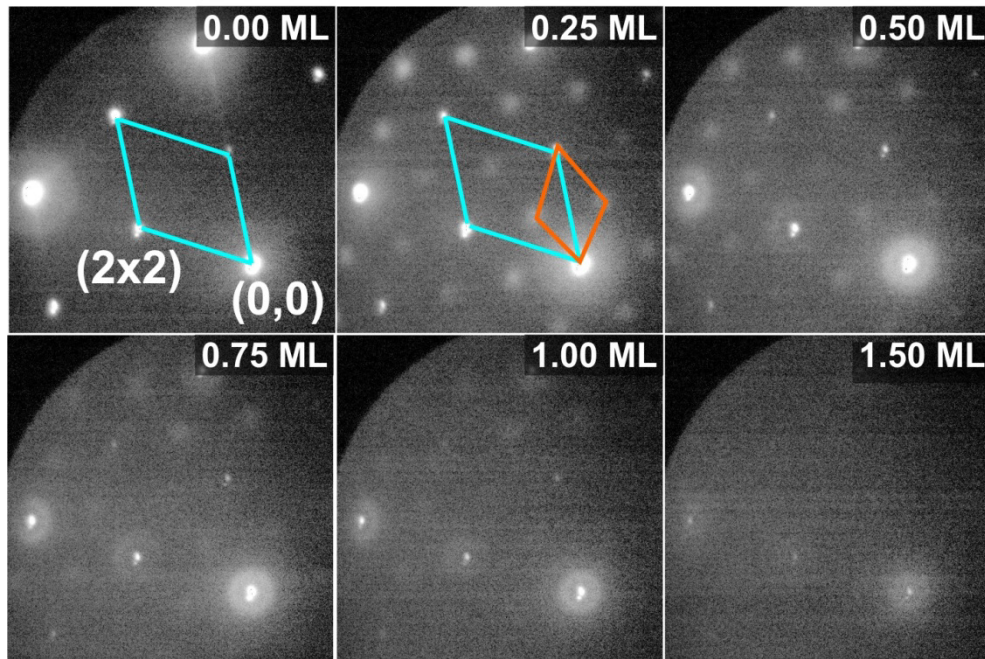


Fig. 2.26: LEED. Formation of the $(2\sqrt{3} \times 2\sqrt{3})R30^\circ$ reconstruction during Fe deposition on initially 1/4 Fe terminated Fe₃O₄ surface at RT. $E_k=19$ eV

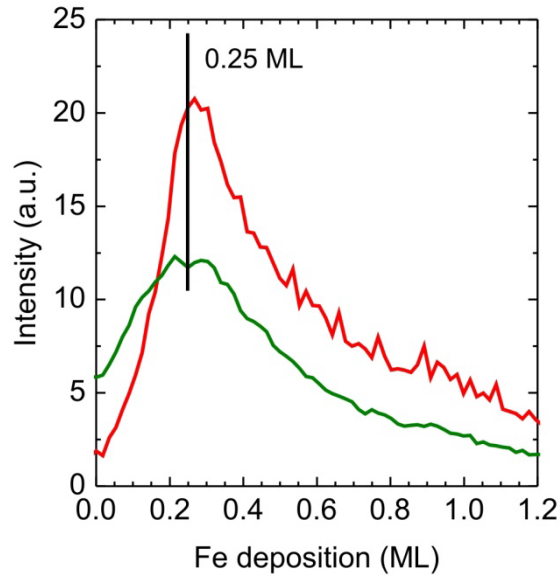


Fig. 2.27: intensity of the (2x2) (in green) and (2√3x2√3)R30° (in red) spots during RT Fe deposition.

The unknown ordered (2√3x2√3)R30° reconstruction represents the periodicity of a new atomic arrangement at the surface. Considering both, 1/4 Fe terminated Fe₃O₄ surface and 1/4 ML deposited Fe, the expected amount of Fe atoms at the surface at the maximum spot intensity is 0.5 ML. The origin of this pattern might arise from the distortion of the Fe atom positions in the terminating layer. Fe does not continue in the natural stacking of the Mix-Trigonal layer (which would preserve the (2x2)), but rearranges in hexagonal patches coherently to the (2√3x2√3)R30° periodicity, as suggested in Fig.2.28.

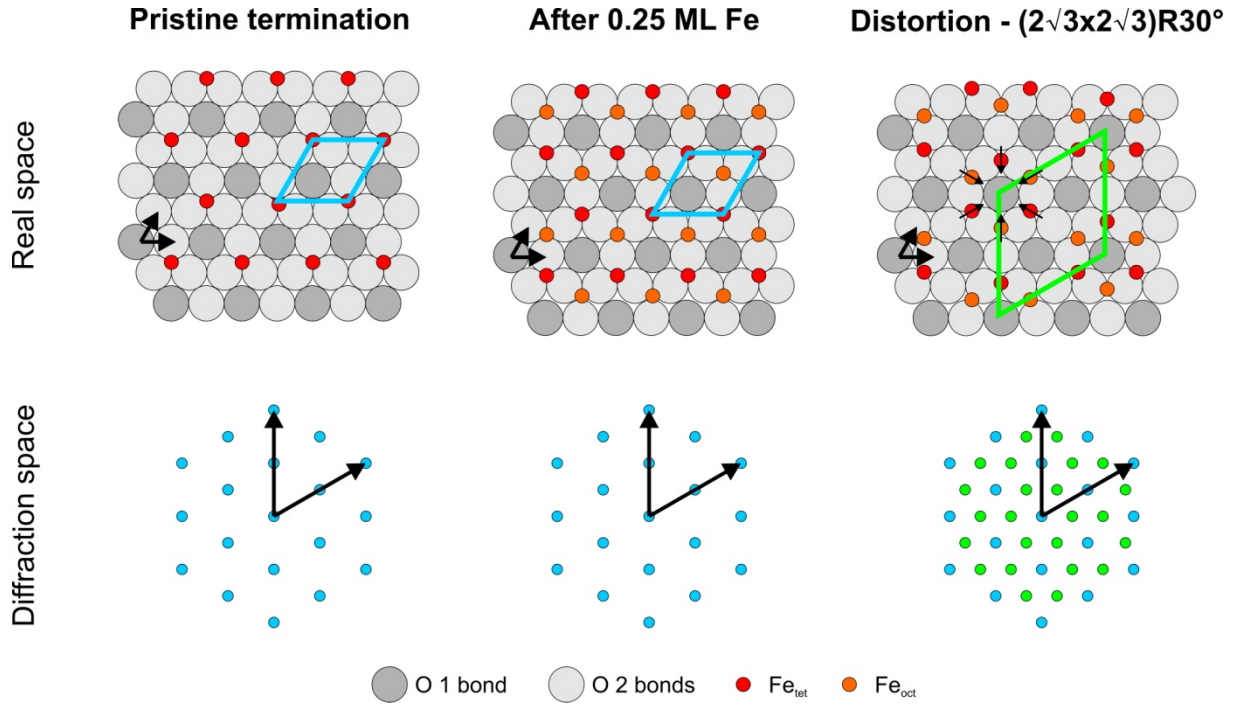


Fig. 2.28: Schematic view of the proposed Fe atomic position distortion induced by Fe deposition (atomic model and relative diffraction pattern). The pristine termination is 1/4 ML Fe-terminated $\text{Fe}_3\text{O}_4(111)$ surface; the 1/4 ML Fe-terminated $\text{Fe}_3\text{O}_4(111)$ with 0.25 ML of Fe (in orange) arranged with the proper stacking sequence of $\text{Fe}_3\text{O}_4(111)$ and the proposed distortion of Fe positions forming the $(2\sqrt{3}\times 2\sqrt{3})\text{R}30^\circ$ structure are compared.

The deposition was repeated on a similar film using a smaller amount of Fe (0.4 ML, RT), to study the thermal stability of $(2\sqrt{3}\times 2\sqrt{3})\text{R}30^\circ$ structure. The film was annealed in UHV up to $T = 950$ K and the sample was observed in real time, alternating the imaging mode between microscopy (LEEM) and diffraction (LEED). The sequence in Fig 2.29b (LEED) shows that the $(2\sqrt{3}\times 2\sqrt{3})\text{R}30^\circ$ structure is stable up to annealing $T < 490$ K; at higher temperature its pattern starts to disappear and only the (2×2) spots remain visible. The disappearance of the $(2\sqrt{3}\times 2\sqrt{3})\text{R}30^\circ$ structure in LEED is related to the appearance of areas of brighter contrast in LEEM, which are uniformly distributed over the surface.

At $T \approx 700$ K we observed the development of darker areas of the surface (LEEM), and the simultaneous development of the biphasic extra spots (LEED). This new termination develops in the temperature range between 700 K and 820 K. At higher temperatures, the black areas at the surface progressively vanish (LEEM); at the same time the biphasic extra spots weaken. At $T \approx 900$ K the (2×2) termination is fully restored.

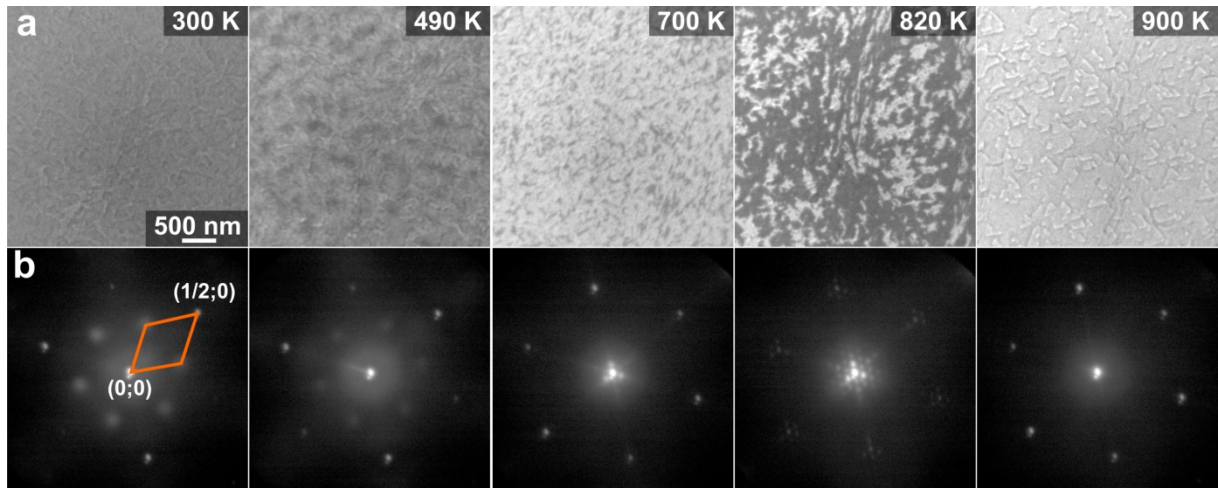


Fig. 2.29: Real time sequence of annealing from RT to 900 K; LEEM (a) and LEED (b). The disappearance of the $(2\sqrt{3} \times 2\sqrt{3})R30$ spots is observed for $T > 450$ K; the biphasic structure develops in the range between $T = 700$ K and $T = 820$ K. $E_k = 19$ eV

Fig 2.30a shows a magnification of the LEED pattern around the (0,0) spot for the biphasic terminated Fe_3O_4 surface. The line scans shown in Fig 2.29b underline that the superstructure periodicity is constant up to $T \approx 820$ K (blue, dark and green lines). At $T > 820$ K the biphasic termination starts to disappear, and simultaneously, its k-space position shifts from 4.8% to 6.1% of the dimension of the FBZ (First Brillouin Zone) (yellow, orange and red lines), corresponding to a decrease of its lateral periodicity in real space.

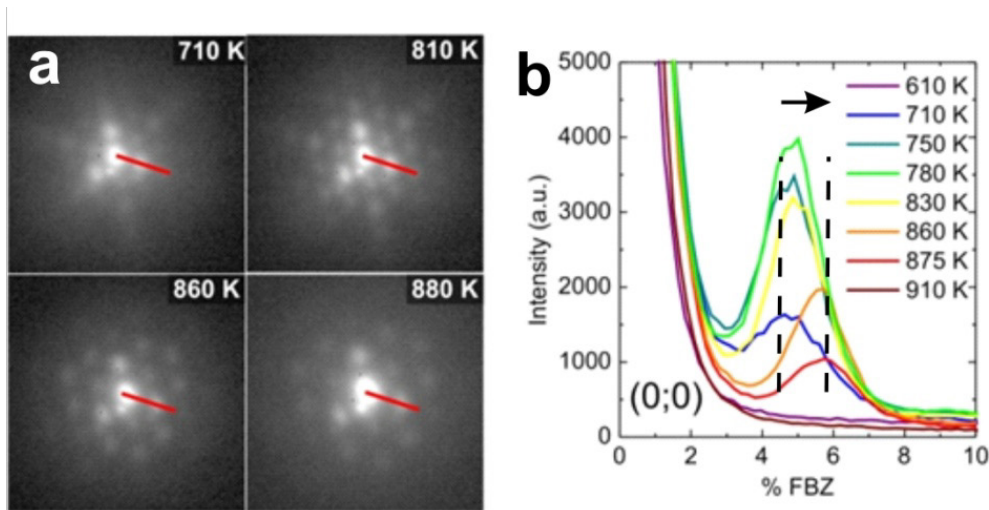


Fig. 2.30: Enlarged LEED patterns of the (0,0) spot during biphasic formation $E_k = 17$ eV. b): linear scan profiles on the red lines in a)

The biphasic termination can also be formed on $\text{Fe}_3\text{O}_4(111)$ directly, by Fe deposition at high temperature, as shown in the LEEM sequence in Fig 2.31. In the experiment, Fe was deposited at $T=800$ K in UHV, again on the initially 1/4 Fe terminated $\text{Fe}_3\text{O}_4(111)$ surface.

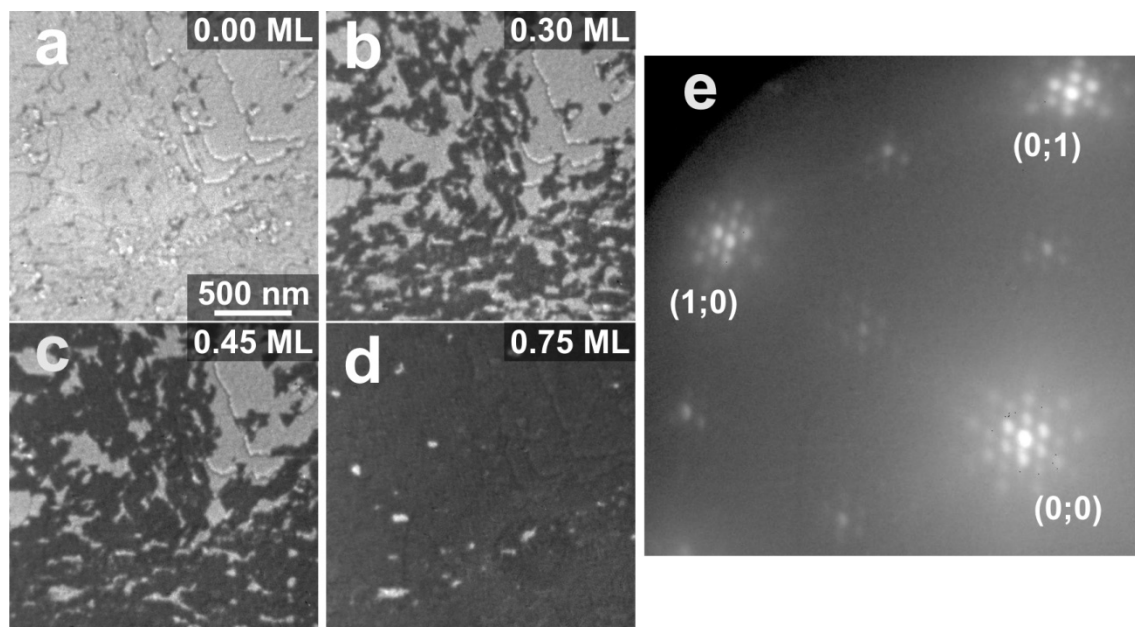


Fig. 2.31: LEEM during of Fe deposition on a $\text{Fe}_3\text{O}_4(111)$ surface at 800 K (a-d). Dark areas are associated to the biphasic terminated film. $E_k = 29$ eV; e) LEED of the fully covered surface. $E_k=58$ eV

The Fe_3O_4 surface was fully covered by the biphasic termination (dark areas) after depositing 0.75 ML of Fe. The LEED pattern of the fully biphasic terminated surface is shown in Fig. 2.31e. SPA-LEED measurements (not shown) exhibit that its periodicity corresponds to 60 Å. This value is similar to the one at the same annealing temperature for the biphasic termination prepared by annealing after RT deposition. Considering the initial 0.25 ML Fe coverage of the starting surface, the total amount of Fe available at the surface is 1 ML.

X-PEEM (Fig 2.32) of the fully biphasic terminated surface was compared to the spectra for the initial Fe_3O_4 surface (1/4 Fe-terminated), showing that the biphasic (blue curve) has an enhanced low binding energy component compared to the initial surface (red curve). The component at lower binding energy is assigned to the Fe^{2+} signal, and indicates that the biphasic termination is reduced compared to bulk Fe_3O_4 . The absence of spatial contrast suggests a homogeneous termination, at least within the spatial resolution of the SMART instrument.

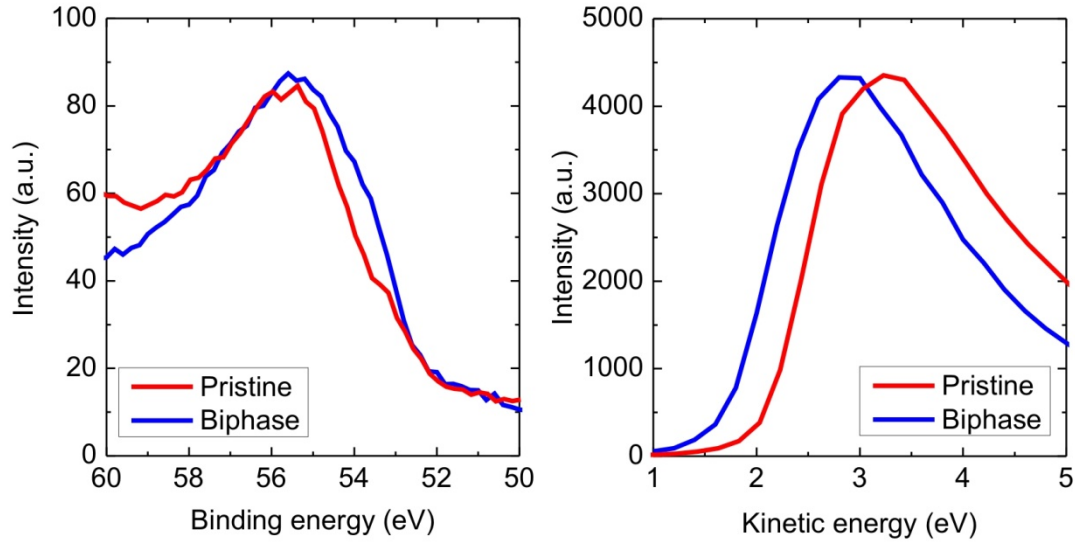


Fig. 2.32: XPS spectra of the Fe 3p core level photoemission line (a) and secondary electron spectra for the pristine and biphas termination. $h\nu = 150$ eV.

The formation of a complete FeO(111) layer, explains in a simple way the observed correlation between deposited Fe and biphas coverage. Clearly this conclusion differs from what is reported in [49], where the biphas was formed by low temperature oxidation of the Fe_3O_4 . However, in this case the treatment of the film is very different: Fe deposition and UHV annealing are extremely reducing conditions. Moreover, *Condon et al.* [94] report the formation of an homogeneous FeO(111) layer on top of the bulk Fe_3O_4 after very reducing treatment of the sample (cycles of Ar^+ sputtering and UHV annealing up to 1000 K).

At $T > 820$ K the superstructure becomes unstable and vanishes. This phenomenon can be related to the removal of Fe atoms via desorption and/or segregation into the bulk and the gradual destruction of the biphas ordering. The real time LEED acquisition shows that while disappearing, the biphas periodicity decreases by $\approx 20\%$, i.e. from 62 Å to 49 Å. This observation is an indication that the long range ordering is a Moiré-like superstructure, rather than an ordered arrangement of different iron oxide domains. In fact, in the latter case, a change of spatial periodicity can only occur if all domains shift coherently by hundreds of Å along the surface. On the other hand, the modification of the Moiré periodicity can be easily explained, assuming that the mismatch between the overlayer and the bulk slightly changes at high temperature. We notice that the Moiré periodicity decreases in real space: this indicates that the mismatch between the topmost and the underlying oxygen layers increases during the transition. One possible explanation is that the lattice constant of the FeO(111) overlayer

expands as a consequence of the Fe removal. However, the driving force of this relaxation is unknown.

2.3 Summary and conclusions

The preparation procedure of well ordered Fe-oxides surfaces and the controlled modification by Fe deposition have been the topic of this chapter, with particular focus on the α -Fe₂O₃(0001) thin films.

Pure α -Fe₂O₃ biphasic terminated, pure Fe₃O₄, and mixed film were grown successfully on Pt(111), Ag(111) and Ru(111) substrates; the preparation of unreconstructed α -Fe₂O₃ termination was not achieved, due to the limited pressure range accessible.

Real time observation of the diffraction pattern shows that the formation of α -Fe₂O₃ proceeds generally through an initial oxidation to Fe₃O₄, which is further oxidized to α -Fe₂O₃. Real space imaging clarifies the influence of the substrate morphology on the supported oxide features, and shows that the oxidation process follows preferential growing fronts, originating from defects of the substrate. Rotational domain size and the presence of dewetted areas in the film have been discussed.

In the second part of this chapter, I have investigated the effects of Fe deposition on biphasic terminated α -Fe₂O₃ and Fe₃O₄.

The study points out that even at RT, the adsorption of the deposited Fe atoms occurs in well-ordered geometries (Moiré patterns): on α -Fe₂O₃ we identified a (1x1) structure, still characterized by long range ordering; on Fe₃O₄ we found a new pattern, up to now unknown, which have $(2\sqrt{3} \times 2\sqrt{3})R30^\circ$ structure.

To coherently explain our experimental observation on the α -Fe₂O₃ film, we have suggested that two different long range-ordered structures can be stably formed depending on the Fe concentration at the surface. The structures were named after their LEED patterns.

The $(\sqrt{3} \times \sqrt{3})R30^\circ$ biphasic reconstruction is the standard termination for the α -Fe₂O₃ thin films grown in our set-up. It can be reversibly transformed into a (1x1) biphasic reconstruction by Fe deposition; this configuration is stable under UHV conditions up to $T \approx 715$ K.

The (1x1) biphasic reconstruction might consist of a FeO(111) overlayer (either Fe- or O-terminated) on top of the bulk Fe-oxide, as suggested in [50], or (ii) of regularly rearranged FeO_x and O-terminated α -Fe₂O₃ domains. The ($\sqrt{3}\times\sqrt{3}$)R30° biphasic reconstruction, which might consist of regularly rearranged FeO_x and α -Fe₂O₃ islands, as suggested by *Condon et al.* [48], or by regularly regularly rearranged Fe- and O-terminated α -Fe₂O₃ domains, as suggested by [95].

It is important to remark, that here the proposed models are based mainly on LEED measurements and should be verified also by other surface science techniques, able to probe the concentration of Fe cations at the surface and in the underneath layers.

In the case of Fe₃O₄, the ($2\sqrt{3}\times 2\sqrt{3}$)R30° structure has been assigned to the distortion of the Fe position. This atomic configuration is stable under UHV annealing up to T \approx 450 K. Excess Fe at the surface (induced by deposition), is also responsible for the reversible development of the biphasic termination in the temperature range between 700 K and 820 K. At higher temperature the (2x2) termination (1/4 Fe-terminated) is restored. The process was characterized both in microscopy and diffraction. The coverage of the biphasic terminated areas is controlled by the amount of extra-Fe deposited. Finally, changes in the biphasic periodicity were observed during its disappearance, most likely as consequence of the O-O interlayer relaxation.

As an outlook, it would be interesting to understand the stability of biphasic terminated Fe₃O₄ and α -Fe₂O₃ under reaction conditions, and compare their reactivity with their standard terminations in catalytic processes. In fact, the formation of an Fe terminated FeO(111) overlayer could enhance the catalytic performance, as it has been shown that the activity of Fe-oxide is strongly related to the acidic anion site at the surface [22]. Moreover, (as will be discussed in more detail later), FeO-encapsulated Pt NPs on Fe₃O₄ were found to be more reactive than bare Pt NPs in CO oxidation due to the formation of a tri-layer (O-Fe switches to O-Fe-O) under reaction conditions [84, 96], which is the active phase for the reaction.

3. Phase transformation in thin iron oxide films: mechanism, velocity and shape of the reaction front

This chapter focuses on the phase transformations between Fe_3O_4 , $\gamma\text{-Fe}_2\text{O}_3$, and $\alpha\text{-Fe}_2\text{O}_3$ thin oxide films (thickness ≈ 10 nm), supported on Pt(111) and Ag(111) single crystals. There are two main topics in the first part of the chapter: first, the identification of the $\gamma\text{-Fe}_2\text{O}_3$ phase from low temperature oxidation of Fe_3O_4 and its structural transformation to $\alpha\text{-Fe}_2\text{O}_3$; secondly, the reversibility condition for the $\text{Fe}_3\text{O}_4 \leftrightarrow \alpha\text{-Fe}_2\text{O}_3$ reaction, stressing the role of the supporting substrate. As we will see, most of the phase transformations investigated occur with moving “phase boundaries” (or “reaction fronts”). The temperature and pressure dependency of the velocity and the shape of the reaction fronts are the topics of the second part of the chapter.

The phase transformation between $\text{Fe}_3\text{O}_4 \leftrightarrow \alpha\text{-Fe}_2\text{O}_3$ involves changes in the composition (i.e. changing the ratio of Fe:O from 3:4 to 2:3) and in the crystal structure (i.e. from spinel to corundum and vice versa), which can occur independently from each other. If only the composition changes through Fe vacancy creation, Fe_3O_4 oxidizes to $\gamma\text{-Fe}_2\text{O}_3$, which has the same crystal structure as Fe_3O_4 [41-43]. On the other hand, the (irreversible) transformation from $\gamma\text{-Fe}_2\text{O}_3$ to $\alpha\text{-Fe}_2\text{O}_3$ is a purely structural phase transformation. The conditions controlling the structure of the product for the $\text{Fe}_3\text{O}_4 \rightarrow \text{Fe}_2\text{O}_3$ reaction (such as oxidation pressure, temperature, internal structure of the crystal) have been debated in the literature already in the 1960s [97-99]. In a large number of studies, it has been pointed out that the minimum temperature required to enable the structural transformation $\text{Fe}_3\text{O}_4 \rightarrow \alpha\text{-Fe}_2\text{O}_3$ depends on the crystal size and the impurities already present in the sample. This is corroborated by the experiments presented here: in fact, the structural transformation takes place only at the pre-existing phase boundary between the inverse spinel and the corundum crystals.

Another aspect investigated in this work is the interaction between the Fe-oxide thin film and the supporting metal substrate, which might influence the behavior of the film. Indeed, *Karunamuni et al.* [100] suggested that in general distinct phase diagrams have to be considered for each kind of substrate. The systematic investigation on thin films grown on Pt(111) and Ag(111) demonstrates that this is the case of the Fe-oxides: mixed $\text{Fe}_3\text{O}_4/\alpha\text{-Fe}_2\text{O}_3$

films can show completely different behavior under similar experimental condition, as discussed in 3.2.4 and 3.2.5.

In the $\text{Fe}_3\text{O}_4 \rightarrow \alpha\text{-Fe}_2\text{O}_3$ transformation, the local kinetics of the phase transformations between Fe-oxides was probed by visualization of the reaction front movements in *real time* and in *real space* under well-defined reaction conditions. Although experimental studies addressing this issue quantitatively are still rare, LEEM/PEEM setups have been already successfully applied to the study of moving reaction fronts on surfaces and thin films [20, 101-106], thanks to their high acquisition rate.

In solid state reactions the local velocity (and consequently the shape) of the reaction front (i.e. the moving phase boundary) is influenced by the gradient of the chemical potential, but also by local stress, point or line defects at the parent/product interface, and their relative crystalline orientations [59, 70, 107-112]. The interplay between thermodynamic and elastic driving forces controls the morphology of the phase boundary. In the cases investigated, the shapes and velocities of the phase boundaries show strong dependencies on temperature, oxygen pressure and on structural defects, such as step bunches of the supporting substrate and domain boundaries in the initial oxide film.

3.1 Phase identification

In the following experiments, the accurate identification of the oxide phase involved in the transformation is a crucial parameter, particularly in the cases Fe_3O_4 and $\gamma\text{-Fe}_2\text{O}_3$. The corundum ($\alpha\text{-Fe}_2\text{O}_3(0001)$) film can be easily distinguished from the spinel structures, ($\text{Fe}_3\text{O}_4(111)$ and $\gamma\text{-Fe}_2\text{O}_3$), by looking at the diffraction space (LEED). In the experiments, the initial and final chemical compositions of the spinel and the corundum phases were probed by X-PEEM at the Fe3p peak. In the following, I will call $\gamma\text{-Fe}_2\text{O}_3$ the inverse spinel phase which is composed only by Fe^{3+} cations, i.e. when no chemical contrast is obtained in XPS between this phase and $\alpha\text{-Fe}_2\text{O}_3$. The presence of Fe^{2+} ions indicates that the spinel structure is Fe_3O_4 , which can be more or less stoichiometric (due to varying Fe vacancies concentration).

All the techniques used in the experiments are surface sensitive, and the probing depth of the sample composition is limited to the first atomic layers (0.5 nm to 2 nm) of the film; consequently, in these studies we cannot directly test the film structure beyond this depth. The film might have a layer structure; however, other investigation methods have never observed (yet) such scenario in similar samples. On the contrary, HR-TEM on $\text{Fe}_3\text{O}_4/\text{Pt}$, prepared under

nearly identical conditions probed that the film has a homogenous structure, from the surface to the support interface. Therefore, the stable film structure, observed at the surface, is assumed to represent the entire film thickness. Clearly, this assumption should be tested by other -bulk sensitive- methods, like TEM.

3.1.1 Phase transformation mechanism

Compositional change: $\text{Fe}_3\text{O}_4 \rightarrow \gamma\text{-Fe}_2\text{O}_3$

During the oxidation, Fe diffuses from the Fe_3O_4 bulk to the surface under the gradient of chemical potential μ_{O_2} ; the Fe excess at the surface is oxidized by adsorbed oxygen [43, 59]. The activation energy for this process is $\Delta E_A \approx 20$ kcal/mol, corresponding to 0.87 eV, as measured in [97, 113, 114].

Structural change: $\gamma\text{-Fe}_2\text{O}_3 \rightarrow \alpha\text{-Fe}_2\text{O}_3$

The structural transformation from spinel to corundum requires the restacking of the oxygen layers from fcc to hcp, and the rearrangement of the Fe cations. The restacking of the oxygen plane proceeds through the movement of in-plane dislocations. The change in coordination due to the O layer restacking induces the simultaneous adjustment of cations in the new structure [59, 60, 62]. This mechanism is called "synchro-shear mechanism" and was suggested for $\gamma \rightarrow \alpha$ transformation in Fe_2O_3 [115]; similar mechanisms have also been suggested for the $\Theta \rightarrow \alpha$ transition in Al_2O_3 [116, 117] and for the reverse transformation (i.e. $\alpha\text{-Fe}_2\text{O}_3 \rightarrow \text{Fe}_3\text{O}_4$) [118].

The process follows the topotactic relationship between the crystalline orientations in the two structures:

- $(111)_{\text{spinel}} // (0001)_{\text{corundum}}$
- $[\bar{1}10]_{\text{spinel}} // [\bar{1}100]_{\text{corundum}}$

In $\gamma\text{-Fe}_2\text{O}_3$ (fcc) and $\alpha\text{-Fe}_2\text{O}_3$ (hcp) the stacking of the oxygen layers can be represented as ABCABC and ABABABA, respectively. Consequently, the fcc|hcp interface between the two oxide structures consists of repeated units of in plane stacking faults of the types: A|C, A|B, B|A and C|B (see Fig. 3.1). During the fcc \rightarrow hcp transformation, the stress arising at the fcc|hcp interface is released by transferring the interfacial O (fcc) atoms into the "correct"

(hcp) position. As a result, the in-plane dislocations defining the phase boundary slip by one atomic distance. The displacement for each oxygen atom is $a_0/\sqrt{3}$, where a_0 is the interatomic O-O distance in the un-deformed O layer; the direction of the displacement is the one that eliminates the planar stacking fault.

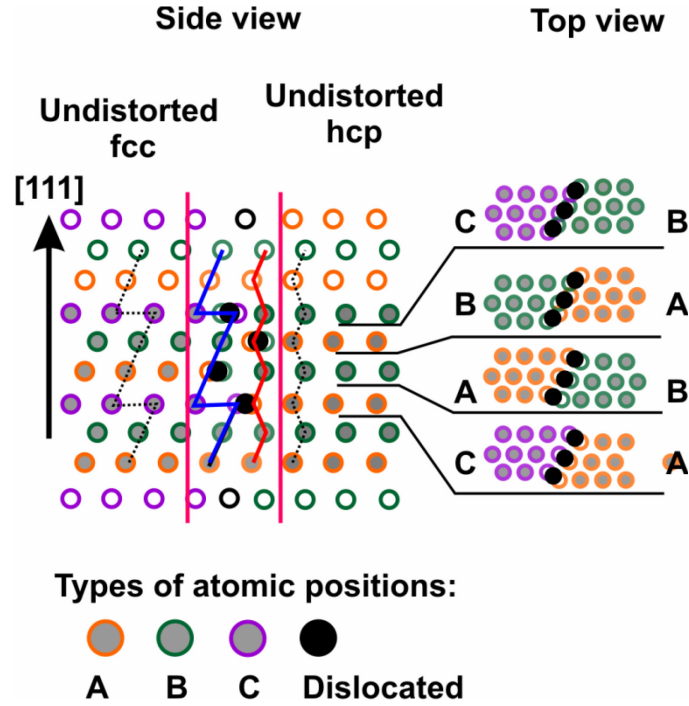


Fig. 3.1: Schematic view of a simplified interface between fcc and hcp structures (resembling the vertical stacking of the O layers in $\gamma\text{-Fe}_2\text{O}_3$ and $\alpha\text{-Fe}_2\text{O}_3$, respectively). Filled black circles denote dislocated atoms assuming an intermediate position at the interface. For simplicity, the layers are assumed to be perfectly aligned in the vertical stacking. The Fe layers are not shown. In the fcc stacking as shown, the A/B, C/A and B/C layers are separated by Kagomé layers, while the B/C, A/B and C/A layers are separated by Mix-Trigonal layers. In the hcp area, all O layers are separated by honeycomb Fe-layers.

In the $(111)_{\gamma\text{-Fe}_2\text{O}_3}$ and $(0001)_{\alpha\text{-Fe}_2\text{O}_3}$ directions, neighboring oxygen planes are separated by Fe layers: alternating Kagomé and Mix-Trigonal in the first, honeycomb in the second.

Simultaneous with the oxygen plane displacement, the Fe atoms rearrange from the spinel (Mix-Trigonal and Kagomé) into the new honeycomb structure by short-range interlayer Fe diffusion. This difference in superstructures (from (2×2) to $(\sqrt{3} \times \sqrt{3})R30^\circ$) accounts for the structural contrast in LEEM, needed to observe the growth of the reaction front. According to the model proposed in ref. [115], the transformation between Kagomé and honeycomb is direct, while the transformation from Mix-Trigonal to honeycomb proceeds through an intermediate Kagomé layer.

Direct transformation $\text{Fe}_3\text{O}_4 \rightarrow \alpha\text{-Fe}_2\text{O}_3$

The “direct” transformation $\text{Fe}_3\text{O}_4 \rightarrow \alpha\text{-Fe}_2\text{O}_3$ differs from the $\gamma\text{-Fe}_2\text{O}_3 \rightarrow \alpha\text{-Fe}_2\text{O}_3$ because the composition of the spinel phase differs from the Fe_2O_3 product after the growth process, as probed by XPS.

In this case, the change of composition through Fe vacancies creation does not occur over the entire extent of the Fe_3O_4 phase but occurs mainly at the phase boundary: during the oxidation reaction, the chemical composition of the parent phase is continuously adjusted close to the advancing reaction front. Locally (i.e. at the phase boundary) the transformation is most likely still a two steps process, involving first a change in composition, immediately followed by the structural transformation. $\gamma\text{-Fe}_2\text{O}_3$ might form as a metastable intermediate phase separating the Fe_3O_4 and the $\alpha\text{-Fe}_2\text{O}_3$. The transformation front would then be spatially extended and consist of two phase boundaries ($\text{Fe}_3\text{O}_4|\gamma\text{-Fe}_2\text{O}_3$ and $\gamma\text{-Fe}_2\text{O}_3|\alpha\text{-Fe}_2\text{O}_3$). The possible creation of a region characterized by an Fe concentration gradient during the reaction cannot be probed in our setup due to the lack of sufficient temporal resolution in X-PEEM. Under static acquisition conditions (i.e. after interrupting the transformation and quenching the sample down to about RT), such a boundary could not be detected. This suggests that this boundary is narrower than the spatial resolution of the X-PEEM, or that it disappears during the quenching before taking the X-PEEM data.

3.2 Experimental observation of the phase transformation

3.2.1 $\text{Fe}_3\text{O}_4 + \text{O}_2 \rightarrow \gamma\text{-Fe}_2\text{O}_3$

The stages involved in the formation of the $\alpha\text{-Fe}_2\text{O}_3$ phase are discussed in chapter 2.1. This characterization shows that during the oxidation, atomic Fe oxidizes first to Fe_3O_4 ($T \approx 500$ K), while the $\alpha\text{-Fe}_2\text{O}_3$ phase develops for $T > 650$ K. At this temperature, the structural transformation from inverse spinel to corundum is enabled. Therefore, to observe the oxidation of Fe_3O_4 to the isostructural $\gamma\text{-Fe}_2\text{O}_3$ the oxidation temperature should be lower than this value.

Initially, a single-phase Fe_3O_4 film was oxidized at the constant oxygen pressure of $p_{\text{O}_2} = 3 \cdot 10^{-5}$ mbar at $T = 620$ K for 11 min (first annealing). The co-existence with the $\alpha\text{-Fe}_2\text{O}_3$ phase was obtained increasing the oxidation temperature up to $T = 775$ K (second annealing). The film composition was characterized at RT by X-PEEM, and bright field LEEM-IV measurements

have been performed before (first annealing step) and after the structural transformation (second annealing). During the cooling, the sample was exposed to oxygen pressure ($p_{O_2}=3.10^{-5}$ mbar) for $T > 450$ K to prevent oxygen desorption from the oxide. The sample was monitored in real time during the low temperature oxidation (data not reported). However, no growing front was observed.

Fig. 3.2 shows the LEEM, X-PEEM and LEED images of: the initial Fe_3O_4 film (Fig. 3.2a-b), the sample after oxidation at $T = 620$ K (first annealing, Fig. 3.2c-e) and the surface after annealing at $T = 775$ K (second annealing Fig. 3.2f-h).

The Fe_3O_4 LEED pattern (Fig. 3.2b) shows a clear (2×2) reconstruction. After the first oxidation, the LEED pattern (Fig. 3.2e) has changed: in addition to the (2×2) spots, it exhibits weak and relatively ordered extra spots, aligned on one of the $(0,1)$ and equivalent crystalline directions. The presence of the (2×2) spots indicates that the inverse spinel structure did not change during the oxidation, while the extra-spots form a partially ordered (9×1) reconstruction. The corresponding LEEM image of the sample (Fig. 3.2c) shows a homogenous surface, similar to the one of the initial Fe_3O_4 phase (Fig. 3.2a). After the second annealing, the LEED (Fig. 3.2h) shows the superposition of the (2×2) reconstruction and the $(\sqrt{3} \times \sqrt{3})R30^\circ$ biphasic termination. The LEEM image (Fig. 3.2f) confirms that the sample is composed of two oxides phases with different contrasts and crystal structures: the inverse spinel is gray and the corundum dark gray. Additionally, FeO areas are visible as black islands in the $\alpha-Fe_2O_3$ phase. The X-PEEM image (Fig. 3.2g) does not show any contrast between the inverse spinel and the corundum phases, while the FeO areas are visible as black islands.

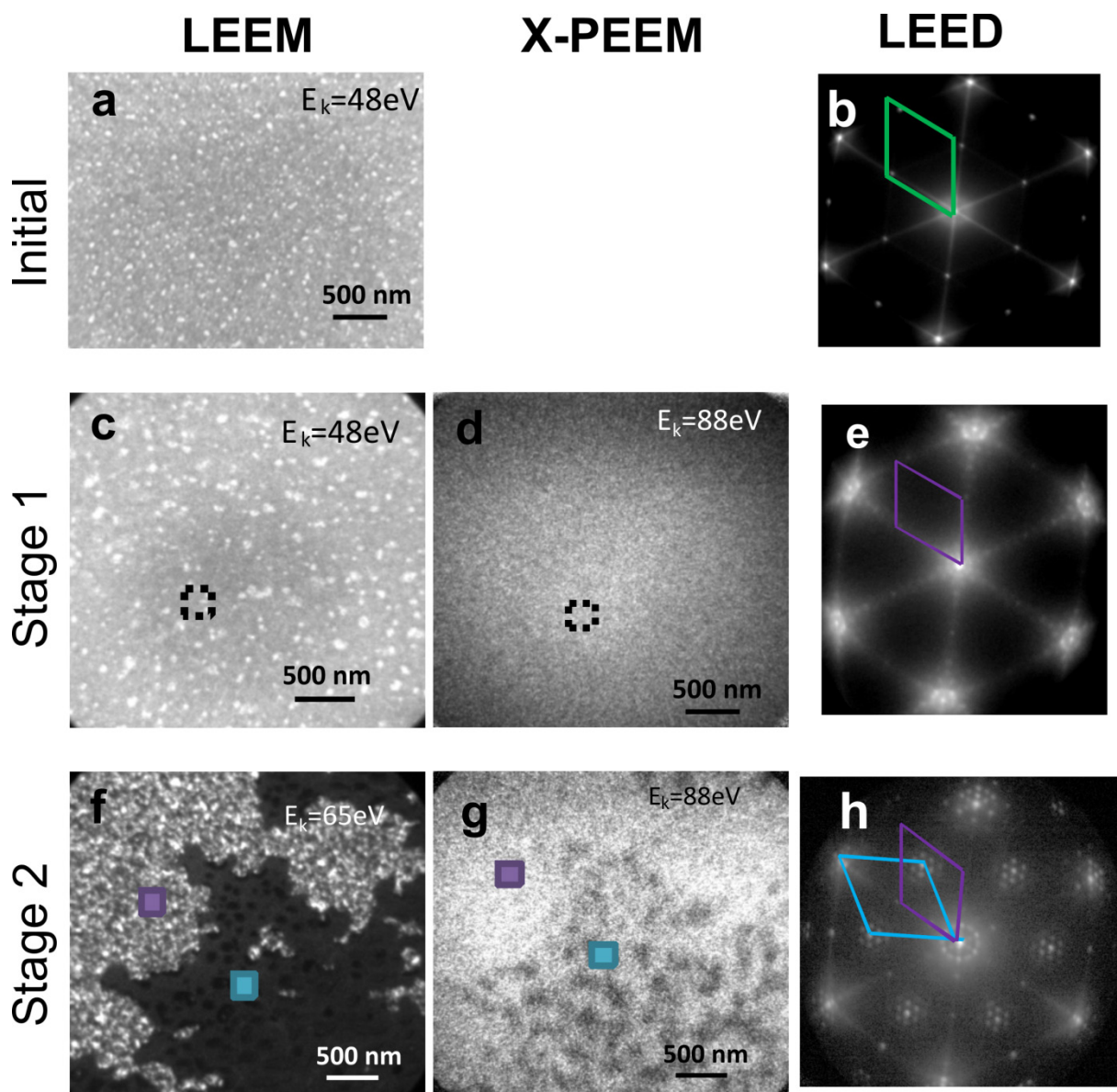


Fig. 3.2a-b) LEEM and LEED images of the initial Fe_3O_4 surface; 3.2c-e)) LEEM, X-PEEM and LEED of the surface after low temperature oxidation. The LEEM image shows that the sample surface is extremely similar to the initial Fe_3O_4 phase; LEED of the surface exhibit an irregular (9x1) reconstruction in addition to the (2x2) superstructure. 3.2f-h) LEEM, X-PEEM and LEED surface after the second annealing to $T=775$ K. The LEEM image shows two-oxide phases: the inverse spinel (gray) and $\alpha\text{-Fe}_2\text{O}_3$ (dark). The black areas in the $\alpha\text{-Fe}_2\text{O}_3$ phase are FeO holes. LEED of the surface exhibits the superposition of the ($\sqrt{3}\times\sqrt{3}$) biphas reconstruction and the (2x2) main spots. The colored squared in the LEEM and X-PEEM images indicate the area considered for the spatially resolved XPS spectra in Fig. 3.3 (E_k of the acquisition is indicated).

The X-PEEM spectra on the Fe3p line were taken at RT after the first and second annealing. In this case, the direct comparison between the X-PEEM spectra of the inverse spinel and of the $\alpha\text{-Fe}_2\text{O}_3$ phases is the most accurate way to evaluate the stoichiometry of the inverse

spinel phase. Fig. 3.3 shows the comparison of Fe3p for the marked areas in Fig 3.2: the blue line represents the α -Fe₂O₃ reference; the black and purple lines are the curves for the inverse spinel phase before and after the second annealing, respectively.

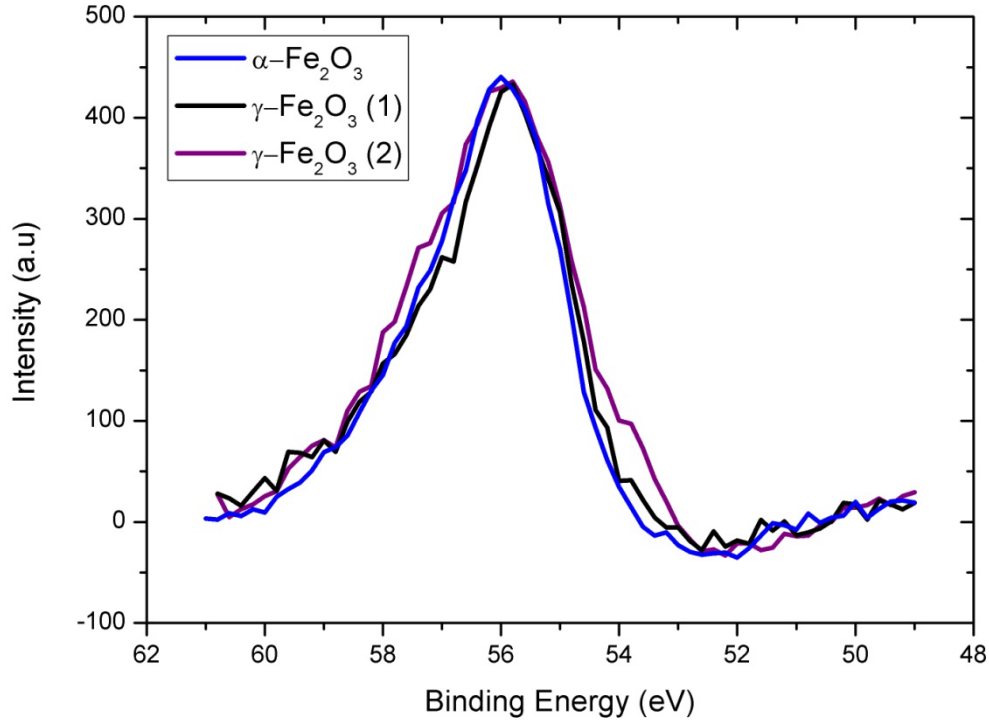


Fig. 3.3: Comparison of Fe3p spectra for intermediate step after initial oxidation (black) and both intermediate state and α -Fe₂O₃, after second oxidation. The integrated areas are indicated by the same colors in Fig 3.2. $h\nu = 150$ eV.

The comparison between the Fe3p signals shows that the additional component at lower binding energy, i.e. the XPS fingerprint of Fe₃O₄, is absent in all spectra. The peak in the Fe3p spectra is assigned to the Fe³⁺ ionic state, as it is the only ionic state present in stoichiometric Fe₂O₃. As the black spectrum underlines, already after the first oxidation step ($T = 620$ K) the inverse spinel phase shares the same stoichiometry of α -Fe₂O₃. These comprehensive analyses, which combine both structural and chemical characterization of the surface, suggest that, most likely, γ -Fe₂O₃ formed during low temperature oxidation. The (9x1) superstructure visible in LEED and associated to the γ -Fe₂O₃ indicates the presence of a partial long range ordering which could be associated to an unknown surface reconstruction. Further studies should be addressed to investigate the nature of this reconstruction.

As pointed out by the XPS spectra, the oxidation of Fe₃O₄ to γ -Fe₂O₃ was already completed after the first oxidation step at $T = 620$ K. However based on the X-PEEM and LEED

measurements we cannot exclude that the oxidation occurring in the spinel phase is only superficial. The conversion of the full thickness of the Fe_3O_4 film to $\gamma\text{-Fe}_2\text{O}_3$ (in these conditions) should be tested with other, bulk sensitive methods [119].

In order to understand the mechanism for the formation of the γ -phase, the experiment was repeated (Fe_3O_4 film, $T = 620\text{ K}$, $p = 3 \times 10^{-5}\text{ mbar}$), and the oxidation was recorded in real time, setting the electron energy at 65 eV. This energy corresponds to a high and low intensity for Fe_3O_4 and $\gamma\text{-Fe}_2\text{O}_3$ respectively, as pointed out from the LEEM-IV curves reported in the next section (Fig. 3.6). In this way, growing fronts of $\gamma\text{-Fe}_2\text{O}_3$ in the Fe_3O_4 phase, if present, should have visible contrast, but none was observed. This can be an indication that the compositional change of the film proceeds uniformly (homogeneous transformation). As cations are the mobile species in oxide, the change in the Fe:O ratio occurs most likely by Fe diffusion to the sample surface (along the $[111]_{\text{Fe}_3\text{O}_4}$ direction), by the interstitial collinear removal mechanism [68, 120, 121]. At the surface, Fe cations in excess react with the adsorbed oxygen, forming new oxide layers.

3.2.2 $\gamma\text{-Fe}_2\text{O}_3 \rightarrow \alpha\text{-Fe}_2\text{O}_3$

The surface shown in Fig. 3.2f, composed by $\alpha\text{-Fe}_2\text{O}_3$ and $\gamma\text{-Fe}_2\text{O}_3$, was annealed in UHV conditions up to 850 K. This treatment induces the structural transformation of the Fe_2O_3 from the γ - to the α -phase. The sequence in Fig. 3.4 shows the growth process at the moving α/γ interface.

The growth starts at $T \approx 650\text{ K}$, in UHV conditions; it proceeds fast and at 790 K the film is almost completely converted to $\alpha\text{-Fe}_2\text{O}_3$; some unconverted islands with inverse spinel structure are also present (see Fig. 3.5b).

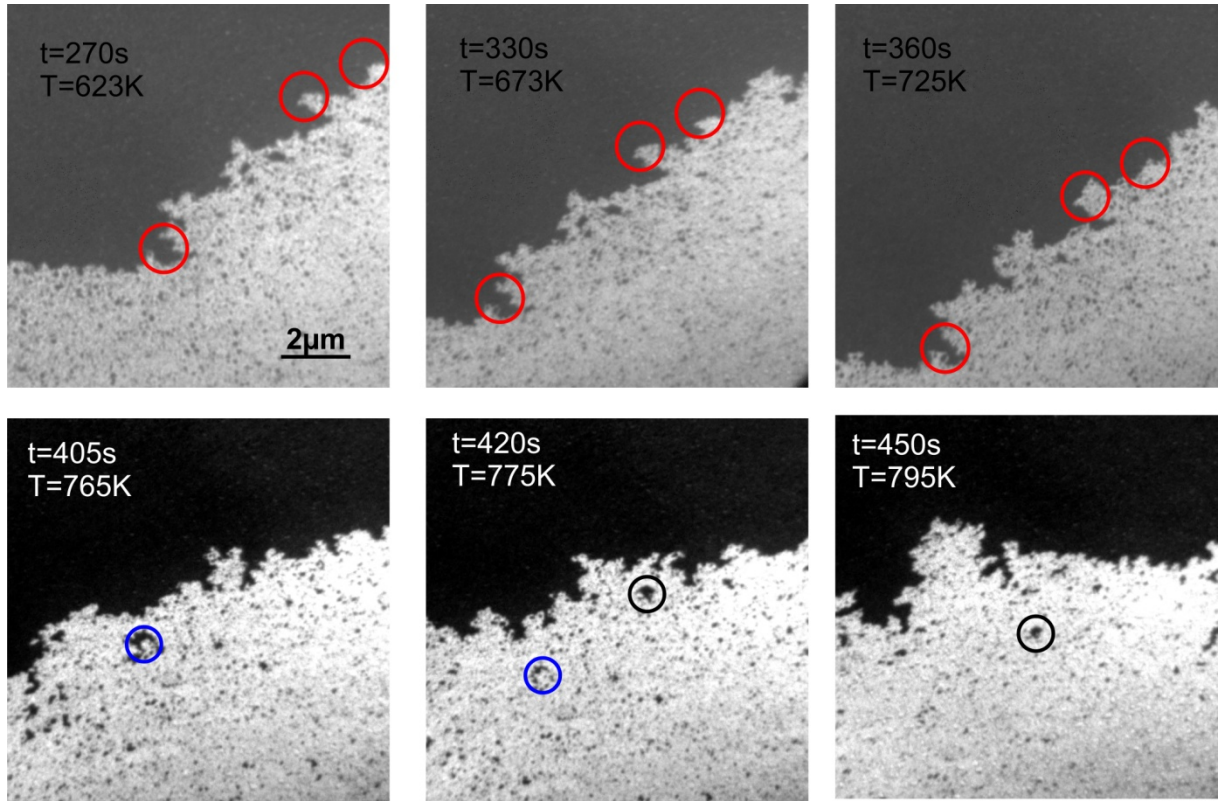


Fig. 3.4: LEEM sequence of final annealing in UHV condition: α -Fe₂O₃ (white) grows on the γ -Fe₂O₃ phase (dark). $E_k=24\text{eV}$

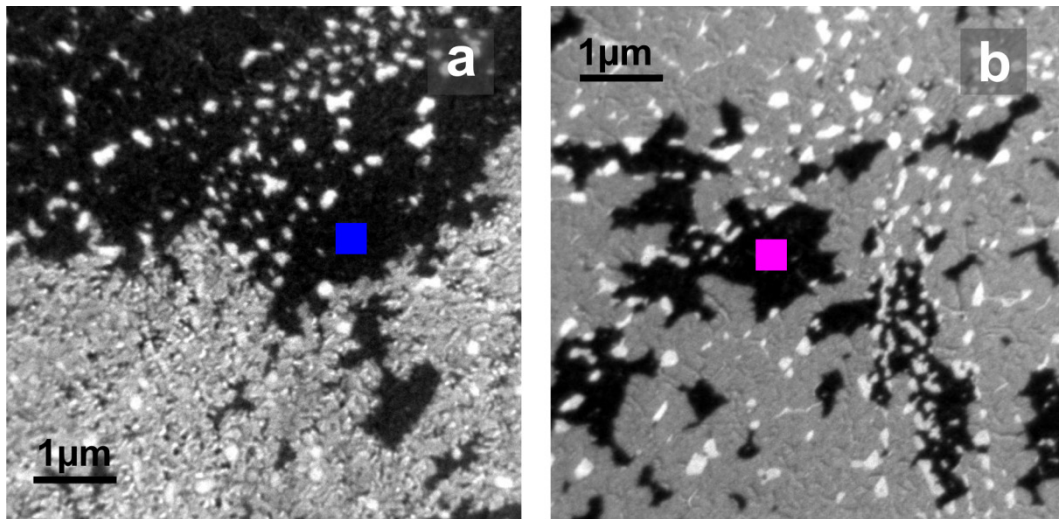


Fig. 3.5: LEEM a) surface after the oxidation; b) surface after UHV annealing: the blue box refers to the area considered for the LEEM-IV profile in Fig. 3.6. $E_k=40\text{ eV}$

The sample surface was characterized also by brightfield LEEM-IV measurements, before and after the completion of the structural transformation.

Fig. 3.6 shows the I-V curves relative to the spinel phase only; the blue and magenta lines are data taken before and after the UHV annealing, respectively; the integration areas are indicated in Fig. 3.5a-b. These data were compared with the Fe_3O_4 brightfield LEEM-IV profiles. Data relative to two Fe_3O_4 terminations are plotted as comparison: the first dataset (red dotted lines) refers to Fe_3O_4 prepared in $p_{\text{O}_2}=1 \times 10^{-6}$ mbar, $T=1000$ K; the second (black dotted lines) refers to Fe_3O_4 after UHV flash ($T=1000$ K).

The blue line ($\gamma\text{-Fe}_2\text{O}_3$) differs substantially from both Fe_3O_4 reference data. On the other hand, the magenta profile (unconverted islands) fits nicely the LEEM-IV for the flashed- Fe_3O_4 termination. In Fig. 3.6, the LEEM-IV of $\gamma\text{-Fe}_2\text{O}_3$ have been compared to the LEEM-IV of Fe_3O_4 exposed to oxygen ($T=3 \times 10^{-5}$ mbar, RT) (Fig. 3.7). These datasets differ substantially, excluding that the difference between the $\gamma\text{-Fe}_2\text{O}_3$ and the Fe_3O_4 LEEM-IV profiles is a simple consequence of adsorbed oxygen on the Fe_3O_4 surface. LEEM-IV supports the X-PEEM results, indicating that a new phase formed during the low temperature oxidation.

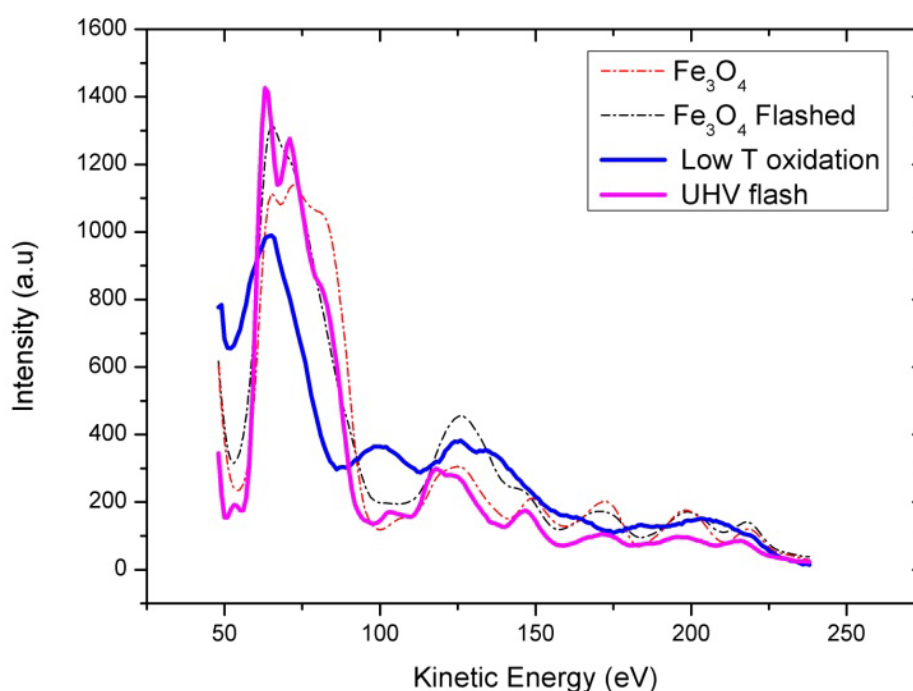


Fig. 3.6: LEEM-IV profiles for the (2x2) surface components after the low temperature oxidation (blue curve), and after the oxidation and the UHV flash (magenta line). For comparison the brightfield LEEM – IV curves for Fe_3O_4 after oxidation ($T=1000$ K, $p_{\text{O}_2}=10^{-6}$ mbar) and after UHV flash ($T=1000$ K) are shown (red and black dotted lines)

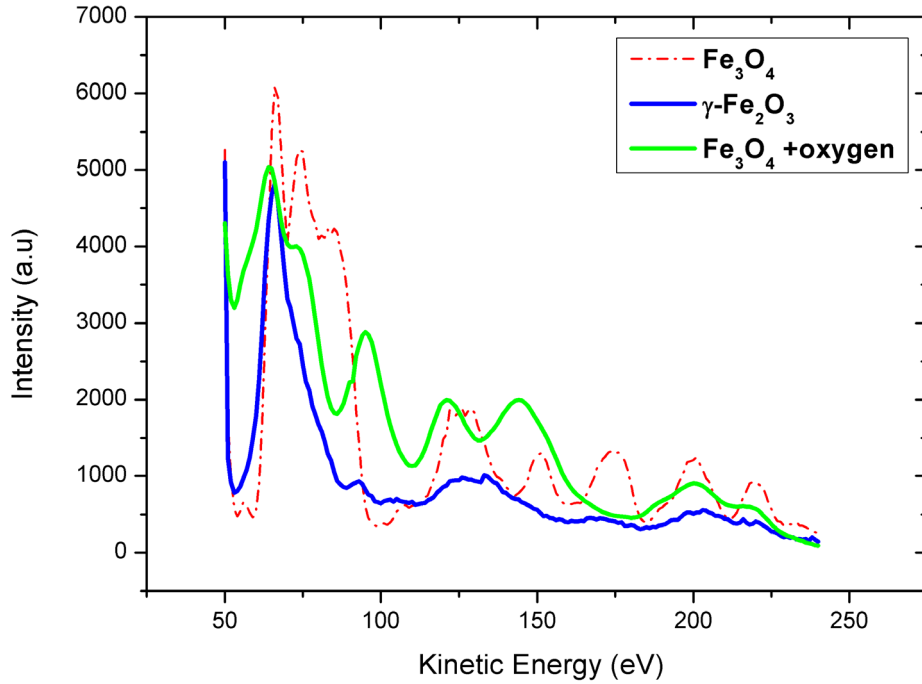


Fig. 3.7: LEEM-IV for O₂ adsorbed at the Fe₃O₄ surface (green curve) and for the (2x2) component after low temperature oxidation (γ-Fe₂O₃). The brightfield LEEM-IV profile for Fe₃O₄ after preparation (T=1000 K, p_{O₂}=10⁻⁶ mbar) is also shown (red dotted line) .

Remarkably, the unconverted islands after the UHV flash were identified as Fe₃O₄ areas, based on the LEEM-IV curves. This might indicate that, during high temperature annealing, the metastable γ-Fe₂O₃ phase transforms into one of the two stable Fe-oxide phases: either its allotrope α-Fe₂O₃ or its isostructural counterpart Fe₃O₄. Similar results were found by [122]. According to this study, the surface termination of naturally grown γ-Fe₂O₃ transforms to Fe₃O₄-like or α-Fe₂O₃-like surface structures when treated under reducing and oxidizing conditions, respectively.

3.2.3 Fe₃O₄ + O₂ → α-Fe₂O₃

The Fe₃O₄ oxidation to α-Fe₂O₃ was studied by LEEM, observing the real time evolution of the phase boundary Fe₃O₄|α-Fe₂O₃ in a mixed film (on Pt(111)) during annealing T = 700 K in p_{O₂}=3x10⁻⁵ mbar.

In the initial surface (Fig. 3.8a) the two oxide phases are easily distinguishable by their contrast: Fe₃O₄ (bright) and α-Fe₂O₃ (dark). FeO holes are additionally visible as white islands, mainly located in the α-Fe₂O₃ area. The film was annealed from RT up to 700 K in highly oxidizing conditions (p_{O₂} = 3x10⁻⁵ mbar O₂ pressure), as shown in the sequence in Fig.

3.8b-i. In the first part of the annealing ($T \approx 500$ K), the LEEM intensity of the Fe_3O_4 area reduces (contrast inversion visible between Fig. 3.8a and Fig. 3.8b). The change in LEEM reflectivity is related to a structural change of the Fe_3O_4 surface; most likely oxygen adsorbs on the surface, changing the Fe_3O_4 termination and/or its structure (this will be further discussed in the final section).

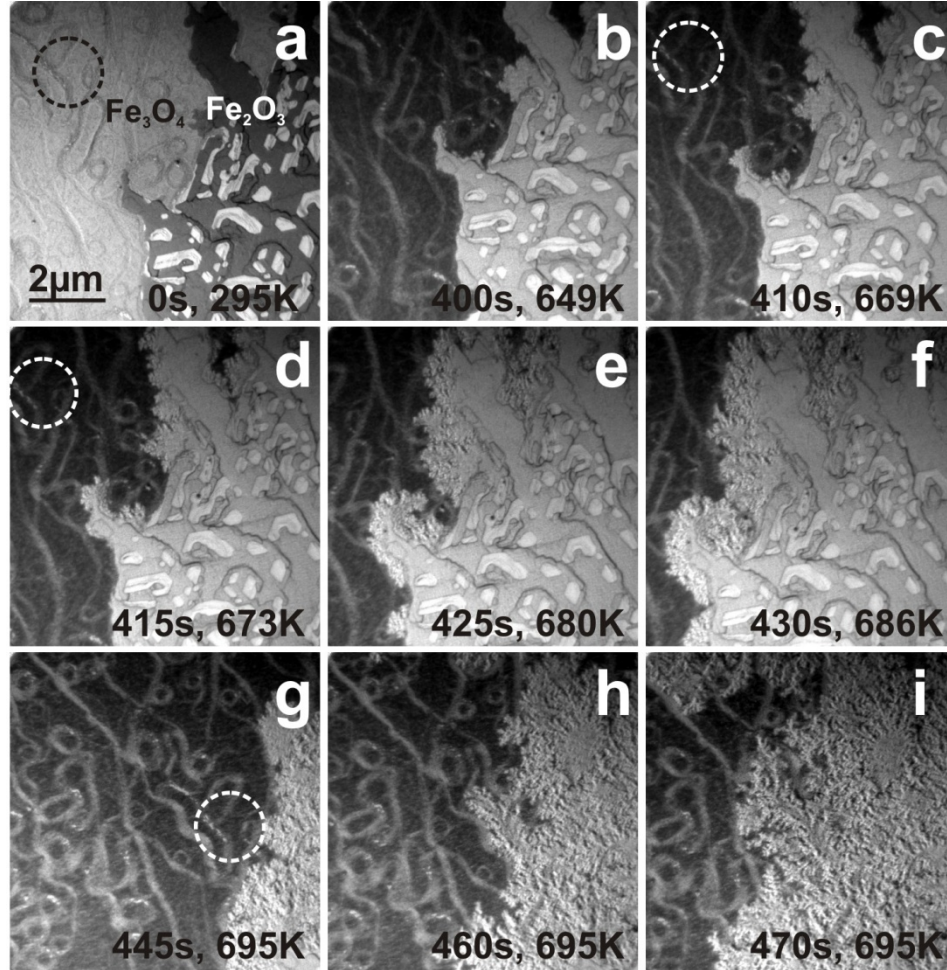


Fig. 3.8: LEEM a) mixed Fe_3O_4 (bright) and $\alpha\text{-Fe}_2\text{O}_3$ (dark) on Pt(111) (in the latter, FeO holes are visible as white areas). b-i) Oxidation front evolution during annealing from RT to $T = 700$ K at constant $p\text{O}_2 = 3 \times 10^{-5}$ mbar. $E_k = 20$ eV

At $T \approx 670$ K (Fig. 3.8c), the $\alpha\text{-Fe}_2\text{O}_3$ domain starts to grow into the Fe_3O_4 phase through a highly ramified dendritic front (Fig. 3.8g). The structure and the directions of the dendrites are discussed in details in the second part of this chapter.

As already discussed in section 3.1.1, the direct transformation involves the simultaneous change of the Fe:O ratio and the rearrangements in the Fe sub-lattice and the restacking of the close-packed oxygen planes. Similarly to the oxidation $\text{Fe}_3\text{O}_4 \rightarrow \gamma\text{-Fe}_2\text{O}_3$, the Fe density is

adjusted by cations diffusion along the $[111]_{\text{Fe}_3\text{O}_4}$ direction. Based on our experimental evidence, it is not possible to exclude that a partial conversion of Fe_3O_4 to $\gamma\text{-Fe}_2\text{O}_3$ might occur as an intermediate step during the annealing, since the structures of these oxides are indistinguishable. However, the conversion of Fe_3O_4 to stable $\gamma\text{-Fe}_2\text{O}_3$ can be excluded under these oxidation conditions by local XPS performed after oxidation. In fact, chemical contrast, indicating the excess of Fe^{2+} in the inverse spinel phase, is generally obtained between the two Fe-oxide phases after cooling down of the sample.

3.2.4 $\text{Fe}_2\text{O}_3 \rightarrow \text{Fe}_3\text{O}_4 + \text{O}_2$ (thin films supported on Ag(111))

The reduction process $\alpha\text{-Fe}_2\text{O}_3 \rightarrow \text{Fe}_3\text{O}_4$ was studied monitoring the UHV annealing of a mixed $\alpha\text{-Fe}_2\text{O}_3/\text{Fe}_3\text{O}_4$ film prepared on a Ag(111) support, following the preparation procedure summarized in Table 2.1.

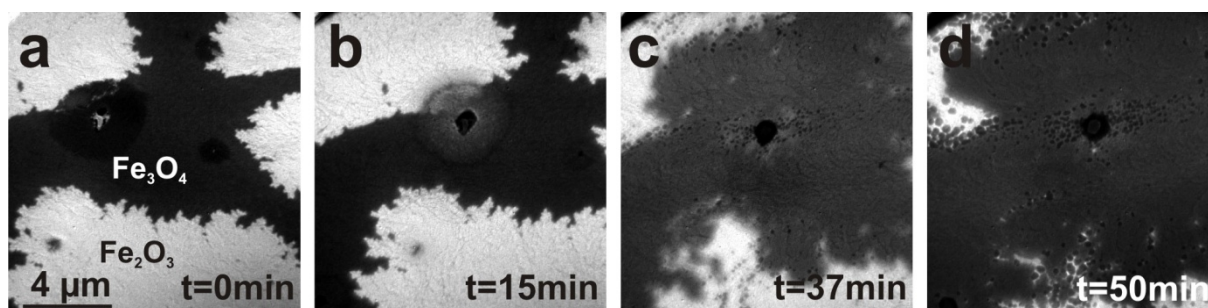


Fig. 3.9: LEEM. Reduction of $\alpha\text{-Fe}_2\text{O}_3$ (white) to Fe_3O_4 (dark), by UHV annealing on Ag(111) support.
 $E_k=24 \text{ eV}$

The mixed film was annealed in UHV from RT to $T = 673 \text{ K}$ for 10 min, then to 773 K (10 min) and finally to $T = 823 \text{ K}$ for 30 min; limiting the temperature was necessary to avoid Ag segregation. The segregation of Ag to the oxide surface was excluded by UV-PEEM (4.9 eV), looking for the secondary emission signal due to the Ag (workfunction 4.6 eV).

The process was observed in real time with LEEM (Fig. 3.9). The enlargement of the Fe_3O_4 island started after 20 min of annealing, i.e. reducing $\alpha\text{-Fe}_2\text{O}_3$ into Fe_3O_4 . The reaction is much slower than all the other cases treated in this chapter. Differently from the other reactions investigated in this chapter, for which Fe diffusion is mainly involved, in this case the process must occur through oxygen desorption.

3.2.5 $\text{Fe}_3\text{O}_4 \rightarrow \text{Fe}_2\text{O}_3 + \text{Fe}$ (thin films supported on Pt(111))

Similarly to what was done on Ag(111), I have monitored the UHV high temperature annealing ($T = 950 \text{ K}$) of a mixed film grown on Pt(111). In this case, unexpectedly, the $\alpha\text{-Fe}_2\text{O}_3$ area enlarged.

The initial surface is shown in Fig. 3.10a-c: the central area consists of a single $\alpha\text{-Fe}_2\text{O}_3$ domain surrounded by Fe_3O_4 ; the Fe_3O_4 phase is composed by two rotational domains (Fig. 3.10b-c).

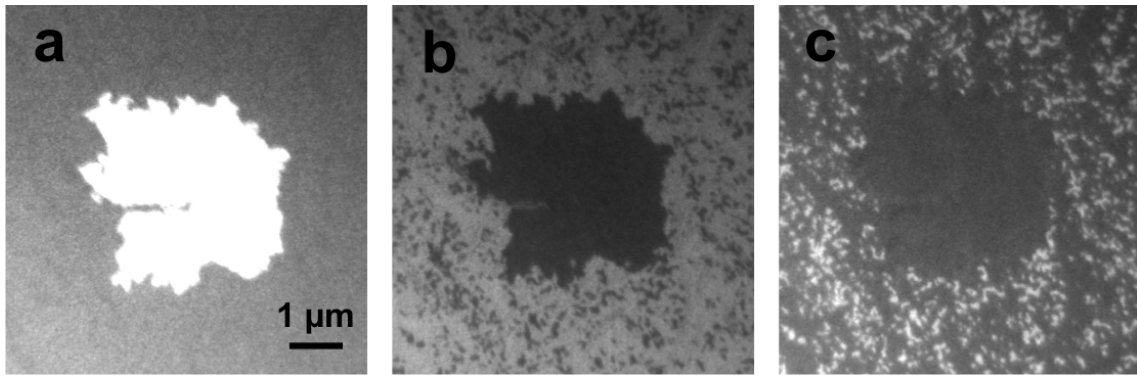


Fig. 3.10: LEEM. Dark-field contrast using: a) $(\sqrt{3} \times \sqrt{3})$ superstructure ($\alpha\text{-Fe}_2\text{O}_3$), $E_k=22 \text{ eV}$; b-c) two rotational domains of (2×2) superstructure (Fe_3O_4), $E_k=24 \text{ eV}$

The sequence in Fig. 3.11 shows the evolution of the central $\alpha\text{-Fe}_2\text{O}_3$ domain during annealing from RT to 950 K, in UHV ($p_{\text{O}_2} \approx 10^{-9} \text{ mbar}$). At about 697 K (Fig. 3.11b) the $\alpha\text{-Fe}_2\text{O}_3$ island starts to enlarge with a rough reaction front. The morphology of the front follows the features of the film morphology: this fact is treated in detail in the second part of this chapter. The growth front speed slows down at a temperature above 860 K. Above 900 K the $\alpha\text{-Fe}_2\text{O}_3$ film starts to dewet: the FeO area (black in the images) increases in size, as expected for this high temperature and a film thickness of 10 nm. The transformation observed experimentally is opposite to what is expected from the phase diagram for stable bulk iron oxides [22, 40], single crystal behavior [91] and in thin films [18].

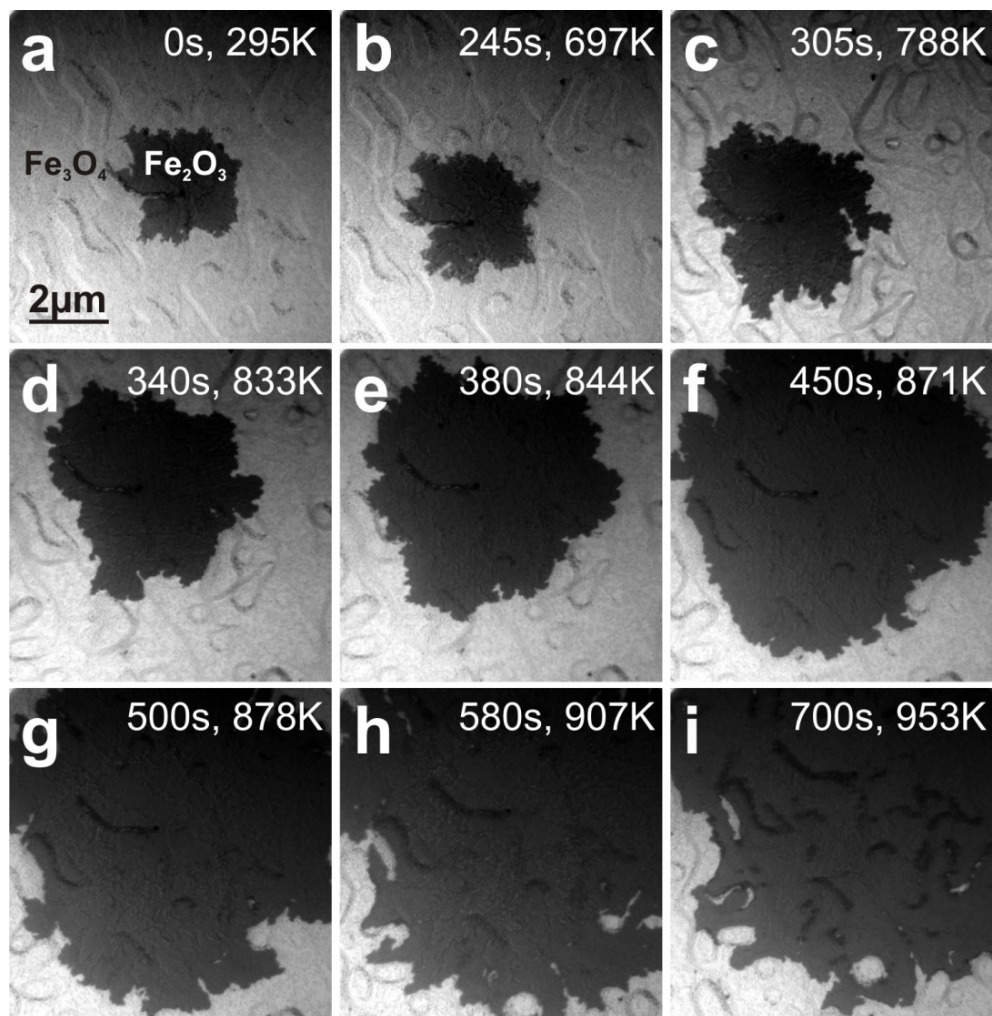


Fig. 3.11: LEEM. Evolution of the central α -Fe₂O₃ domain (dark) in the Fe₃O₄ matrix (light grey) during annealing from RT to 950 K in UHV. Step bunches resembling the substrate morphology and FeO holes (dark contrast near the steps) are visible. $E_k=29$ eV

Under these experimental conditions (UHV annealing), there is no O₂ available in the system for further oxidation of the film. The ratio of Fe:O can be only lowered if the Fe cations diffuse either to the surface or to the oxide/Pt interface. The enrichment of Fe on the surface was excluded by XPS and LEED. Therefore, the Fe diffusion must proceed down to the film/substrate interface. The excess of Fe can either form a layered FeO_x structure in the film, or dissolve in the substrate. Even though I could not probe the vertical structure of the film, it is very likely that the excess Fe dissolves in Pt(111), rather than forming a (reduced) layered structure. In fact, only in this way the opposite observations on Pt and Ag can be explained: the layered Fe₂O₃/FeO structure of the film should form under the same conditions both on Pt and on Ag; in contrast, Fe can be dissolved in the Pt bulk [123, 124], but not in the Ag bulk [125]. Another argument against the formation of a layered structure in such conditions comes

from TEM investigations. $\text{Fe}_3\text{O}_4/\text{Pt}(111)$ thin films prepared with analogous preparation procedures as ours show an homogeneous internal structure [85], rather than a layered structure.

The time scales required for the two opposite transformations differ substantially: on $\text{Pt}(111)$ the conversion of the visible Fe_3O_4 area takes a few minutes, while almost one hour is necessary for the $\alpha\text{-Fe}_2\text{O}_3$ on $\text{Ag}(111)$. This indicates that Fe diffusion (and subsequent segregation into the Pt substrate) can be more easily activated than the oxygen desorption (the dominant process on the $\text{Ag}(111)$ surface), in full agreement with the fact that in oxides bulk diffusion of cations (in this case Fe [121, 126]) is favored over oxygen diffusion [127].

UHV annealing of $\text{Fe}_3\text{O}_4/\text{Pt}(111)$ without $\alpha\text{-Fe}_2\text{O}_3$ interface

The results of the previous experiment raise the question: can $\alpha\text{-Fe}_2\text{O}_3$ spontaneously nucleate during UHV annealing of a $\text{Fe}_3\text{O}_4/\text{Pt}(111)$ sample as a direct consequence of Fe diffusion? To answer this questions I have investigated UHV annealing of a single phase Fe_3O_4 film on $\text{Pt}(111)$ (i.e. preexisting $\alpha\text{-Fe}_2\text{O}_3$ defects were absent in the range $\pm 100\text{ }\mu\text{m}$).

A $\approx 10\text{ nm}$ thick $\text{Fe}_3\text{O}_4/\text{Pt}(111)$ (Fig. 3.12a) film was annealed in UHV for 55 min at temperature above 820 K: first 40 min at $T=823\text{ K}$ followed by 15 min $T=883\text{ K}$. As a comparison, on the mixed film the structural transformation $\text{Fe}_3\text{O}_4 \rightarrow \alpha\text{-Fe}_2\text{O}_3$ started at $T=650\text{ K}$. No indication of $\alpha\text{-Fe}_2\text{O}_3$ nucleation was observed during this time. The LEED pattern of the sample surface after the annealing is reported in Fig 3.12b, showing the (2×2) superstructure.

Fig 3.12c-d show the LEEM images of the final surface taken at different electron energies. In the first image, the white contrast arises from the FeO islands, indicating that the oxide film (gray contrast) dewetted because of Fe removal during the annealing. The second image is taken at 65 eV. At this energy, there is contrast between Fe_3O_4 and $\gamma\text{-Fe}_2\text{O}_3$ (according to the LEEM-IV curves in Fig 3.6): $\gamma\text{-Fe}_2\text{O}_3$ is darker than Fe_3O_4 . As seen in the image, two oxide phases with different contrast are visible in the film. The Fe composition in the two areas was probed by X-PEEM at the Fe3p peak (Fig 3.13). The spectra were integrated over the area indicated in Fig 3.12c: X-PEEM data (Fig 3.13) show that some areas have a decreased Fe^{2+} component (red spectrum), suggesting that Fe-defective Fe_3O_4 formed because of Fe removal from the oxide film.

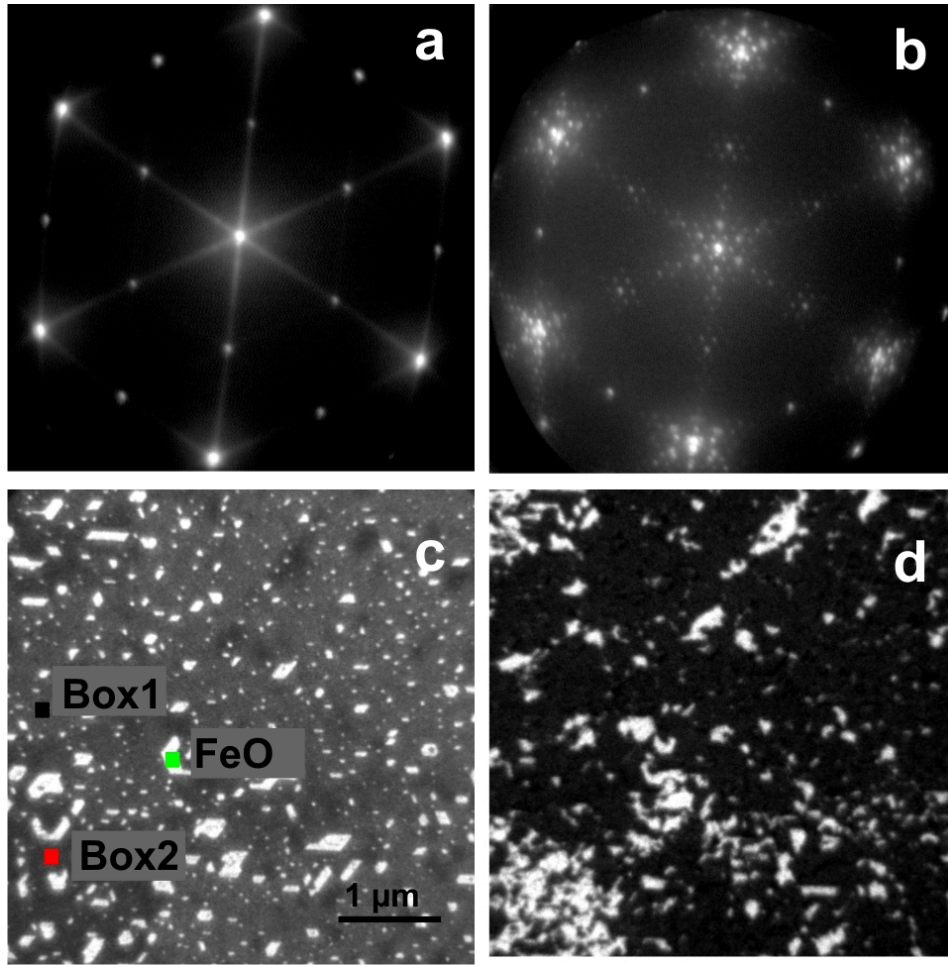


Fig. 3.12: a-b) LEED of the initial Fe_3O_4 surface and after 55 min of UHV annealing at $T > 820$ K, respectively. $E_k = 38$ eV (a); $E_k = 48$ eV (b). Fig 3.12c-d) LEEM of the final surface: $E_k = 50$ eV and $E_k = 65$ eV respectively. The areas used for the spectra in Fig.3.13 are indicated.

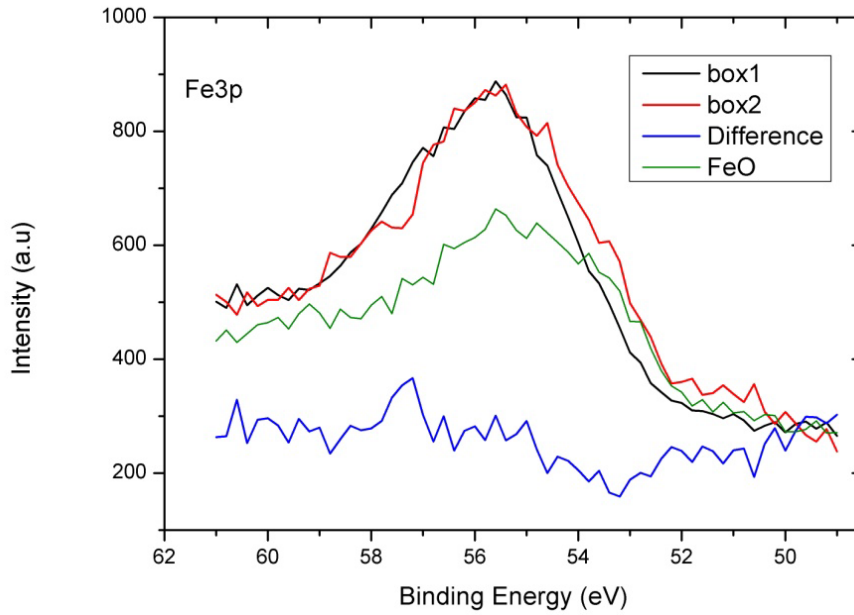


Fig. 3.13: XPS spectra at the Fe3p from selected regions indicated in Fig. 3.12c. $h\nu = 150$ eV.

The development of a different contrast in LEEM at 65 eV and the formation of the superstructure in LEED might be interpreted as the initial formation of γ -Fe₂O₃, but this needs further verification through investigations specifically devoted to this topic.

Remarkably, the growth of the α -Fe₂O₃ phase was not observed during UHV annealing when the Fe₃O₄| α -Fe₂O₃ phase boundary was absent. On the contrary, Fe removal from the films occurs in these conditions, as indicated by the film dewetting seen in the X-PEEM measurement. Spontaneous nucleation of a new phase requires super-saturation in the system: UHV annealing is clearly not one of these cases. Therefore, the Fe₃O₄ \rightarrow α -Fe₂O₃ transformation occurs only at the phase boundaries between α -Fe₂O₃|Fe₃O₄, if present. This was already suggested in [97, 98, 121, 128]

Fe dissolution in Pt(111)

The occurrence of dissolution of Fe in the Pt(111) substrate from the oxide film can be probed indirectly. For instance, one monolayer thick FeO(111)/Pt(111) (preparation: deposition of 1 ML at RT to avoid dissolution and annealing in oxygen atmosphere), decomposed by annealing above 1100 K in UHV. Under these conditions, Fe dissolves in the Pt bulk, as checked by subsequent annealing in oxygen and the observed formation of FeO. In addition, during the cleaning cycle of the Pt(111) substrate, FeO(111) forms on the Pt surface upon flashing the support in oxygen atmosphere, even though no Fe had been deposited before.

Fe dissolution into the Pt(111) bulk from some oxide islands was also directly observed. In this case, the sample was composed by α -Fe₂O₃ islands with FeO holes. Fe was deposited in oxygen atmosphere ($p_{O_2}=3 \times 10^{-5}$ mbar; $T = 830$ K), and during deposition FeO_x islands (grey contrast) formed in the middle of the FeO hole visible in Fig. 3.14a as the area with sharp borders and white contrast; the surrounding α -Fe₂O₃ film is dark gray. Once the Fe deposition stopped, the FeO_x structures dissolve in Pt(111), as shown in the sequence in Fig. 3.14b-g. The fine structure visible inside the FeO hole (Fig. 3.14g) forms as soon as the material is incorporated underneath the FeO layer, and resembles the initial distribution of the FeO_x islands.

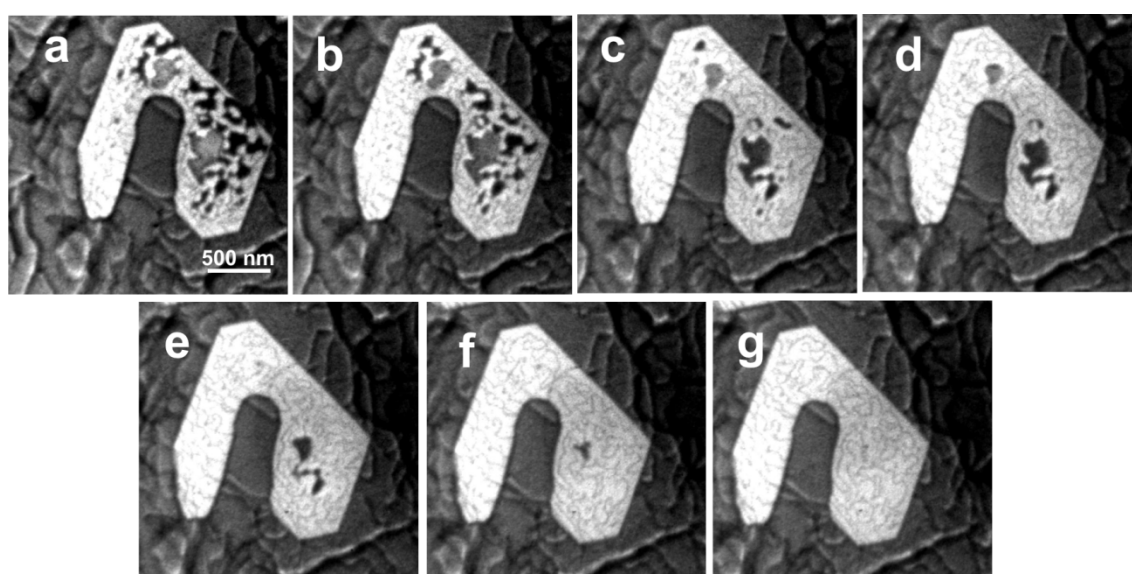


Fig. 3.14: LEEM. Dissolution of FeO_x structure grown on FeO/Pt(111) (holes in the α -Fe₂O₃ film). $T=830$ K. The overall sequence lasts 5 min; $p=3 \times 10^{-5}$ mbar. $E_k=19$ eV

3.2.6 Fe deposition α -Fe₂O₃/Pt(111) : α -Fe₂O₃ \rightarrow Fe₃O₄

On Pt(111), UHV annealing leads to a decrease of the Fe:O ratio. This occurs because thermal desorption of oxygen from α -Fe₂O₃ is slower than Fe diffusion from Fe₃O₄. Therefore, α -Fe₂O₃/Pt(111) can be reduced by intentionally increasing the Fe:O ratio of the system, for instance, by Fe deposition on the sample surface. The data presented in the following were already discussed in the context of α -Fe₂O₃ biphasic (1x1) reconstruction. Here we focus mainly on the formation of the Fe₃O₄ phase.

Fe was deposited (3 ML at RT) on an complete α -Fe₂O₃ film with bi-phase structure (LEEM and LEED in Fig. 3.15a-b, respectively). FeO holes are visible along the step bunches of the substrate (bright islands in Fig. 3.15a).

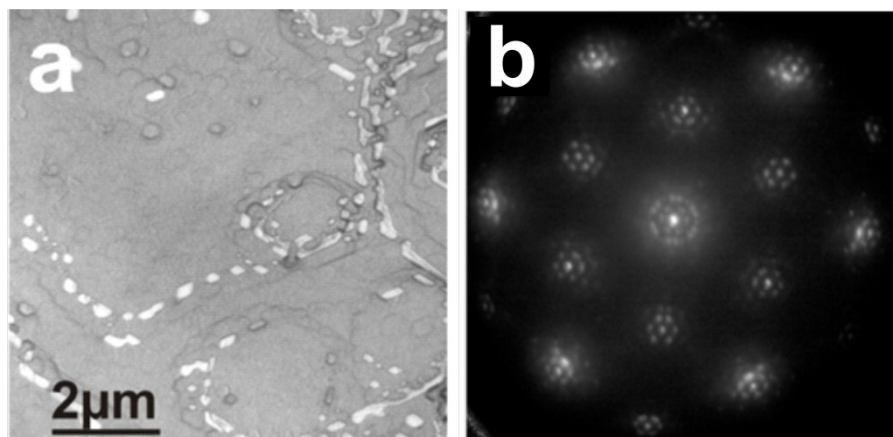


Fig. 3.15: a) LEEM and b) LEED of the starting surface consisting in a single phase α -Fe₂O₃ and FeO areas, supported on Pt(111). $E_k = 41$ eV

The sample was first annealed in UHV from RT to 700 K (5 min) and kept at $T = 700$ K for 90 s, before cooling down to RT again. In the second annealing step, the temperature was raised to 800 K (5 min) and kept for 100 s. Fe deposition and both annealing steps were observed in *real time* in LEEM (Fig. 3.16).

During the first annealing, the reduction of the α -Fe₂O₃ surface to Fe₃O₄ occurred in two steps. First, the surface intensity changed uniformly around $T = 570$ K (Fig. 3.16a-d), indicating the formation of a different homogeneous phase at the surface. In a second step, areas with dark contrast developed, preferentially surrounding the FeO holes (Fig. 3.16e-i). The sample was cooled down to RT, to characterize the two components.

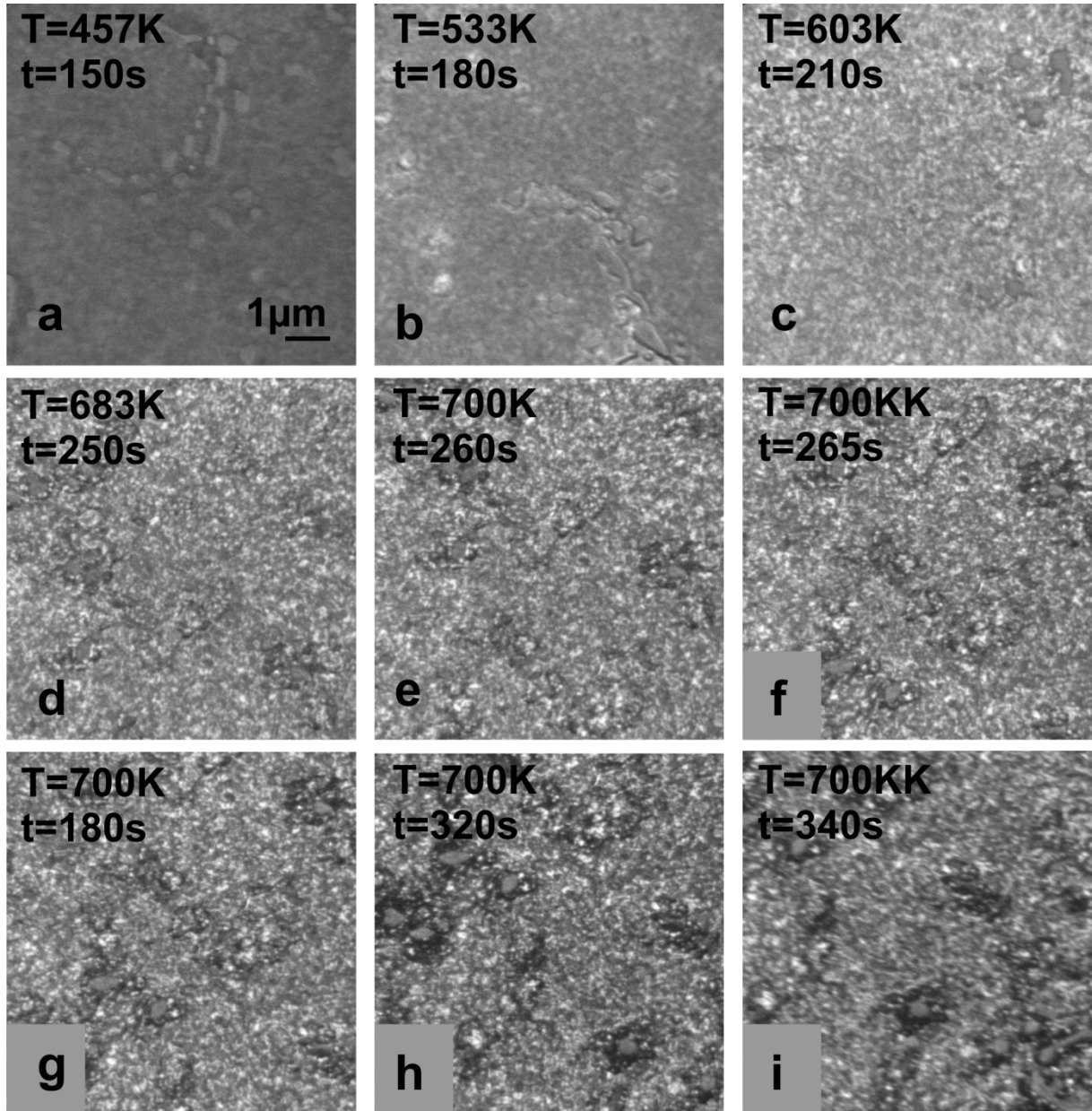


Fig. 3.16: LEEM. Evolution of the α -Fe₂O₃ surface during UHV annealing, induced by deposited Fe diffusion (after 3 ML deposition at RT). $E_k=24\text{eV}$

The LEEM and LEED of the surface after the first annealing step are shown in Fig. 3.17a-b.

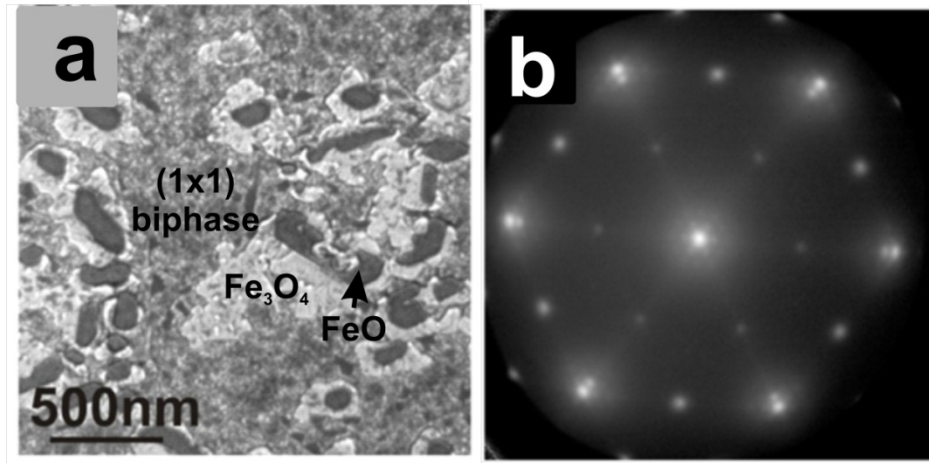


Fig. 3.17: LEEM (Fig. 3.18a), LEED (Fig. 3.19b) of the surface after first annealing, consisting in Fe₃O₄ (light domains), FeO holes (dark) and (1x1) biphasic termination (light grey) $E_k=24$ eV and $E_k=40$ eV respectively

LEED shows the superposition of the (2x2) reconstruction of Fe₃O₄ and the (1x1) biphasic reconstruction; the $(\sqrt{3}\times\sqrt{3})R30^\circ$ biphasic reconstruction of the α -Fe₂O₃ phase is completely absent. Darkfield imaging with the main diffraction spots of Fe₃O₄ and bi-phase shows that the Fe₃O₄ phase has formed (bright domains in Fig 3.17a.) nearby FeO holes (dark); the majority of the surface consists of the (1x1) bi-phase reconstruction (gray), (data refer to the discussion in Chapter 2.2).

The *real time* sequence of the second annealing (from RT to 800 K) in UHV is shown in Fig 3.18.

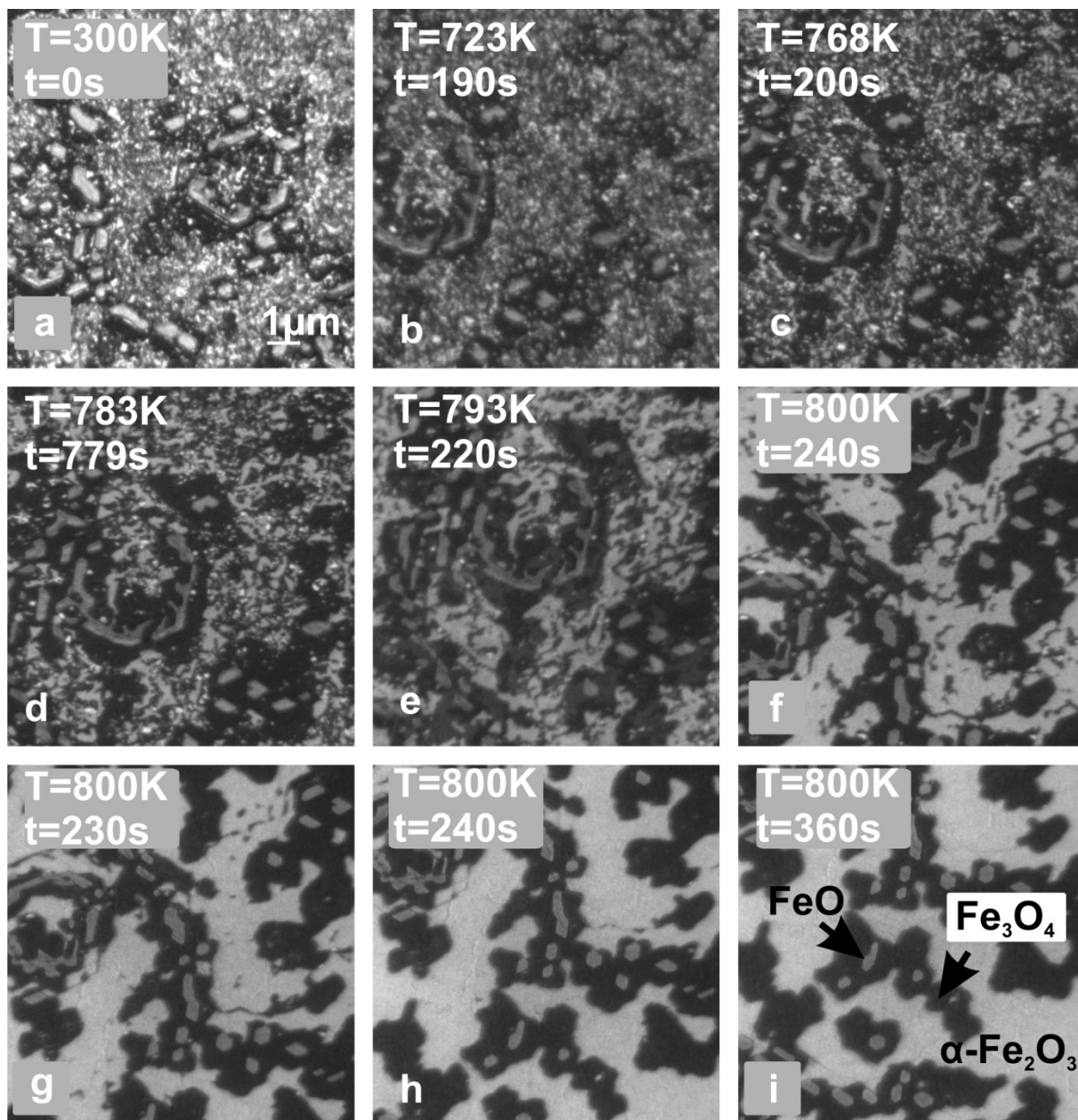


Fig 3.18: LEEM. Surface during second annealing in UHV; Fe₃O₄ domains (dark) and FeO holes (gray) enlarge; (1x1) biphas termination transforms to α-Fe₂O₃ (light grey). E_k=24 eV

The biphas terminated regions (gray disordered area) start to convert to the α-Fe₂O₃ (light gray contrast) at T ≈ 715 K (Fig 3.18b). During the fast process (completed in ≈170 s), both FeO and Fe₃O₄ enlarge and get well-defined boundaries. The annealing was stopped after all (1x1) biphas terminated areas were fully converted to α-Fe₂O₃. As already discussed in chapter 2.2, this indicates that the (1x1) biphas termination has formed on top of α-Fe₂O₃. Fig 3.19 shows the LEEM and LEED pattern of the final surface. The XPS spectra from the α-Fe₂O₃ and Fe₃O₄ confirm that the two oxide phases are chemically different (Fe²⁺ component), as shown in Fig 3.20.

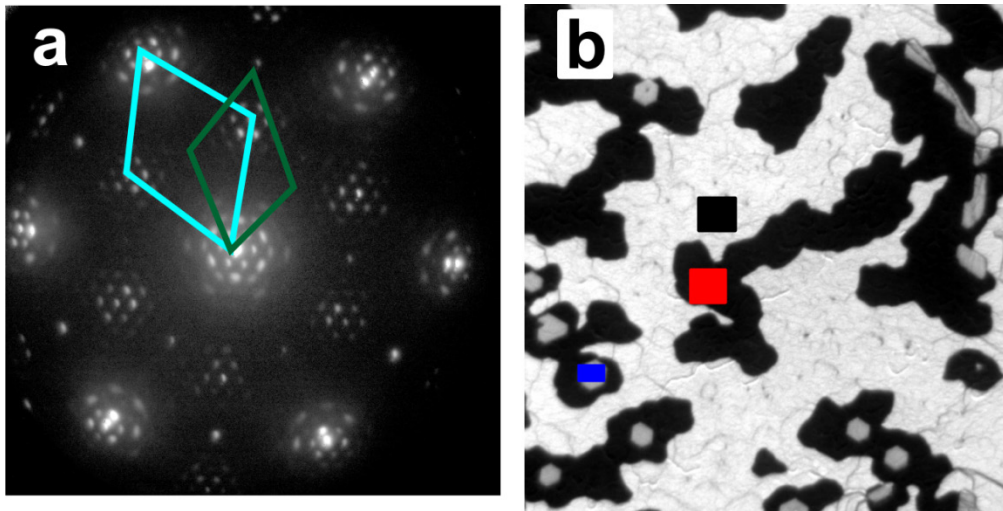


Fig. 3.19 a-b) LEED and LEEM of the final surface ($E_K=41$ eV and $E_K=24$ eV respectively); in the LEEM image is indicated the area considered in the local XPS spectra in (Fig. 3.20).

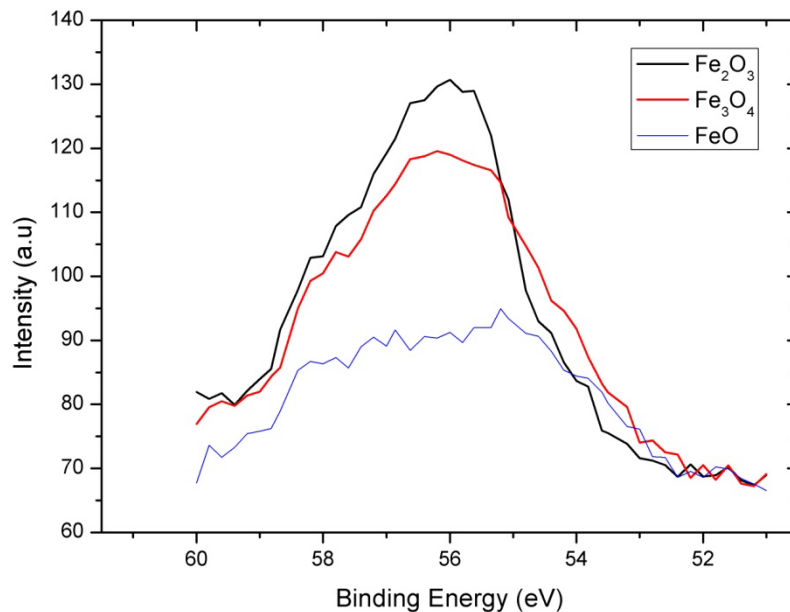


Fig. 3.20: XPS spectra at the Fe3p from selected regions indicated in Fig. 3.19b. $h\nu=150$ eV

In this experiment, the reduction of $\alpha\text{-Fe}_2\text{O}_3 \rightarrow \text{Fe}_3\text{O}_4$ on Pt(111) is driven by thermally activated diffusion of deposited Fe into the oxide film. After annealing at 700 K only part of the surface converts to Fe_3O_4 , while the remaining part shows the (1x1) biphasic termination formed on top of bulk $\alpha\text{-Fe}_2\text{O}_3$. This reduction reaction is slower than the oxidation of Fe_3O_4 . One reason for this is that iron diffusion is less favored in $\alpha\text{-Fe}_2\text{O}_3$ than in Fe_3O_4 [129] [126]. This can also explain why Fe remains longer on top of $\alpha\text{-Fe}_2\text{O}_3$ ((1x1) biphasic reconstruction). The second annealing to 800 K enables the (almost) complete diffusion from

the surface, as indicated by the fact that the (1x1) biphasic termination is fully reconverted to the $(\sqrt{3}\times\sqrt{3})R30^\circ$ biphasic reconstruction of $\alpha\text{-Fe}_2\text{O}_3$.

3.3 Average and local speed of the reaction front

The experiments presented in the first part of the chapter underline that all the transformations involving the structural rearrangement occur at the moving reaction front between the oxide domains (heterogeneous reactions). Moreover, the choice of the supporting substrate (in this case Pt(111) and Ag(111)) can strongly affect the observed transformation.

In this section, I focus on the detailed investigations of the (average and local) kinetics of the $\text{Fe}_3\text{O}_4|\alpha\text{-Fe}_2\text{O}_3$ and $\gamma\text{-Fe}_2\text{O}_3|\alpha\text{-Fe}_2\text{O}_3$ phase boundaries, studying the temporal evolution of the reaction front under different experimental conditions, by direct observation of the propagation of the phase transformation. As discussed in the next section, under certain assumptions, the front velocity measures the reaction rate.

I have focused on the following reactions:

- $\text{Fe}_3\text{O}_4 \leftrightarrow \alpha\text{-Fe}_2\text{O}_3$: direct compositional and structural transformation in both directions
- $\gamma\text{-Fe}_2\text{O}_3 \rightarrow \alpha\text{-Fe}_2\text{O}_3$: pure structural transformation (irreversible).

The temperature dependence of the various transformation velocities was used to estimate the effective activation energies for the processes involved in the transformation. In all cases considered the parent and product phases already co-existed on the sample (mixed film), excluding the initial nucleation process from the analysis.

The transformation $\text{Fe}_3\text{O}_4 \rightarrow \gamma\text{-Fe}_2\text{O}_3$ is not under discussion, because no reaction front was detected, as already presented in 3.2.1.

3.3.1 Methods: measurement of the reaction front velocity

Fig 3.21 gives an overview of the real time LEEM observations of the different phase transformations. All the experiments shown in the image were already discussed in 3.2, except for the oxidation $\text{Fe}_3\text{O}_4 \rightarrow \alpha\text{-Fe}_2\text{O}_3$ at $p_{\text{O}_2}=1\times 10^{-6}$ mbar. In each sequence of the images, the same surface region is shown; annealing temperatures and time are indicated. The sequences exhibit two main characteristics of the reaction front: its shape and its average velocity.

Assuming that the sample thickness¹ and thickness of the converted layer are constant, the experimental front velocity v is proportional to the reaction rate $R = \frac{d\alpha}{dt}$, where α is the fraction of converted material at a given time. In fact, given: A converted surface area, d the film thickness and $V = A \cdot d$ the volume of the converted oxide film, then the conversion rate is:

$$\frac{d\alpha}{dt} \propto \frac{dV}{dt} = \frac{\partial A}{\partial t} d + \frac{\partial d}{\partial t} A \xrightarrow{d=const} \frac{d\alpha}{dt} \propto \frac{\partial A}{\partial t} d = v L d$$

where L is the width of the front.

For a thermally activated reaction with constant rate-determining step, we expect Arrhenius behavior:

$$v = v_0 e^{-\frac{E_A}{k_B T}}$$

where v_0 is the pre-exponential, E_A the activation energy, T the absolute temperature, and k_B the Boltzmann constant.

¹ This approximation is valid in thin films, as the variation of the sample thickness is small compared to the surface area.

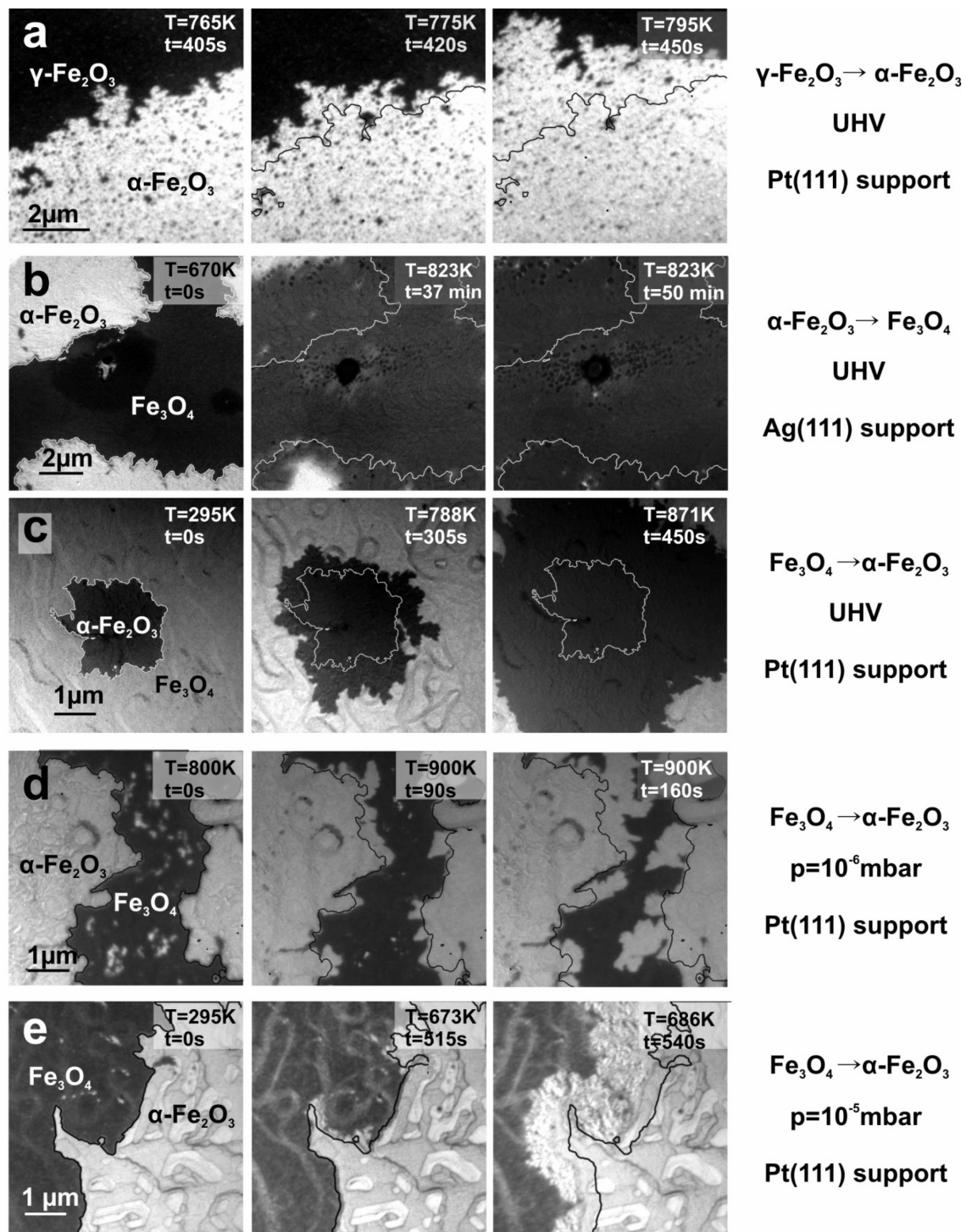


Fig. 3.21: Overview of LEEM images of the observed transformations. Annealing in UHV (Fig 3.21a-c) and in oxygen pressure ($p_{\text{O}_2}=1 \times 10^{-6}$ mbar in Fig 3.21d and $p_{\text{O}_2}=3 \times 10^{-5}$ mbar Fig 3.21e). The different crystalline phases ($\alpha\text{-Fe}_2\text{O}_3$, $\gamma\text{-Fe}_2\text{O}_3$ and Fe_3O_4) are labelled in the images. The contrast depends on the kinetic energy of the LEEM image (i.e. a) 23 eV, b) 24 eV, c) 29 eV, d) 24 eV, e) 20 eV). Pt(111) is used as support, except for b), where the film is supported on Ag(111). Temperature and time are indicated in the images.

During the experiments, the "mixed" films were annealed under isobaric conditions (UHV, $p_{O_2} = 1.0 \times 10^{-6}$ mbar, or $p_{O_2} = 3 \times 10^{-5}$ mbar) and observed in real space. The front velocity $v_{boundary} = \Delta s_{boundary} / \Delta t$ was evaluated from the *real time* LEEM images, as the average phase boundary displacement ($\Delta s_{boundary}$) that occurred in the time interval Δt . This procedure was applied also during the annealing stage (temperature not constant over time).

There are three main issues affecting the acquisition and evaluation of the experimental data. First, the reaction fronts exhibit complicated shapes: smoothing of these shapes was necessary to determine an "average velocity". Secondly, the reaction rates vary appreciably, depending on sample temperature, oxygen pressure, and substrate. Therefore, the microscope magnification, the acquisition time and the annealing rate were optimized to follow the processes with sufficient accuracy. Thirdly, the thermal sample drift moves the region of interest out of the FoV (Field of View), and manual adjustment of the sample position was necessary to move the studied sample region back into the FoV. Consequently, the heating procedure could not be identical for all experiments. All these facts affect the precision of the measurement: the maximum error for the velocity is safely below the threshold value of 20 %, attributed to the experimental data.

3.3.2 Temperature dependency of average front motion

Fig 3.22 displays the temperature dependence of the average front velocities for the five conversions considered (Arrhenius plot). The reaction velocities vary considerably, i.e. from 1 nm/s (reduction $\alpha\text{-Fe}_2\text{O}_3 \rightarrow \text{Fe}_3\text{O}_4$ on Ag(111)) to more than 200 nm/s (oxidation $\text{Fe}_3\text{O}_4 \rightarrow \alpha\text{-Fe}_2\text{O}_3$ at $p_{O_2} = 3 \times 10^{-5}$ mbar on Pt(111)). Based on the absolute value of the average front velocity, one can make a **first classification**: "*fast*" or "*slow*" transformation. The structural transformation $\gamma\text{-Fe}_2\text{O}_3 \rightarrow \alpha\text{-Fe}_2\text{O}_3$ in UHV and the $\text{Fe}_3\text{O}_4 \rightarrow \alpha\text{-Fe}_2\text{O}_3$ at $p_{O_2} = 3 \times 10^{-5}$ mbar are **fast**, while the reduction $\alpha\text{-Fe}_2\text{O}_3 \rightarrow \text{Fe}_3\text{O}_4$ and the $\text{Fe}_3\text{O}_4 \rightarrow \alpha\text{-Fe}_2\text{O}_3$ observed in UHV and $p_{O_2} = 1 \times 10^{-6}$ mbar are **slow**.

Most datasets show an exponential dependence, suggesting that the reaction is controlled by a constant, thermally activated process. For these cases exponential fits have been performed, leading to a *effective activation energy* for the reaction. The parameters of exponential fits $v = v_0 \exp(-E_A/k_B T)$ are listed in Table 3.1. The fitting curves are included in Fig. 3.22 as solid lines.

There are two exceptions to the simple exponential trend: the conversion $\text{Fe}_3\text{O}_4 \rightarrow \alpha\text{-Fe}_2\text{O}_3$ by UHV annealing observed on Pt(111) and the oxidation $\text{Fe}_3\text{O}_4 \rightarrow \alpha\text{-Fe}_2\text{O}_3$ at $p_{\text{O}_2}=3 \times 10^{-5}$ mbar.

In the case of the UHV annealing of $\text{Fe}_3\text{O}_4 \rightarrow \alpha\text{-Fe}_2\text{O}_3$ the slowdown of the reaction velocity at high temperature might arise from the activation of the reverse transformation (i.e. the reduction $\alpha\text{-Fe}_2\text{O}_3 \rightarrow \text{Fe}_3\text{O}_4$), decreasing the total transformation rate. Therefore, the process is modeled as the sum of two exponential contributions, for the direct and the reverse transformation: $v = v_{01} \exp(-E_{A1}/k_B T) - v_{02} \exp(-E_{A2}/k_B T)$.

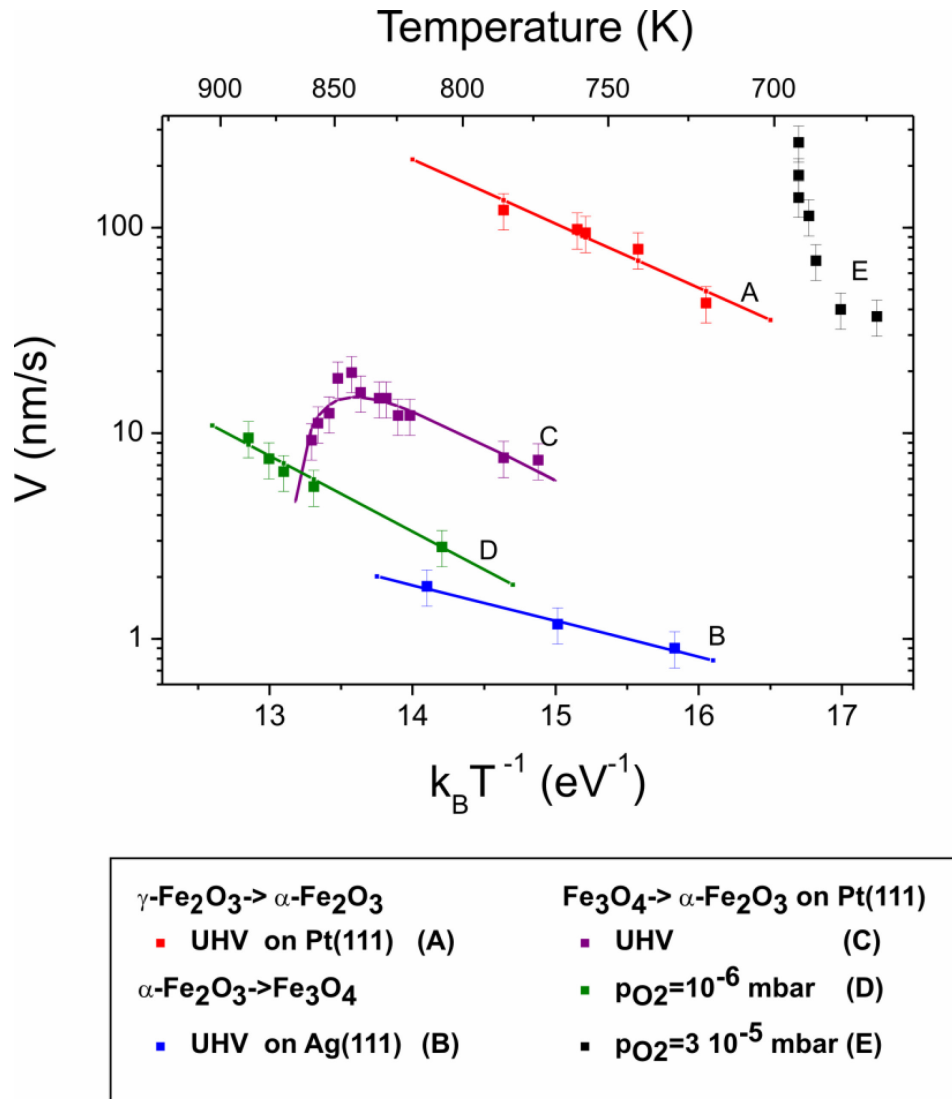


Fig. 3.22: Arrhenius plot of the average front velocities for the transformations (i) $\gamma\text{-Fe}_2\text{O}_3 \rightarrow \alpha\text{-Fe}_2\text{O}_3$ in UHV (A), (ii) $\text{Fe}_3\text{O}_4 \rightarrow \alpha\text{-Fe}_2\text{O}_3$ in UHV (C), $p_{\text{O}_2}=10^{-6}$ mbar (D), $p_{\text{O}_2}=3 \times 10^{-5}$ mbar (E) and $\alpha\text{-Fe}_2\text{O}_3 \rightarrow \text{Fe}_3\text{O}_4$ in UHV (B). The oxide films for the transformations A, C, D and E were grown on Pt(111), whereas B) was grown on Ag(111). Lines give exponential fits. Note that the behavior of $\text{Fe}_3\text{O}_4 \rightarrow \alpha\text{-Fe}_2\text{O}_3$ in $p_{\text{O}_2}=3 \times 10^{-5}$ mbar (E) does not show an exponential dependency on the inverse temperature; therefore no Arrhenius fit has been done.

A clear deviation from the exponential dependence is observed for the oxidation at 3×10^{-5} mbar (E). In particular, the front shape shows dense dendritic structures while the temperature dependence of the front velocity is affected by an increase even at constant temperature. Consequently, these data were not used to extract an activation energy. The intensity change observed during the annealing (see section 3.2.3) suggests that the film surface has a different structure or possibly even corresponds to a different phase under these conditions (see also the following section).

As may be expected, the purely structural transformation $\gamma\text{-Fe}_2\text{O}_3 \rightarrow \alpha\text{-Fe}_2\text{O}_3$ is much faster than the direct $\text{Fe}_3\text{O}_4 \rightarrow \alpha\text{-Fe}_2\text{O}_3$ observed at low or vanishing O_2 pressures. In fact, in the first case (purely structural rearrangement) point defects (Fe vacancies) are already present in the lattice and do not need to be created, while in the latter, long range Fe diffusion is required to adjust the Fe:O ratio before the structural rearrangement can occur. Consequently the transformation $\gamma \rightarrow \alpha$ involves only the restacking of the oxygen planes and short range Fe diffusion, within the unit cell [59]. Even though the activation energies of the two reactions have similar values (0.7 eV and 0.85 eV), the reaction rates differ strongly, due to different pre-exponentials. The much faster rate of the purely structural conversion can be attributed to a larger density of reactive centers for this simple conversion.

Substrate	Transformation	Slope (eV)	Intercept $\log(v_0)$	Type of Transformation (XPS)
Pt(111)	$\text{Fe}_3\text{O}_4 \rightarrow \alpha\text{-Fe}_2\text{O}_3$ ($p_{\text{O}_2} = 10^{-6}$ mbar)	0.85+/-0.075	5.68+/-0.43	Compositional Structural
	$\text{Fe}_3\text{O}_4 \rightarrow \alpha\text{-Fe}_2\text{O}_3$ ($p_{\text{O}_2} = \text{UHV}$)	0.82 +/-0.087	6.08 +/- 0.53	Compositional Structural
	Dominating low T			
	$\text{Fe}_3\text{O}_4 \rightarrow \alpha\text{-Fe}_2\text{O}_3$ ($p_{\text{O}_2} = \text{UHV}$)	(4.3 +/-0.4)	(26 +/- 2)	Compositional Structural
	Dominating high T			
	$\gamma\text{-Fe}_2\text{O}_3 \rightarrow \alpha\text{-Fe}_2\text{O}_3$ ($p_{\text{O}_2} = \text{UHV}$)	0.7 +/- 0.1	6.5 +/- 0.43	Structural
Ag(111)	$\alpha\text{-Fe}_2\text{O}_3 \rightarrow \text{Fe}_3\text{O}_4$ ($p_{\text{O}_2} = \text{UHV}$)	0.40 +/-0.038	2.7+/- 0.25	Compositional Structural

Table 3.1: Fit parameters of Arrhenius plot in Fig 3.22: the transformations observed, the supporting substrates, and the pressure are indicated. The last column states the transformation type based on XPS characterization.

The oxidation processes of $\text{Fe}_3\text{O}_4 \rightarrow \alpha\text{-Fe}_2\text{O}_3$ in UHV and $p_{\text{O}_2}=1 \times 10^{-6}$ mbar have similar activation energies. The rate-determining process is most likely the same, i.e. Fe diffusion in the $[111]_{\text{Fe}_3\text{O}_4}$ direction, occurring preferentially at the phase boundary. In both cases the activation energy estimated by the Arrhenius plot agrees well with the published value for bulk oxidation which is dominated by Fe diffusion [114]. Under UHV conditions, Fe diffusion to the Pt substrate decreases the Fe/O ratio [34], probably forming a subsurface Fe-

Pt alloy layer [123]. The high temperature reduction of the observed total rate for the transformation of Fe_3O_4 into $\alpha\text{-Fe}_2\text{O}_3$ might be the consequence of the partial reconversion of $\alpha\text{-Fe}_2\text{O}_3$ into Fe_3O_4 . The process can have two main driving forces: (i) the decrease of oxygen surface concentration by activation of oxygen desorption, as already discussed in [34], or (ii) the decrease of Fe dissolution in Pt by saturation of the Fe concentration in the subsurface Fe-Pt layer. However, oxygen desorption is the most probable cause for the reaction slowdown, this hypothesis should be confirmed by additional measurements. Indeed, studies on the Fe-Pt system [123, 130] show that UHV annealing at $T > 850$ K induced the bulk diffusion of Fe into a Pt single crystal. Moreover, oxygen desorption from the subsurface region of biphase terminated $\alpha\text{-Fe}_2\text{O}_3$ occurs under similar experimental conditions, as reported in [92]. Assuming that the rate decrease in UHV is due to oxygen desorption, the dataset can be used to estimate the desorption energy of oxygen, giving a value around 4 eV. This value fits well the high activation energy for oxygen diffusion in Fe_3O_4 (264 kJ/mol [131], corresponding to about 2.7 eV) and in $\alpha\text{-Fe}_2\text{O}_3$ (4.1 kJ/mol [132]). A similar activation energy (3.5 eV) was also calculated for the oxygen desorption from the $\text{Fe}_3\text{O}_4(111)$ surface [133]. Interestingly, the reaction slowdown does not occur for the reaction at $p_{\text{O}_2} = 1 \times 10^{-6}$ mbar, suggesting that adsorbing oxygen from the gas phase prevents the decrease of oxygen surface concentration.

Unexpectedly, the UHV conversion is faster than that at $p_{\text{O}_2} = 1 \times 10^{-6}$ mbar. In fact, under UHV only one diffusion path contributes to the decrease of the Fe density in the film (to the Pt substrate), while under oxygen two: not only the contribution of Fe diffusion to the bottom of the film, but also to its surface, where it can react with oxygen. If these two possible paths were independent, then the diffusion process should be faster in $p_{\text{O}_2} = 1 \times 10^{-6}$ mbar (two diffusion channels) than in UHV (one diffusion channel), leading to a faster oxidation. Alternatively, the two paths can compete with each other, as one process tends to accumulate Fe at the surface, the other at the oxide/substrate interface. The experimental observation could be interpreted as follows: the Fe flux is directly proportional to the Fe gradient within the oxide film (Fick's first law of diffusion), for instance from the surface towards the support interface. If the oxidation process, which reduces the Fe concentration at the surface, decreases this gradient, then the flux of Fe atoms diffusing into the bulk is reduced. In this case, the net effect of these two diffusive processes is to reduce the effective flux of Fe cations from the film. This can explain why there is a lower reaction rate for $\text{Fe}_3\text{O}_4 \rightarrow \alpha\text{-Fe}_2\text{O}_3$ transformation during the annealing in $p_{\text{O}_2} = 1 \times 10^{-6}$ mbar compared to the UHV case. Another possibility is that the internal structure of the film (for instance Fe_3O_4 rotational domain

distribution or step bunches) is different in the two situations: the number of crystallographic defects slowing down the reaction rate (see next section) might be higher in a sample oxidized at $p_{\text{O}_2} = 1 \times 10^{-6}$ mbar.

On Ag(111), the UHV annealing led to the reduction process $\alpha\text{-Fe}_2\text{O}_3 \rightarrow \text{Fe}_3\text{O}_4$. The activation energy estimated from the experimental data is much lower than for the reverse transformation ($\text{Fe}_3\text{O}_4 \rightarrow \alpha\text{-Fe}_2\text{O}_3$) and also lower than expected for oxygen desorption (3.5 eV [133]). Furthermore, the reaction rate is distinctly lower in this case compared to all the other reactions (lower pre-exponential factor). These findings are extremely contradictory. In fact, the much lower T-dependence shows that neither the Fe diffusion nor the O desorption are the rate-determining steps in this case. The slow step might be different here, and should be investigated in further studies.

3.3.3 Reaction front morphology: local kinetics

Focusing on the front shapes, two morphologic regimes can be differentiated: dendritic and non-dendritic (see Fig 3.23). According the classification based on the transformation speed, the reactions occurring with a **dendritic front** are the “**fast**” reactions ($\gamma \rightarrow \alpha\text{-Fe}_2\text{O}_3$ transformation and high pressure $\text{Fe}_3\text{O}_4 \rightarrow \alpha\text{-Fe}_2\text{O}_3$ oxidation), while **non-dendritic front** characterizes the “**slow**” reactions. In the following, I discuss two examples for the $\text{Fe}_3\text{O}_4 \rightarrow \alpha\text{-Fe}_2\text{O}_3$ oxidation.

Influence of substrate defects and crystalline domains

The roughening of the fronts might have many causes: here, I focus on the effects of the substrate topography and of the crystalline defects (rotational domains) on the boundary shape. The example considered is the oxidation $\text{Fe}_3\text{O}_4 \rightarrow \alpha\text{-Fe}_2\text{O}_3$ occurring in UHV on Pt(111) (discussed in section 3.2.5). The LEEM images in Fig. 3.23a-b are a brightfield and a darkfield of the same area before the annealing. In Fig. 3.23a the contrast has been enhanced to underline the position of the step bunches of the Pt(111), which are still visible underneath the ≈ 10 nm thick Fe_3O_4 film (dark or bright thick lines visible in Fig. 3.23a). As already shown in section 3.1.5, the Fe_3O_4 phase consists of two rotational domains, while the $\alpha\text{-Fe}_2\text{O}_3(0001)$ island (in the center) consists of one rotational domain. The colored lines in the two images show the growth of the $\alpha\text{-Fe}_2\text{O}_3$ domain; the lines were taken every 20 s along the phase boundary (annealing temperature $T \approx 785$ K). The superposition of these lines with the LEEM images allows to correlate the step bunches and rotational domains with the shape of

the front and the local velocity. The propagation of the phase boundary slows down when approaching a step bunch (see lower left area in Fig. 3.23a), as indicated by the smaller distances of subsequent borderlines. Consequently, the transformation front shape resembles that of step bunches, which are smooth and nearly straight. However, the step bunches do not completely block the propagation, as the front motion continues after a while (see extension in the red curve in the lower left of Fig. 3.23a).

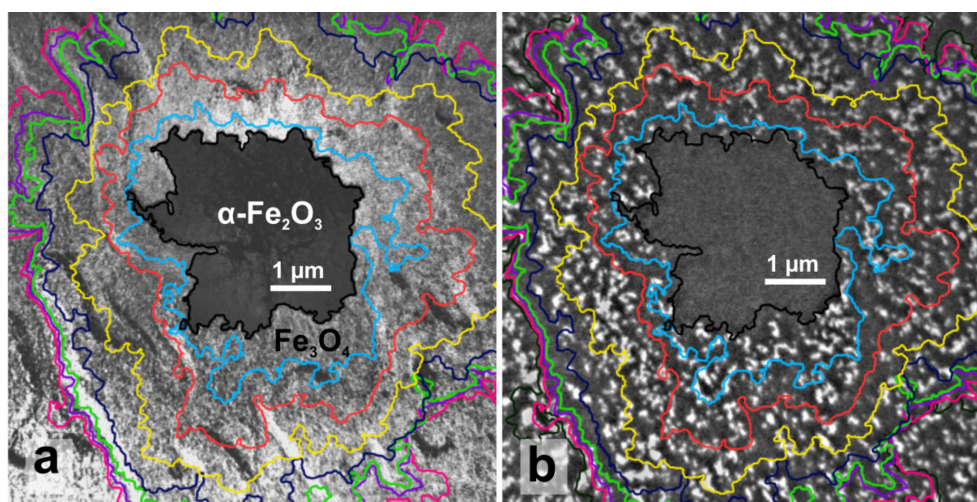


Fig. 3.23: LEEM. Influence of substrate step bunches (Fig. 3.23a) and of the initial rotational domains in the Fe_3O_4 phase on the front morphology and local front velocity (Fig. 3.23b). LEEM image (a) shows step bunches as dark and bright lines; dark field image (b) shows the rotational domain as bright and dark area. Colored lines represent the conversion boundary, taken every 20 s at 785 K in UHV. The front follows clearly the boundaries between rotational domains.

In contrast to the smoothing occurring at step bunches, the front roughens in surface regions between the step bunches (for instant at the lower center in Fig. 3.23a-b). The superposition of the borderlines with the rotational domains (Fig. 3.23b) shows strong similarities between the front curvature and the border of the rotational domains. Moreover, the position of the transformation front often coincides with the Fe_3O_4 antiphase boundaries. A detailed examination shows that the front velocity decreases at the antiphase boundary between neighboring Fe_3O_4 rotational domains, causing a local slow-down of the front, leading to the correlation between the shape of the front and that of antiphase boundaries. The velocity through both types of rotational domains is the same, which fits very well to the symmetry of the crystalline structures. In fact, the restacking mechanisms of the two types of Fe_3O_4 rotational domains (ABCABC and CBACBA) are energetically equivalent for the ABAB

stacking of $\alpha\text{-Fe}_2\text{O}_3$ (in the restacking mechanism, only the direction of the atomic motion is different in the two cases).

The influence of the anti-phase domain boundaries on the reaction velocity is an interesting finding. Anti-phase domains are defects in the internal structure of the Fe_3O_4 phase. Their boundaries are regions where two different crystalline stacking interface (for instance ABCABC||ACBACB). Consequently, the domain walls are rich of defects such as stacking faults, in-plane dislocations and vacancies, and might hinder the atomic movements needed for the transformation. There might be another reason for the observed slowdown. Remembering that the $\alpha\text{-Fe}_2\text{O}_3$ island grows by enlargement of one rotational domain (for instance ABABAB), it is clear that the restacking mechanism has to change each time the reaction front reaches a domain boundary in the Fe_3O_4 film.

Summarizing these observations, both kinds of structural defects slow down the motion of the transformation front. This affects the shape of the front, which locally adopts the shape of the line defects: smooth and elongated at step bunches and rough at the small rotational domains. Other factors, not considered in the present work, might also change the local rate of the reaction, such as the presence of dewetted areas in the film, dislocations, or changes of the local film thickness.

The deceleration of the front is clearly visible in the LEEM images, but its effect on the overall reaction rate is small, because the surface portion of step bunches and of antiphase domain boundaries is in the order of only a few percent.

Dendritic shapes: crystalline directions and substrate defects

Now I focus on the dendritic shapes of the reaction front. The example considered is the oxidation of the mixed $\text{Fe}_3\text{O}_4/\alpha\text{-Fe}_2\text{O}_3$ film at an oxygen pressure of 3×10^{-5} mbar, i.e. for the case of unusual kinetics. In Fig. 3.24 the temporal development of the phase boundary (Fig. 3.24a,c every 2 s; Fig. 3.24b every 1 s) during the $\alpha\text{-Fe}_2\text{O}_3$ growth is indicated by the colored lines. The bright, wide lines in the images are step bunches of the Pt(111) substrate, which are partially decorated by FeO defects and adsorbed oxygen during oxidation. For a more detailed view, Fig. 3.26b and Fig. 3.26c show two zoomed-in regions, marked as yellow areas in Fig. 3.26a.

The $\alpha\text{-Fe}_2\text{O}_3$ grows through highly dense dendritic structures whose branches develop along specific orientations. The directions in the LEEM images correspond exactly to those in the LEED image; the inserted LEED pattern indicates the $\alpha\text{-Fe}_2\text{O}_3$ crystalline directions. The dendrites develop mainly in the $[\bar{1}\bar{2}10]$ -and equivalent- directions of the $\alpha\text{-Fe}_2\text{O}_3$ crystal; some branches are also oriented along the $[1\bar{1}00]$ direction (blue and red arrows in Fig 3.24c, respectively). The growth of the branches along $[\bar{1}\bar{2}10]$ is faster than in the $[1\bar{1}00]$ direction. In other words, the front velocity in the $[\bar{1}\bar{2}10]$ direction is the highest, followed by that in the $[1\bar{1}00]$ direction. The velocities in all other directions are even smaller. This strong non-isotropic growth along preferred crystalline directions leads to the observed dendritic growth.

As in the case of UHV annealing, the dendritic branches follow the substrate step bunches (see e.g. the area in Fig. 3.24a marked by *); moreover, changes in the dendrite orientation during their growth are also correlated to step bunches, which hinder the front motion (see branches marked with ** in Fig. 3.24a).

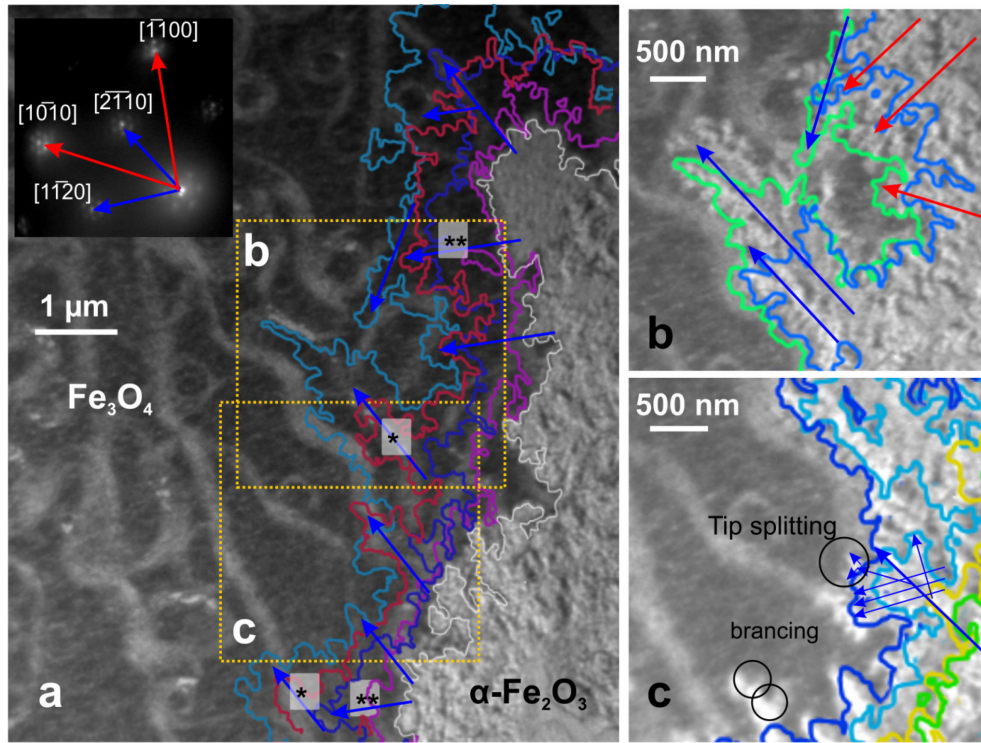


Fig. 3.24: LEEM. Front evolution at $T=700\text{ K}$; $p_{\text{O}_2}=10^{-5}\text{ mbar}$. Fig. 3.24a) Influence of preexisting step bunches on the dendrite directions, during the front evolution (colored lines every 2 seconds). The crystalline orientations are indicated. Bright lines in the Fe_3O_4 region are step bunches of the Pt(111) substrate. $E_k=20\text{ eV}$. Fig. 3.24b: dendrite branching and tip splitting during the $\alpha\text{-Fe}_2\text{O}_3$ front growth. $E_k=20\text{ eV}$ (line every 1 s). Fig. 3.24c: details of the dendrite: growth directions are outlined. The front displacement (during same time interval of 2s) along the $\langle 1\bar{2}10 \rangle$ or equivalent crystalline directions (blue arrow) is almost twice as fast as in the $\langle 1\bar{1}00 \rangle$ and equivalent directions (red). $E_k=20\text{ eV}$.

During the $\alpha\text{-Fe}_2\text{O}_3$ growth, the main dendrite trunk splits into minor branches, which are tilted against each other by a fixed angle of $\pm 60^\circ$, corresponding to the equivalent crystalline orientations of the main dendrite.

The formation of dendritic islands during crystal growth (for instant Pt or Ag homoepitaxy [134, 135] or Ag/Pt(111) [136, 137]) is often explained using the model of diffusion limited aggregation (DLA [138, 139]). A well-known example in three dimensions is the formation of snowflakes. Dendritic nano-structured $\alpha\text{-Fe}_2\text{O}_3$ crystals have been synthesized by [140, 141] from liquid solutions. *Bharathi et al.* and *Cao et al.* observed that the branches follow the favorite $[1\bar{1}00]$ (and equivalent) growth direction; they attributed this growth mode to the maximization of the non-polar $(1\bar{1}00)$ and equivalent planes. However, this argument does not hold for the present experimental findings. The reason for this difference might be that in our case the $\alpha\text{-Fe}_2\text{O}_3$ crystal does not grow from liquid solution, but from a solid state phase

(Fe₃O₄) and thus with a different kind of interface. Moreover, in this case, the transformation does not involve a real long distance diffusion process, but rather the hopping of atoms from one coordination type to another. Therefore, in this case, the dendrite formation might occur because of the directional anisotropy in the hopping probability of the atoms from the old to the new structural configuration. The resulting anisotropy might depend on the atomic structure of the α -Fe₂O₃||Fe₃O₄ interface along these two crystallographic directions, which cannot be probed with our surface sensitive techniques.

Shape dependence on oxygen pressure

As the above discussion points out, the transformation fronts show two different characteristic morphologies: rather smooth fronts for annealing in UHV and in a low oxygen pressure (10^{-6} mbar), but dendritic in higher oxygen pressure ($p_{O_2}=3 \times 10^{-5}$ mbar). The transition between these two transformation regimes is shown in the sequence of images in Fig. 3.25a-i. During acquisition, the O₂ pressure was decreased from 3.0×10^{-5} mbar to 1.8×10^{-6} mbar; the temperature of the sample increased from 700 to 775 K.

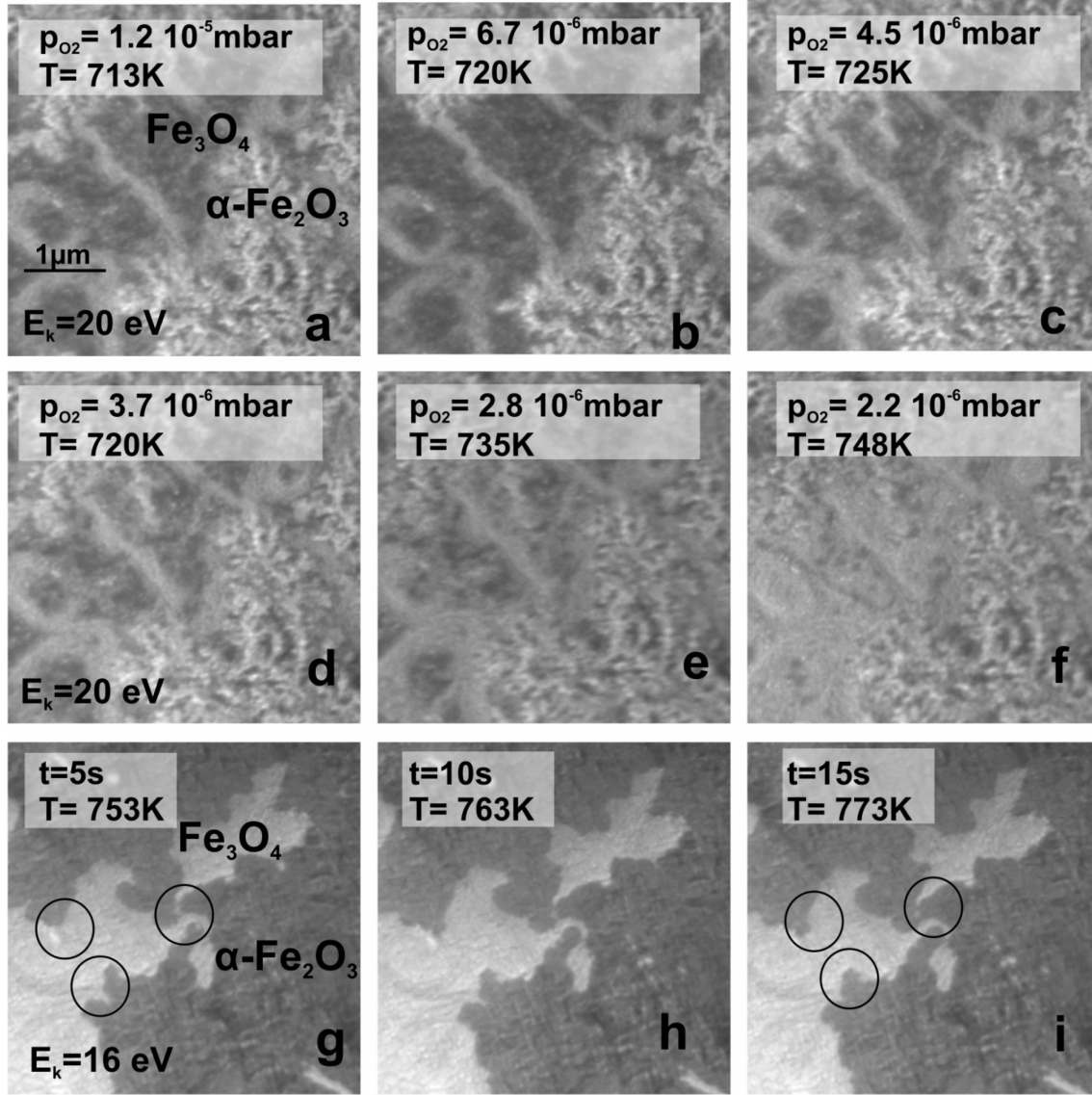


Fig. 3.25: LEEM. Evolution of oxidation dynamics when the pressure is lowered from 3×10^{-5} mbar (in Fig. 3.25a) to 1.8×10^{-6} mbar (in Fig. 3.25i). Intensity change of the Fe_3O_4 phase is visible in Fig. 3.25d-f); the change in the contrast of the Fe_3O_4 phase as consequence of the pressure decrease, and might indicate a structural change. $E_k=20$ eV. Fe_3O_4 g-i) front evolution at $p_{\text{O}_2}=1.9 \times 10^{-6}$ mbar (constant); $E_k=16$ eV. The contrast changes between f and g are due to the change in electron kinetic energy and focus.

During the pressure decrease the front velocity slowed down dramatically at $p_{\text{O}_2} \approx 6.7 \times 10^{-6}$ mbar (Fig. 3.27b-c). Further decrease to $p_{\text{O}_2} < 2.8 \times 10^{-6}$ mbar (Fig. 3.25c-e) led to a change in the LEEM contrast, most likely related to a decrease of oxygen surface coverage. This might indicate a structural change of the Fe_3O_4 termination or even to a change of the crystal phase from $\gamma\text{-Fe}_2\text{O}_3$ to Fe_3O_4 . This last suggestion is based on the observation that $\gamma\text{-Fe}_2\text{O}_3$ was produced in similar oxidation pressures (at lower temperature) (620 K, 3×10^{-5} mbar, see section 3.2.1). At lower pressure, the oxidation has not completely stopped, as seen in the

areas marked by circles in Fig. 3.25i. but the front velocity has dropped by almost two orders of magnitude (from $v \approx 180$ nm/s to $v \approx 2.5$ nm/s)), despite the temperature increase. In addition, the morphology of the front has changed from dendritic to rather smooth: the roughness of the front is now most likely determined by support and film defects. In contrast to the higher-pressure dendritic growth, the front does not favor any specific growth direction. The observed morphological transition is induced by the change of the pressure, as the iron oxide film and support topography are identical. The influence of the temperature on the transformation regime is negligible, as in the isobaric annealing experiment no temperature induced modification of the transformation regime was observed.

The observed transition, also associated to a strong slowdown of the reaction rate, might be the consequence of a change in the oxidation regime, from conditions “far from thermodynamic equilibrium” (fast oxidation at $p_{O_2} = 10^{-5}$ mbar) to “quasi equilibrium” conditions (slow transformation at lower pressure). In fact, usually smooth fronts are thermodynamically more favored than rough fronts.

3.4 Conclusions

This chapter presents an extensive study on the phase transformations between three Fe oxide phases (α -Fe₂O₃, γ -Fe₂O₃, Fe₃O₄), based on the combination of real time imaging (LEEM), chemical (XPS), and structural characterization (LEED).

Our experiments show that the structural transformations from inverse spinel to corundum (Fe₃O₄ \rightarrow α -Fe₂O₃ or γ -Fe₂O₃ \rightarrow α -Fe₂O₃) and the reverse transformation (α -Fe₂O₃ \rightarrow Fe₃O₄) are heterogeneous processes (i.e. with reaction fronts). On the other hand, the purely compositional change Fe₃O₄ \rightarrow α -Fe₂O₃ is a homogeneous process.

All these experiments underlined the critical role of the interface as promoter in the structural rearrangement, as the transformation always occurs through a moving boundary.

The Fe₃O₄ \rightarrow α -Fe₂O₃ transformation is "direct": in fact, the Fe diffusion does not occur homogeneously in the Fe₃O₄ phase (forming γ -Fe₂O₃) but only locally at the boundary. This interpretation is based on the chemical characterization of the initial and final film composition.

Comparing the behavior of the mixed films on Pt(111) and Ag(111) upon UHV annealing, Fe diffusion to the Pt bulk was identified as the reason for the unexpected "oxidation" in the low-

pressure regime, demonstrating how strong the substrate influence on the system behavior can be. The reduction of $\alpha\text{-Fe}_2\text{O}_3$ /Pt(111) is obtained by deposition of Fe and its incorporation in the oxide film. Fe diffusion alone, however, does not induce the structural change, which occurs only at the boundary with a preexisting $\alpha\text{-Fe}_2\text{O}_3$ defect.

Particular attention was given to the developing reaction fronts and their morphology and velocity. Two classes of propagating reaction boundaries were identified: (i) slow fronts (1-10 nm/s) with rather smooth shapes and (ii) fast fronts (100 nm/s) with dendritic shapes. The front shapes are influenced by defects in the support and in the oxide film, such as step bunches and rotational domains. Effective activation energies for the transformation processes were obtained from the temperature dependences, indicating that Fe diffusion within the oxide film is in most cases the limiting step of the process.

Still, some open questions remain.

The first open question is the anomalous temperature dependence of the oxidation front at $p_{\text{O}_2} = 3 \times 10^{-5}$ mbar. One possible explanation is that, during the annealing, the Fe_3O_4 phase converts into $\gamma\text{-Fe}_2\text{O}_3$ before the transformation to $\alpha\text{-Fe}_2\text{O}_3$ starts, at least in the top-most layers. In fact, at the same pressure (3×10^{-5} mbar) but lower temperature, the oxidation $\text{Fe}_3\text{O}_4 \rightarrow \gamma\text{-Fe}_2\text{O}_3$ was achieved (section 3.2.1). This superficial $\gamma\text{-Fe}_2\text{O}_3$ -layer might then transform fast and with dendritic shape to $\alpha\text{-Fe}_2\text{O}_3$ as soon as the temperature is high enough to enable the structural transformation. The process would be similar to that observed in UHV for $\gamma \rightarrow \alpha$. The γ -phase produced under these conditions (a few minutes at $p_{\text{O}_2} = 3 \times 10^{-5}$ mbar of oxygen and 650 K) is not stable and converts back to Fe_3O_4 when the O_2 pressure is reduced.

Remarkably, the γ -phase produced by low temperature oxidation (by 10 min reaction) is stable: cooling down first in oxygen (down to 450 K) and subsequently to RT in UHV changes neither structure nor composition (in XPS, no Fe^{2+} component was found). The possible reason for this difference could be that in the latter case the entire film thickness is converted and therefore stable, whereas in the former only the top-most layers are converted and are therefore unstable. Alternatively, quenching the $\gamma\text{-Fe}_2\text{O}_3$ in O_2 atmosphere might be a critical step in the stabilization of this oxide phase.

Another question concerns the “low” pressure oxidation of Fe_3O_4 , for which we found that the reaction rate is lower in $p_{\text{O}_2} = 1 \times 10^{-6}$ mbar of oxygen than in UHV. As said, this might be due to two opposite diffusion processes, or to the internal structure of the film.

Finally, further experiments should be addressed to identify the slower step in the reduction process on $\text{Ag}(111)$.

4. Pt Nanoparticles Supported on Fe-oxides thin films: Fe₃O₄/Pt(111) and biphasic terminated α -Fe₂O₃/Pt(111)

This chapter focuses on the characterization of the interaction of Pt nanoparticles (NPs) with two supporting iron-oxides thin films: Fe₃O₄ and biphasic terminated α -Fe₂O₃. Particular attention is given to the real time investigation of the encapsulation process. Pt NPs supported on well-ordered Fe₃O₄ thin films represent a model system of nano-structured model catalysts, which exhibits the so-called SMSI (*Strong Metal - Support Interaction*) when treated in reducing conditions. High resolution STM [9, 86] and TEM [85] measurements have shown that Pt NPs undergo encapsulation by a thin FeO monolayer when annealed at T \approx 850 K in UHV. The FeO(111) is O-terminated and Fe is in direct contact with Pt [85].

Interestingly, the reactivity of the system is enhanced by the encapsulation [9, 12, 84, 86, 96]. The reactivity of CO oxidation under reaction conditions was studied on both, Pt NPs and on single crystals, showing that the FeO/Pt(111) catalyst has a higher reactivity in CO₂ production than bare Pt(111) [96] and Fe₃O₄. Combined STM measurements and DFT calculations suggest that the high pressure reactivity is related to the formation of an O-Fe-O trilayer, which is the active phase for the reaction [142]. The enhanced reactivity after encapsulation is peculiar to this system. Usually, encapsulation passivates the metallic component of the catalyst by covering its active sites [74, 143].

The Pt NPs are prepared by Pt deposition on the oxide support (in UHV condition and at various deposition temperatures, i.e. T \approx 100 K, T=RT [86] and T \approx 700 K [52]). Extensive STM studies [86], have characterized the morphology of the Pt NPs depending on different deposited amount of Pt and annealing temperatures.

The interface between the encapsulated NPs and the Fe₃O₄ has been studied by HRTEM and STEM [85]. In this way, *Willinger et al.* show that the interface between the encapsulated Pt NPs and the support consists in the Kagomé (3/4 ML Fe atoms) layer of the Fe₃O₄. At this interface, the number of Fe-Pt bonds is maximized. The Kagomé layer is not the stable termination for the pristine Fe₃O₄ film (under these conditions), which is the 1/4 Fe terminated Mix-Trigonal layer [88]. However, the Kagomé layer is the next Fe-containing layer below the Mix-Trigonal, in the vertical stacking of Fe₃O₄(111). The interface between the Pt NPs and the film is formed from the stable termination by removing the terminating Fe and O layers from the oxide film. This provides part of the material forming the encapsulating layer [85]. Additional

material (Fe) has to be removed from the oxide film to complete the encapsulating layer, as the amount of Fe and O from the first layer is not sufficient to cover completely the NPs. This can happen, in principle, following two mechanisms: either Fe migrates through the Pt particle (via alloying) from Fe₃O₄ bulk (underneath the particle), or Fe migrates onto the Pt surface from the surrounding area. Careful investigation of the film structure surrounding the Pt particles supports the second mechanism [85], i.e. the encapsulation occurs most likely via surface diffusion of Fe atoms on the NPs surface.

Two driving forces are proposed for the process [96]. The first one is the minimization of the surface energy of the system, i.e. the surface energy of the uncovered NPs ($\gamma_{\text{Pt}(111)}$) is higher than that of the encapsulated particles ($\gamma_{\text{FeO/Pt}(111)}$). Alternatively, the charge transfer occurring at the NP/support interface drives the process. The accumulation of negative charge at the Pt NPs surface drives the diffusion of the Fe cations across the surface.

This system has been also studied in our group, to probe the encapsulation process in real time [52]. The characterization of the Pt-Fe₃O₄ system was mainly based on LEED and integrated X-PEEM measurements. The experiments presented in [52] consolidate the STM results obtained by *M. Lewandowsky* [86]. In LEED, the fingerprint of the encapsulation is the appearance of extra spots of the FeO/Pt(111) Moiré pattern. X-PEEM measurements show that in the NPs, the Pt 4f core level peak shifts to higher binding energy compared to the value obtained for the Pt(111) single crystal. This effect was assigned to size-dependent effects. SPA-LEED data proved that the NPs have a slightly contracted lattice constant, compared to the Pt(111) single crystal. Such distortion is greater if the platinum is deposited at RT than at higher temperatures. Pt deposition at 700 K causes the direct encapsulation of the NPs.

The microscopic visualization of isolated particles could not been achieved (neither in LEEM nor in PEEM) [52], although the nanoparticles size (≈ 10 nm) [9, 86] [85] is higher than the resolution limit of the SMART instrument (2 nm, in LEEM mode). In fact, even under “optimal” acquisition conditions (constant temperature and “perfect” alignment), single flat objects can be individually identified only if they are sufficiently separated (e.g. for ≈ 10 nm big NPs, each one has to be at least ≈ 30 nm (center to center) apart from the closest one). As the supported NPs are mutually closer than this distance, the surface appears in LEEM as uniformly corrugated, as already discussed in [52]. Moreover, during the sample annealing the thermal drift of the sample itself and the thermal expansion of the manipulator (and related

defocus) contribute to the blurring of the image. Consequently, high magnification imaging of single particles is challenging under such experimental conditions.

The first part of the chapter integrates these results, combining real time LEED, SPA-LEED, real time XPS and X-PEEM. Different issues were addressed with these techniques such as:

- The steps in the formation of the NPs and their encapsulation were characterized by separated annealing cycles with XPS.
- The role of O₂ pressure on the encapsulating process was investigated by real time XPS.
- The influence of the Pt deposition temperature on the NP size/shape (and subsequent quality of the encapsulating layer) was evaluated by comparing results at: RT, T=620 K and T=700 K [52].

In the second part of the chapter, I present the experiments on Pt NPs supported on biphasic terminated α -Fe₂O₃. Although previous results [86] show that Pt NPs supported on the (1x1) O-terminated α -Fe₂O₃ do not undergo encapsulation², a different behavior is expected for biphasic terminated α -Fe₂O₃, due to the abundance of surface Fe. It is generally accepted that encapsulation does not occur on stoichiometric crystals but only on strongly reduced oxides [74]. On biphasic terminated α -Fe₂O₃, the focus of the investigation focused was the characterization of the annealing process by direct comparison with the Fe₃O₄ support; therefore, I used a mixed α -Fe₂O₃/ Fe₃O₄ film.

In the following experiments, mainly Ru(0001) was used instead of Pt(111) as a substrate. This choice allows to exclude that XPS and LEED of the encapsulated NPs (Moiré FeO/Pt(111)) can be affected by the substrate contribution from dewetted areas of the film³.

Finally, I tried to obtain single particle resolution by increasing the particle size. To this end the amount of deposited Pt was increased, from 1 to > 2 ML. Unfortunately, however, real time imaging of single NPs encapsulation was still not achieved for the same reasons listed above.

² The STM study indicates that some NPs may have been encapsulated, most likely by Fe₃O₄ or α -Fe₂O₃-like structure.

³ For systems grown on Pt(111), the dewetted areas are structurally identical to the encapsulated Pt NPs, as both objects are constituted by a thin FeO layer on top of Pt(111). LEED, X-PEEM, LEEM and LEEM-IV investigations cannot distinguish between these two systems.

4.1 Pt NPs on Fe₃O₄

4.1.1 Pt NPs formation and encapsulation: X-PEEM and real time LEED X-PEEM.

The work of *A. Sala* [52] clarified that encapsulation of the Pt NPs supported on Fe₃O₄ is enabled by annealing temperatures above 700 K. We integrate those data characterizing the NPs before and after the encapsulation by XPS, separating the annealing stage into two steps.

During the experiment, 2 ML of Pt were deposited at RT on the freshly prepared Fe₃O₄ surface supported on a Ru(0001) substrate. In the first annealing stage the temperature was raised up to T≈620 K in UHV, while in the second stage it was annealed to T = 850 K in UHV. Finally the sample was annealed again to T = 850 K in p_{O2} = 1x10⁻⁶ mbar to test if there is any effect of external O₂ pressure on the encapsulating layer.

After each annealing step, the surface was cooled down to RT to acquire X-PEEM spectra on Pt4f and Fe3p core lines in static conditions, while the evolution of the system was followed in real time by LEED.

This preparation procedure (≈2 ML of Pt deposition at RT and subsequent annealing in UHV) was already subject of the STM characterization by *M. Lewandowski* [86]. The progressive modification of the Pt overlayer at each annealing stage in the experiment reproduces well the STM observations (Fig 4.1).

As deposited, the Pt overlayer consists of 2 ML high irregular islands, covering almost totally the oxide surface (Fig 4.1a). Annealing at 600 K enables partial ordering of the surface, as consequence of thermally activated Pt diffusion: the particles enlarge and assume 3D shapes, leaving fractions of exposed oxide area in between (Fig 4.1b). Finally, well-shaped 3D nanoparticles form after annealing at T = 850 K (Fig 4.1c). Their surface is covered by the encapsulating FeO layer, which is indicated by the presence of the Moiré structure surrounding the (0,0) spot. Further annealing in p_{O2} = 1x10⁻⁶ mbar does not induce significant changes in the LEED pattern

Remarkably, SPA-LEED (not shown) proves that the Moiré pattern has the periodicity of the FeO/Pt(111) superstructure. The extra-spots can only arise from the encapsulated NPs, as the supporting single crystal is Ru(0001) in this case. As already discussed in chapter 2, the periodicity of the FeO/Ru(0001) differs significantly from that of FeO/Pt(111), excluding that the satellites are produced by dewetted areas of the Fe₃O₄ film.

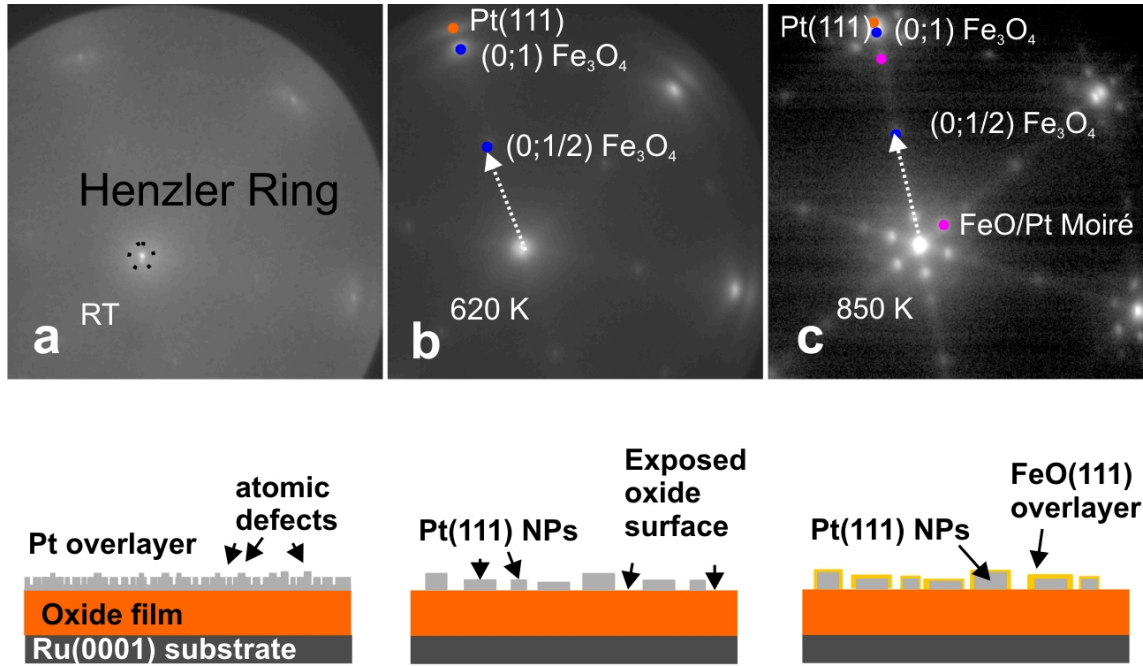


Fig. 4.1: LEED patterns (top) and relative schematic drawing of the surface (bottom) during the three steps in the Pt NPs formation on the Fe₃O₄/Ru(0001), Fig 4.1a) shows the surface after deposition of 2 ML Pt on the Fe₃O₄ film; deposition at RT in UHV conditions. The formation of the Henzler ring during epitaxy is associated to the formation of islands of deposited material [27, 28, 53, 144]. The surface is characterized by islands having a peaked size distribution and random orientations. The uniform background denotes the presence of high concentrations of randomly distributed atomic defects Fig 4.1b) The LEED pattern of the same film after annealing in UHV condition up to T=620 K, The surface exhibits the Pt(0,1) spots and the (2x2) reconstruction of the support, indicating that the Pt overlayer has agglomerated in bigger Pt(111) clusters. The contribution from the Fe₃O₄ (2x2) reconstruction originates from exposed areas of the supporting oxide surface, meaning that a fraction of 3D islands has formed. The background intensity decrease is associated to the ordering of the Pt overlayer. The absence of the Moiré pattern indicates that the Pt NPs are not encapsulated. Fig 4.1c) The LEED pattern of the same film after annealing in UHV condition up to T=850 K, The surface shows the FeO(111)/Pt Moiré pattern indicating that the NPs Pt are encapsulated . E_K=38 eV.

X-PEEM data

X-PEEM signal at the Fe3p and Pt4f core level peak were acquired. This choice was made to try to visualize single particle signals. However, under these conditions, X-PEEM does not resolve any single NPs signal, mainly due to two reasons: first, their average size is smaller than the instrumental resolution, which in PEEM mode is 18 nm, i.e. 7 times worse than in LEEM (due to space charge effects) [36]; secondly, the single NPs are not separated enough to be singularly detected.

Two main technical issues affect the X-PEEM data. The absolute intensity value along the spectra is affected by the combined effects of the grazing beam incidence and the thermal contraction of the manipulator (which occurs as consequence of the sample annealing), causing instrumental misalignment. During the acquisition (each point in the spectra corresponds to an image; the overall spectra is acquired in 30-40 min), the photon beam may shift along the image. The movement of the beam during this time influences the acquired electron intensity. This is particularly evident in the Pt spectra (see for instance Fig 4.3b). This is the reason why, in the data presented here, the theoretical intensity ratio between the 7/2 and 5/2 peaks is not preserved. This problem affects both Fe and Pt acquisitions.

Another problem with those data arises when coming to the absolute calibration of the binding energy values. The absolute energy value depends on the beam-line alignment as well as on the optical alignment of the microscope: the beam line settings influence the incoming E_{photons} , while the omega filter and energy slit alignment influence E_k . The absolute binding energy calibration should be related, therefore, to the Fermi edge of a metal. As I could not do such calibration under the conditions of these experiments, such procedure was not applied to the data presented here. However, the relative calibration of the binding energy between the following datasets is reliable because all spectra were acquired with the same microscope and beamline settings, (i.e. the monochromator position was never changed). For these reasons, the discussion focuses mainly on relative energy shifts between the Pt4f signals at different steps of the NPs formation and encapsulation. Indeed, even if the absolute value of the fitting result might be incorrect, some interesting consideration can still be made.

The Fe3p and the Pt4f spectra (integrated over the image), taken at different experimental steps, are shown in Fig 4.2 and Fig 4.3, respectively. The beam line settings were: photon energy $h\nu=200$ eV; energy resolution $\Delta E=0.5$ eV.

Fig. 4.2 presents the Fe3p profiles for the clean Fe₃O₄ film (black line), the Fe₃O₄ film after Pt deposition at RT (2ML) (red line) and the Fe₃O₄ film supporting the encapsulated NPs (green line). These last datasets are rescaled by a multiplicative factor of 1.6 in order to have the same background level as for the clean Fe₃O₄ signal.

Just after deposition, the Fe3p signal (red line) is strongly damped, due to the presence of the Pt overlayer. The Fe3p profile just after the encapsulation (green line) shows an evident difference from the clean Fe₃O₄ signal: the relative intensity in the low binding energy region

of the spectrum is higher. Lower binding energy is associated to lower atomic coordination. If one considers that Fe_3O_4 is composed by Fe atoms in the ionic states Fe^{3+} and Fe^{2+} , the additional component at lower binding energy suggests an excess of Fe^{2+} at the surface occurring after encapsulation. The excess of Fe^{2+} originates from the $\text{FeO}(111)$ in the encapsulating layer. However, in the final spectrum, the Fe^{3+} component is not completely damped; such component most likely arises from the exposed oxide surface between the NPs, consistently with the LEED.

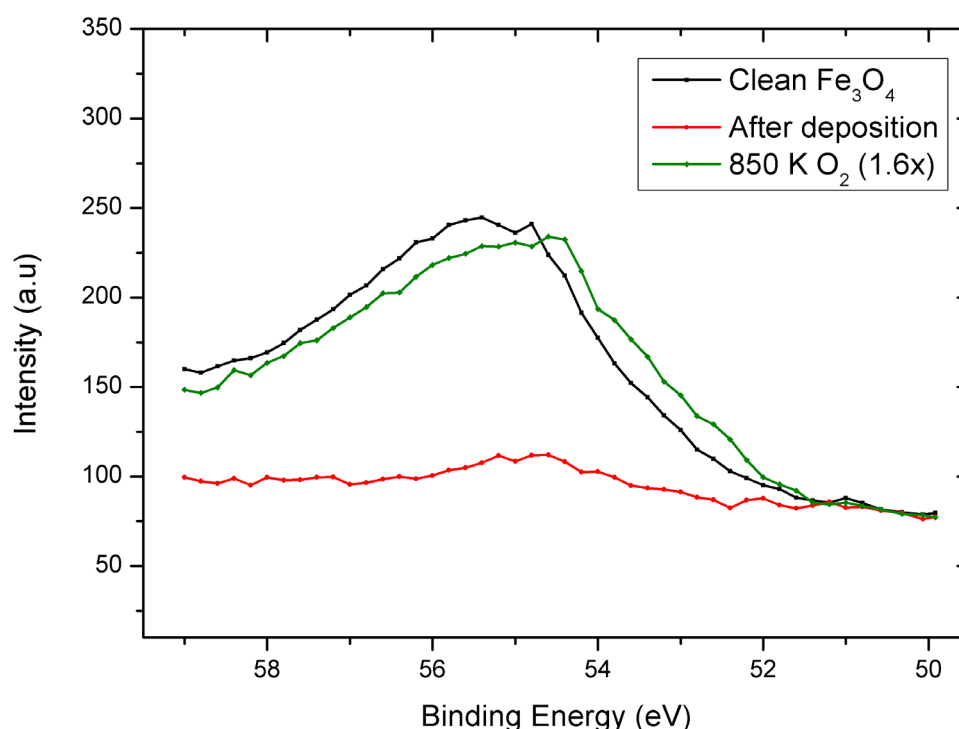


Fig. 4.2: XPS spectra of the Fe3p core level for: the clean Fe_3O_4 support (black line), Pt overlayer after RT deposition on the Fe_3O_4 support (red line) and the encapsulated NPs after the annealing at $T=850$ K in $p_{\text{O}_2}=10^{-6}$ mbar (green line). $h\nu=200$ eV

The Pt4f peaks (Fig 4.3) were fitted with an asymmetric Lorentzian line shape to take into account the electron shake-up effects [145]. The FWHM reproduces the experimental energy resolution of our experiment, which results from the independent sum of the energy resolution of the beamline and the Ω -filter (0.8eV), and it is set as fitting constraint. During the fitting procedure, I have tried to maintain the intensity ratio between the peaks as close as possible to the theoretical ratio expected for 7/2 and 5/2 (i.e. $4/3=1.33$). The expected doublet separation (3.2-3.4 eV) [146] has been set as fitting constraint, to overcome, at least partially, the issue related to the peaks' intensity.

In the Pt4f spectra, each peak is much wider than the expected instrumental energy resolution of the experiment. Consequently, using two fitting components for each peak was necessary. The higher binding energy component is assigned to the bulk contribution, while the lower binding energy component to the surface contribution [52]. Table 4.1 shows the fitting results.

	Deposited Pt		Bare Pt clusters		Encapsulated Pt clusters (UHV)		Encapsulated Pt clusters (O ₂)	
Pt4f	7/2	5/2	7/2	5/2	7/2	5/2	7/2	5/2
Surface								
Binding energy (eV)	70.41	73.71	70.36	73.71	70.53	73.83	70.55	70.80
Area (a.u)	235	169	110	35	170	119	155	109.85
FWHM (eV)	0.8	0.8	0.8	0.8	0.8	0.8	0.8	0.8
Bulk								
Binding energy (eV)	70.92	74.22	70.9	74.25	70.9	74.20	70.9	74.15
Area (a.u)	260	140	93	29	45	31.5	40	25.6
FWHM (eV)	0.8	0.8	0.8	0.8	0.8	0.8	0.8	0.8

Table 5. 1: Fitting results obtained from Fig 4.3. The peaks FWHM and the doublet separation are set as fitting constraints.

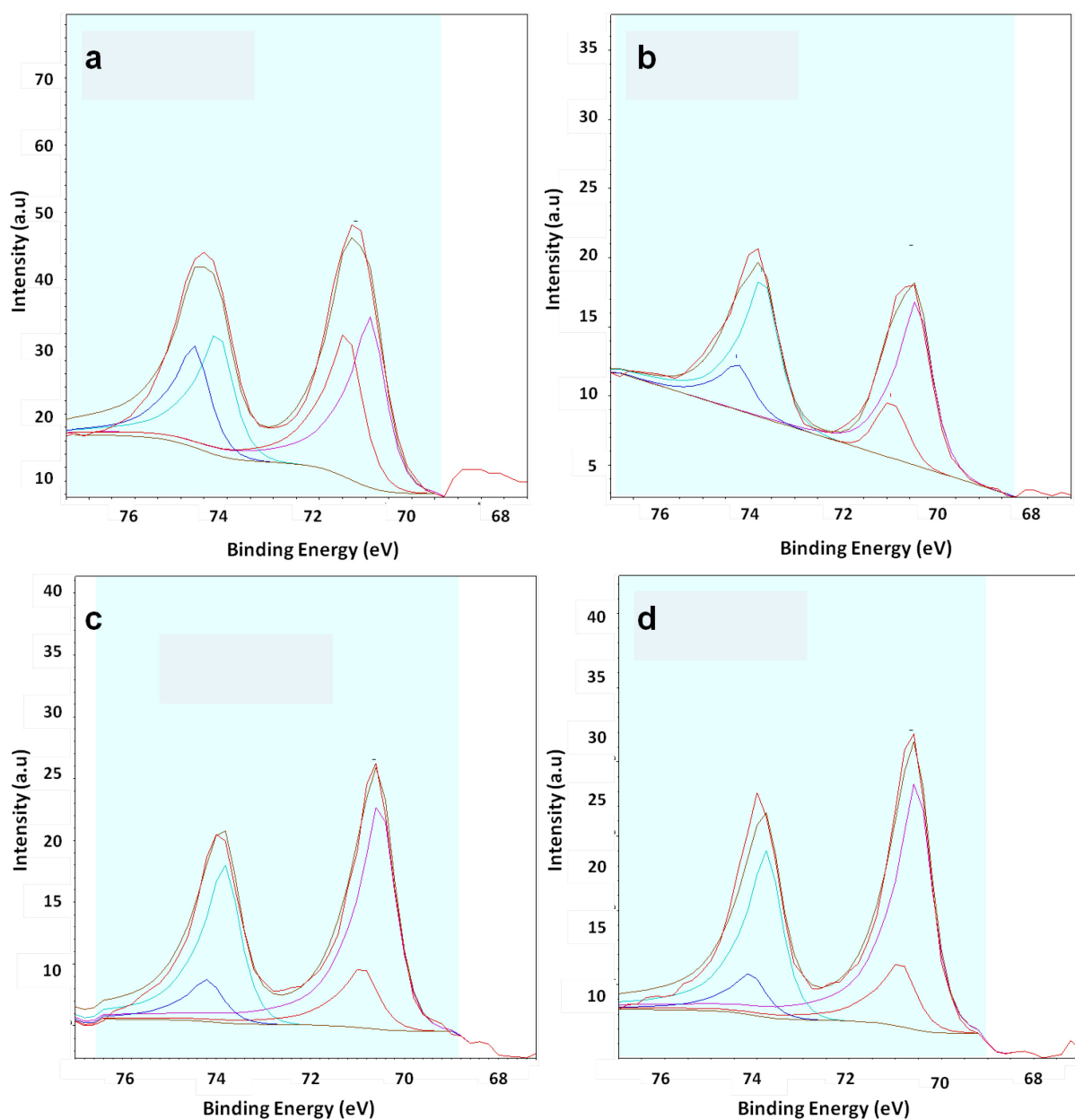


Fig. 4.3: XPS at the Pt4f core level for: Fig 4.3a) the Pt overlayer after deposition at RT (2 ML), Fig 4.3b) uncovered Pt NPs obtained after annealing at T=620 K in UHV, Fig 4.3c) Pt NPs encapsulated by FeO(111) skin after UHV annealing at T=850 K; Fig 4.3d) Pt NPs encapsulated by FeO(111) skin after UHV annealing at T=850 K after annealing at T=850 K in $P_{O_2}=1.0 \times 10^{-6}$ mbar. The blue areas in the image mark the data range considered for background evaluation. Red lines correspond to the experimental data, while the brown lines indicate the fitted curves. $h\nu=200$ eV

After encapsulation (by annealing at $T=850$ K), the Pt4f surface component shifts by $\Delta E=+0.2$ eV compared to the XPS of the bare NPs, while during the clustering process ($T=620$ K) of bare Pt NPs no significant energy shift is observed. On the other hand, the binding energy for the bulk component before and after encapsulation does not change. The shift of the surface component most likely originates from the Fe-Pt interaction at the interface between the NPs and the encapsulating oxide layer. The same shift is observed in the platinum signal for the FeO-covered Pt(111) single crystal [52]; moreover, similar energy shifts have also been found in the case of Fe-Pt alloy [123, 147]. Further annealing in O_2 does not induce additional changes in the Pt4f XPS peak. This can be interpreted in two ways: either the encapsulating layer was already stably formed in the previous annealing step, or the encapsulation process occurs under high temperature annealing both in UHV and in O_2 pressure. This last point (i.e. the influence of the presence of O_2 in the gas phase on the encapsulation process) is the topic of section 4.1.2.

Concluding this section, the shift of the Pt4f surface component $\Delta E=+0.2$ eV can be considered as the XPS fingerprint of the encapsulation.

Real time LEED

Real time LEED provides a further characterization of the temperature dependence for the modification of the Pt overlayer due to the clustering and encapsulation processes. Therefore, I evaluated how the intensity of the Pt(0,1) spots and of the satellite spots of the Moiré superstructure (FeO(111)/Pt(111)) change during the sample annealing, as consequence of the NPs encapsulation. The sample was prepared as in the previous case: 2ML of Pt were deposited at RT in UHV on top of a $Fe_3O_4/Ru(0001)$ oxide film. In this case, the annealing to $T=850$ K in UHV was performed using a single annealing stage, and followed in real time in LEED. The intensities of the spots was acquired by evaluation of the intensity in defined areas of the LEED pattern, coinciding to the Pt(1,0) and to FeO(111)/Pt(111) satellite spot positions; the background intensity was subtracted from the raw data (Fig 4.4).

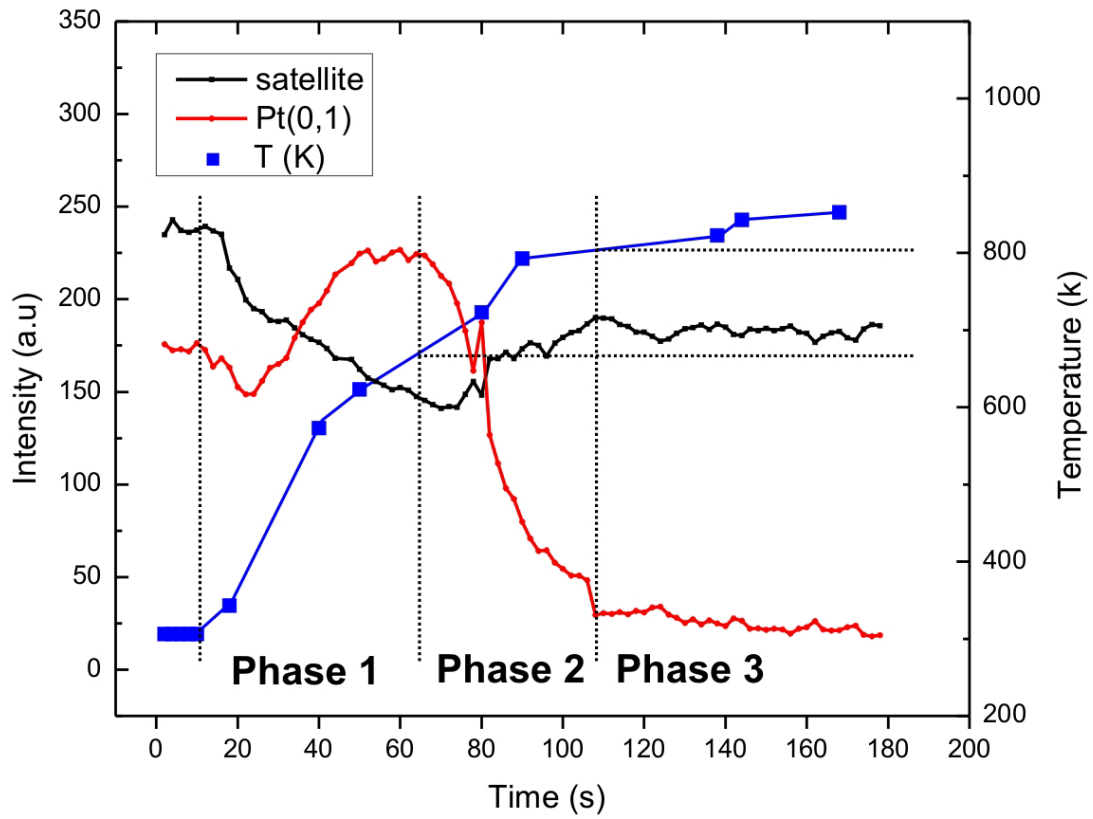


Fig. 4.4: Intensity profile of selected LEED spots during the annealing from RT to $T=850$ K (UHV). The sample consists of 2 ML of Pt deposited at RT on $\text{Fe}_3\text{O}_4/\text{Ru}(0001)$. The red line corresponds to Pt(0,1); the black line to the FeO(111)/Pt(111) satellite; the blue squares indicate the corresponding temperature (scale at right). $E_k=38$ eV

Just after deposition, both the Pt(1,0) and the satellite spots show a non-zero intensity. In the first case, the intensity arises from the Pt(111) disordered clusters which form the overlayer; in the second case, the intensity arises from the Henzler ring, which has a k -space position close to that of the satellite spots.

Based on the changes in the intensity profiles, one can indentify three phases occurring during the annealing process.

In the first stage (70 s, $T \approx 650$ K), the Pt(0,1) intensity increases and reaches its maximum at $T \approx 600$ K, as the Pt(111) clusters form from the disordered Pt overlayer. During the process, the Henzler ring surrounding the (0,0) spot (related to the size distribution of the Pt clusters) vanishes (ordering of the Pt NPs), causing the intensity decrease of the black profile. The initial decrease of the Pt(0,1) intensity (20 s, $T \approx 375$ K) is an effect of the ordering of the layer, which reduces the non-crystalline background intensity. During the second phase, the

decrease of the Pt(0,1) intensity indicates that the NPs start to be covered by the oxide layer. However, the Moiré pattern of the satellite increases later, when the encapsulating layer is ordered enough to produce diffraction spots.

In the final stage, the intensities of both spots (superstructure and Pt(0,1)) are constant, meaning that the encapsulation is complete (100 s; $T \approx 800$ K).

4.1.2 Encapsulation in $p_{O_2} = 1.5 \times 10^{-7}$ mbar

In a number of studies on metal/oxide systems, the encapsulation of the supported NPs was observed after reducing treatments [74-78, 148-152]. In some metal/oxide systems (such as M-TiO₂), the presence of O vacancies is believed to enable the process [74]. Therefore, one might expect that the encapsulation of the Pt NPs is hindered if the system is annealed in O₂ atmosphere.

On the other hand, it is known that the Fe-O chemical affinity is higher than Fe-Pt. It was shown that the presence of O₂ facilitates the segregation of Fe dissolved in Pt [52, 123, 147]; the Fe-O binds together, forming a FeO layer on the Pt surface. This suggests that the presence of O₂ in the gas phase might facilitate the formation of the FeO skin at the NPs surface.

On this basis, I investigated the influence of O₂ in the gas phase on the NPs encapsulation during annealing. The support is a 10 nm thick Fe₃O₄ film on a Pt(111) crystal. The amount of deposited Pt is 2 ML and annealing temperature $T = 890$ K. The annealing, in oxygen atmosphere, was followed in the so-called “dispersive-plane” mode. In this acquisition mode, the dispersive plane of the Ω -filter is imaged on the detector (the horizontal coordinate represents the energy dispersion), enabling real time XPS. We focused on the real time evolution of the Pt4f peak (Fig 4.5). Differently from X-PEEM, i.e. there is no spatial information (the signal is integrated over a FoV of 4 μ m). However, energy shifts can be recorded in real time.

During the annealing thermal expansion of the manipulator changed the illumination condition: the photon beam shifted out of the “acquisition region” probed by the microscope. Therefore, during the experiment continuous manual adjustment of the sample position was necessary to bring the photon beam into the correct position. For this reason, the absolute signal intensities are not proportional to Pt coverage at the surface.

In the experiment the pressure was set at $p_{O_2}=1.5 \times 10^{-7}$ mbar because the valve between the beamline and the main chamber of the SMART microscope can be opened only for pressures lower than $\approx 3 \times 10^{-7}$ mbar.

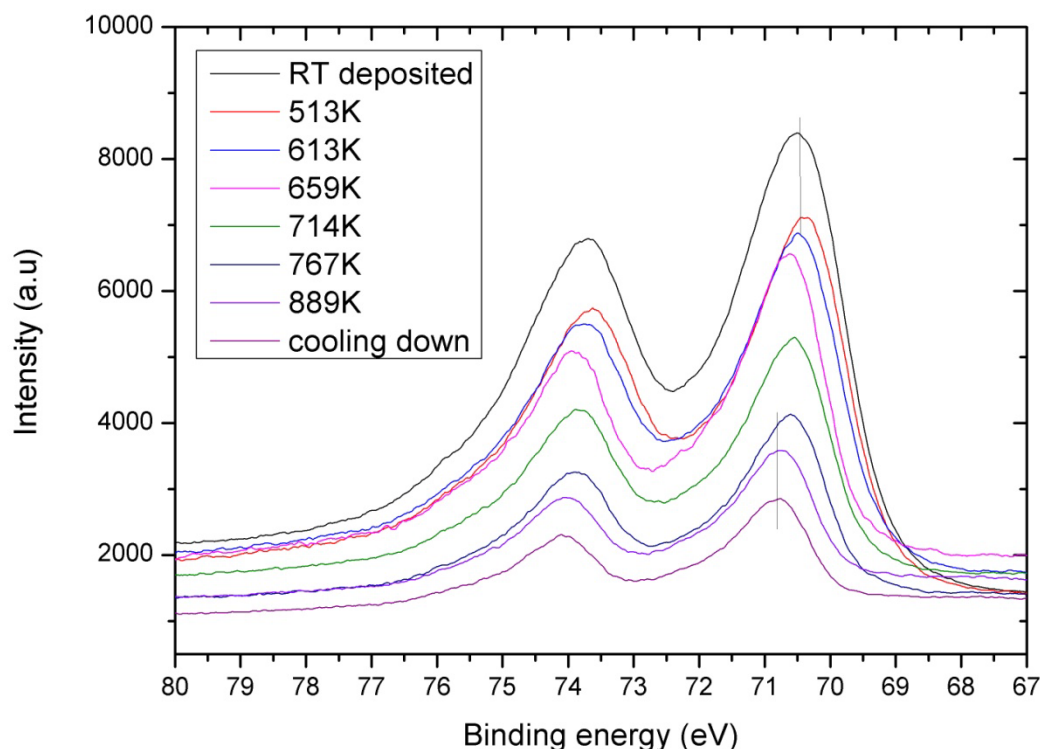


Fig. 4.5: Real time XPS (dispersive plane mode) on the Pt 4f core level peak during annealing from RT to 890 K in $p_{O_2}=1.0 \times 10^{-7}$ mbar; prior to the annealing 2 ML of Pt were deposited on $Fe_3O_4/Pt(111)$. In this experiment the energy window in a single image was set to 20 eV. $h\nu=175$ eV

Fig 4.5 shows the Pt4f spectra acquired during the annealing. Each spectrum was taken at a different temperature. The peak intensities are arbitrarily rescaled to help the visualization of each peak. The binding energy of the peaks is constant up to temperatures between 513 and 613 K, but shifts to higher values at higher temperatures. The maximum shift is $\Delta E=0.23$ eV for $T \approx 890$ K. During the cooling of the sample no further energy shift is observed.

The LEED and LEEM of the final surface are displayed in Fig 4.6a-b. The surface consists in Fe_3O_4 and $FeO/Pt(111)$, as the LEED pattern points out. In LEEM small white objects are visible. At $E_k=19$ eV $FeO(111)$ is brighter than $Fe_3O_4(111)$. Therefore, the bright dots consist in $FeO/Pt(111)$. Because in this case the film support was $Pt(111)$, the $FeO/Pt(111)$ features can be either encapsulated NPs or dewetted areas of the Fe_3O_4 film. However, the objects' size, irregular shape, mutual proximity and coverage indicate that the objects are most likely

NPs, rather than holes in the supporting oxide. Remarkably, in X-PEEM (Fig 4.6c) at the secondary energy (5.1eV), single objects are distinguishable, but unfortunately at the core level energies no contrast was obtained, maybe due to low signal to background ratio.

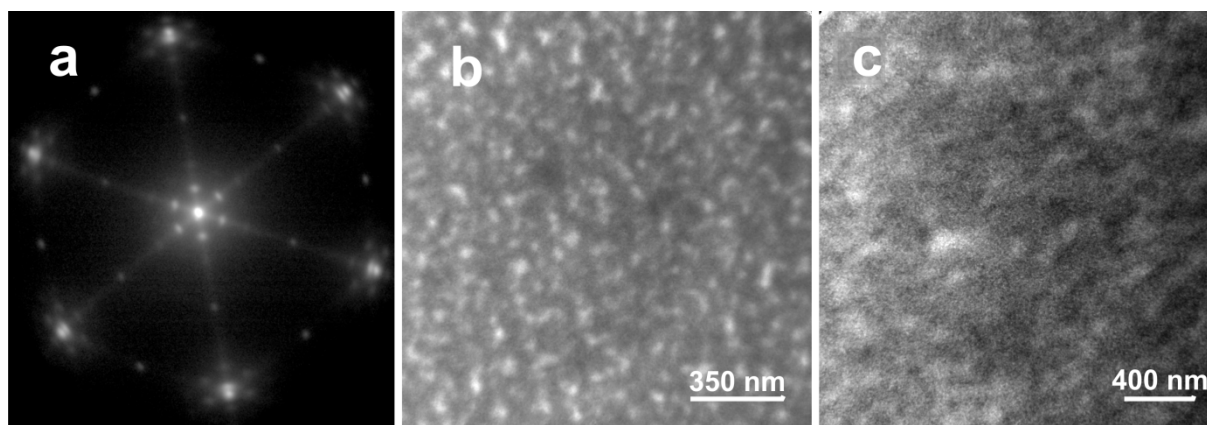


Fig. 4.6: Surface after the annealing of 2 ML Pt/Fe₃O₄ after annealing in $p_{O_2}=1 \times 10^{-7}$ mbar at $T=850$ K. LEED (a), LEEM (b), X-PEEM (c) at the secondary energy for the Pt NPs on Fe₃O₄/Pt(111). $E_K=38$ eV (a), 19 eV(b) and 5.1 eV (c).

Discussion

In this experiment Pt(111) was used as the oxide support film; therefore, the objects constituted by FeO/Pt(111) cannot be identified univocally as NPs. However, it is reasonable to conclude that the majority of the surface consists in encapsulated Pt NPs supported on the Fe₃O₄ substrate. In fact, extensive dewetting of the film is not likely to occur under these conditions (the system was annealed for 7 min in O₂ atmosphere, which does not cause dewetting). Moreover, the objects (size, distribution and shape) differentiate strongly from those of the dewetted areas, which typically form as consequence of UHV annealing.

For $T > 610$ K, real time XPS measures a continuous energy shift of the Pt4f peak during the sample annealing. This energy shift can be interpreted as the fingerprint of the encapsulation process (i.e. the FeO layer is forming), as discussed in the previous section. There is a slight difference between the shift value obtained in the two datasets (UHV and O₂ annealing). However, the X-PEEM spectroscopic data in section 4.1.1 were affected by the variation of the illumination intensity during the acquisition. This has likely altered the fitting results to some small extent. In comparison to the UHV experiment, the presence of oxygen seems to lower the temperature at which the encapsulation of the NPs starts ($T \approx 613$ K). However, the observed difference of 35 K can also result from a slightly different calibration of the

thermocouples used for the temperature measurements. Despite these slight differences, the encapsulation process shows the same fingerprints with or without external oxygen.

This might give some indications on the encapsulation mechanism. For instance, if Fe-Pt intermixing would be directly involved in the formation of the encapsulating layer, the process should be suppressed (or slowed down) in oxygen rich conditions, as external O₂ hinders Fe-Pt alloying. On the contrary, if the process proceeds through the superficial migration of Fe cations on Pt clusters, then the O₂ in the gas phase can bind to the Fe atoms. The formation of the superficial FeO layer should be facilitated.

The outcome of our experiment confirms this second encapsulation mechanism, which was already suggested by *A. Sala* [52] and supported by TEM measurements [85]. The same encapsulation mechanism was also suggested for the Pt/ TiO₂ [74] system.

4.1.3 Influence of deposition temperature on NPs shape and size

The NPs size and shape can be influenced by the deposition temperature [52], i.e. the temperature of the sample during deposition. I investigate the level of ordering of Pt NPs forming on Fe₃O₄ film during deposition (2 ML) at T=620 K, in UHV conditions. The analysis relies mainly on SPA-LEED results, by comparing the NPs produced by deposition at RT (and subsequently annealed) and at 700K [52].

At T=620 K no encapsulation is expected, based on the data presented in section 4.1, as well as the thermal dewetting of the Fe₃O₄ film, which is extremely slow at this temperature. After deposition, the sample was then annealed in p_{O2}=1.0x10⁻⁶ mbar up to T=850 K to induce the NPs encapsulation. The deposition was followed in real time using the XPS dispersive mode (Fig 4.7); spectra related to RT deposition are shown for comparison in Fig 4.8. As the spectra were acquired at constant temperature, the photon beam does not shift over the sample surface during the acquisition. Therefore, in this case the intensity of the XPS peaks correlates to the Pt coverage. Neither at RT nor at 620 K the binding energy of the Pt4f peak shifts, indicating that the NPs were not encapsulated.

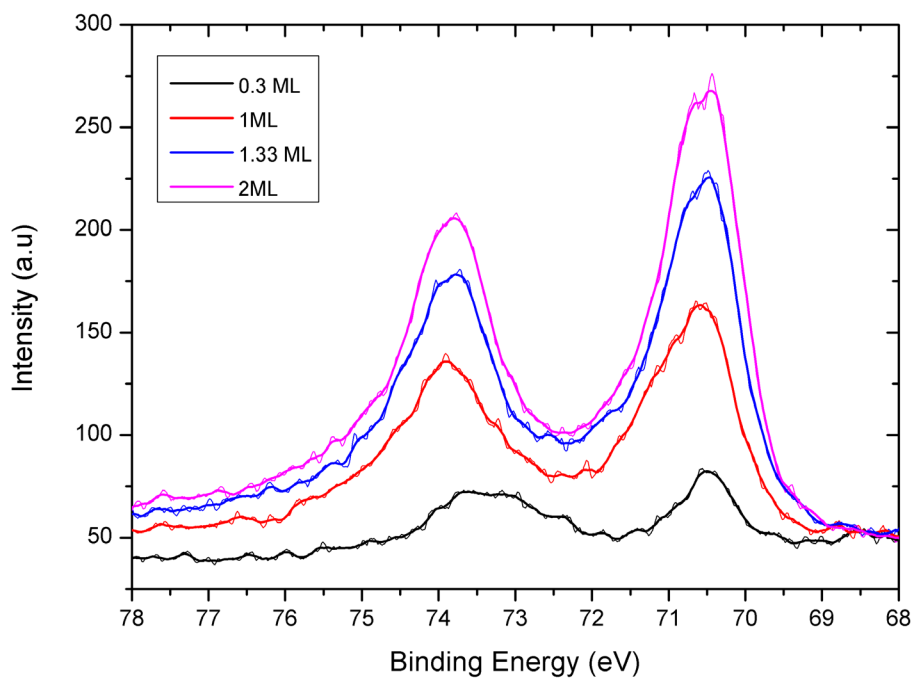


Fig. 4.7: Real time XPS on the Pt 4f peak during deposition at 620 K in UHV; 2 ML of Pt have been deposited on $\text{Fe}_3\text{O}_4/\text{Pt}(111)$. $h\nu=20.0\text{ eV}$

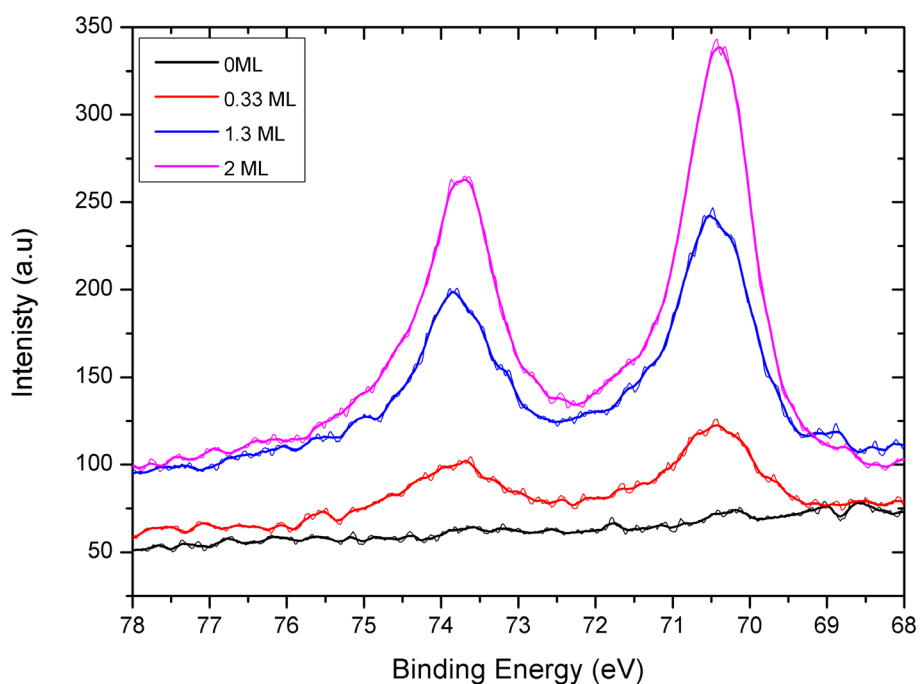


Fig. 4.8: Real time XPS on the Pt 4f peak during deposition at RT in UHV; 2 ML of Pt have been deposited on $\text{Fe}_3\text{O}_4/\text{Pt}(111)$. $h\nu=200\text{ eV}$

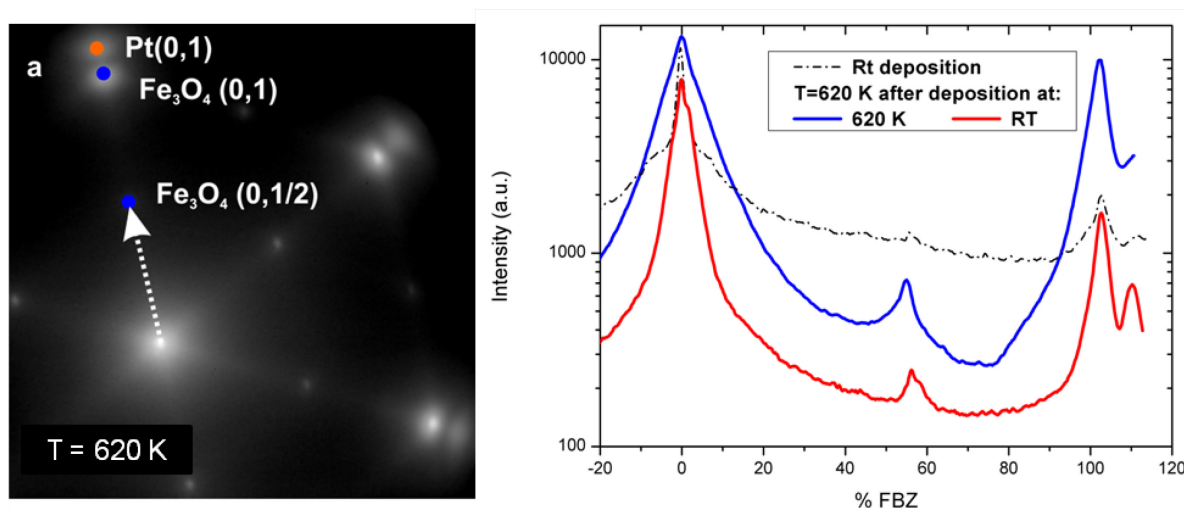


Fig. 4.9: LEED of the surface after 2 ML Pt deposition at 620 K in UHV (a) $E_k=38$ eV. Fig 4.9b) Comparison between the SPA-LEED for NPs obtained at 620K after: direct deposition at 620K (blue line) and RT (red line). The profile after RT deposition is shown for comparison (black dotted line).

The LEED pattern of the surface after deposition (in 4.9a) shows the (2x2) spots of the supporting Fe_3O_4 and the $\text{Pt}(1,0)$ and equivalent spots, which cannot be distinguished in the LEED image acquired after RT deposition (Fig. 4.1a). The similarities between this LEED pattern and the one in Fig. 4.1b indicate that deposition at this temperature lead to the direct formation of 3D Pt NPs. The absence of the $\text{FeO}/\text{Pt}(111)$ superstructure spots attests that the NPs are not encapsulated, consistently with the XPS data Fig 4.7. Fig 4.9b shows the comparison between two spot profiles: the blue curve for the NPs formed by direct deposition at 620 K and the red curves for the NPs formed by annealing ($T=620$ K) after RT deposition (red curve). The spot profile of the RT deposition is also provided (dotted line). The comparison between the red and the blue curve profiles underlines that the (0,0) spot is much broader when the NPs are formed directly by high temperature deposition, meaning that the average size is smaller.

The LEED pattern in Fig. 4.10a refers to the surface after annealing $T=850$ K. Unsharp $\text{FeO}/\text{Pt}(111)$ superstructure spots arise as fingerprint of the encapsulation process.

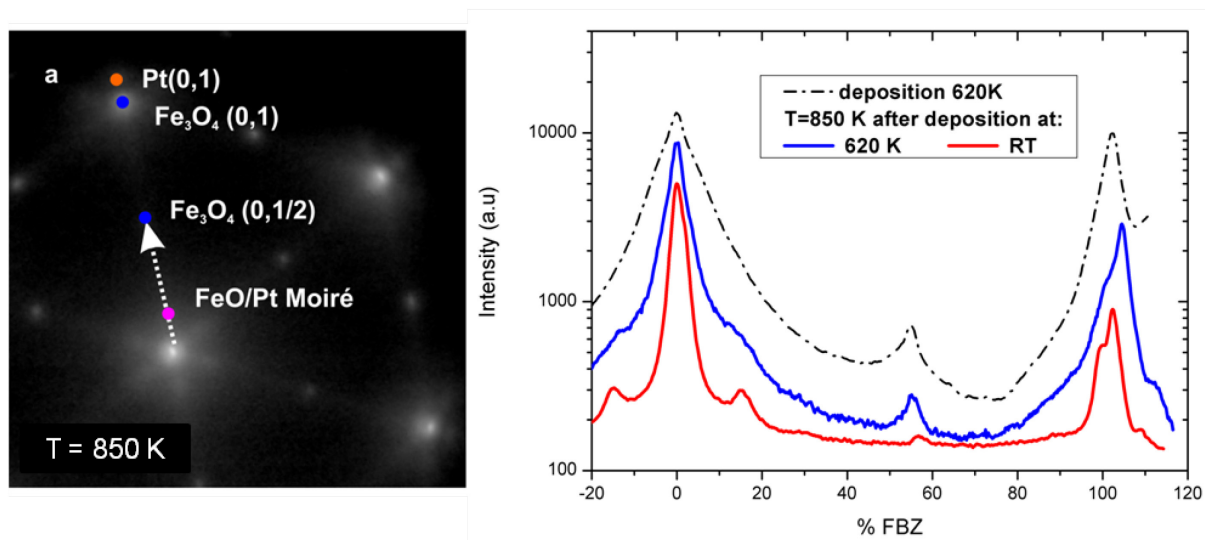


Fig. 4.10: LEED of the surface after annealing at $T=850$ K. 2 ML Pt were deposited at 620K in UHV (a) $E_k=38$ eV. Fig 4.10b Comparison between the SPA- LEED for NPS obtained at 850 K after: direct deposition at 620 K (blue line) and RT (red line). The profile of the surface after deposition at 620K is shown for comparison (black dotted line).

Similar to what was done previously, in Fig. 4.10b the spot profile of this surface (blue curve) was compared to the one obtained after annealing at the same temperature (850 K) after RT deposition (red curve). The black dotted line reported is the profile for the surface just after deposition at 620 K. Comparing the blue and the black curves, we see that the (0,0) spots sharpened during the annealing to 850 K. This behavior indicates that partial ordering of the surface has occurred during the annealing and that the NPs increased their size. On the other hand, the layer is less ordered compared to the one obtained after RT deposition and subsequent annealing: the blue curve is much broader than the red curve and the biphasic peaks are almost undistinguishable from the (0,0) profile; the same is true also for the outer peaks.

Discussion

Pt deposition at 620 K induces the direct formation of 3D NPs. The direct formation of clusters is confirmed by the presence of the Pt(111) (0,1)-and equivalent- spots as well as by the presence of (2x2) Fe_3O_4 reconstruction, arising from exposed oxide surface between the clusters. Both, XPS and LEED results attest that no encapsulation has taken place during deposition.

The direct formation of 3D clusters is enabled by diffusive processes of the deposited Pt atoms on the oxide surface. At high temperature, the kinetic energy of the adsorbed Pt atoms is high enough to overcome the diffusion barrier. However, this does not occur during RT deposition, where arriving Pt atoms do not diffuse and form a very irregular and weakly ordered overlayer. 3D clusters of bare Pt can be produced also by RT deposition and subsequent annealing at 620 K, as already discussed in 4.1. The NPs produced following this last procedure are more ordered (bigger size) than those formed directly by deposition at 620 K, as the SPA-LEED analysis points out. Similar consideration applies to the surface ordering after the encapsulation of the particles.

I consider first the data relative to the annealing at 620 K. The differences between the outcomes of two preparations cannot be explained by different diffusion coefficient, as the annealing temperature is the same. Also, the amount of deposited material is the same (2 ML) in both experiments. The most obvious difference between these two preparations is the amount of Pt available during the annealing. After RT deposition, the Pt overlayer consists in an homogenous distribution of irregular Pt islands 2 ML high, as shown by STM measurements [86]. Particle coarsening occurs via Ostwald ripening [52, 86]. At $T=620$ K the NPs form following, most likely, another type of mechanism (i.e. “diffusion and nucleation”). The same formation mechanism was suggested in [52] for the direct formation of nano-cluster during deposition at 700 K. At $T=620$ K, the diffusion length of Pt is low: for instance, homoepitaxial Pt/Pt(111) deposition at $T=600$ K (presented in 1.6.2) shows that the nucleation of Pt islands occurs in poorly ordered 3D shape. Most likely, the same thing occurs under the conditions of this experiment, resulting in the formation of a poorly ordered overlayer.

Further annealing of the sample ($T=850$ K in $p_{O_2}=1.0 \times 10^{-6}$ mbar) does not improve the ordering of the surface (Fig 4.10): the NPs are encapsulated (hexagonal shadows around (0,0) spots), but the quality of the encapsulating layer is poor (weak and broad satellite spots). In particular, the ordering of the encapsulated NPs prepared by high temperature deposition, even if improved after the annealing at 850 K, is lower compared to the one obtained after RT deposition. This behavior suggests that the morphology of the particle influences the encapsulation process: the migration of the Fe atoms from the supporting oxide might be hindered on poorly ordered Pt film. Similarly, the FeO(111) might not form an ordered layer on top of unordered NPs surfaces.

Finally I compare these data with the outcomes of a deposition experiment at 700K, which was discussed in [52]. *A. Sala* found that Pt deposition at 700 K forms highly ordered NPs, which are directly encapsulated [52]. SPA-LEED analysis showed that ordering of the NPs is higher than for the ones obtained by RT deposition and annealing [52], which is opposite to the case discussed above. Also in this case the formation of the NPs is believed to occur following a “diffusion and nucleation” mechanism [52]. There are two main differences between these two deposition experiments, resulting in surfaces characterized by extremely different ordering. The first is the deposition rate (4 ML/h in the present work; 0.3 ML/h in [52]), the second is the deposition temperature ($T=620$ K in the present work and $T=700$ K in [52]). Both factors (deposition flux and deposition temperature) contribute to the NPs ordering: on one hand, high deposition rates generally favor the formation of disordered clusters and on the other, the deposition temperature influences the diffusion length of Pt atoms adsorbed at the surface. For instance, homo-epitaxial experiments (section 1.6.2) outline that while the Pt film shows an ordered layer-by-layer mode at $T\approx 700$ K, at 600 K the deposited material forms more or less disordered islands, as the diffusion length of Pt atoms is lower. This last difference is most likely the reason for the observed behavior.

4.2 Investigation on the Pt NPs supported on biphasic terminated α -Fe₂O₃

The topic of the first part of the chapter is the interaction of Pt NPs with the Fe₃O₄. The second part investigates how the NPs interact with the α -Fe₂O₃ support. As in all the other experiments presented in this work, the α -Fe₂O₃ film is biphasic terminated. In previous experimental investigations by *M. Lewandowsky* [86], the Pt NPs supported on the O-terminated α -Fe₂O₃ surface do not exhibit SMSI. However, in this case the α -Fe₂O₃ surface was biphasic terminated, and therefore iron-rich. The excess of Fe atoms at this surface might have a predominant influence on the interaction between the substrate and the NPs.

Two questions are addressed in the following experiment: first, does encapsulation of the Pt NPs supported on α -Fe₂O₃ (biphasic terminated) occur in a similar way as on Fe₃O₄? Secondly, is the encapsulating layer on both oxide supports the same, i.e. FeO(111)?

To answer these questions, I investigated a mixed Fe₃O₄/ α -Fe₂O₃ film. A mixed film enables the direct comparison between the two supporting phases: differences between Fe₃O₄ and α -Fe₂O₃ can be immediately ruled out. This way, the effects of little differences in the experimental conditions are avoided because the two oxides are studied in the very same

experimental (i.e. the amount of deposited Pt, temperature, pressure) and acquisition conditions (instrumental alignment and beamline settings). The behavior of the Fe_3O_4 , already intensively investigated, was used as a reference.

For this experiment, I took advantage of the spatial resolution in X-PEEM (integrated methods do not allow to separate the contributions from the two areas). The XPS spectra from the two oxide phases are taken simultaneously (same image); this is important to outline reliable energy shifts and intensity differences, which play a crucial role for the direct comparison of the encapsulation mechanism on the two oxide phases, as discussed later in the text.

4.2.1 Results

The mixed film was produced by oxidation of $\text{Fe}_3\text{O}_4/\text{Ru}(0001)$ following the procedure described in chapter 2. The contribution from each oxide phase can be separated in LEEM, local LEED and X-PEEM.

Fig 4.11 shows the sample surface prior to Pt deposition: the area with dark contrast in the center is Fe_3O_4 ; the lighter area consists in biphasic terminated $\alpha\text{-Fe}_2\text{O}_3$ while the white domains are $\text{FeO}(111)$ holes in the film. This assignment is based on local LEED and X-PEEM. The presence of $\text{FeO}(111)$ regions indicated that the film is dewetted (deep holes down to the $\text{Ru}(0001)$ substrate) but this can be neglected in the following discussion, as they contribute neither to the Pt signal from the NPs (XPS) nor to the $\text{FeO}/\text{Pt}(111)$ superstructure of the encapsulating layer (LEED). The mixed film was produced by oxidation of $\text{Fe}_3\text{O}_4/\text{Ru}(0001)$ following the procedure described in chapter 2.

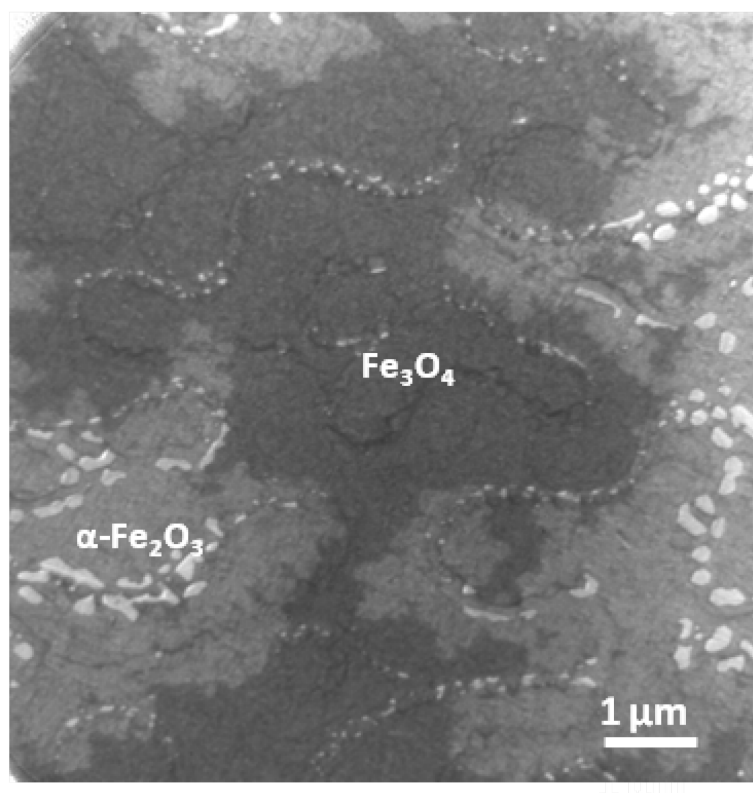


Fig. 4.11: LEEM. Initial surface consists in a mixed $\text{Fe}_3\text{O}_4/\alpha\text{-Fe}_2\text{O}_3$ (dark and light grey respectively). FeO holes are present. $E_k=38\text{eV}$

2.6 ML of Pt (2.6 ML) were deposited at RT under UHV conditions. The sample was first annealed at 620 K in UHV; then a final annealing stage up to $T=850\text{ K}$ was performed in O_2 pressure ($p=10^{-6}\text{ mbar}$). The surface was cooled down to RT after each step to perform LEEM, X-PEEM at the Pt4f and Fe3p peaks as well, as LEED. The annealing was followed in real time in LEED; however, the real time data are not presented because, during annealing stages, there was no control on the composition of the probed area ($\alpha\text{-Fe}_2\text{O}_3$, Fe_3O_4 or both) due to the thermal drift. The real time characterization of the Pt/ $\alpha\text{-Fe}_2\text{O}_3$ systems (XPS and LEED) should be investigated on a single phase $\alpha\text{-Fe}_2\text{O}_3$ film, and this remains a topic for future experiments.

LEED Data

The local LEED data of the Fe_3O_4 area resemble at each experimental stage the ones already presented in Fig. 4.1. Therefore, I present only the local LEED pattern for the $\alpha\text{-Fe}_2\text{O}_3$ phase (Fig 4.12). The similarities between Fig 4.12 and Fig 4.1 after each experimental step are evident (the same key feature can be identified in both images, such as, the presence of the Henzler ring, the presence or absence of the oxide main diffraction spots, ...). This indicates

that on α -Fe₂O₃ the Pt overlayer undergoes the same modifications discussed for Fe₃O₄ in section 4.1.1: i.e. i) after deposition at RT, the oxide surface is completely covered by a disordered overlayer; ii) after annealing at 620 K, the NPs enlarge and thicken, leaving exposed oxide areas at the surface ($(\sqrt{3} \times \sqrt{3})R30^\circ$ spots); iii) a clear reconstruction around the (0,0) spot arises after annealing at 850 K. Remarkably, in Fig. 4.12b and Fig. 4.12c, the extra-spots of the α -Fe₂O₃ biphas reconstruction (whose spatial periodicity is roughly half of the FeO/Pt(111) superstructure) are absent, meaning that the long range ordering at the surface is lost.

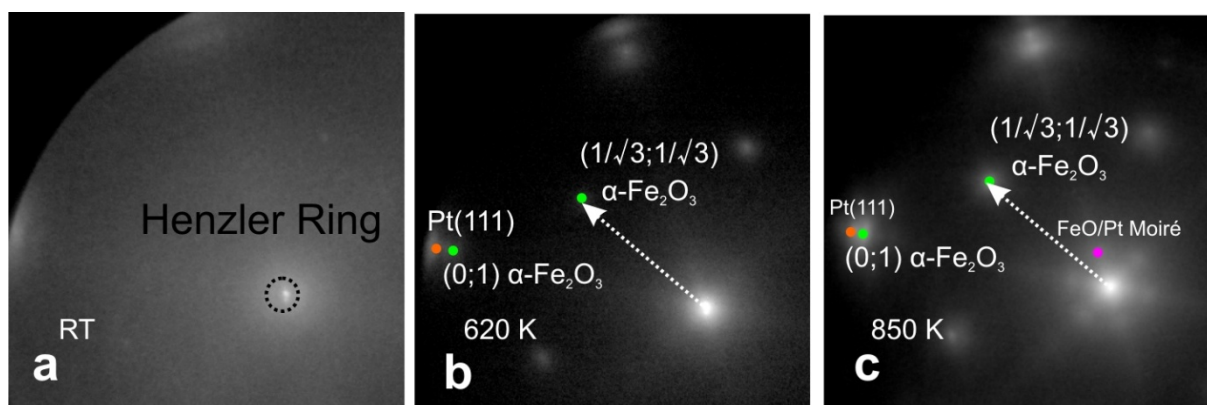


Fig. 4.12: LEED patterns relative to the three steps in the Pt NPs formation on the α -Fe₂O₃/Ru(0001). Fig 4.12a) shows the surface after RT (UHV) deposition 2.6 ML of Pt on the α -Fe₂O₃ film. The main diffraction oxide spots, as well as the biphas superstructure spot are completely damped; the non-crystalline background is high, indicating an high concentration of atomic defects at the surface. In the outer part of the pattern shadows are visible, arising most likely from the unordered Pt clusters. Fig 4.12b) The LEED pattern of the same film after annealing in UHV condition up to T=620 K. The surface shows the Pt(0,1) spots and the $(\sqrt{3} \times \sqrt{3})$ reconstruction of the support, indicating that the Pt overlayer has agglomerated in bigger Pt(111) clusters. The absence of the Moiré pattern indicates that the Pt NPs are not encapsulated. Fig 4.12c) The LEED pattern of the same film after annealing in UHV condition up to T=850 K, The surface shows the FeO(111)/Pt moiré pattern indicating that the NPs Pt are encapsulated.

$E_k = 38$ eV.

Fig 4.13 shows the SPA-LEED profile of the weak satellite spots present in 4.12c (black curve). The red curve is the spot profile of the local LEED from the Fe₃O₄ area (same experiment); the SPA-LEED of the encapsulated NPs on Fe₃O₄ have been reported as reference (data relative to Fig 4.1c). The SPA-LEED analysis shows that the k-space position of the superstructure spots in the α -Fe₂O₃ and Fe₃O₄ datasets (same experiment) is the same. Furthermore, its periodicity is that of FeO/Pt(111) Moiré structure. As the oxide film is supported on Ru(0001), this contribution can only arise from the encapsulating layer on the Pt

NPs, and not from dewetted area of the film (which contributes to the FeO/Ru(0001) superstructure, clearly distinguishable from the FeO/Pt(111)).

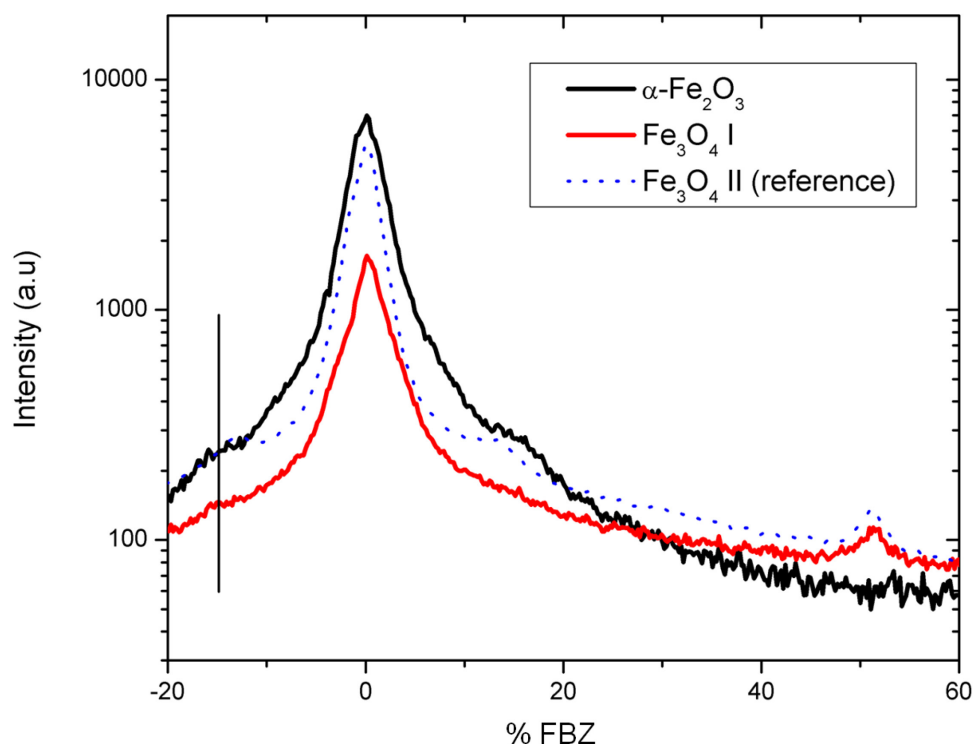


Fig. 4.13: SPA-LEED profiles for the Pt NPs annealed to $T=850\text{K}$ on: $\alpha\text{-Fe}_2\text{O}_3$ (0001) (black profile) and Fe_3O_4 (111) (red curve) in the same experiment (based on local LEED). For comparison is shown the SPA-LEED profile (blue dotted line) of encapsulated Pt NPs on Fe_3O_4 (111) from Fig 5.1c. The x axis is calibrated on the Fe_3O_4 (1x1) reconstruction (O layer periodicity).

X-PEEM data

The spatial resolution of X-PEEM allows to separate the XPS spectra from Fe_3O_4 and $\alpha\text{-Fe}_2\text{O}_3$ regions of the oxides, which is a key point in this experiment. However, the same technical consideration made in 4.1 applies also to this case: the illumination shifts along the image during the acquisition, because of the cooling down of the sample. The Fe3p and the Pt4f X-PEEM spectra (integrated over the image) were taken after deposition and each annealing step. Fe3p spectra were acquired also for the clean Fe_3O_4 and $\alpha\text{-Fe}_2\text{O}_3$ surfaces, prior to the deposition.

The Pt4f peaks are shown in Fig 4.14. The contributions from Fe_3O_4 (red line) and $\alpha\text{-Fe}_2\text{O}_3$ (black line) have been separated.

A first qualitative analysis shows two interesting facts. First, while just after deposition the Pt4f signal has the same intensity on both phases, after the first annealing step the peak intensity in the α -Fe₂O₃ is higher than in the Fe₃O₄ one; the same is true for the spectra after the encapsulation. Secondly, despite the overall intensity difference, the spectra profiles from each phase are similar (both, position and shape).

The peaks have been fitted to extend this first comparison to a more quantitative level, and should be considered carefully. As already discussed, the changes in the photon beam positions during the acquisition influences most likely also the value of the binding energy for the fitted component. However, the spectra for the Fe₃O₄ and the α -Fe₂O₃ regions have been acquired simultaneously, which means that they are affected by this misalignment in the same way.

The fitting of the Pt4f spectra followed the same guidelines presented in section 5.1.2. In particular: i) an asymmetric Lorentzian line shape [145] was used; ii) the peak FWHM reproduces the energy resolution of the experiment (0.8 eV) and it was set as fixed fitting constraint; iii) the intensity ratio between the 7/2 and 5/2 peaks was kept as close as possible to theoretical ratio of 4/3; iv) the expected doublet separation (3.2-3.4 eV) [146] was set as fixed fitting constraint.

Table 4.2 summarizes the fit results. Also in this case the peaks could be fitted assuming two components, which are assigned to surface and bulk contributions of the NPs. The differences between the absolute values obtained in this experiment and the one obtained in 5.1 is due to the different beam line setup.

The spectra from Fe₃O₄ and α -Fe₂O₃ regions were fitted independently and the components in each dataset have the same binding energies. For both supports the binding energy of the Pt4f surface component after encapsulation in O₂ pressure shifts by $\Delta E = +0.17$ eV. On the experimental basis, we can safely say that the NPs supported on α -Fe₂O₃ have the same XPS fingerprint as those supported on Fe₃O₄. The shift ($\Delta E \approx +0.2$ eV) is assigned to the Pt-Fe interaction at the FeO/Pt interface.

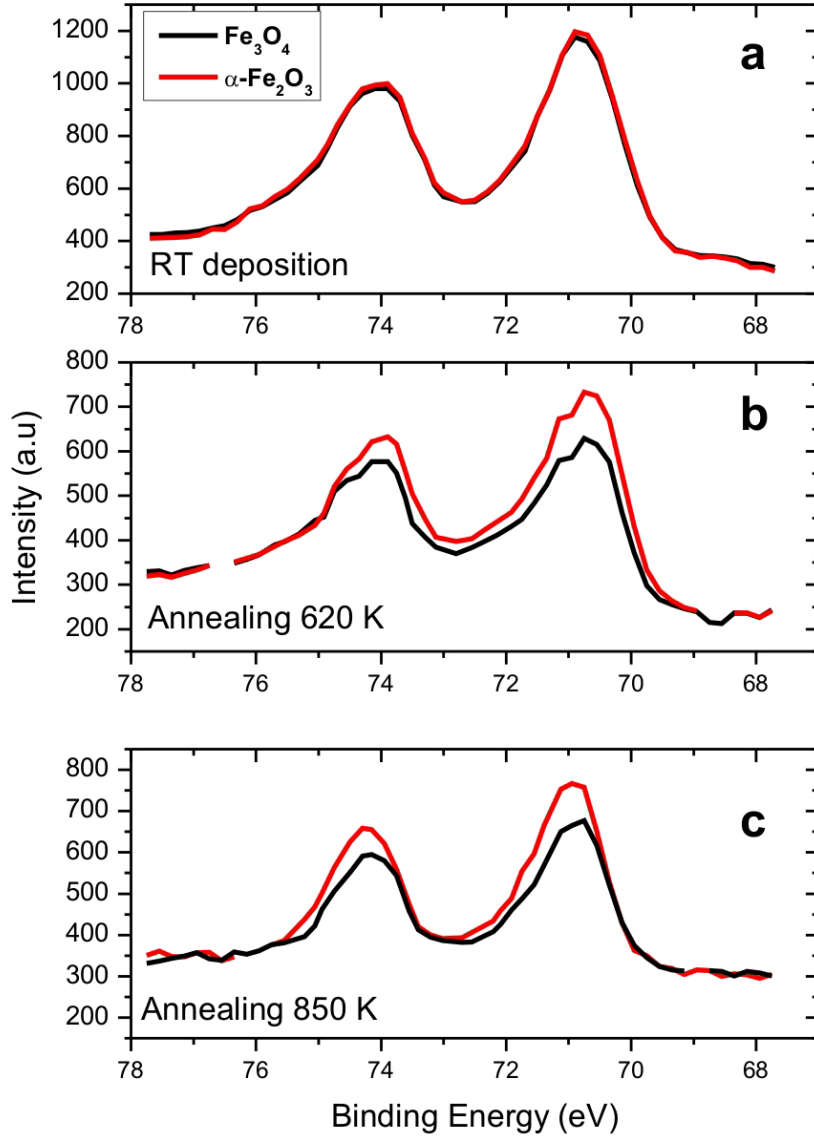


Fig. 4.14: XPS at the Pt4f core level peak. The contributions from Fe_3O_4 (red) and $\alpha\text{-Fe}_2\text{O}_3$ (black) are separate. The spectra refer to: Fig 4.14a) the Pt layer as deposited at RT (2 ML); Fig 4.14b) the first annealing at 620 K ; Fig 4.14c) and the final annealing at 850 K. The intensity is rescaled to the background level. The intensity difference between the spectra arises just after the first annealing stage.

$h\nu=200\text{ eV}$

The intensity differences, discussed qualitatively above, can be quantified from the two datasets (Fe_3O_4 and $\alpha\text{-Fe}_2\text{O}_3$) as the ratio between the fitted peak areas (for each component). While just after encapsulation the intensity ratio is $A_{\text{Fe}_2\text{O}_3}/A_{\text{Fe}_3\text{O}_4}=1.0\pm0.1$, after the first annealing step we have $A_{\text{Fe}_2\text{O}_3}/A_{\text{Fe}_3\text{O}_4}=1.15\pm0.07$; after the encapsulation $A_{\text{Fe}_2\text{O}_3}/A_{\text{Fe}_3\text{O}_4}\approx1.14\pm0.02$. As deposited Pt coverage and acquisition conditions (photon flux, detector) are the same for both areas, the intensity difference is real and not an instrumental artefact.

	Deposited Pt		Bare Pt clusters		Encapsulated Pt clusters (O ₂)	
Pt4f	7/2	5/2	7/2	5/2	7/2	5/2
Surface						
Binding Energy (eV)	70.39	73.64	70.36	73.62	70.53	73.82
Area (a.u) Fe ₃ O ₄	602	421	383	248	263	168
Area (a.u) α -Fe ₂ O ₃	610	418	428	305	305	188
Ratio A _{α-Fe₂O₃} /A _{Fe₃O₄}	0.99	1.01	1.12	1.22	1.16	1.12
Bulk						
Binding Energy (eV)	70.94	74.19	70.97	74.22	70.98	74.3
Area (a.u) Fe ₃ O ₄	529	359	180	108	218	139
Area (a.u) α -Fe ₂ O ₃	523	362	202	123	250	155
Ratio A _{α-Fe₂O₃} /A _{Fe₃O₄}	1.01	0.99	1.12	1.14	1.15	1.12

Table 5. 2: fit results from the XPS spectra at the Pt4f core level line from the spectra in Fig 4.14. The FWHM and the doublet separation are set as fitting constraint.

In the condition of the experiment ($h\nu=200$ eV, electron kinetic energy $E_{k\approx 125}$ eV, the electron mean free path is ≈ 1 nm), the Pt signal originates mainly from the two top most layers of the NPs. As after the first annealing ($T=620$ K) the Pt NPs are uncovered, for this dataset the intensity difference can have two main reasons:

- a higher NPs coverage on α -Fe₂O₃,
- a partial damping of the signal by the developing encapsulating layer on Fe₃O₄⁴

⁴ even if, as outlined by the previous analysis, the annealing temperature is too low to enable encapsulation.

In the last case, however, the intensity difference should disappear after the encapsulation is completed on both surfaces, which is not the case in our data.

While the Pt spectrum is sensitive to the Pt coverage at the surface, the Fe3p spectra, is sensitive to exposed areas of the supporting oxide. Therefore, it provides an independent estimation of the exposed oxide coverage. In particular I focused on the data acquired after the annealing at $T=620$ K (uncovered Pt NPs), plotting the intensity difference between the signal from the α -Fe₂O₃ and Fe₃O₄ regions, and integrated over areas of the same size (Fig. 4.15, thick blue curve). The advantage of looking at the difference between the spectra is that Fe³⁺ and Fe²⁺ components can be easily separated.

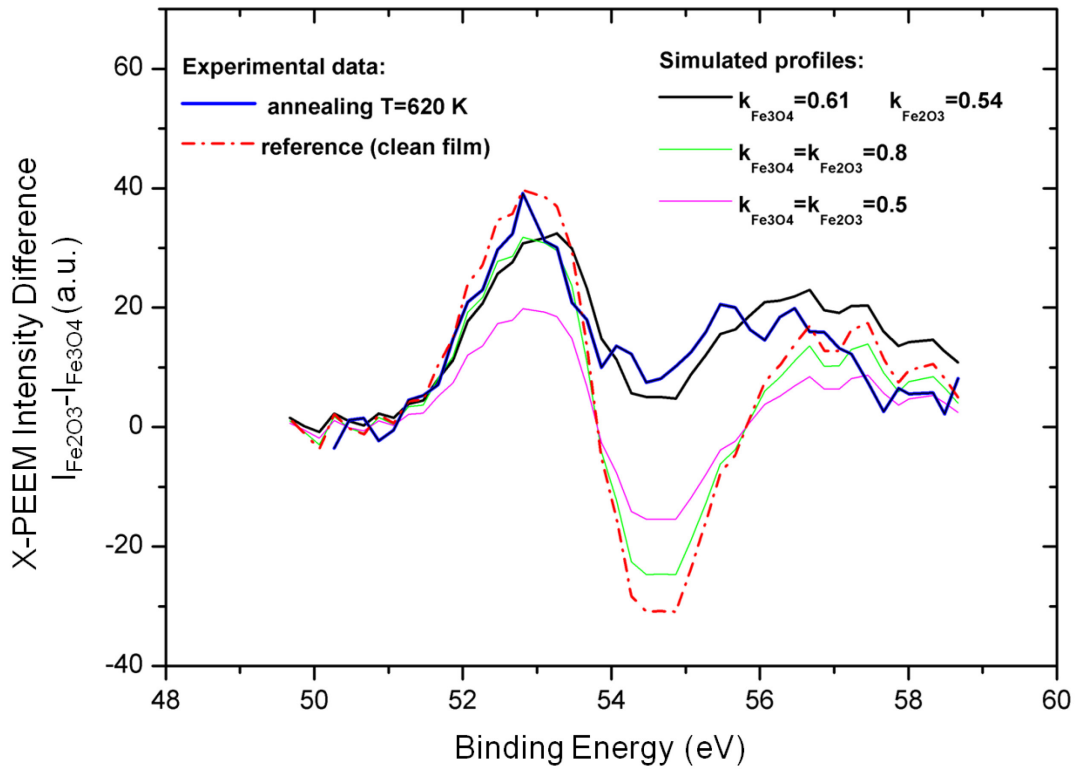


Fig. 4.15: Difference between Fe₃O₄ and α -Fe₂O₃ X-PEEM signal at the Fe3p core line for the clean surface (red dotted line) and after the first annealing at $T=620$ K (blue line). The other curves have been calculated by rescaling the clean oxide spectra. The straight thin lines were calculated assuming that both oxides expose the same fraction of area ($k_{Fe2O3} = k_{Fe3O4}$). The dotted lines, which resembles quite well the experimental data reproduces the case $k_{Fe2O3} = 0.513$ and $k_{Fe3O4} = 0.615$.

The experimental curves in Fig 4.15 were calculated from the data as:

$$I_{diff}(E_b) = I_{Fe2O3}(E_b) - I_{Fe3O4}(E_b),$$

Where E_b is the binding energy, $I_{Fe2O3}(E_b)$ and $I_{Fe3O4}(E_b)$, represent the Fe3p XPS peak intensity for the α -Fe₂O₃ area for the Fe₃O₄, respectively (the subtraction is done point by point). The spectra have been rescaled to the common background level prior to subtraction.

In the Fig 4.15, is also shown the dataset for the clean oxide surface before the deposition (dotted red line). The intensity the Fe₃O₄ and α -Fe₂O₃ spectra (integrated over the same areas) before deposition (clean oxides). As the data has been acquired integrating the signal from areas of the same extension, than $\theta_{Fe3O4} = \theta_{\alpha-Fe2O3}$. Moreover, this coverage can be arbitrarily set as “unitary”, i.e. $\theta_{Fe3O4} = \theta_{\alpha-Fe2O3} = 1$ and the spectra used as reference for the unitary coverage ($\theta_{Fe3O4} = \theta_{\alpha-Fe2O3} = 1$). The reference spectra were singularly rescaled and subsequently subtracted to reproduce the experimental data after the annealing at T=620 K, obtaining the simulated profiles as:

$$I'_{diff}(E_b) = k_{Fe2O3} \cdot I_{Fe2O3}(E_b) - k_{Fe3O4} \cdot I_{Fe3O4}(E_b),$$

Where $I'_{diff}(E_b)$ is the simulated intensity and k_{Fe2O3} , k_{Fe3O4} are numerical factors which represent the fractions of exposed oxide surface (between the NPs) contributing to the Fe3p spectra. As the surface is partially covered by Pt, than k_{Fe2O3} , $k_{Fe3O4} < 1$; their values were varied (manually) assuming that both oxides exposed the same ($k_{Fe2O3} = k_{Fe3O4}$) or different ($k_{Fe2O3} \neq k_{Fe3O4}$) fraction of area. The experimental data were best reproduced with the values: $k_{Fe2O3} = 0.54$ and $k_{Fe3O4} = 0.61$ (black line in Fig 1.15), giving the ratio $k_{Fe3O4}/k_{Fe2O3} = 1.12$. This value is equivalent to the ratio between the coverage of the exposed oxide areas, i.e. $\theta_{Fe3O4}/\theta_{\alpha-Fe2O3} = 1.12$ and it is consistent to the intensity ratio between the Pt signals from the Fe₃O₄ and α -Fe₂O₃ regions ($A_{Fe3O4}/A_{Fe2O3} \approx 1/1.14$). Consequently, the NPs coverage is different on the two supports: $\theta_{\alpha-Fe2O3}^{NPs}/\theta_{Fe3O4}^{NPs} \approx 1.14 \pm 0.05$.

4.2.2 Discussion

This experiment was addressed to characterize the interaction of Pt with the biphasic terminated α -Fe₂O₃ support. The same experimental steps are investigated as for the Fe₃O₄ case (section 4.1): deposition at RT, annealing at 620 K and annealing at 850 K. While the

deposition and the first annealing were performed in UHV, the final annealing was performed in $p_{O_2}=10^{-6}$ mbar, to prevent further dewetting of the oxide film. As already discussed in the previous sections, the effects of O_2 in the gas phase on the encapsulation process, if any, are extremely small (see section 4.1.2).

The NPs interaction with the two supporting oxides is directly compared under the very same experimental conditions, thanks to the usage of a mixed $\alpha\text{-Fe}_2\text{O}_3$ / Fe_3O_4 film. The local LEED and the X-PEEM measurements point out that the Pt NPs supported on the biphasic terminated $\alpha\text{-Fe}_2\text{O}_3$ film undergo encapsulation, following the same steps as on Fe_3O_4 : the disordered Pt overlayer, formed by RT deposition, orders in bare Pt(111) nano-clusters during annealing up to $T=620$ K. Annealing at 850 K enables the NPs encapsulation by an FeO layer.

Experiments on Pt deposition on the O-terminated $\alpha\text{-Fe}_2\text{O}_3$ surface were done by *M. Lewandowski* [86]. As already anticipated, the outcome on the O-terminated $\alpha\text{-Fe}_2\text{O}_3$ surface under the same treatment is completely different: in fact, the Pt NPs did not undergo encapsulation. In this experiment, the film is biphasic terminated, which is a Fe rich termination. The presence of Fe atoms at the surface might be a key factor enabling the encapsulation. The encapsulation on the biphasic terminated $\alpha\text{-Fe}_2\text{O}_3$ is most likely driven by the same driving force as for Fe_3O_4 . In the literature it is suggested: (i) the first is the minimization of surface energy of the system (ii) the charge transfer between Pt and oxide: encapsulation occurs by the migration of positively charged Fe atoms on the negatively charged Pt clusters.

Remarkably, after the first annealing, the biphasic satellite spots have broaden into a diffuse shadow, meaning that the long range ordering at the surface is lost. It might be that the long range ordering (60 Å) vanishes under the random clusters (≈ 10 nm) which are distributed on top. After encapsulation, the migration of material from the top layer on the NPs, during the formation of the encapsulating layer (as found by *Williger et al.* in the Fe_3O_4 system [85]) might also contribute to the loss of long range ordering. Knowing which is the interface between the NPs and the $\alpha\text{-Fe}_2\text{O}_3$ oxide (whether the biphasic termination or in the honeycomb layer from the bulk oxide) can give a definitive answer to this question.

We now come to the overall intensity difference between the Pt4f spectra acquired from the Fe_3O_4 and $\alpha\text{-Fe}_2\text{O}_3$, which affects the data after the two annealing stages. Based on the combined analysis of the Pt4f and Fe3p spectra we found that the more probable reason for

the intensity difference is the different Pt NPs coverage at the surface of the two oxides. The origin of the different Pt NPs coverage might depend on the NPs shapes. In fact, in the experiment, the coverage of deposited Pt is the same on both supports and it is unlikely that during the annealing massive diffusion of Pt has occurred from one oxide region to the other. Therefore, the overall volumes of the NPs is assumed to be the same, and the difference arises from the surface area. The estimation gives that averagely the NPs on $\alpha\text{-Fe}_2\text{O}_3$ are $\approx 10\%$ larger than on Fe_3O_4 (or equivalently, the NPs on Fe_3O_4 are $\approx 10\%$ higher than on $\alpha\text{-Fe}_2\text{O}_3$). The difference is small but still appreciable in the X-PEEM data. On the O-terminated $\alpha\text{-Fe}_2\text{O}_3$ surface, the Pt clusters were on average higher than on Fe_3O_4 (respectively: 5 ML (or higher) and 4ML high).

This fact might indicate that the adhesion energy of Pt on the oxide surface is influenced by the amount of Fe atoms at the surface: the Fe-Pt interaction increases most likely the Pt tendency to wet the oxide surface, while the opposite behavior should be expected for the Pt-O interaction. If this is the case, it would explain the difference between Pt coverage on the two supporting oxides observed in the present experiment and in [86]. In fact, the amount of Fe cations is higher on the biphasic terminated $\alpha\text{-Fe}_2\text{O}_3$ surface than on the Fe_3O_4 termination, while is absent on the O-terminated $\alpha\text{-Fe}_2\text{O}_3$ film. While experimental data for the adhesion energy between Pt and Fe_3O_4 are available [9, 86], there is no experimental determination for $\alpha\text{-Fe}_2\text{O}_3$.

4.3 Summary

This chapter discussed the encapsulation process of Pt NPs supported on both Fe_3O_4 and $\alpha\text{-Fe}_2\text{O}_3$ oxides. The SPA-LEED analysis clarifies that in both cases the encapsulating layer consists in an FeO layer (most likely O terminated). Real time LEED and XPS indicate that the encapsulation is enable for at $T > 650$ K and induces the shift of the binding energy of the surface component Pt4f core level peak by $\Delta E = +0.2$ eV . The shift arises from the Pt-Fe interaction occurring at the FeO/Pt interface.

The effect of O_2 in the gas phase on the encapsulation process was discussed, as well as the deposition temperature on the NPs morphology.

Comparing the results obtained on the biphasic terminated $\alpha\text{-Fe}_2\text{O}_3$ with those obtained on the O-terminated $\alpha\text{-Fe}_2\text{O}_3$ sample in [86] allows to distinguish the key role of superficial Fe cations in enabling the encapsulation process. The interaction between surface Fe and

deposited Pt is most likely the origin of the different particle shape when supported on biphasic or oxygen terminated α -Fe₂O₃ or Fe₃O₄.

Unfortunately, single particle contrast in core level X-PEEM was not obtained, as well as the real space observation of encapsulation. These topics remain for future works as well as the of real time XPS and LEED for the α -Fe₂O₃ phase.

5. Simulation of LEEM-image contrast

FeO/Pt nanoparticles (NPs) grown on Fe_3O_4 are an example of nano-structured catalysts undergoing SMSI. In the previous chapter, the system was discussed in detail. As anticipated, if the Fe_3O_4 film is supported on Pt(111), chemically and structurally sensitive methods (LEEM, XPEEM, LEED and LEED-IV) are incapable of directly distinguishing between encapsulated Pt-NPs or dewetted areas (holes in the film), as shown in figure Fig 5.1.

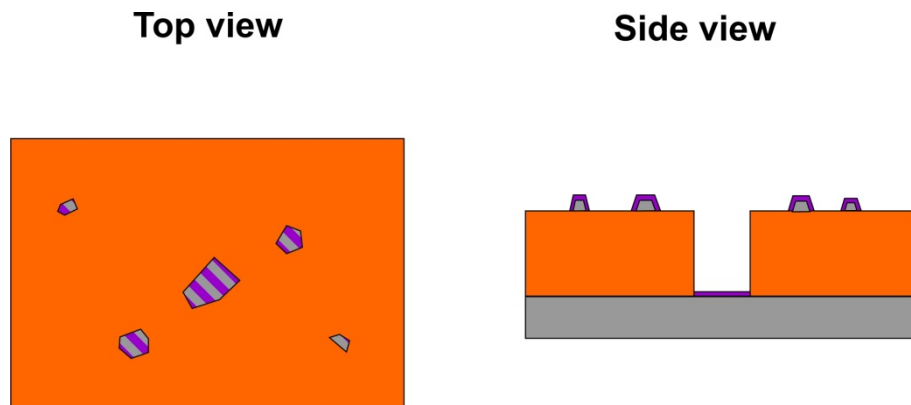


Fig. 5.1: Schematic view of the FeO/Pt NPs supported on Fe_3O_4 /Pt(111)

This is an example of a system in which the nature of the visible features can be identified univocally only by accessing the vertical morphology of the surface. In this chapter, I investigated the possibility to distinguish between NPs and holes in the system based on the analysis of their contrast profile in LEEM imaging. In the last years, several attempts were done to better understand and correlate the intensity profiles in the image to the surface morphology. These attempts have mainly treated the effect of the phase shift in homogeneous surfaces, without including changes in the scattered wave amplitude [24, 25]. However, the complex scattering amplitude needs to be included to treat surfaces composed by more than one material (so called mixed phase-amplitude objects). Within our working group, the Fourier formalism was already applied to simulate the contrast profiles of 1D line defects of an homogeneous sample [52]. In particular, the aim was to study the subsurface dislocation networks in Fe_3O_4 thin films supported on Pt(111) single crystal [52]. The analysis was based on the comparison between simulated and experimental contrast profiles. Several dislocation geometries were considered, as well as energy and focus scans. This procedure successfully

outlined the morphology of the dislocations, which originates at atomic defects at the interface between the Pt(111) substrate and the overgrown Fe₃O₄ film.

From this starting point, the new code was developed to treat 2D images, and mixed phase-amplitude objects.

The basics of image formation theory, presented in section 5.1, are followed by the detailed description of the mathematics and code used in section 5.2. The code, based on IDL programming language, has been developed within our research group, with the collaboration of Dr. H. Marchetto and Dr. A. Sala and the technical support of Elmitec GmbH.

The newly developed code is benchmarked against existing theoretical predictions in 5.3.1 (phase object). Section 5.3.2 presents the simulation results for a mixed-amplitude object. Conclusions are discussed in section 5.4.

5.1 Electron waves treatment

LEEM contrast can be categorized in **phase** and **amplitude** contrast; accordingly, **phase** and **amplitude** objects can be defined [23, 25]:

- a **pure amplitude object** induces only variations in the incoming wave amplitude and does not affect the phase.
- a **phase object** describes the opposite ideal case (e. g. an homogeneous surface with different height), which modifies only the phase of the backscattered electron waves.

The phase contrast arises from the interference phenomenon occurring between the partial wave of an electron with different phases. The phase shift can arise from differences in: (i) the optical paths, when the reflection occurs at different heights (**step contrast**), (ii) the imaginary part of the reflected amplitude, when reflection occurs on two materials or interfaces (the latter is called **quantum size contrast**).

The phase shifts depends on the electron wavelength λ_e at the surface (i.e. on $1/\sqrt{E_e}$), the step height and the imaginary part of the reflected amplitude: all these variables, as well as λ_e , define in-phase or out-of-phase interference conditions.

In defocus conditions, the microscope images an object plane on the detector, which is **behind** (under-focus) or **in front** (over-focus) the sample surface; in those planes, the interference fringes of the backscattered electron waves have propagated and can be visualized.

The first attempt to treat quantitatively the image formation in LEEM was proposed by *Chung* and *Altman* [25, 110], who introduced the wave-optical formalism. In this approach, LEEM phase contrast is modeled as the interference of Fresnel diffracted waves generated at the atomic step. This treatment predicted several key aspects of the step contrast experimentally observed in LEEM, such as: the energy dependence of interference fringes, at and near the step, and contrast reversal between over-focus and under-focus conditions. However, the wave-optical treatment has two main limitations: first, its application is limited to pure phase objects and more importantly, the instrumental aberrations (i.e. chromatic and spherical) are introduced in an approximate way, by convoluting the simulated intensity with a Gaussian instrumental response function.

Recently, Fourier optic formalism, originally developed for TEM imaging, was adapted to describe LEEM image formation [23, 24, 153]. With this approach the phase contrast, the amplitude contrast and instrumental aberration are consistently calculated, overcoming the restrictions of the wave optical approach.

The basics of the approach, applied to TEM microscopy can be summarized as following:

- $\psi_{out}(x, y)$ represents the reflected wave front in real space. It describes the phase and amplitude modification of the incoming electron beam (described by a planar wave) after the interaction of the electron beam with the sample (2D surface).
- $PSF(x, y)$, or *Point Spread Function*, describes the response of the LEEM microscope to a point source
- $\psi_{image}(x, y)$ describes the modifications of the reflected electron beam ($\psi_{out}(x, y)$) after the propagation through the optical system:

$$\psi_{image}(x, y) = \psi_{out}(x, y) \otimes PSF(x, y)$$

- $I_{image}(x, y)$ is the intensity distribution on the detector, i.e. the LEEM image:

$$I_{image}(x, y) = (\psi_{image}(x, y)) \cdot (\psi_{image}^*(x, y)) \cdot$$

The calculations are performed in the Fourier space (“frequency space”) rather than in the real space, because the description of the instrumental effects is easier in this coordinate system. The calculation of the image function performed in Fourier space simplifies the convolution into a product of Fourier transforms:

$$\varphi_{image}(q) = FFT(\psi_{out}(x, y)) \cdot FFT(PSF(x, y))$$

The Intensity distribution on the detector is:

$$I_{image}(x, y) = FFT^{-1}(\varphi_{image}(q)) \cdot FFT^{-1}(\varphi_{image}^*(q))$$

The Contrast Transfer Function (CTF) is the Point Spread Function in frequency space:

$$CTF(q) = FFT(PSF(x, y))$$

The $CTF(q)$ takes into account all the instrumental effects in the form [23]:

$$CTF(q) = M(q) \cdot W(q, \Delta z) \cdot E_c(q, \Delta E) \cdot E_s(q) \cdot E_u/I(q)$$

where

- $M(q)$ describes the frequency cut off by the contrast aperture, located in the Back Focal plane of the objective lens; the aperture limits the angular acceptance of the reflected beam, i.e cutting out electrons emitted with larger angles:

$$M(q) = \begin{cases} 1 & \text{if } |q| < |q_{max}| \\ 0 & \text{if } |q| > |q_{max}| \end{cases}$$

- $W(q, \Delta z)$ takes into account deviation from the ideal optical path due to the defocus (Δz) and the spherical aberration C_s . An optical system corrected up to the second aberration order is described by:

$$W(q, \Delta z) = \exp\left(-i\pi/2 \left((C_s \lambda_b^3 q^4) - 2\Delta z \lambda_b q^2\right)\right)$$

where λ_b indicates the electron wave length after the objective lens acceleration ($\lambda_b \propto 1/\sqrt{E_{k_b}}$).

- $E_c(q, \Delta E)$ models the effects of the chromatic aberration C_c due to an energy spread ΔE of the electron beam, with kinetic energy E :

$$E_c(q, \Delta E) = \exp\left(-(\pi C_c \lambda_b q^2)^2 / 16 \ln(2) \cdot \Delta E / E\right)$$

The other two factors take into account the effect of finite dimensions of the source ($E_s(q)$) and the instabilities of the objective lens current ($E_U / I(q)$); these effects are negligible in high resolution LEEM microscopes [23].

5.1.1 The specific case of LEEM

The formalism introduced above describes the relationship between $\psi_{out}(x, y)$ and $\psi_{image}(x, y)$ in any intermediate image plane of the microscope, with arbitrary magnification. In the present work, consistently with the approach adopted by other LEEM groups [23, 25, 154, 155], $\psi_{out}(x, y)$ and $\psi_{image}(x, y)$ are calculated in “artificial” image planes, defined opportunely. These planes are chosen so that: (i) the overall magnification of the optical system is unitary, (ii) the beam is accelerated. In this way, the Fourier formalism used in TEM imaging (where there is no acceleration of the electron beam) can be applied to LEEM, but the effects of (i) the contrast aperture and (ii) the value of the aberration coefficients need to be recalculated coherently.

Focusing on the effects of contrast aperture, one finds that the maximum acceptance angle is set by the contrast aperture size Δ_{CA} (see Fig 5.2b):

$$\alpha_{max} = \Delta_{CA} / 2 \cdot f_{T1}^{-1} \quad \text{and} \quad q_{max} = 2\pi \alpha_{max} / \lambda_e$$

In the real LEEM microscope, the electron beam, reflected at the sample, is magnified by the objective lens, and accelerated by the electrostatic field between the sample and the objective lens (see Fig 5.2.a). Therefore, the relationship between α_{max} and α_{max}^0 at the sample plane is:

$$\alpha_{max}^0 = \left(M_\alpha \cdot \lambda_e / \lambda_b \right) \alpha_{max}$$

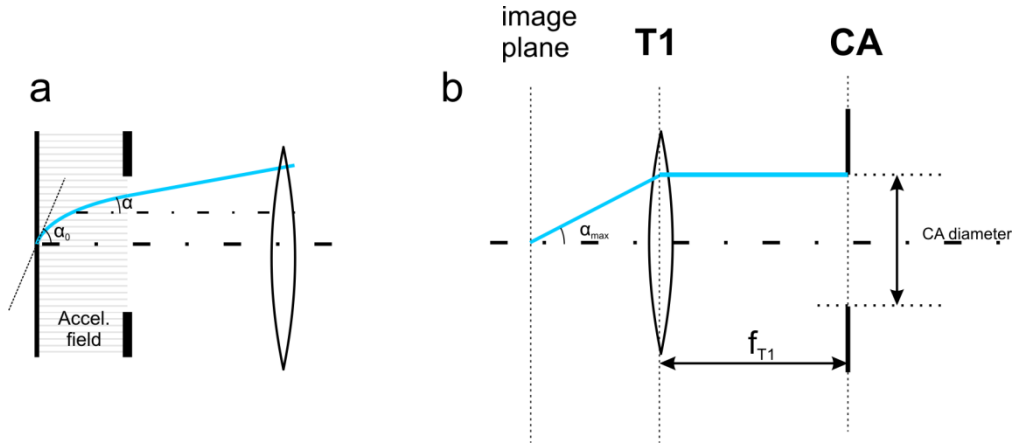


Fig. 5.2a: Relationships between the angles at the sample and after the acceleration, assuming the overall system magnification as $M=1$: $\alpha = \alpha_0 \lambda_e / \lambda_b$. In the real microscope, the angle is magnified by the objective lens ($M_o=18$) and then projected 1:1 at the exit of the beam splitter. Fig. 5.2b: Relationship between the angles in the image plane (at the beam splitter) and the positions in the plane of the contrast aperture.

The detector resolution is calculated by a Gaussian convolution of the final image. The Gaussian FWHM represents the detector resolution limits, which, for the SMART detector is 1/300 of the FoV (mainly caused by the channel plate screen setup).

5.2 The 2D algorithm

The Fourier formalism describes accurately how a “guessed” surface ($\psi_{out}(x, y)$) is imaged by the microscope [23, 24, 155]. This allows the quantitative comparison between simulated and real images. The comparisons are generally based on 1D intensity scans perpendicular to the investigated surface features (called “**contrast profiles**”). The appearance of the surface depends on the focus and the interference conditions, the latter being given by the electron energy and the phase shift. Consequently, a reliable 3D model of the surface should reproduce the contrast profiles of the real image in focus and/or energy scans. A focus (energy) scan consists in a collection of images of the same area of the surface. In each image of a focus (energy) series, the focus (energy) is changed in regular steps, while all the other acquisition parameters are kept constant.

The Fourier formalism was implemented in a program written in the IDL language by Dr. Marchetto. The calculation procedure can be summarized as follow:

- $\varphi_{out}(q)$ is calculated as the 2D discrete Fourier Transform of $\psi_{out}(x)$ which represents the simulated surface in real space and is obtained from 2D external inputs (see 5.2.2)
- $\varphi_{image}(q)$ is obtained by the relationship $\varphi_{image}(q) = \varphi_{out}(q) \cdot CTF(q)$; where the function $CTF(q)$, explicitly given in section 5.2.1, has been adapted to simulate the real SMART microscope; the electron energy at the surface and the defocus can be set as inputs.
- $\psi_{image}(x)$ is obtained from $\varphi_{image}(q)$ by applying the inverse Fourier transformation
- Finally the output , i.e. the final image is calculated from the relationship:

$$I_{image}(x) = \psi_{image}(x) \cdot \psi_{image}^*(x)$$

All the calculations are performed in the coordinate system defined at the sample side, due to the convention described above. Therefore, $\psi_{image}(x, y)$ and $I_{image}(x, y)$ are defined “at the sample surface” and not at “the detector”.

All values used in the CTF resemble the SMART optical properties (see Table 6.1), and have been extracted from [52]. Table 5.1 summarizes the rescaled instrumental parameters:

Parameter	Value	Unit
C_s	0.254	m
C_c	-95	mm
$U_g=E_k$	0-100	eV
$U_b=E_b$	15	keV
M_a	18	
L_{T1-CA}	45	mm
Δ_{AD}	30 - 10	μm
Δz	-30 - 30	μm
$L_{Sample- objectiveLens}$	2.3	mm
ΔE (energy spread e-gun)	0.5	eV

Table 5.1: rescaled instrumental parameter used to compute the CTF of the SMART microscope

5.2.1 Definition of the Object function

$\psi_{out}(x, y)$ is a 2D function describing the topography (phase object) and the “composition” (amplitude object) as the product of two functions, $\psi_{step}(x, y)$ and $\psi_{amplitude}(x, y)$, respectively the topography of the surface and its reflectivity.

$$\psi_{out}(x, y) = \psi_{step}(x, y) \cdot \psi_{amplitude}(x, y)$$

Explicitly,

$$\psi_{step}(x, y) = e^{i\Delta\phi_{step}} = e^{i\frac{4\pi}{\lambda_e}\Delta h(x,y)}$$

Where λ_e is the wavelength of elastically backscattered electrons and $\Delta h(x,y)$ is the function which defines the topography of the 2D surface.

$$\psi_{amplitude}(x,y) = A(x,y) = \begin{cases} A_1 e^{i\phi_1} \\ A_2 e^{i\phi_2} \end{cases} = \begin{cases} A_1 e^{i\Delta\phi_{amplitude}} \\ A_2 \end{cases}$$

The function $A(x,y)$ describes the local reflectivity of the surface. The overall phase shift is:

$$\Delta\phi_{out}(x,y) = \phi_{step}(x,y) + \phi_{amplitude}(x,y) = \frac{4\pi}{\lambda_e} \Delta h(x,y) + \Delta\phi_{amplitude}$$

In the code, the functions $\Delta h(x,y)$ and $A(x,y)$ are loaded from external 2D matrices, allowing the independent definition of the surface morphology and reflectivity (see Fig 5.3).

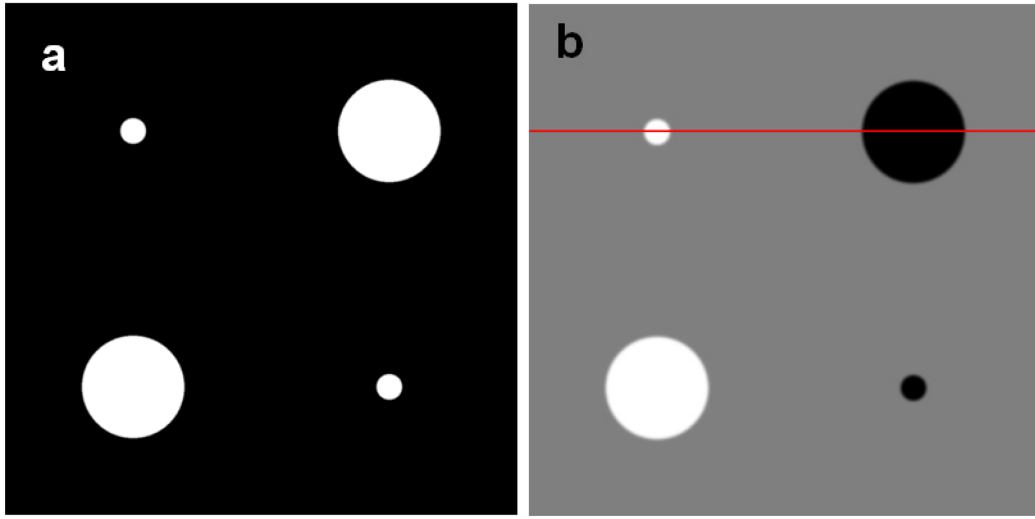


Fig. 5.3: Example of the definition of the external inputs for a surface composed by four islands on a flat substrate (different composition). The left islands are hills while the right islands are holes. Fig 5.3a defines the function $A(x,y)$, i.e. the composition of the surface. The white area have reflectivity “1”, black has reflectivity “-1”, assuming the values $A_1 e^{-i\Delta\phi}$ and A_2 respectively. Fig 5.3b defines the function $h(x,y)$, i.e. the topography of the surface. Colors define the value attributed to the pixel: white = +1, gray = 0, black = -1, assuming the values $+\Delta h, 0, -\Delta h$, respectively. $A_1, A_2, \Delta\phi$ and Δh are given as independent inputs. The contrast profile of the simulated image is scanned along the red line.

The matrices, as loaded by the program, are defined by integer values (1,0,-1 for the phase object; 1,-1 for the amplitude); in the first calculation step these values assume the value of the external inputs, which define the “guessed” step height ("StepHeight") or the Amplitude ("AmpLow" "AmpHigh"); the latter parameter is the real part of the reflected amplitude. An additional parameter (“AtomicShift”) gives the phase shift resulting from the imaginary part of the reflected amplitude.

With this approach, we can easily deal with pure phase object ("AmpLow"="AmplHigh", "AtomicShift"=0), pure amplitude object ("StepHeight"=0 "AtomicShift"=0) or any situation in between.

The real part of the amplitude factor in real conditions can be evaluated from the experimental data using the relationship:

$$\sqrt{I_1} / \sqrt{I_2} = A_1 / A_2$$

where I_1 and I_2 are the intensities for the two phases considered at a given electron energy. As, the absolute value of the intensity depends on the acquisition (channel plate, acquisition time, flux of the illuminating electron beam, FoV ...) the intensity ratio should be evaluated for values of I_1 and I_2 obtained under the same acquisition conditions (for instance in the same image), taking care that the data should be taken from flat region of the sample.

5.3 Results and Discussion

5.3.1 Simple Phase object

To test the reliability of the developed program, I have simulated the behavior of simple phase objects, and compared our results to those already available in literature [25, 153, 156]. The reflectivity of the surface is constant; the phase shift arises only by the topography of the surface $\Delta h(x,y)$. Remembering the conditions for constructive interference at normal incidence and the de-Broglie relation between E_e and λ_e , we find:

- **constructive** $\Delta\varphi = 2n\pi$ $E_C^1 = h^2 (2m_e)^{-1} (2\Delta h)^{-2}$; $E_C^n = n^2 E_C^1$
- **destructive** $\Delta\varphi = (2n + 1)\pi$ $E_D^1 = \frac{1}{4}E_C^1$; $E_D^n = (2n + 1)^2 E_D^1$

Where Δh is the distance between proximal scattering centers.

We tested in-phase, out-of-phase and intermediate situations on a simple step, for under/in/over focus conditions ($\Delta z = \pm 30 \mu m$, $\Delta z = 0^5$). In the specific case, the step height is $\Delta h = 0.612 \text{ nm}$; the energies considered are $E_C^1 = 1 \text{ eV}$, $E_D^1 = 0.25 \text{ eV}$, $E_{\pi/2}^1 = 0.0625 \text{ eV}$, $E_{3\pi/2}^1 = 0.5625 \text{ eV}$, $E_C^2 = 4 \text{ eV}$ for phase shifts $\Delta\varphi = 2\pi, \pi, \pi/2, 3\pi/2, 4\pi$ respectively. The

⁵ Δz is the position of the plane which is imaged on the screen; in defocus conditions the plane is in front or behind the sample surface

appearance of the simulated surface (phase object) is shown in Fig 5.4. The three graphs in Fig 5.5 shows part of the contrast profiles along the red line in Fig. 5.4, in under-, in- and over- focus conditions respectively.

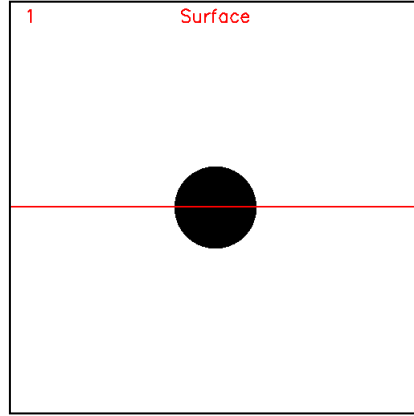


Fig. 5.4: The Phase object considered in the simulation is a circular hill. The red line inside the marked region in the image represents the plotted profile in Fig. 6.7a-c; FoV 200 nm

At **constructive interference** $\Delta\phi=2\pi$ conditions (black line) the intensity is constant on both sides of the step and also across the step. This happens in all three focus conditions. Consequently steps are invisible.

At **destructive interference** $\Delta\phi=\pi$ (red line), the step appears darker than the rest of the surface (low intensity), while the sides of the step are brighter than the surroundings (high intensity fringes). The minimum of the intensity profile is always centered at the step position for all focus condition. On the contrary, the maximum intensity fringes are closer in focus condition and further away in under and over focus. This means that the step appears larger in over-focus or under-focus.

At $\Delta\phi= \pi/2, 3\pi/2$ (blue and green curves respectively) asymmetrical position of the minimum fringes respect to the step location is observed. For $\Delta\phi= \pi/2$ in under-focus condition the intensity minimum is shifted towards the lower side of the step, while in over-focus it is shifted towards the upper side of the step. Therefore, in a focus series the apparent step position changes. The opposite behavior is observed for $\Delta\phi= 3\pi/2$. Also in this case the step is brighter at its sides, compared to the rest of the surface. Non-in-focus conditions induce an asymmetrical behavior also for the first maxima fringes, which are brighter on one side of the step. Moreover, there is an inversion of this intensity asymmetry from under-focus to over-focus.

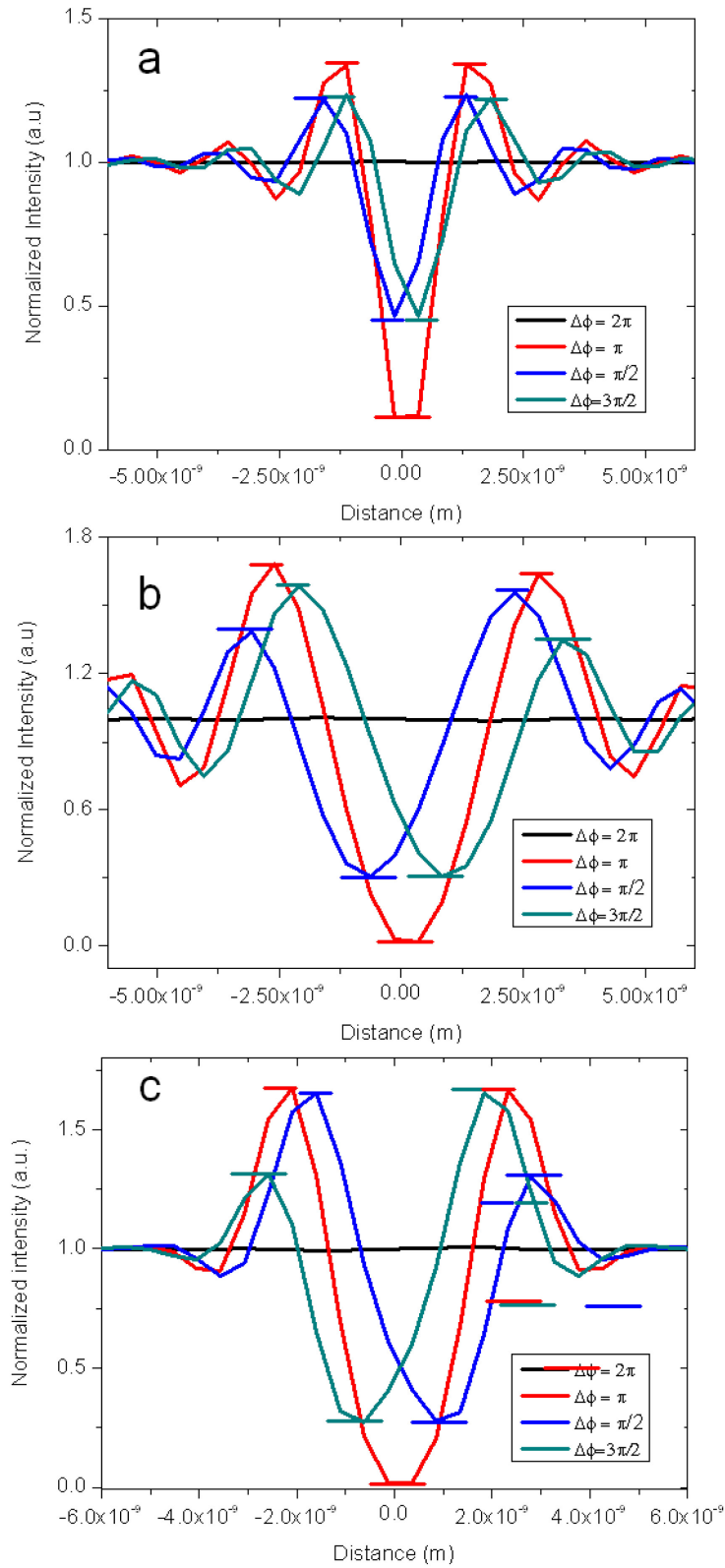


Fig. 5.5: Simulated intensity profiles for the left step in image 6.6 in: a) under-focus, b) in-focus, d) over-focus, for different interference conditions. The step is centered at $x = 0$.

This analysis is in full agreement with the theoretical results obtained in [25, 153]. The contrast profile inversion in out of phase conditions from under- to over- focus is the main feature of “**contrast reversal**” [25, 154]. Based on the asymmetries in out of phase conditions, the step direction can be determined combining energy and focus scans. In real images, only the first order interference fringes are visible due to the instrumental resolution of the real detector, as presented in detail in [52] and [23, 110].

5.3.2 Pure Amplitude and mixed Amplitude-phase object

The next section focuses on the simulations of the image contrast of a mixed amplitude-phase object. The application is the simulation of real surfaces composed by two materials (or more materials), which have a variable height difference.

The free parameters in the simulation are: the electron energy, the defocus, the real part of the reflected amplitude and the phase shift. While the first two can be controlled by the acquisition conditions, the last two depend on the system. The first three parameters are determined from the experimental data, while the phase shift is not. In the following treatment, the electron energy, the focus and the real part of the reflected amplitude reproduce the experimental conditions used to image a mixed surfaced composed by FeO/Pt(111) and Fe₃O₄ area ($E_e=38$ eV; $\Delta z=15\mu\text{m}$; $A_1=51$ $A_2=22$). This choice limits the study to the effects of the phase shift $\Delta\phi_{out}$ only, reducing the number of free parameter in the simulation.

The phase shift between reflected waves arises from two contributions: from the surface topography $\Delta\phi_{step} = (4\pi/\lambda e)\Delta h$, and from the complex part of the reflected amplitude $\Delta\phi_{amplitude} = (\phi_1 - \phi_2)$; the exact values of both contributions are unknown in the experiments.

Mixed-phase amplitude object

Fig 5.6 summarizes the under-, in- and over- focus behavior of a surface composed by four islands of high reflectivity (reproducing FeO/Pt) on a support with low reflectivity (Fe₃O₄). The input surface is shown in Fig 5.3. The big islands (top right and bottom left corners in Fig 5.6) have a diameter of 20 nm, the small ones 5 nm (top left and bottom right corners in Fig 5.6). The fourth column shows the contrast profile along the line indicated in the figure for all three focus conditions. The values: $\Delta\phi_{out}=0, \pi/2, \pi, 3\pi/2$ have been considered (first, second, third and forth rows, respectively).

In the first row, the simulated phase shift is $\Delta\phi_{out} = 0$. According to the nomenclature adopted in [23] this is a “pure amplitude object”. The islands are brighter than the substrate due to the higher reflectivity (real part of the reflected amplitude). The absolute intensity in out-of-focus conditions depends on the value for the defocus. In this case ($\Delta z = 15 \mu\text{m}$), the maximum value of the in-focus intensity (black line) is lower than in out-of-focus; its absolute value depends on the object size. The contrast profile in over- (red line) and under-focus (blue line) is identical. Big (20 nm) and small (5 nm) islands appear different under the same out-of-focus condition: the large object appears bright while the small ones appear black. Moreover, interference fringes are visible in out-of-focus at the border of the islands. As a consequence of the interference, the borders of the objects are brighter than in focus. For the same reason, the small island appears darker in the center. This can be understood as following: the first interference minimum is located at the center of the object (destructive interference), and the first maximum at the borders.

Also the condition $\Delta\phi = \pi$ (third row) gives identical out-of-focus contrast profiles, having a maximum value higher than in focus, at the given defocus value $\Delta z = 15 \mu\text{m}$. Compared to the case $\Delta\phi = 0$, the intensity is higher in the object center, and lower at the border. Again, this is a consequence of the interference: the first intensity maximum occurs at in the center of the object, while the first minimum at the borders. Such behavior (at $\Delta\phi = \pi$) is opposite than the one observed for the “pure amplitude object” ($\Delta\phi = 0$).

In the second and fourth rows are $\Delta\phi = \pi/2$ and $\Delta\phi = 3\pi/2$, respectively. These two situations differ from the cases $\Delta\phi = 0$ and $\Delta\phi = \pi$ for the out-of-focus intensity, which have different absolute intensity maxima.

Comparing the two contrast profiles, the inverted behavior in over- and under- focus is observed: for $\Delta\phi = \pi/2$ the intensity is higher in under-focus than in over-focus (constructive and destructive interference respectively) while for $\Delta\phi = 3\pi/2$ the behavior is the opposite.

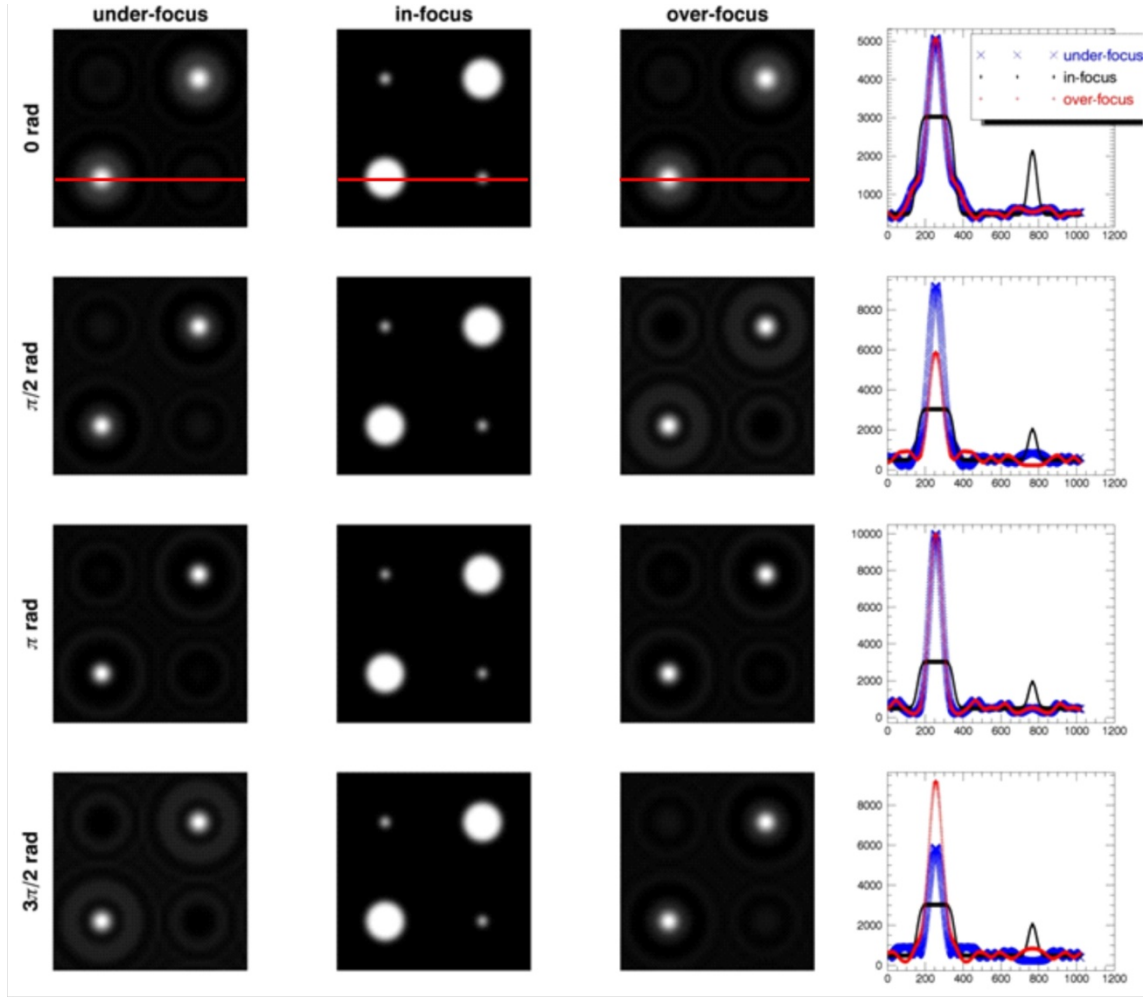


Fig. 5.6: Intensity behavior in under- (first column), in- (second column) and over- focus (third column) of a surface composed by four islands with high reflectivity (reproducing FeO/Pt) on a support with low reflectivity (Fe_3O_4). The forth column represents the contrast profile in the three images along the red line.

Each row corresponds to a different value of the step height: 0; ± 1 nm and ± 16 nm. In the second and third rows the object on the left side of the image have a positive step height (hills), while the right objects have a negative step height (holes).

The inversion from over to under-focus intensities generalizes to a mixed amplitude-phase object, the **contrast reversal** discussed for the simple-phase object (see 5.3.2).

The value $\Delta\phi_{\text{out}}$ does not affect significantly the in-focus images (and their contrast profiles) in Fig 5.6. However, a deeper analysis outlines that the phase shift induces some modifications of the in focus contrast profile, as summarized by the 2D plot in Fig 5.7 The plot is a collection of 1D contrast profiles, evaluated along the red line in Fig 5.6 (horizontal axes). The intensity is given in grey scale; the white features on the left and right side of the image represent the contrast for the 20 nm and 5 nm wide islands, respectively.

The vertical axes correspond to the value of $\Delta\phi$, which varies $[0, 2\pi]$.

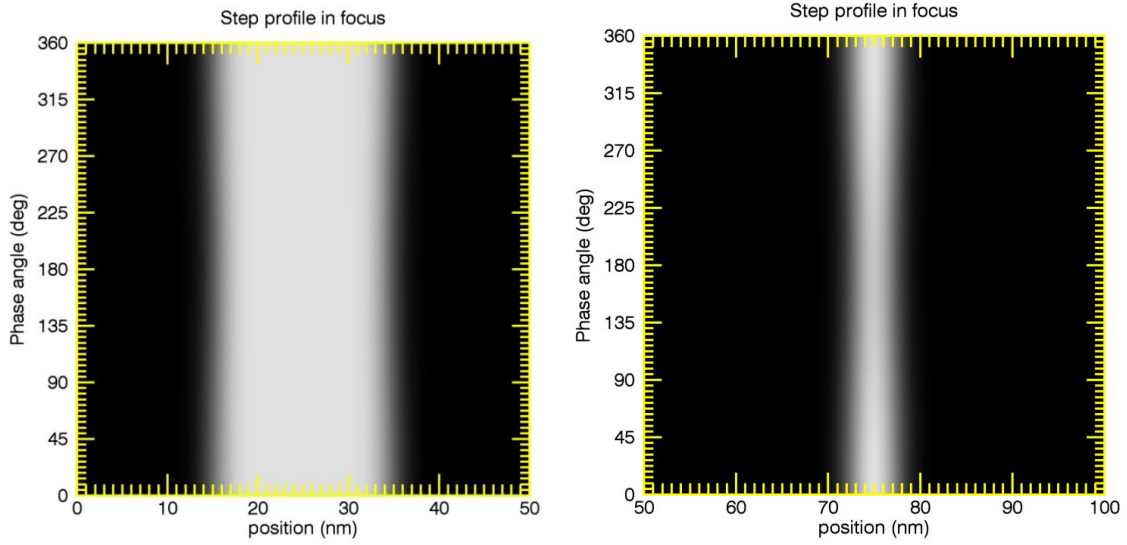


Fig. 5.7: Effect of the phase shift on the in-focus contrast profile, given by the step height (vertical axes). The horizontal axes correspond to the position along the red line in Fig 5.6. The intensity is given in black-with scale. The feature on the left and right side of the image represent the 20nm and 5nm wide islands, respectively. $\Delta\phi$ varies between $[0, 2\pi]$

Looking at the 5 nm island (Fig 5.7b), the absolute value of the intensity contrast profile maximum is modified by the change in the interference conditions (it is slightly darker at $\Delta\phi_{out} = 180^\circ$). Moreover, the value of $\Delta\phi$ affects the borders of the islands, periodically changing the apparent lateral dimensions of the object. The effect is greater the smaller is the lateral size of the object: for the 20 nm object (Fig 5.7a) these modulations are almost negligible.

5.3.3 Discussion

Summarizing the results of the simulation for a mixed phase and amplitude object, the value of

$$\Delta\phi_{out} = \Delta\phi_{amplitude} + \frac{4\pi}{\lambda_e} \Delta h$$

affects prominently the out-of-focus intensity profile, as a consequence of the interference between reflected waves. Periodic modulation of the in-focus contrast profile has also been

determined. The value $\Delta\phi_{out}$ can be determined by studying the features of the contrast profile variation in a focus series; moreover, if one of the two contributions to $\Delta\phi_{out}$ is known, the other can be determined.

In the case of a **phase object**, the value Δh can be experimentally obtained by the relationships:

$$\Delta h = \frac{h}{2\sqrt{m_e E_1^C}} \quad \text{or} \quad E_1^C = \frac{h^2}{8m_e \Delta h^2}$$

Where E_1^C is the electron energy corresponding to the first constructive interference condition. The value E_1^C can be found in an energy scan (in focus conditions) as following. Based on the contrast features, the set of energies satisfying the condition $\Delta\phi_{step} = 0$ ($E_n^C = n^2 E_1^C$) can be measured (i.e. the borders of the object are invisible). As the interference order n corresponding to E^n is unknown, at least three consecutive energy values $E_n^C, E_{n+1}^C, E_{n+2}^C$ are necessary. The value of E_1^C is:

$$E_1^C = (E_{n+2}^C - E_{n+1}^C)/2 - (E_{n+1}^C - E_n^C)/2$$

Based on the energy separation of the constructive interference conditions, it is possible to distinguish qualitatively deep and small objects. In fact, the expected energy separation between interference maxima is much smaller in the first case than in the second one⁶.

Let us now discuss the application of the simulation to mixed amplitude and phase objects. In particular, the aim was to study the surface composed by FeO/Pt and scattered on the Fe₃O₄ surface, and determine the objects height. The topographic contribution to the phase shift, and therefore the object height Δh , could be evaluated in a focus series (and/or an energy series) if the value $\Delta\phi_{amplitude}$ is known. This is not the case for the investigated system. For this reason, it is not possible to conclude whether the FeO/Pt objects at the surface are NPs or holes in the film, with the present data.

However, the complex value of the scattering amplitude $A(E) = e^{-i\phi(E)}$ of the backscattered beam can be theoretically calculated within the dynamical scattering theory, for each material

⁶ For example (i) $\Delta h=16\text{nm}$ ($E_{n+1}^C - E_n^C$) ≈ 0.5 eV at $E_n^C = 20$ eV; (ii) $\Delta h=1\text{nm}$ ($E_{n+1}^C - E_n^C$) ≈ 5 eV at $E_n^C = 20$ eV.

composing the surface; i.e. $\Delta\phi_{amplitude}(E) = \phi_1(E) - \phi_2(E)$. If $\Delta\phi_{amplitude}(E)$ has a weak dependency on the electron energy (i.e. $\Delta\phi_{amplitude}(E) \approx \text{const}$ at least in the energy range used for the energy scan), the same procedure, described above for a phase object can be adopted. Otherwise, one should explicitly include the amplitude phase shift to obtain $\Delta\phi_{step}$ from $\Delta\phi_{out}$.

On the other hand, the value $\Delta\phi_{amplitude}(E)$ can be experimentally determined from a focus series, if the height difference between two objects with different reflectivity is known (“reference sample”). In that case, as $\Delta\phi_{out}$ and $\Delta\phi_{step}$ are known (from the simulation and from the value Δh respectively), $\Delta\phi_{amplitude}$ is also determined:

$$\Delta\phi_{amplitude} = \Delta\phi_{out} - \Delta\phi_{step}.$$

$\Delta\phi_{amplitude}$ (at a given energy) depends only on the sample composition. Therefore, once its value is determined in a “reference sample”, it can be used to investigate the topographic phase shift in samples having the same composition.

The reference sample needs to satisfy some constraints:

- The sample thickness needs to be uniform on a large scale in order to avoid local variation of Δh . This requires the preparation of extremely flat samples (the local variation of Δh should be much smaller than the electron wavelength λ_e)
- Preferentially, the copresence of the two materials under investigation should be acquired. Both surfaces should be flat.
- The exact value of Δh should be known with sub-Å accuracy⁷.

During the last years, many studies have exploited the Quantum Size Contrast in LEEM to determine precisely the total film thickness of very thin films (few monolayers) [25, 155, 157-159], taking advantage of the so-called Quantum Size Effect (QSE). QSE results from the interference between electron waves reflected at the film surface and at the interface between the substrate and the film. The QSE interference modulates periodically the reflected electron intensity, forming intensity peaks, called Quantum Interference Peaks (or QIP), in the LEEM-

⁷ Systems showing layer-by-layer growth are for instance good candidate for this procedure.

IV curves at very low energy. The number of QIPs depends on the number of layers in the film [25, 155, 157-159]. Consequently, the film thickness and the number of layers in the film can be accurately determined by the LEEM-IV measurements at very low energy.

5.4 Conclusions

The developed algorithm uses the CTF Fourier formalism to treat 2D images and gain 3D information on the surface features by focus or energy scans. As developed, the algorithm can be applied to homogenous surfaces or surfaces composed by two materials.

For homogeneous surfaces, the predictions of the algorithm reproduce the contrast features expected from the literature [23, 25, 153] for a single step. In the case of mixed amplitude and phase objects the interference between reflected waves (phase shifts) influences mainly the out-of-focus contrast profiles. The simulation results point out that the value $\Delta\phi_{out}$ can be determined studying the features of the out-of-focus contrast profile experimentally obtained in a focus series. However, the application of this procedure to gain the correct 3D information on the real sample requires the exact determination of the imaginary part of the reflected amplitude.

In the case of the mixed FeO/Pt(111) and Fe₃O₄ system, this value is not known, and this impeded the application of the simulation on the experimental data.

The value $\Delta\phi_{amplitude}$ might be determined either theoretically or experimentally. As discussed, the Quantum Size contrast in LEEM might provide accurate measurements of the film thickness.

The applicability of such methods for the determination the experimental value $\Delta\phi_{amplitude}$ remains an interesting topic for future work.

6. Optical development of an energy filter for LEEM/PEEM application

In this chapter the electron-optical development of an imaging energy filter for a new LEEM/PEEM microscope, called SMART-2, is presented. The SMART-2 is the further development of the SMART (or SMART-1). The expectation for the new microscope is to obtain in AC-PEEM (Aberration Corrected):

- energy resolution $\Delta E < 100$ meV
- Spatial resolution $\Delta x < 1$ nm in the high magnification mode.

The SMART-1 is the first successfully operating aberration corrected LEEM/PEEM microscope, and it was built up within a large collaboration among world-renowned research institutions (namely, Uni. Würzburg, TU Clausthal and TH Darmstadt, the Fritz-Haber-Institut der Max-Planck-Gesellschaft, BESSY and LEO Elektronenmikroskopie GmbH) [2]. The key components of this instrument are:

- An innovative sector field without energy dispersion
- A tetrode mirror for aberration correction
- A magnetic Ω -shaped imaging energy filter
- Dedicated imaging optics

This instrument is a prototype that fulfilled its expectations by reaching unprecedented lateral resolution (2.6 nm in LEEM and 18 nm in X-PEEM) and energy resolution (180 meV) [36]. The difference between lateral resolution in LEEM and X-PEEM has been shown to be due to space charging in X-PEEM. It is foreseen that this gap between the two methods may be overcome or reduced by inserting appropriate beam intensity limiting apertures in the instrument.

The development of the SMART-2 aims at fulfilling mainly two requirements: higher transmission by implementing the tetrode mirror and sector field in a commercial instrument, and by substituting the magnetic Omega-shaped imaging energy filter (or Ω -filter) of the SMART-1 with a fully electrostatic equivalent system. The imaging energy filter aims at

improving the energy resolution below 100 meV. The development of the latter will be treated in this chapter.

Such electrostatic energy filter combines four 80° deflecting elements disposed along an omega shape. Electrostatic energy filters operate at low kinetic energies to improve energy resolution, requiring suitable deceleration and acceleration optics. In this work, the overall imaging properties of this energy filtering system have been characterized and optimized.

The main theoretical challenges in developing an Omega-shaped electrostatic energy filter are:

- The characterization of the aberration coefficients of the combined four deflecting elements
- Adapting the retarding and accelerating optics of the Ω -filter to fit an existing commercial instrument
- Reduction of the imaging aberrations by insertion of appropriate multipole correctors

As the thorough treatment of the topic in all its details is extremely elaborated, I restrict the contribution to this work to the technical description of the filtering system; however, the theoretical calculations, the simulation procedure and the full characterization of the lens system are presented in the appendixes.

The initial design of the new electrostatic Ω -filter was done by Dr. Marchetto and Dr. Rombolá, who finalized the conceptual and theoretical design by calculating all relevant aberration coefficients. The filter has been simulated by direct electron ray tracing with the program Lorentz 3D [160] (Boundary Element Method). The basis of the filter working principle and its aberrations are summarized in paragraph 6.1.

Since an electrostatic energy filter has to be operated at reduced kinetic energy (i.e. pass energy) appropriate **retarding** and **acceleration optics** were designed. The electron kinetic energy within the filter is about 10 times smaller compared to the microscope column. The main challenges in electron deceleration are: to transfer image and diffraction planes in the correct positions at the entrance of the Ω -filter, to avoid to introduce further aberrations, easy operation mode and to be adaptable to the existing commercial microscope optics. Moreover, the acceleration optics has to fulfill similar requirements and to project the energy dispersion

in the plane of the exit slit. In both cases, the optical properties of the lens systems were characterized as a function of voltages and electrode geometries with direct electron ray tracing. These calculations, as well as mechanical and optical constraints are used to setup the decelerating and the accelerating systems, presented in sections 6.2.1 and 6.2.2 respectively. The theoretical expectations were tested by direct electron tracing simulations.

Section 6.3 deals with the reduction of the inherent aberrations calculated for the electrostatic Ω -filter by multipoles. In section 6.4 the final energy and spatial resolution of the system are discussed, followed by the conclusions, presented in section 6.5.

6.1 Electrostatic Ω -filter

Ideally, an imaging energy filter should separate the electrons with different kinetics energy, without affecting the image [161, 162]. Originally, the electron-optical design of the magnetic Ω -filters was developed by Rose, for application to TEM. The SMART-1 Ω -filter represents the first implementation in a LEEM microscope, basing on the work by Krahl and Lanio [161, 162]. This system is the first working imaging filter, correcting up to the second aberration order by hexapoles and operating in UHV [2].

We adopt the same notation used in the work of Rose and Krahl [162, 163]:

- The optical axis is the z direction.
- Each ray is defined by its starting condition, i.e. at the object plane ($z=0$) of the Ω -filter (which is the image plane at the entrance of the filter):
- Positions: γ and δ (along the x and the y axis respectively)
- Angles: α and β (in the xz and yz planes, respectively)
- Energy: $\kappa = \Delta E / E_{\Omega} = (E_K - E_{\Omega}) / E_{\Omega}$ where E_{Ω} is the pass energy of the Ω -filter (in this case $E_{\Omega} = 2$ keV), and E_K the kinetic energy of the electron ray.
- The starting conditions may be expressed in vector notation as:

$$\begin{pmatrix} x \\ y \\ x' \\ y' \\ \Delta E/E_\Omega \end{pmatrix}_{z=0} = \begin{pmatrix} \gamma \\ \delta \\ \alpha \\ \beta \\ \kappa \end{pmatrix}$$

- The position and angle of any electron ray on a generic plane along the optical axes can always be expressed as functions of the starting variables.

$$\begin{pmatrix} x(\alpha, \beta, \gamma, \delta, \kappa) \\ y(\alpha, \beta, \gamma, \delta, \kappa) \\ x'(\alpha, \beta, \gamma, \delta, \kappa) \\ y'(\alpha, \beta, \gamma, \delta, \kappa) \\ \kappa \end{pmatrix}_z$$

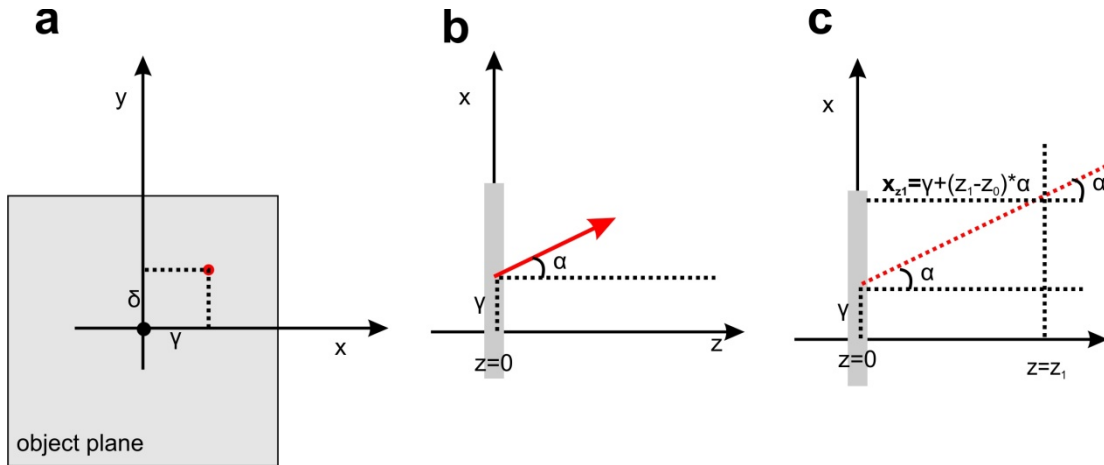


Fig. 6.1: Definition of the ray parameters at the object plane of the Ω -filter (i.e. at the image plane at the entrance). Fig 6.1a) starting position in the xy plane. Fig 6.1b) angle α and position in the xz plane. The definition of the angle β in the yz plane is equivalent. The ray position and direction are functions of the starting parameters, in any other plane along the optical path (Fig 6.1c).

Fig 6.2 shows the electrostatic system developed by Dr. Marchetto and Dr. Rombolá. The system consists of 4 toroidal sectors of 80° operating at the voltage $V = \pm 80$ V (inner and outer electrode respectively). Each sector acts as a thick lens with focal length $f = 99.84$ mm. The distance between the sectors entrance (and/or exit) and the corresponding image/diffraction plane is 18.63 mm. This means that the drift space between two adjacent sectors is 37.26 mm. The system is symmetric with respect to its central plane and to the vertical coordinate.

The position at the final image plane of any electron ray passed through the filter is a function of its starting variables, which is normally approximated by a Taylor expansion. The order of the Taylor expansion defines the “**aberration order**”. The **first order** optical properties and the **second order** aberration coefficients (Table A1.1, Appendix 1) were calculated by direct electron beam tracing, after simulation of the electrode distribution (using Lorentz-E software [160]).

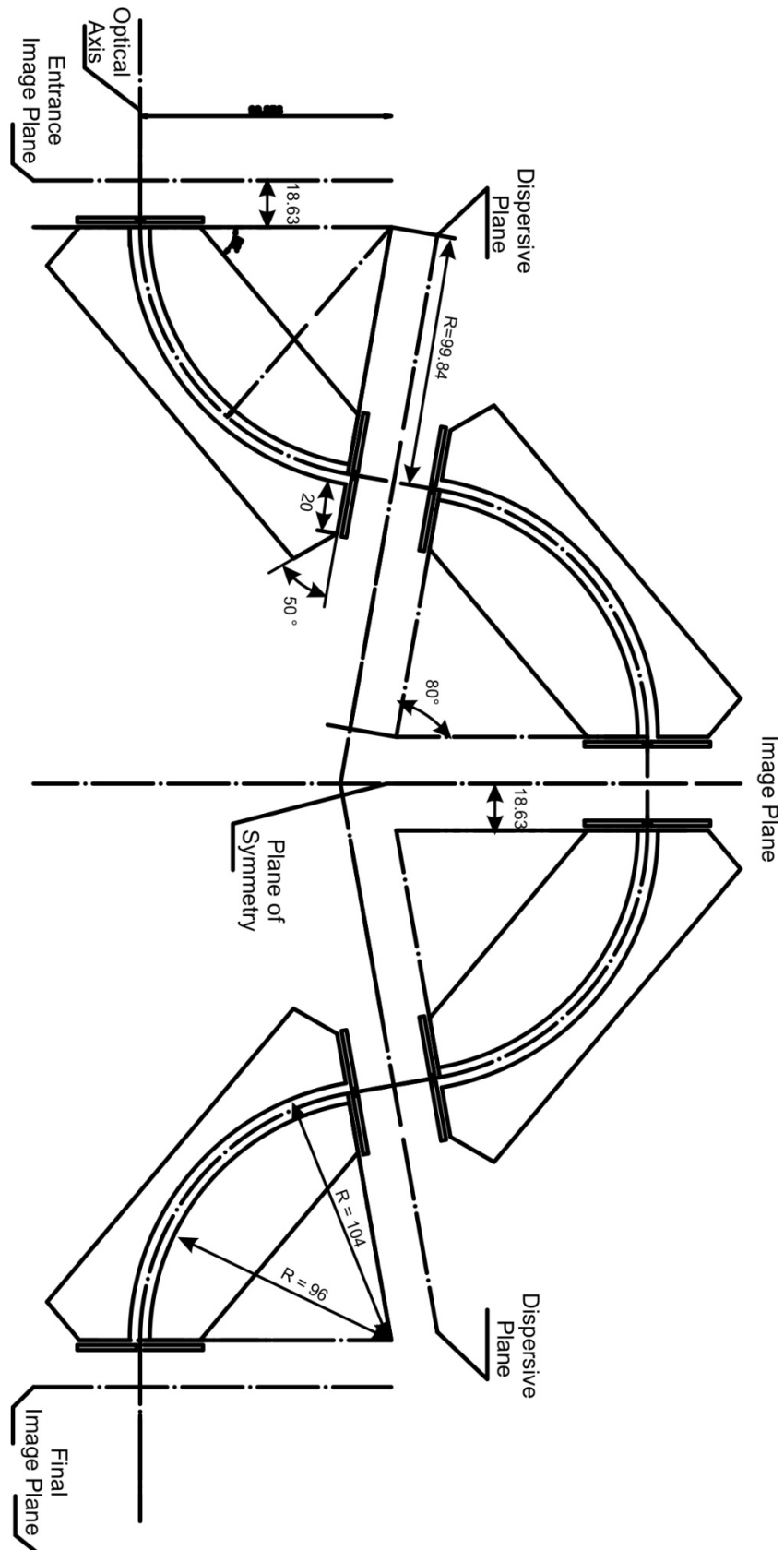


Fig. 6.2: Scheme of the electrostatic omega filter developed by Dr. Marchetto and Dr. Rombolá. Image and dispersive plans (i.e. diffraction planes) are indicated; distances are given in mm

6.1.1 First order optical properties (energy dispersion)

At the first order, the filter is a 1:1 imaging system, which introduces energy dispersion in the angle in the xz plane. At the final image plane of the Ω -filter, this can be expressed as:

$$\begin{pmatrix} x \\ y \\ x' \\ y' \\ E \end{pmatrix}_{z_{exit}} = \begin{pmatrix} \gamma \\ \delta \\ \alpha + C_k \kappa \\ \beta \\ \kappa \end{pmatrix} \quad (6.1)$$

meaning that the exit angle in the xz direction is energy dependent:

$$\alpha_{out} = \alpha_{in} + C_k \Delta E / E_\Omega$$

where ΔE is the deviation from the pass energy E_0 , $E_0=2$ keV and C_k is **angular energy dispersion coefficient**, which is the sum of the dispersion occurring in each sector. Consequently:

$$C_k = \frac{(\alpha_{out} - \alpha_{in})}{\Delta E} = \frac{\Delta \alpha}{\Delta E}$$

The angular dispersion introduced by the filter can be converted in linear energy dispersion by a lens behind the final image plane. In the Back Focal Plane of this lens, the linear dispersion of the beam is:

$$C_{k_{linear}} = \frac{\Delta x_{BF}}{\Delta E}$$

and the electron energies can be filtered mechanically by a slit without affecting the image (see Fig. 6.3). The width of the slit and the **linear dispersion coefficient** determine the energy resolution of the system: $\Delta E = \Delta_{slit} / C_{k_{linear}}$.

For the discussed electrostatic Ω -filter, the Back Focal plane is at infinity. The beam is focused by the **Accelerating System** (or "AS"), whose optical properties define univocally

the relationship between the angular and the linear dispersion coefficients, i.e. the value $\frac{\Delta x_{BF}}{\Delta E} \left(\frac{\Delta \alpha_{out}}{\Delta E} \right)$ (see Appendix 4 and section 6.2.3).

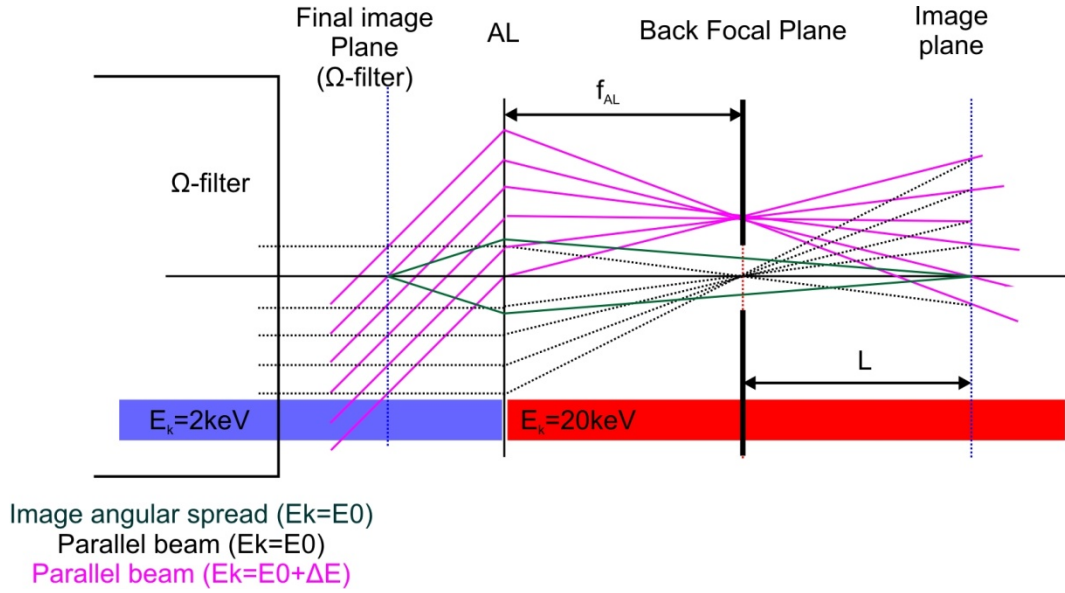


Fig. 6.3: Energy filtering principle at the first diffraction plane after the Ω -filter

6.1.2 Second order optical properties (aberration coefficient)

It can be shown (see [162] and Appendix 1) that many of the **second order aberration coefficients** are zero due to the axial and planar symmetry of the sector arrangement. At the **final image plane** the exit ray positions and angles can be written at the second order as functions of the starting parameters ($\alpha, \beta, \gamma, \delta, \kappa$), in the form:

$$x(\alpha, \beta, \gamma, \delta, \kappa) = \gamma + \frac{1}{2} (A_{\alpha\gamma} \cdot \alpha\gamma + A_{\beta\delta} \cdot \beta\delta + A_{\alpha\kappa} \cdot \alpha\kappa + A_{\gamma\kappa} \cdot \gamma\kappa + A_{\kappa\kappa} \cdot \kappa^2) \quad (6.2a)$$

$$y(\alpha, \beta, \gamma, \delta, \kappa) = \delta + (B_{\alpha\delta} \cdot \alpha\delta + B_{\gamma\beta} \cdot \gamma\beta + B_{\beta\kappa} \cdot \beta\kappa + B_{\delta\kappa} \cdot \delta\kappa) \quad (6.2b)$$

$$\begin{aligned} \frac{dx}{dz} &= x'(\alpha, \beta, \gamma, \delta, \kappa) \\ &= \alpha + C_{\kappa} \cdot \kappa + \frac{1}{2} (C_{\alpha\alpha} \cdot \alpha^2 + C_{\beta\beta} \cdot \beta^2 + C_{\gamma\gamma} \cdot \gamma^2 + C_{\delta\delta} \cdot \delta^2 + C_{\alpha\kappa} \cdot \alpha\kappa \\ &\quad + C_{\gamma\kappa} \cdot \gamma\kappa + C \cdot \kappa^2) \end{aligned} \quad (6.2c)$$

$$\frac{dy}{dz} = y'(\alpha, \beta, \gamma, \delta, \kappa) = \beta + (D_{\alpha\beta} \cdot \alpha\beta + D_{\gamma\delta} \cdot \gamma\delta + D_{\beta\kappa} \cdot \beta\kappa + D_{\delta\kappa} \cdot \delta\kappa) \quad (6.2d)$$

where the coefficient of the type I_{jk} are the second order aberration coefficients of the Ω -filter. As the **final image plane** of the Ω -filter is projected on the detector, the aberrations in \underline{x} and \underline{y}

determine the spatial resolution of the system, while their derivatives \underline{x}' and \underline{y}' (which are positions in the Back Focal Plane of the AS) limit the energy resolution. As defined, the geometric aberrations depend only on the starting position and angle, while all the coefficients which depend on the energy (variable κ) are chromatic aberrations.

The strategy followed in this work to improve the spatial and energy resolution of the system is based on the implementation of multipole correctors, as done by Lanio and Krah1 for the magnetic Ω -filter for TEM and as implemented in the SMART-1 [161, 164]. Despite the many similarities, however, there are strong differences between the optical properties of magnetic and the electrostatic Ω -filter:

- In the electrostatic filter, the **passing energy of the electrons** is reduced to $E_\Omega=2$ keV. The adaptive optics system has a crucial role for both aberration correction and for energy resolution. The magnetic filter does not require pre-optics deceleration because the electrons are passing through the filter at full energy (typically, $E_\Omega=15$ keV).
- In the magnetic system, the geometrical aberrations are the leading terms because the electrons have high kinetic energy (corresponding to small values of $\kappa = \Delta E/E_\Omega$). In the electrostatic system, the chromatic aberrations are predominant (high values of $\kappa = \Delta E/E_\Omega$).
- Each sector of the magnetic Ω -filter has two different focal points for the x and for the y coordinate. Differently, the electrostatic sectors have symmetric focusing in both directions. This is a crucial point for the practical treatment of the aberration correction, as the hexapole field acts mainly on rays far from the optical axes. The consequence is that, while in the first case the aberration correction in the γ and δ variables can be corrected independently, in the second case, this is not possible.

For all these reasons, the principles for aberration correction developed for the magnetic system by Rose and Krah1 [162] and Lanio [161], cannot be simply extended to the new electrostatic system under development.

6.2 Adaptive optics

The adaptive optical system consists of two distinct lens systems: the first one is a **retarding system** (RS), connecting the transfer optics to the Ω -filter, and the second one is an

accelerating system (AS), connecting the Ω -filter to the projector system. Both systems are composed by electrostatic lenses.

These systems aim for:

- Slow down the incoming electron beam from the nominal starting energy (typically $E_0=20$ keV in the microscope) to the passing energy of the Ω -filter (typically $E_\Omega=2$ keV).
- Accelerate the outgoing electron beam from the passing energy of the Ω -filter to the final energy in the projector (typically $E_0=20$ keV).
- Transfer the image and diffraction planes from fixed entrance to fixed exit conditions.

6.2.1 Introduction and definitions

An **electrostatic lens** consists of two (or more) parallel electrodes with central holes, set at voltages V_1 and V_2 respectively. The common axis is called the **optical axis**.

A charged particle (e.g. an electron) entering the electric field between the electrodes travels in a superposition of an inhomogeneous and homogeneous field (see Fig 6.4).

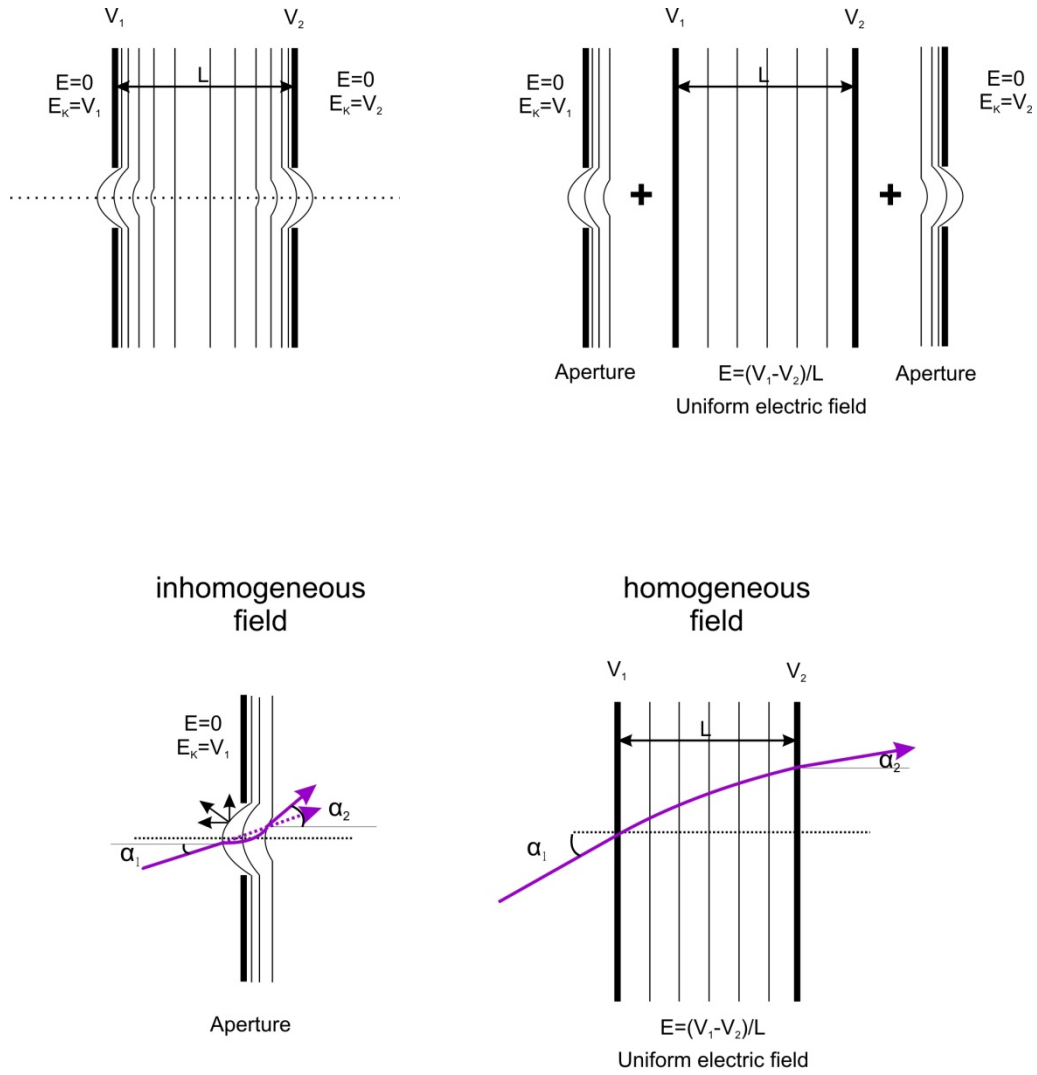


Fig. 6.4: Basic description of an electrostatic lens; E indicates the electric field acting on the electrons passing through that area. E_k indicates the electron kinetic energy.

The ray trajectory through the lens can be conveniently described by introducing the Principal Planes (or PPs) of the lens, analogously to light optics. The principal planes are defined as the hypothetical planes at which the whole deflection is assumed to occur.

The action of the electrostatic lens on an electron ray, referred to the PPs, can be described by the “**transfer matrix**” of the lens, similarly to light optics. The detailed treatment of the electron optics principles can be found in [162, 165, 166] and in Appendix 2. In Appendix 2 all the transfer matrices are given for the lens systems discussed in this text.

The following notation will be adopted for all the lens systems discussed in the next sections (see Fig 6.5):

Optical system:

- PP_1 and PP_2 are the positions of the two Principal Planes, referred to the geometric center of the lens
- $\Delta PP = PP_2 - PP_1$ is the distance between the two principal planes of the lens. For a thin lens $\Delta PP \approx 0$; ΔPP can be both positive or negative for a thick lens. For the retarding system $\Delta PP < 0$; while $\Delta PP > 0$ for the accelerating system
- a is the distance between the object plane (or first image plane) and the first Principal Plane (PP_1)
- b is the distance between the second Principal Plane (PP_2) and the final image plane of the lens system
- c is the distance between the second Principal Plane (PP_2) and the first Principal Plane (PP_1) of two subsequent lenses
- L is the distance between the back focal plane and the image plane
- f is the focal length of the lens; in the case of an immersion lens, two directions will be specified
- LS_{tot} is the total length of the system. For the decelerating system it is calculated from the first image plane to the entrance of the Omega filter ($LS_{tot}=a+b+c+ \Delta PP +18.63$ mm). Similarly, for the accelerating system, LS_{tot} is calculated from the exit of the omega filter to the final image plane (before the projector) ($LS_{tot}=a+b + \Delta PP +18.63$ mm)
- M_α and M_L are the angular and lateral magnifications

Lens geometry

- s is the distance between the electrodes constituting the lens; if the lens is asymmetric s_1 is the distance between the first and the second electrodes and s_2 is the distance between the second and the third electrodes.
- D is the diameter of the electrode aperture; if the lens is asymmetric D_1, D_2 and D_3 are the diameters of the first, the second and the third electrodes, respectively.

-
- The figure consists of two main parts. The top part is a ray diagram of an optical system. It shows an object plane on the left, followed by two lenses, L1 and L2, separated by a distance L . The geometric center of the system is marked. The principal planes of the first lens are labeled PP_1 and PP_2 , with a distance ΔPP between them. The focal length of the second lens is f . The distance from the object plane to the first lens is a , and the distance from the second lens to the image plane is b . A back focal plane is indicated. The bottom part shows the lens geometry. The first lens is orange and the second is green. They have a diameter $D = 10$ mm, separation $s = 5$ mm, and thickness $t = 1$ mm. A reference coordinate system is shown with the optical axis at $z=0$. The lenses are labeled V_1 and V_2 .

- 3) the required angular magnification is $M_\alpha = -1/1.4$ ⁸
- 4) the diffraction plane, which is in the first lens of the adaptive optics has to be focused to infinity (i.e. it is a parallel beam)
- 5) Mechanical constraints set the minimum distance between FFL and the first electrode of the lens system to 30 mm = $(a - PP_1 - s - 3/2 \cdot t)$; once the lens geometry is fixed (giving PP_1 , s and t), this conditions sets the minimum value for a ;
- 6) The image plane position should be in the field free zone after the lens system lens;
- 7) The lens should not exceed 20 cm of length (LS_{tot}).

These conditions can be satisfied by the combination of a **retarding immersion lens** ("RL") and an **Einzel lens** ("L1"), as shown in Fig. 6.6. The explicit transfer matrices describing the system can be found in Appendix 2.

The image plane position b after Einzel lens, the angular and lateral magnifications (M_α and

M) are functions of the construction parameters f_{RL} , $\sqrt{E_0/E_\Omega} f_{\text{L1}}$ and the starting position a :

$$\text{a) } b = (a \cdot f_{\text{L1}} + \sqrt{E_0/E_\Omega} (-a + f_{\text{RL}}) \cdot f_1) \cdot a^{-1}$$

$$\text{b) } M_\alpha = a \cdot f_{\text{L1}}^{-1}; M_L = M_\alpha^{-1} \cdot \sqrt{E_0/E_\Omega}$$

⁸ this result is a compromise between energy dispersion (i.e. energy resolution) and second order chromatic aberration (lateral resolution) introduced in the filter;

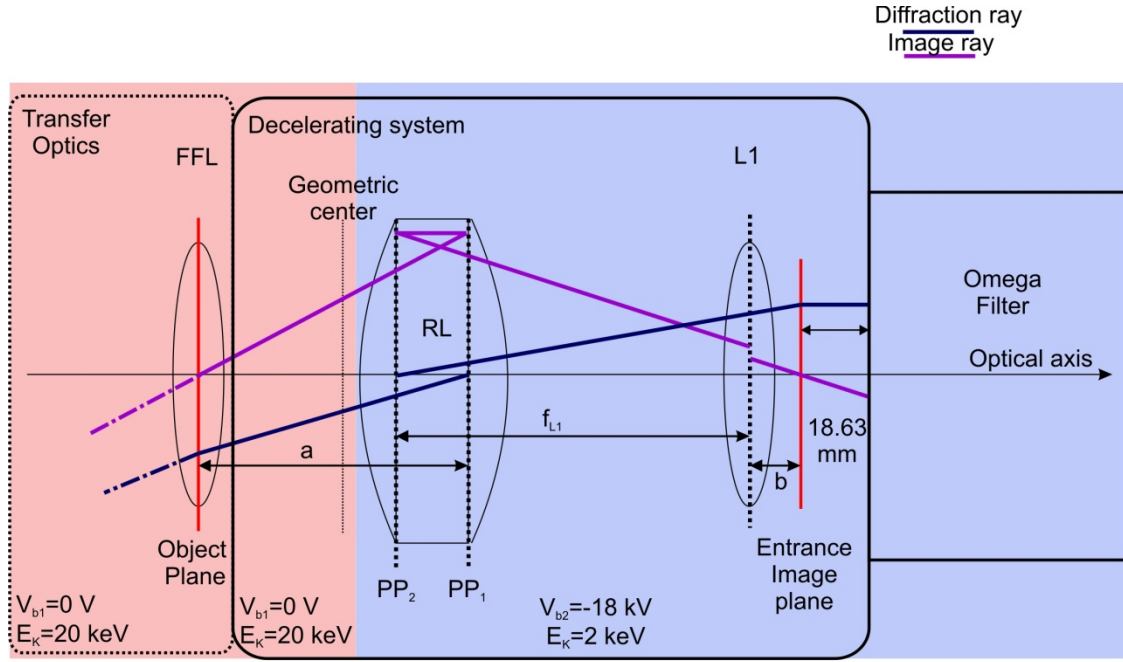


Fig. 6.6 Scheme of the Retarding System, composed by an immersion and an Einzel lens, which fulfill the entrance conditions for the electrostatic Ω -filter.

Based on the relations above, the constraints 1-6 can be rewritten:

- i. condition 1) fixes the entrance and exit potential of the immersion lens $V_{b1}=0$ kV and $V_{b2}=-18$ kV
- ii. condition 3) sets the ratio between f_{L1} and a : $f_{L1}/a=1.4$
- iii. condition 4) sets the distance between the PP_{2RL} and L1: $c=f_{L1}$; the condition on the lateral magnification in condition 2) becomes: $M_L=f_{L1}/a \sqrt{E_0/E_\Omega} = -4.3$.
- iv. conditions 5-6-7) sets mechanical constraints to the lens design. The field free zone can be considered ≈ 15 mm after L1 (see Appendix 3). Therefore the requirement is $b(a, f_{L1}) > 15$ mm; the lens length (LS_{tot}) can be expressed as function of the system parameter a and f_{RL} : $LS_{tot} = a - \Delta_{PP} + f_{L1}$.

Appendix 3 presents the optical properties (i.e. focal lengths and PP positions) of an **Einzel** and an **immersion lens** depending on the voltages of the central electrode, and the influence of geometrical parameters (such as internal aperture diameter, electrode distance and thickness) calculated by direct electron ray tracing.

The results of the analysis in Appendix 3 can be summarized as:

- The **Einzel lens** is a thin and symmetric lens; the focal length range $f_{L1} > 10$ mm.
- The **Immersion lens** is a thick and asymmetric lens (the geometrical and optical centre does not coincide). The focal length range is limited and depends on the specific field distribution, i.e. the lens geometry.

For this reason, it is crucial to find the designs of RL which can be implemented in the retarding system, fulfilling constraints 1-6. The optimization of the immersion lens geometry is discussed in Appendix 3.

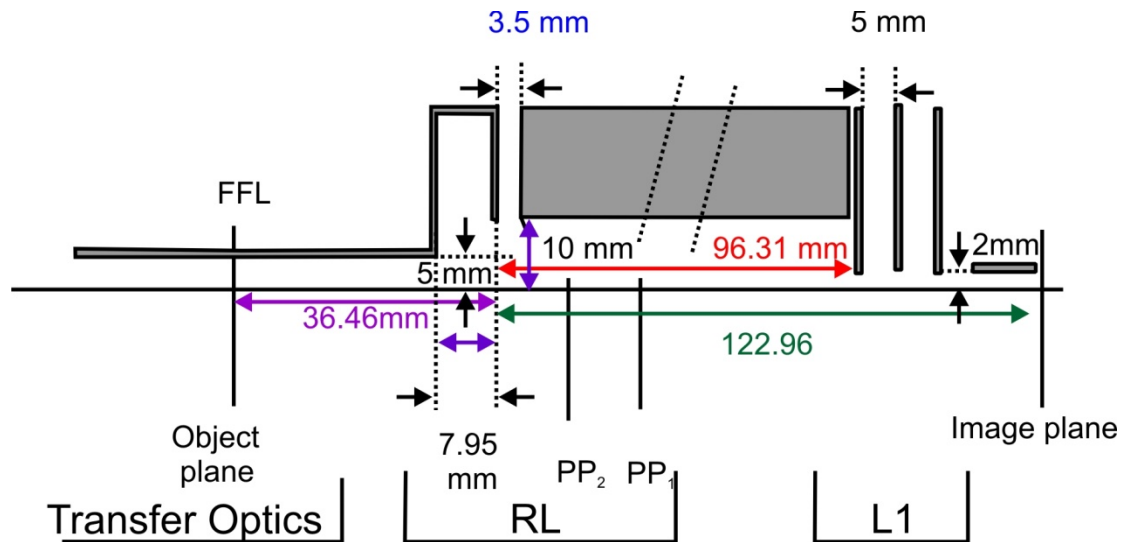


Fig. 6.7: Electrode distribution realizing the Retarding System as simulated, after the optimization of the system geometry.

Once the geometry of the RS that fulfills the constraints i-iv (shown in Fig 6.7) was determined, the expectations were tested by electron ray tracing. The trajectories of the electron beam through the “complete” lens system were simulated. The results are shown in Fig 6.8.

The green lines are the trajectories of two rays starting on the optical axis at the centre of FFL (First Field Lens), which is the object plane for the RS and the last intermediate image plane of the previous optics. The initial kinetic energy is $E_k = 20$ keV. Each intersection of these rays

with the optical axis defines an image plane for the microscope. The image plane of RS should be 18.63 mm in front of the Ω -filter entrance.

The purple lines are the trajectories of electrons, which cross the optical axis at the diffraction plane of the system. Each intersection of these rays with the optical axis defines a diffraction plane for the microscope. As we can see, the two rays are parallel at the exit of the system. The lateral magnification of the system M_L is given by the ratio between the image size x_2 and the object size x_1 (see Fig. 6.8).

The values for M_L , M_α and the image plane position obtained from the simulation agree with the values previously calculated. The final electron energy is $E_k=2$ keV. The length of the system, from the center of FFL to the aperture of the Ω -filter is ≈ 180 mm.

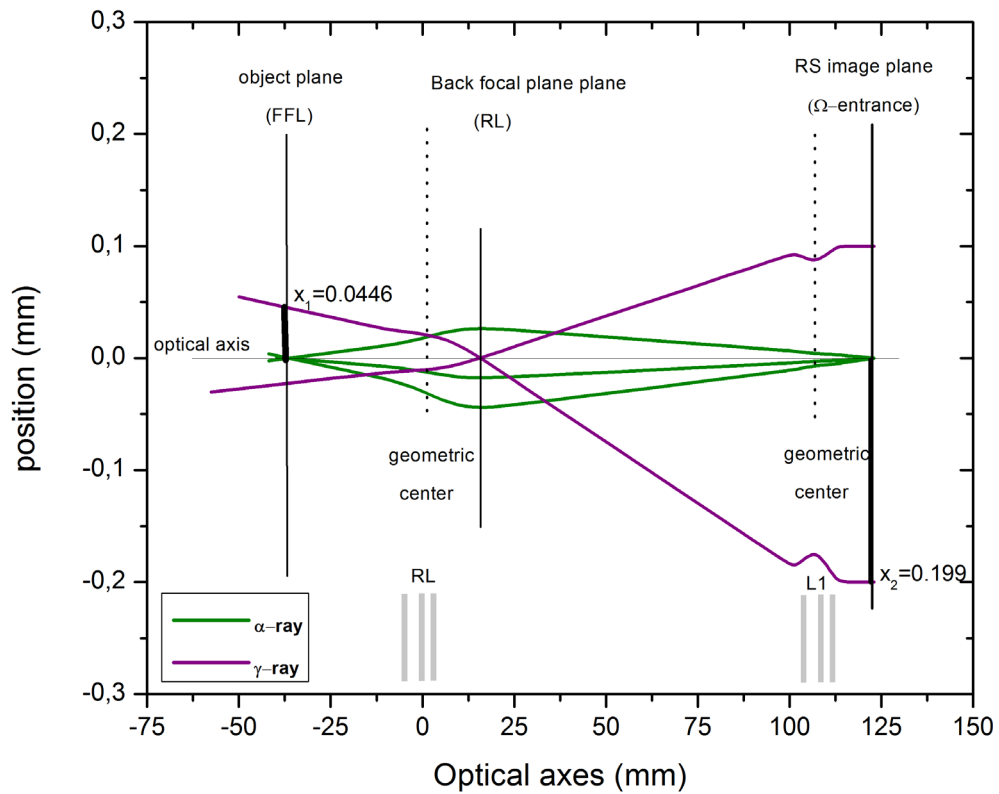


Fig. 6.8: Simulated electron trajectories along the optical path in the Retarding System. The α -rays indicate the image rays, while γ -rays represent the diffraction beam. The starting kinetic energy is $E_k=20$ keV; the final $E_k=2$ keV.

6.2.3 Accelerating System

The **accelerating system** (AS) accelerates the electrons from $E_\Omega = 2$ keV, at the exit of the Ω -filter, to $E_0 = 20$ keV. At the exit, the electron energy is filtered by a slit inserted in the dispersive plane, which here is the Back Focal plane of the AS system. The subsequent image plane is transferred to the 2D detector by the projection system. Both, the energy selection plane and the intermediate image plane have to be located in the field free zone after AS.

The maximum electron energy spread at the intermediate image plane after the energy selection plane follows the relationship (see equations in Appendix 4):

$$\Delta E_{max} = \frac{\Delta_{slit} \sqrt{E_2/E_1}}{C_k \cdot f_{AS}} = \frac{\Delta_{slit}}{M_\alpha \cdot C_k \cdot L} \quad (6.3)$$

Where f_{AS} is the focal length of the AS, M_α its angular magnification and L is the distance between image and back focal plane, C_k is the angular dispersion of the Ω -filter. (see Fig 6.3 and Fig A4.1).

From Eq. 6.3 we see that the energy resolution is influenced mainly by the slit size and the focal length of the system.

In the final image plane after the Ω -filter (i.e. the object plane for the AS), the **maximum angle** for the beam with the correct energy E_Ω is: $\Delta\alpha_{image} = 0.15$ mrad, as defined by the Elmitec transfer lens system. This beam has to pass fully through the exit slit. In term of energy, the value $\Delta\alpha_{image} = 0.15$ mrad corresponds to $\Delta E = 0.075$ eV ⁹

For this reason, the desired energy resolution is limited to the range:

$$\Delta E > 0.075 \text{ eV}.$$

⁹ ($\Delta E = \Delta\alpha_{image} / C_k = 0.15 \text{ mrad} / 2 \text{ mrad/eV}$)

The simplest accelerating system (AS) is composed by one immersion lens (AL). The energy resolution $\Delta E > 0.075 \text{ eV}$ is obtained by an optimized combination of the slit size and the focal length of AL, i.e. Δ_{slit} and f_{AL} .

Fig 6.9 shows the expected energy resolution in the back focal plane of AL for different possible slit sizes, as function of the lens focal length (in this case $f_{\text{AS}} = f_{\text{AL}}$): assuming that the energy slit width is $3 \mu\text{m}$, than $f_{\text{AL}} = 62 \text{ mm}$.

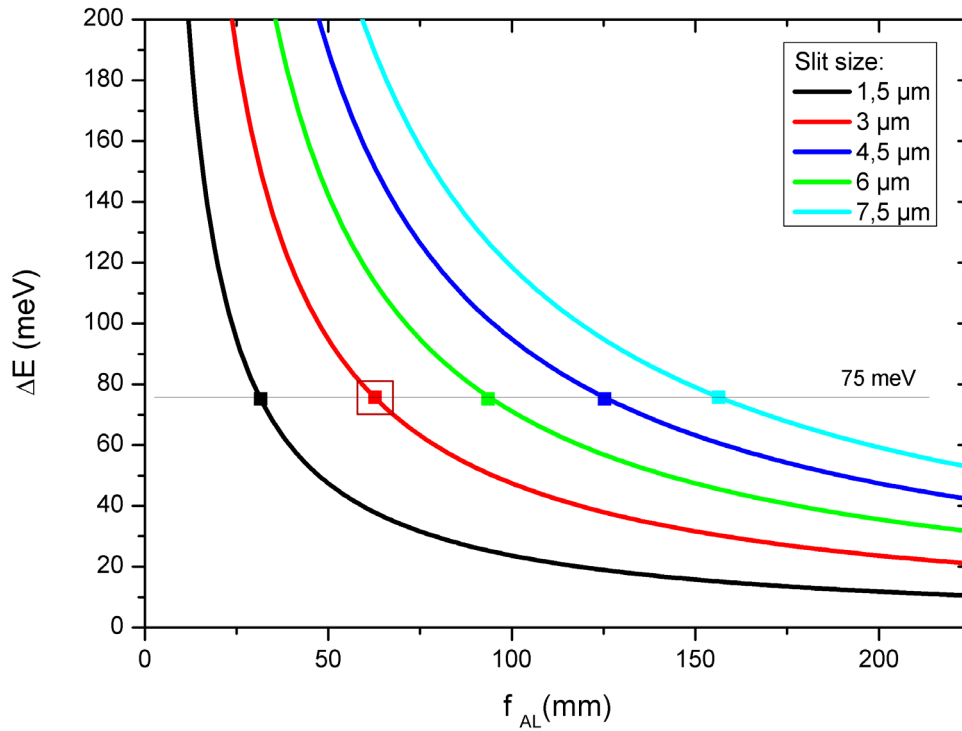


Fig. 6.9: Energy resolution dependency on the focal length of the AS; the angular dispersion of the filter is $C_k=2 \text{ mrad/eV}$. In the case of a 1-lens system (Acceleration lens AL) $f=f_{\text{AL}}$. Slit sizes are indicated. In the next discussion I have assumed $\Delta_{\text{slit}} = 3 \mu\text{m}$

The electrodes distribution and voltages (see Appendix 5) was optimized to obtain $f_{\text{AL}}=61.84 \text{ mm}$; this focal length combined with a slit width $\Delta_{\text{slit}}=3 \mu\text{m}$ corresponds theoretically to $\Delta E=0.077 \text{ eV}$. The value of f_{AL} is set by the energy resolution; all the properties of the optical system (such as the magnification M_L and the image plane position b) are unequivocally determined by the distance a . The total length of the system should be minimized: $LS_{\text{tot}} = a + \Delta PP + b(a, f)$.

M_L and b have been directly evaluated for different starting positions a by electron ray tracing. The results obtained are summarized in Fig 6.10; the detailed description of the simulation procedure can be found in Appendix 5.

The linear relation between angles in the object plane (i.e. energy) and positions (in the back focal plane) is verified (Fig 6.10b); moreover the electron position in the back focal plane is independent on the starting position a . The linear dispersion coefficient is $C_k^{\text{Linear}} = 39.1 \mu\text{m/eV}$. This value is slightly higher than the linear dispersion coefficient ($C_k^{\text{Linear}} = 35 \mu\text{m/eV}$) for the magnetic Ω -filter implemented in the SMART-1 microscope, operating at the passing energy $E_\Omega = 15 \text{ keV}$. For $\Delta_{\text{slit}} = 3 \mu\text{m}$ only angles which are smaller than $\Delta\alpha = \pm 0.078 \text{ mrad}$ at the achromatic image plane after the Ω -filter can pass through the slit opening. This value correspond to $\Delta E = 75 \text{ meV}$.

As already said, short lenses are desirable: this is the case for $a = 55 \text{ mm}$ (Fig 1.10c) with a final image lateral magnification is $M_L = 0.56$ (Fig 6.10a).

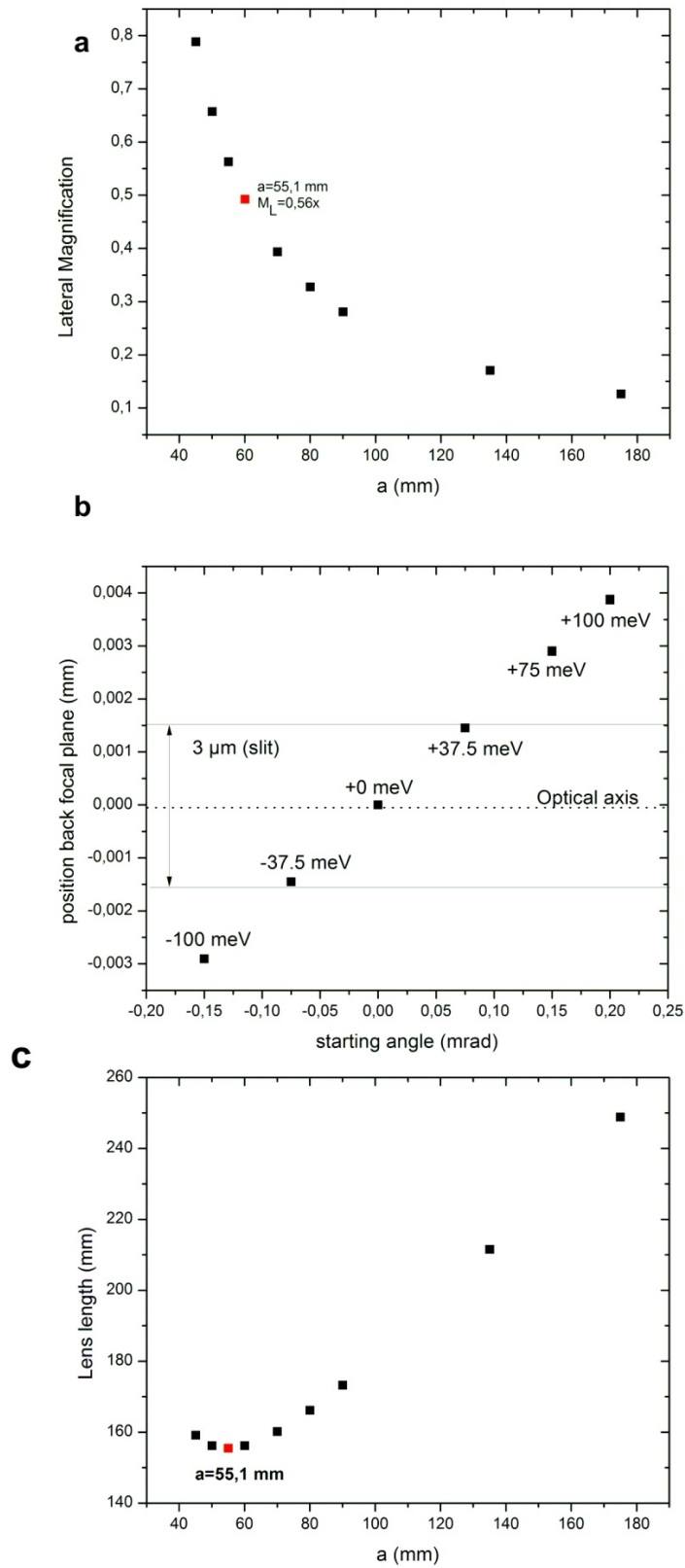


Fig. 6.10: Characterization of the accelerating system as function of the starting conditions by means of direct electron rays tracing. Fig 6.10a) M_L as function of the starting position; Fig 6.10b) Position in the back-focal plane (and corresponding energy resolution) as function of starting angle; c) Lens length as function of the starting position

Fig 6.11 reports the electron trajectory through the system with $a = 55$ mm. Purple lines represents the diffraction rays (parallel incoming beam), while the green curves are image rays, starting on the optical axis at the image plane after the Ω -filter. As already stated before, their crossing with the optical axes defines the diffraction plane position and the image plane position, respectively. Also in this case, the values for M_L , M_α , image plane position and diffraction plane position obtained by the simulation agree with the calculated values.

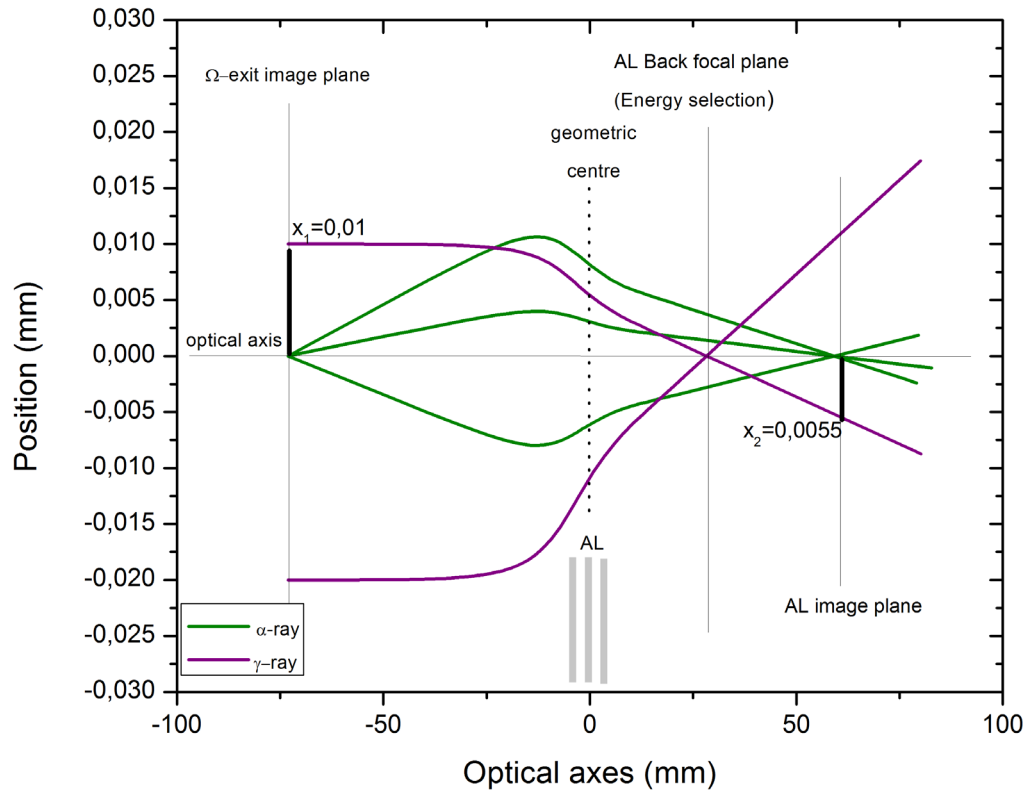


Fig. 6.11: Simulation of electron trajectories along the optical path of the AS. The α rays indicate the image beam, while γ -rays represent the diffraction beam. The starting kinetic energy is $E_k=2$ keV; the final $E_k=20$ keV. The starting value of $a=55.1$ mm; $M_L=0.56$

The final lens design is shown in Fig 6.12.

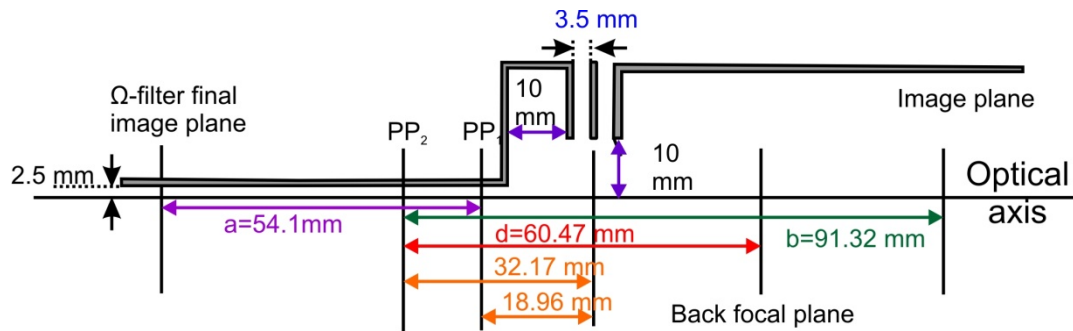


Fig. 6.12: Scheme of the simulated accelerating system. The final image plane of the Ω -filter, PP positions, back focal plane and final image plane are indicated.

6.2.4 Projective Optics

The AS system connects the Ω -filter with the projective optics, which is designed to finally project an highly magnified image of the sample on the detector. The magnification range introduced by the projector system fixes the total magnification range accessible to the microscope, which is $M_{\text{tot}} [5 \cdot 10^2; 1 \cdot 10^5]$. The optimization of the projector system to the desired total magnification range is discussed in detail in Appendix 6.

It can be shown (Appendix 6) that the distance between the image plane after AL and the first lens of the projector influence the magnification range of the projector system. The evaluation in Appendix 6 shows that the Elmitec projector system fits the requirements, if the distance between the AL image plane and the detector first lens is 5.3 mm.

6.3 Hexapole Correction

Optical elements of multipole fields of order n , generate n th-order effects (desired) and $n+1$ (and higher) order aberrations, which are undesired. Aberrations of order $n+1$ (i.e. introduced by multipoles of order n) can be corrected by multipole fields of order $n+1$ [162-165].

Hexapole fields have second and higher order effects, whereas quadrupole fields have first order properties (focusing). Hexapoles can therefore be used to correct second order image

aberrations without changing the first order properties of the system. Hexapole correction (magnetic) was already successfully implemented in the SMART-1 Ω -filter [1, 2, 161].

However, the differences between the magnetic and the electrostatic system (see section 6.1), requires a full investigation of aberration correction in the electrostatic case. The hexapole arrangement within the filtering system was studied from first principles, by combining "a-priori" theoretical treatment with the simulation.

The next sections are organized as follows:

- In 6.3.1, the equations describing the hexapole deflection are introduced.
- In 6.3.2, the validity of the theoretical equations given in 1.3.1 was tested by direct electron ray tracing. The simulated hexapole geometry was designed to fit in the Ω -filter, and the deflections coefficients and the system dimensionality were evaluated.
- Section 6.3.3 presents the procedure used to predict the optical effects of an hexapole field located in the drift space between the Ω -filter sectors. The explicit analytic expression of the hexapole deflection, as function of the starting condition of the incoming electron beam, is discussed, as well as the symmetries of the system.
- In section 6.4, I discuss the optimization of the hexapole correction within the Ω -filter, based on the considerations made in 6.3.2 and the explicit deflection coefficients calculated following the procedure in 6.3.3. The expected energy and lateral resolution for the corrected system are given.

As shown in 6.3.2, not all the aberration coefficients can be corrected. However, under opportune conditions the system resolution can be considerably improved.

6.3.1 Hexapole deflection

An electrostatic hexapole consists of the symmetric rearrangement of six electrodes around the optical axis. The potentials applied to the electrodes are $+V$ and $-V$ alternately. The potential distribution of the hexapole field [167] can be expressed in Cartesian coordinates (see Fig 6.13 for the coordinates definition) as:

$$\varphi(x, y) = \frac{V}{a_0^3} (x^3 - 3xy^2) = k(x^3 - 3xy^2)$$

Where a_0 is the inner radius of the hexapole and V is the voltage applied.

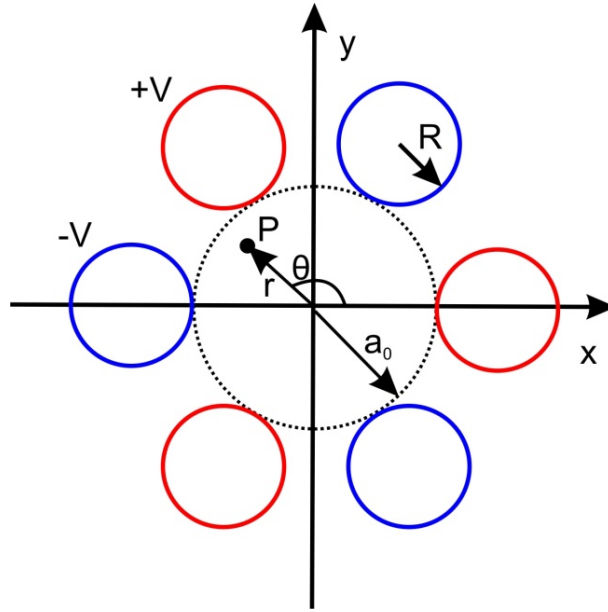


Fig. 6.13: Scheme of an ideal hexapole, aligned along the optical axes z (out of the page). a_0 is the internal radius, R is the electrodes radius. Ideally $R=0.5a_0$

The electron trajectories deflections, namely Δx , Δy , $\Delta \alpha$ and $\Delta \beta$, have been calculated up to the third order in [167] by integration of particle motion equation. The transfer matrix for an hexapole are given as function of: (i) the effective axial extent of the hexapole field t , the ratio between its kinetic energy E_K and the hexapole voltage V and the particle coordinate $(x_0, y_0, \alpha_0, \beta_0)$ at the entrance plane of the hexapole. However, the expressions given in [167] are considerably simpler if referred to the hexapole mid-plane coordinates (see Appendix 7 and Fig. 6.14 for the coordinate definition). The second order solutions for the particle trajectory due to the hexapole deflection can be written as (eq. 6.4a-d):

$$\Delta x^m = + A (x^m \alpha_0 - y^m \beta_0) \quad (6.4a)$$

$$\Delta y^m = - A (y^m \alpha_0 + x^m \beta_0) \quad (6.4b)$$

$$\Delta \alpha = B ((x^m)^2 - (y^m)^2) - \frac{A}{2} (\alpha_0^2 - \beta_0^2) \quad (6.4c)$$

$$\Delta \beta = -2B(x^m y^m) + A \alpha_0 \beta_0 \quad (6.4d)$$

Where (see Fig 6.14):

- x^m, y^m are the coordinates of the unperturbed ray considered at multipole mid-plane
- α, β are the incoming ray directions component in the xz and yz planes respectively
- $\Delta x^m, \Delta y^m$ are the deviation from x^m, y^m , if the outgoing deflected trajectory is back-projected to the mid-plane of the hexapole
- $A = +K \frac{t^3}{6}$ and $B = -Kt$
- $K = \frac{3}{2} \frac{V}{a_0^3 \cdot E_k}$ is the "hexapole strength"

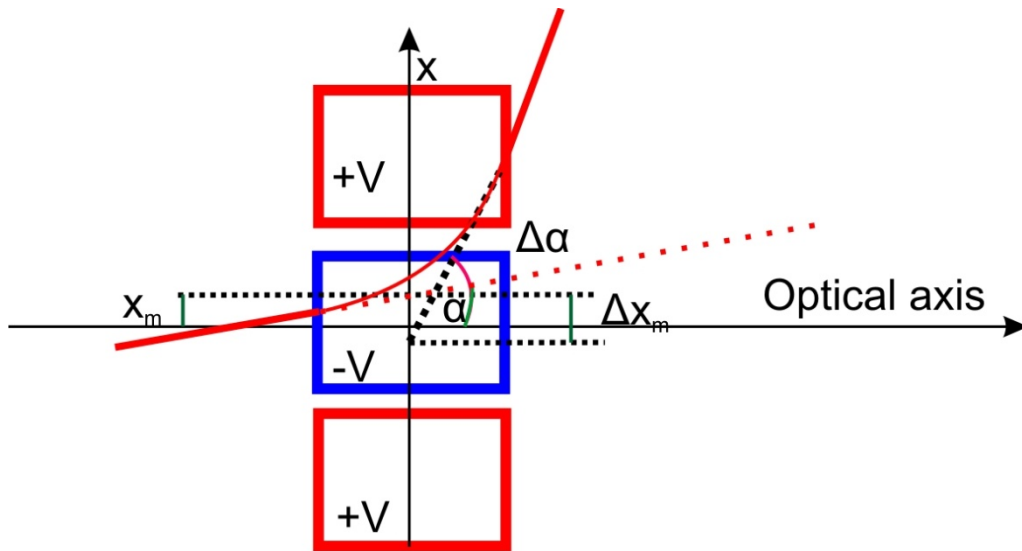


Fig. 6.14: Definition of the hexapole mid-plane coordinates $x^m, y^m, \alpha, \beta, \Delta x^m, \Delta y^m, \Delta \alpha$ and $\Delta \beta$

The above relations can be obtained from those given in [167] by translating the origin of the coordinate system at the center of the multipole.

6.3.2 Simulation of hexapole field and deflection.

The range of validity of the above equations was tested by direct electron beam tracing. The direct evaluation of the electron ray deflections was implemented using Lorentz-E (see Appendix 3 and Appendix 7 for the computational details). Several hexapole geometries have been considered, varying:

- Internal diameter a_0

- electrode length
- electrode diameter R
- The electrodes voltages considered are: 25V and 50V, 100V, 500V. V=0V was used to calculate the unperturbed trajectories.

In order to verify all the theoretical relationship between the coefficients, I have tested all possible combinations of two non-zero ray starting variables (i.e. α_0 - x_0 , α_0 - y_0 , α_0 - β_0 , x_0 - y_0 , x_0 - β_0 , y_0 - β_0) and proceeded as follow:

1. The ray deflections ($\Delta\alpha$, $\Delta\beta$, $\Delta\gamma$, $\Delta\delta$) from their unperturbed trajectory were measured in a plane after the multipole
2. the deflection ($\Delta\alpha$, $\Delta\beta$, $\Delta\gamma$, $\Delta\delta$) were projected onto the hexapole mid-plane, obtaining ($\Delta\alpha^m$, $\Delta\beta^m$, $\Delta\gamma^m$, $\Delta\delta^m$)
3. The coefficients were obtained by multiple polynomial fits in the plot for the "projected" deflections ($\Delta\alpha^m$, $\Delta\beta^m$, $\Delta\gamma^m$, $\Delta\delta^m$) vs. (α_0 , β_0 , x^m , y^m)

In this way, the relationships between the deflection coefficients, given in the previous paragraph, were numerically verified, and the dependence of the coefficients A and B on the hexapole geometry and voltage evaluated. The parameters K and t were obtained using the

relationships $K = \sqrt{-\frac{B^3}{6A}}$ and $t = \sqrt{\frac{6A}{B}}$ (given $A = +K\frac{t^3}{6}$ and $B = -Kt$)

Summarizing the results given in Appendix 7, the theoretical scaling law for the hexapole strength $K = \frac{3}{2} \frac{1}{a_0^3} \frac{V}{E_K}$ is verified if the internal radius a_0 of hexapole is bigger than 3 times the diameter of the incoming beam and if the applied voltage $V < 500V$ (at the kinetic energy of 2 keV). The deviation from the scaling law are attributed to the predominance of higher order effects.

For all the geometries evaluated (i.e. fitting the drift space between the sectors, and for reasonable values of the starting conditions ($x^m \approx 1$ mm; $\alpha_0 \approx$ mrad), the relative angular deflection $\Delta\alpha^m/\alpha^m$ is almost four order of magnitude bigger than the relative spatial deflection $\Delta x^m/x^m$ (due to the coefficients B and A, respectively). This fact is extremely important when choosing the correction strategy to implement in the Ω -filter, as discussed in section 6.4.3.

6.3.3 Hexapole Deflection in the Ω -filter

A ray passing through a hexapole field undergoes second order deflections, which depend on its coordinate in the hexapole mid-plane. On the other hand, the ray coordinates in any plane along the optical axis of the Ω -filter are functions of the starting conditions ($\gamma, \delta, \alpha, \beta, \kappa$) at the entrance plane of the filter. Consequently, the ray coordinates in the hexapole mid-plane are functions of the hexapole location along the axis of the Ω -filter and the entrance conditions.

The aim is to find the analytical expression at the Ω -filter final image plane of the second order deflections introduced by a hexapole, centered at the plane P along the Ω -optical axis, in terms of the starting variables ($\gamma, \delta, \alpha, \beta, \kappa$). To do so, one needs to map the entrance plane into the plane P, which is in the drift space between the four deflection sectors (see Fig 6.15). As each sector acts as a dispersive lens on the incoming electron beam, there are linear relationships between the coordinates in each image (or diffraction) plane, as indicated in Fig 6.15. In the following, the image and diffraction planes are named after the notation in Fig 6.1.5.

Moreover:

- L is the distance between the hexapole position P (in the drift space between the sectors) and the closest image or diffraction plane. The value L is defined as positive if the multipole shifted behind the relative image or diffraction plane along the electron optical path, and negative if shifted in front of it. $L=0$ if the hexapole is un-shifted (Fig 6.16).
- The multipole voltage distribution can have two orientations, leading to two opposite deflections. In the following $K = \frac{3}{2} \frac{1}{a_0^3} \frac{V}{E_K}$ is defined as positive if the deflection Δx^m has the same sign of x^m ; K is negative in the opposite case (Fig 6.16a).

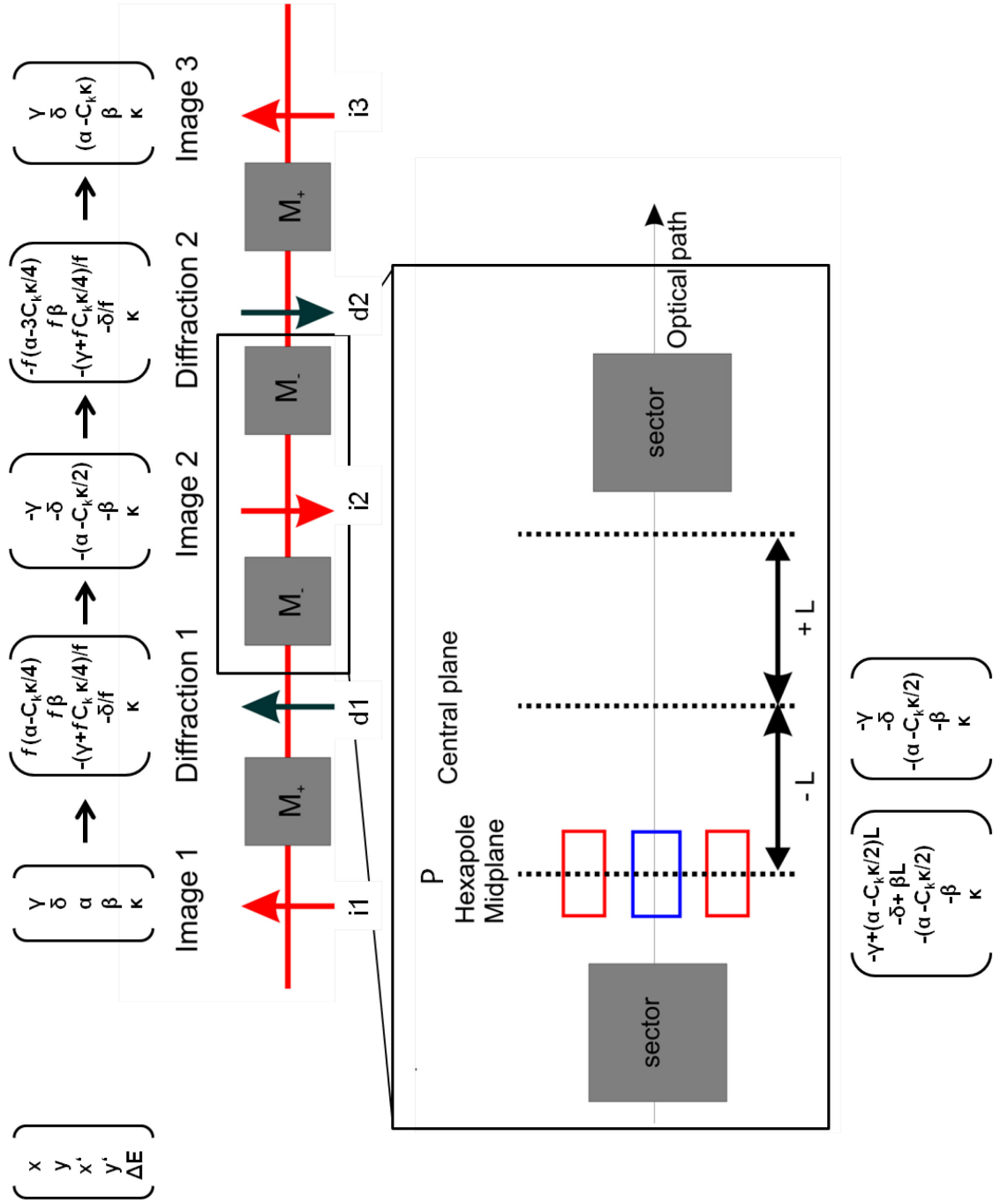


Fig. 6.15 Notation adopted in the following text. The image and diffraction planes along the Ω -filter are named as in the figure. The coordinate transformations occurring in each deflecting sector are indicated. The sign of L (i.e. the distance from the hexapole mid-plane to the central plane) is defined as in the image.

The analytic expression for the second order deflections was evaluated for a multipole centered in the **three image planes**, in the **two diffraction planes** and shifted $\pm L$ in the five possible drift spaces. Moreover, also the symmetric and antisymmetric combinations of hexapoles shifted with respect to the central plane were considered (see Fig 6.167b-c).

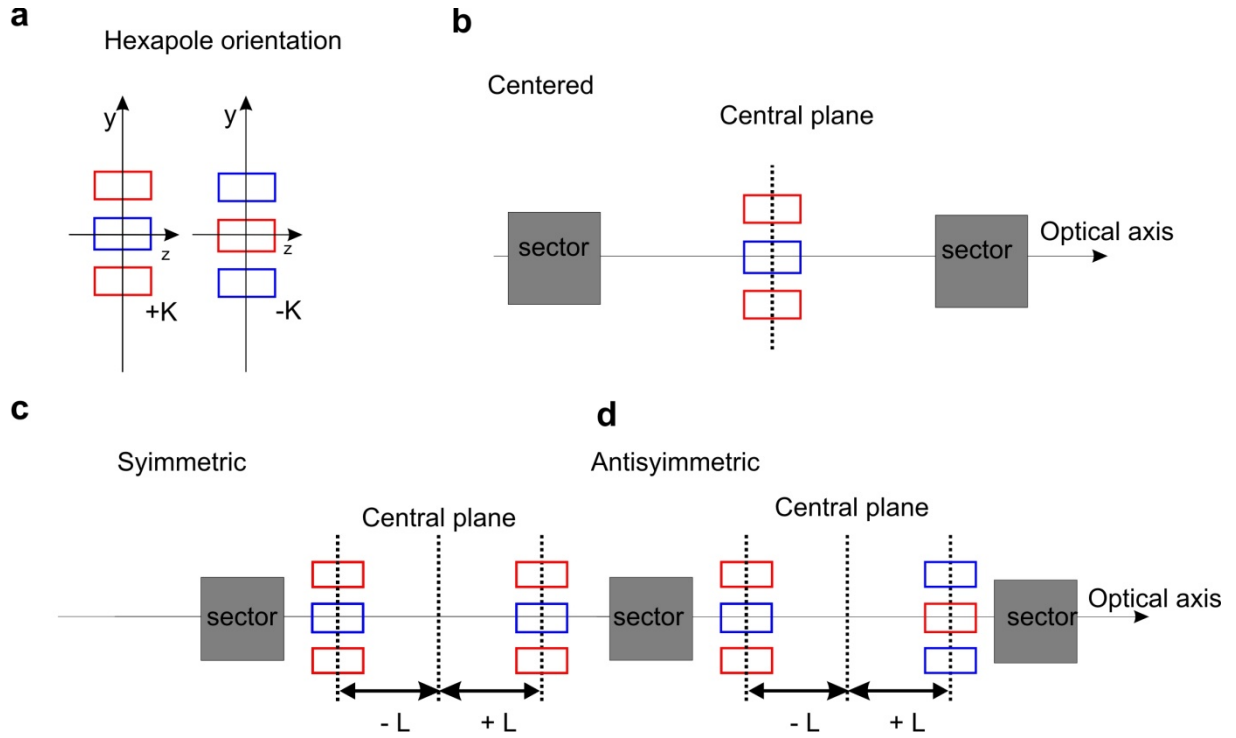


Fig. 6.16: Definition of Hexapole orientation (a); Combinations of hexapoles investigated in the present work.

The explicit deflection coefficients were calculated applying the transfer matrices formalism. The matrices for the drift space between sectors, the sectors, and for the hexapoles are given in Appendix 2.

1. The starting ray variables are described by the ray vector V_{in} . Its projection at the final Ω -image plane is V_{out} . The hexapole is centered in the plane P.
2. the ray vector V_P in the plane P is found by applying the transfer matrices (for the sectors and the drift space between the sectors) to the initial ray vector V_{in}
3. the hexapole deflection ΔV_P is found by applying the transfer matrices on the ray vector V_P

4. The vector $V_P^H = V_P + \Delta V_P$ is projected at the final image plane by applying the transfer matrices for the sectors and the drift space. The projected vector is V_{out}^H . The deflection introduced by the hexapole in the plane P, is $H^P = V_{out} - V_{out}^H$

The list of the deflection coefficients is given in Appendix 7.

6.3.4 Symmetries of the system

Projected at the final image plane, the effect of the hexapole centered at the plane "P" is described by the vector:

$$H^P = \begin{pmatrix} H_x^P \\ H_y^P \\ H_{x'}^P \\ H_{y'}^P \\ 0 \end{pmatrix}$$

Where the components H_x^P and H_y^P are positions, and $H_{x'}^P$ and $H_{y'}^P$ are angles. All four components are function of the variables $(\gamma, \delta, \alpha, \beta, \kappa, L, K)$.

At this point, the notation is further simplified. In the following, the index P denotes the drift space, where the hexapole is located. The convention adopted for the P index is: $i1, i2, i3$ are the drift spaces containing the first, second or third image plane of the Ω -filter (see Fig 6.15), respectively. The index $d1$ and $d2$ are the drift spaces containing the first or the second diffraction plane of the Ω -filter. The distance L, giving the hexapole mid-plane position in the drift space, is always explicitly given¹⁰. If the hexapole is centered at the image/diffraction plane, $L=0$ and its deflection is indicated as H_0^P .

The deflection of the hexapole in the drift space P, shifted by +L, can be always rewritten as:

$$H^P(\gamma, \delta, \alpha, \beta, \kappa, L, K) = H_0^P + L^2 \cdot H_S^P + L \cdot H_{AS}^P \quad (6.5)$$

where H_0^P is the action of an hexapole in the center of the drift space (H_0 is independent on L); $L^2 \cdot H_S^P$ is the symmetric term and depends only on the absolute value of the shift L; $L \cdot H_{AS}^P$ is

¹⁰ Following this notation the term $H^{i2}(\gamma, \delta, \alpha, \beta, \kappa, -L, K)$ denotes an hexapole shifted by L behind the second image plane of the Ω -filter (i.e. between the second and third sector, as shown in image 1.15)

the antisymmetric term and depends on the sign of L (+L or -L if the hexapole is located in front of or behind the central plane, respectively).

Due to the relationship above, the combination of two multipoles shifted symmetrically about the central plane ($L_1=-L_2$) yields in (see Fig 6.16c-d):

- The symmetric contribution: $H^P(+L, +K) + H^P(-L, +K) = 2(H_0^P + L^2 \cdot H_S^P)$

$$(K_1=K_2)$$

- The antisymmetric contribution: $H^P(+L, +K) + H^P(-L, -K) = 2 L \cdot H_{AS}^P$

$$(K_1=-K_2)$$

The Ω -filter has multiple symmetries, relating the coordinates in each internal plane, which apply also to the hexapole deflection.

To point out the symmetries between the deflection coefficients, it is convenient to separate H^P into the geometric and chromatic contributions: H_g^P , depending only on the starting conditions $(\alpha, \beta, \gamma, \delta)$, and $H_c^P(\alpha, \beta, \gamma, \delta, \kappa)$, respectively.

$$H^P(\gamma, \delta, \alpha, \beta, \kappa, L, K) = H_g^P(\gamma, \delta, \alpha, \beta, L, K) + H_c^P(\gamma, \delta, \alpha, \beta, \kappa, L, K)$$

H_g^P and H_c^P can be also separated in un-shifted (H_0^P), symmetric (H_S^P) and antisymmetric (H_{AS}^P) contributions.

For the geometric terms, we have:

$$H_g^{i1}(\gamma, \delta, \alpha, \beta, L, K) = H_g^{i2}(\gamma, \delta, \alpha, \beta, L, -K) = H_g^{i3}(\gamma, \delta, \alpha, \beta, L, K) \quad (6.6a)$$

$$H_g^{d1}(\gamma, \delta, \alpha, \beta, L, K) = H_g^{d2}(\gamma, \delta, \alpha, \beta, L, -K) \quad (6.6b)$$

Due to the coordinate inversion between the sectors, there are exchange symmetries between the components (angles and positions) between diffraction and image planes, as shown in the example below¹¹:

¹¹ The relationships are consequences of the inversion between position and angular coordinates, occurring in the sectors

$$\begin{pmatrix} H_g^{i1}(\gamma, \delta, \alpha, \beta, L, K) \\ H_g^{i1}(\gamma, \delta, \alpha, \beta, L, K) \\ H_g^{i1}(\gamma, \delta, \alpha, \beta, L, K) \\ H_g^{i1}(\gamma, \delta, \alpha, \beta, L, K) \\ 0 \end{pmatrix} = \begin{pmatrix} f \cdot H_g^{d1}(\gamma/f, -\delta/f, \alpha \cdot f, \beta \cdot f, L, K) \\ f \cdot H_g^{d1}(\gamma/f, -\delta/f, \alpha \cdot f, \beta \cdot f, L, K) \\ 1/f \cdot H_g^{d1}(\gamma/f, -\delta/f, \alpha \cdot f, \beta \cdot f, L, K) \\ 1/f \cdot H_g^{d1}(\gamma/f, -\delta/f, \alpha \cdot f, \beta \cdot f, L, K) \\ 0 \end{pmatrix} \quad (6.7)$$

Where f is the sectors focal length.

Relationships similar to (6) and (7) do not apply to the chromatic contributions H_c^P . In fact, the chromatic term results from the dispersion introduced by each sector in the filter. In the image planes there is only angular dispersion (in xz plane), while both angular and linear dispersion are present in the diffraction plane. The angular dispersion introduced in each sector adds up, while lateral dispersion cancels out finally. Consequently:

$$H_c^{i3}(\gamma, \delta, \alpha, \beta, \kappa, L, K) \neq 2 \cdot H_c^{i2}(\gamma, \delta, \alpha, \beta, \kappa, -L, -K)$$

$$H_c^{d1}(\gamma, \delta, \alpha, \beta, \kappa, L, K) \neq 2 \cdot H_c^{d2}(\gamma, \delta, \alpha, \beta, \kappa, -L, -K)^{12}$$

$H_c^{i1} = 0$ because there is no dispersion at the first image plane (in front of the filter).

In Table 6.1 and Table 6.2 the expressions of second order Ω -filter aberrations ($\Delta\Omega$) are compared to the deflections coefficients of: (i) a hexapole centered at the second image plane (H_0^{i2}), (ii) an antisymmetric combination of hexapoles in the first diffraction plane ($L \cdot H_{AS}^{d1}$) and (iii) a hexapole centered at the first diffraction plane (H_0^{d1}). The chromatic and geometric contributions are separated, because the symmetries discussed above apply only to the geometric contributions. The coefficients are projected at the Ω -final image plane. Table 6.1 collects the terms affecting the lateral resolution (i.e. the positions in the final image plane); Table 6.2 those affecting the energy resolution (i.e. the angles in the final image plane). The explicit value of Ω -filter aberration coefficient can be positive or negative (see explicit values listed in Table A1.1 and Table A2.2).

By direct comparison between the expressions in Table 6.1 and Table 6.2, we notice that the geometrical filter aberrations ($\Delta\Omega_g$) have the same type of dependency on the entrance

¹² $H_c^{i3}(\gamma, \delta, \alpha, \beta, \kappa, L, K) = 2 \cdot H_c^{i2}(\gamma, \delta, \alpha, \beta, \kappa, -L, -K) + \Delta H_c^{i3}(\gamma, \delta, \alpha, \beta, \kappa, L, K)$ and $H_c^{d2}(\gamma, \delta, \alpha, \beta, \kappa, L, K) = 2 \cdot H_c^{d1}(\gamma, \delta, \alpha, \beta, \kappa, -L, -K) + \Delta H_c^{d2}(\gamma, \delta, \alpha, \beta, \kappa, L, K)$. Moreover $\Delta H_c^{i3} \approx 0$

conditions $(\alpha, \beta, \gamma, \delta, \kappa)$ as the deflections introduced by: the hexapole centered in the second image plane (H_{0g}^{2i}) and the antisymmetric combination of the two shifted multipoles in the diffraction plane (LH_{ASg}^{d1}). The coefficient H_{0g}^{1d} is affected by the inversion between angles and positions (eq. 6.7). As consequence, the hexapole centered in the diffraction plane (ΔH_{0g}^{d1}) introduces second order contributions which: (i) do not compensate the aberration coefficients and (ii) degrade further the system performances. The same is true for the antisymmetric combination of the two shifted multipoles in the image plane (LH_{ASg}^{i2}) (see Appendix 7).

Lateral resolution (positions)

	$\Delta\Omega$	H_0^{i2}	$ L \cdot H_{AS}^{d1}$	H_0^{d1}
				$A/2f \cdot (\gamma^2 - \delta^2)$
Δx_g	$\textcolor{red}{A}_{\alpha\gamma} \cdot \alpha\gamma + A_{\beta\delta} \cdot \beta\delta$	$-A \cdot (\alpha\gamma - \beta\delta)$	$+2BfL \cdot (\alpha\gamma - \beta\delta)$	
				$-Bf^3(\alpha^2 - \beta^2)$
	$+ \textcolor{red}{A}_{\gamma\kappa} \cdot \gamma\kappa$	$+2A \cdot C_k^* \cdot \gamma\kappa$	$-2BfL \cdot C_k^* \cdot \gamma\kappa$	$+A \cdot C_k^* \cdot \gamma\kappa$
Δx_c	$+A_{\alpha\kappa} \cdot \alpha\kappa$		$+2Bf^2LC_k^* \cdot \alpha\kappa$	$+2BC_k^*f^3 \cdot \alpha\kappa$
	$+A_{\kappa\kappa} \cdot \kappa^2$		$-2Bf^2LC_k^{*2} \cdot \kappa^2$	$+(A/2 - Bf^3)C_k^{*2} \cdot \kappa^2$
				$-A/f \cdot \gamma\delta$
Δy_g	$B_{\alpha\delta} \cdot \alpha\delta + B_{\gamma\beta} \cdot \gamma\beta$	$+A(\alpha\delta + \gamma\beta)$	$-2BfL(\alpha\delta + \gamma\beta)$	
				$+2Bf^3 \cdot \alpha\beta$
	$B_{\beta\kappa} \cdot \beta\kappa$		$-2Bf^2LC_k^* \cdot \beta\kappa$	$-2Bf^3C_k^* \cdot \beta\kappa$
Δy_c	$+ \textcolor{red}{B}_{\delta\kappa} \cdot \delta\kappa$	$-2AC_k^* \cdot \delta\kappa$	$+2BfLC_k^* \cdot \delta\kappa$	$-AC_k^* \cdot \delta\kappa$

Table 6.1: Second order Ω -filter aberration coefficients for the position coordinate (first column) are compared to the second order deflection of: a hexapole centered at the second image plane (second column); an antisymmetric combination of hexapole in the first diffraction plane (third column) and a hexapole centered at the first diffraction plane (fourth column). Chromatic and geometric contributions are separated. The leading aberration coefficients are indicated in red (see discussion in section 6.4 for details); the Ω -filter aberration coefficients can have both positive and negative sign (see Table A1.1).

Energy resolution (angles)

	$\Delta\Omega$	H_0^{i2}	$ L \cdot H_{AS}^{d1}$	H_0^{d1}
$\Delta x'_g$	$C_{\gamma\gamma} \cdot \gamma^2 + C_{\delta\delta} \delta^2$	$-B \cdot (\gamma^2 - \delta^2)$	$+L(3A/2f^3 - BL^2/f^3)(\gamma^2 - \delta^2)$	$-A/f \cdot (\alpha\gamma - \beta\delta)$
	$C_{\alpha\alpha} \cdot \alpha^2 + C_{\beta\beta} \beta^2$	$+A/2 \cdot (\alpha^2 - \beta^2)$	$-B f L \cdot (\alpha^2 - \beta^2)$	
	$+C_{\gamma\kappa} \cdot \gamma\kappa$		$-L(2BL^2/f^2 - 3A/f^2) \cdot C_k^* \cdot \gamma\kappa$	$+A/f \cdot C_k^* \cdot \gamma\kappa$
$\Delta x'_c$	$C_{\alpha\kappa} \cdot \alpha\kappa$	$-2 A \cdot C_k^* \cdot \alpha\kappa$	$+2BfL \cdot C_k^* \cdot \alpha\kappa$	$-AC_k^* \cdot \alpha\kappa$
			$-L(B(f^2 + L^2)/f - 3A/2f) \cdot C_k^{*2} \cdot \kappa^2$	
	$+C_{\kappa\kappa} \cdot \kappa^2$	$+2 A \cdot C_k^{*2} \cdot \kappa^2$		$+A \cdot C_k^{*2} \cdot \kappa^2$
$\Delta y'_g$	$-D_{\gamma\delta} \cdot \gamma\delta$	$+2B \cdot \gamma\delta$	$(2B \cdot L^3/f^3 - 3AL/f^3) \cdot \gamma\delta$	$A/f(\alpha\delta + \gamma\beta)$
	$D_{\alpha\beta} \cdot \alpha\beta$	$-A \cdot \alpha\beta$	$+2 B f L \cdot \alpha\beta$	
	$D \cdot \beta\kappa$	$+2 A C_k^* \cdot \beta\kappa$	$-2 B f L \cdot C_k^* \beta\kappa$	$+A C_k^* \beta\kappa$
$\Delta y'_c$	$+D_{\delta\kappa} \cdot \delta\kappa$		$(B \cdot L^3/f^2 - 3AL/2f^2) C_k^* \delta\kappa$	$-A/f C_k^* \cdot \delta\kappa$

Table 6.2: Second order Ω -filter aberration coefficients for the angular coordinate (first column) are compared to the second order deflection of: a hexapole centered at the second image plane (second column); an antisymmetric combination of hexapole in the first diffraction plane (third column) and a hexapole centered at the first diffraction plane (fourth column). Chromatic and geometric contributions are separated. The leading aberration coefficients are indicated in red (see discussion in section 6.4 for details); the Ω -filter aberration coefficients can have both positive and negative sign (see Table A2.2).

It follows that second order geometrical Ω -aberrations can be appropriately corrected only by means of (i) one single hexapoles located in the image planes, (ii) the symmetric combination of shifted multipoles in the image plane, (iii) the antisymmetric combination of shifted multipoles in the diffraction planes.

As already anticipated at the beginning of this section, not all the chromatic coefficients can be corrected, either because the hexapole deflection does not introduce the correction terms (H_{0g}^{2i}) or because the sign of the Ω -aberration coefficients is not the same as the hexapole corrections.

6.4 Strategies for aberration correction

The overall system resolution (energetic and lateral) is given by the magnitude of the deviations Δx , Δy , $\Delta x'$ and $\Delta y'$. These values depend not only on the aberration coefficient, but also on the ranges that the starting conditions ($\alpha, \beta, \gamma, \delta, \kappa$) assume.

The worst resolution (i.e. the biggest deviation) occurs for extreme values of the starting parameters. In the following evaluation, I have considered rays for which all parameters assume the maximum value allowed, corresponding to the worst possible situation: the minimum energy (ΔE_{\max}) and spatial resolutions (Δx_{\max}).

The lateral and energy resolutions were calculated using the following formulas:

$$\Delta x = \sqrt{\sum_{ij} \left(A_{ij} + \sum_n H_{x'ij}^n \right) \cdot (i_{\max} \cdot j_{\max})^2}$$

$$\Delta y = \sqrt{\sum_{ij} \left(B_{ij} + \sum_n H_{y'ij}^n \right) \cdot (i_{\max} \cdot j_{\max})^2}$$

$$\Delta E = C_k^{-1} \sqrt{\sum_{ij} \left(C_{ij} + \sum_n H_{x'ij}^n \right) \cdot (i_{\max} \cdot j_{\max})^2}$$

Where, the indexes i and j vary among of entrance variable ($\alpha, \beta, \gamma, \delta, \kappa$), i_{\max} , j_{\max} are the maximum values that the starting variables can assume, the term in parenthesis are the second order coefficients, resulting from the filter aberrations and sum of the hexapole contributions. For the lateral resolution, only Δx will be discussed in this section, as $\Delta x > \Delta y$.

6.4.1 Entrance conditions

The ranges of (γ, δ) at the entrance of the Ω -filter depend on the desired FoV and the magnification of the transfer optics:

$$(\gamma, \delta) = \pm \frac{FoV}{2} \cdot M_{transf} \cdot M_{RL} \quad (6.8)$$

the maximum value is +/- 1mm, which corresponds to the mechanical size of the opening at the entrance of the Ω -filter. However, this value can be reduced, depending on the settings of the transfer optics. Under operating conditions of an electron lens system, only 30% of the maximum beam size should be used to avoid extreme aberration effects.

The angles (α, β) are determined by the angular acceptance of the contrast aperture (CA) and the transfer optics:

$$(\alpha, \beta) = \pm CA_{\alpha} \cdot 1/M_{transf} \cdot \sqrt{E_{\Omega}/E_0} \cdot 1/M_{RL} \quad (6.9)$$

Where CA_{α} is the angular acceptance of the contrast aperture, E_{Ω} is the passing energy of the filter (2keV) and E_0 is the electron kinetic energy in the optical column (20 keV). The values considered for the contrast aperture size are: $CA_{\alpha}=11$ mrad, $CA_{\alpha}=7$ mrad, $CA_{\alpha}=4$ mrad. Whereas the 11 mrad aperture is optimized for aberration correction at $E_k=100$ eV (at the sample), the smaller aperture can be used at lower energies. The value $CA_{\alpha}=11$ mrad corresponds to an aperture size of $CA=100 \mu m$ in the Elmitec system.

$\kappa = \pm 0.25$ eV, and corresponds to the energy spread of the electron beam.

6.4.2 Energy Resolution

The explicit determination of the aberration coefficients (see Appendix 1) shows that the aberrations effecting angle $\Delta x'$ in the xz plane are completely dominated by the $C_{\gamma\gamma}$ coefficient. The deflection $\Delta x'$ causes a blurring (x direction) in the Back Focal Plane of the energy filter, affecting the energy resolution of the system. As the coefficient $C_{\gamma\gamma}$ is 10^2 times bigger than $C_{\delta\delta}$, the extent of the blurring depends almost entirely on the initial γ -range (starting x-position).

In the final image plane (PEEM image), the effect of the aberration $\Delta x' \propto C_{\gamma\gamma} \cdot \gamma^2$ is to introduce a parabolic energy gradient from the center to the outer part of the image in the x direction. At the center of the image ($\gamma=0$), the energy is limited only by the angular spread of the beam, $\Delta\alpha$, set by the angular acceptance of the CA _{α} (see eq. 6.9) and by the energy slit. The electron energy is $E_k = E_0 + \Delta E_{min}$, with $\Delta E_{min} = C_k^{-1} \cdot \Delta\alpha$, where C_k is the angular dispersion coefficient of the filter. At the border of the image (x direction) the electrons have $E_k = E_0 + \Delta E_{min} + \Delta E_{abb}$, where $\Delta E_{abb} \approx C_{\gamma\gamma} \cdot \gamma^2 / C_k \approx 250\text{meV}$ for $\gamma = \pm 1 \text{ mm}$.

As $C_{\gamma\gamma} \gg C_{\delta\delta}$, the full correction of $C_{\delta\delta}$ does not practically improve the energy resolution. Moreover, as the hexapole correction is symmetric in the x-y direction¹³, i.e. the full correction of the $C_{\gamma\gamma}$ coefficient introduces an uncompensated factor $\Delta x' \approx -C_{\gamma\gamma} \cdot \delta^2$. Consequently, the energy gradient in the final image turns by 90° (y direction). Alternatively $C_{\gamma\gamma}$ can be reduced to half of its value $C_{\gamma\gamma}/2$ (i.e. introducing the same dependence $C_{\gamma\gamma}/2$ in δ), improving the energy resolution by $1/\sqrt{2}$ ¹⁴. The energy gradient in the PEEM image becomes symmetric in the xy direction.

The simplest correction strategy consists in limiting the γ/δ range at the entrance of the filter. This can be done by choosing opportunely the lateral magnification of transfer optics (and that of the one projector system). Moreover, the coefficient $C_{\gamma\gamma}$ is reduced to half value by a hexapole centered at one of the image planes (in the following the hexapole is located at the first image plane).

Fig 1.17 shows the expected energy resolution for such a system (straight lines), as function of the FoV, in X-PEEM, or the AoI (Area of Interest) in selected area in XPS, depending on three different CA sizes. The “theoretical” resolution limit ΔE_{min} for different CA size is also given (“sharpest point” in Fig. 6.17). Deviations from this value are caused by effects of second order aberrations. The magnification of the transfer optics (indicated in the image) is

¹³ $H_x^p \propto (\gamma^2 - \delta^2)$, Table 1.3.

¹⁴ the energy resolution for the uncorrected system is $\Delta E \approx C_k^{-1} \cdot \sqrt{(C_{\gamma\gamma} \gamma^2)^2}$ while inserting a $C_{\gamma\gamma}/2$ correction

$$\text{yields } \Delta E \approx C_k^{-1} \cdot \sqrt{\left(C_{\gamma\gamma}/2 \gamma^2\right)^2 + \left(C_{\gamma\gamma}/2 \delta^2\right)^2}$$

set to limit the γ/δ range to $\gamma/\delta = \pm 0.7$ mm in the entrance plane of the Ω -filter. In selected area XPS the energy resolution from integrated signal over the AoI, is given by the values in Fig. 6.17. In X-PEEM mode, the same values correspond to the energy resolution at the border of the image.

While at the lowest magnification, second order effects becomes negligible and the energy resolution is completely determined by the contrast aperture size (i.e. slit size limited), the energy resolution is affected by aberrations at higher magnifications.

However, the energy resolution is $\Delta E < 100$ meV over a wide range of FoVs (FoV $< 9\mu\text{m}$), depending on the CA aperture size. For bigger FoV, the resolution limit is anyway higher than 100 meV, due to the angular spread of the image (i.e. the size of the contrast aperture).

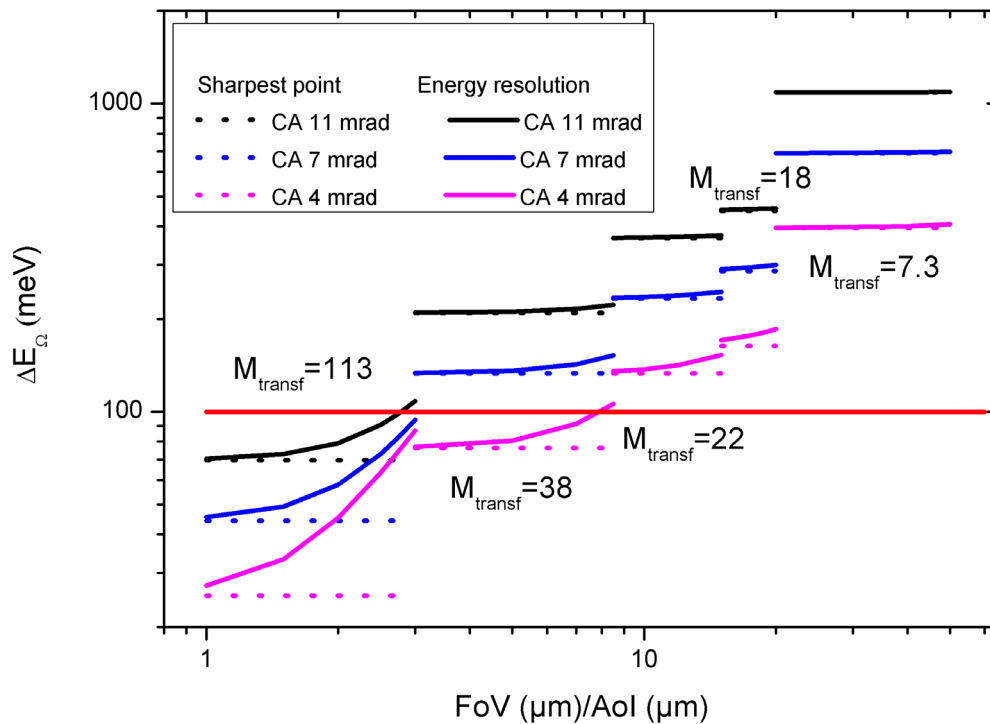


Fig. 6.17: Expected Energy resolution for the system evaluated for: $\gamma_{\text{max}} = 0.7$ mm; the transfer optics magnification is indicated (M_{trans}). The sharpest point corresponds to the CA angular spread, i.e. the minimum possible energy resolution; in the PEEM image correspond to the energy at the center of the image.

6.4.3 Lateral resolution

As discussed in section 6.3.4, the Ω - aberration can be corrected only by hexapoles in the image planes (either centered or symmetrically rearranged), or the antisymmetric combination of hexapoles in one of the diffraction planes.

The analytical calculation shows that multipoles in the three image planes can be combined in such a way, that they compensate the **geometric coefficients** $A_{\gamma\alpha}$, $A_{\beta\delta}$, $B_{\beta\gamma}$ and $B_{\alpha\delta}$. However, such combination introduces an angular deflection $(\Delta x', \Delta y')$ ¹⁵ of 10 mrad, i.e. introducing an energy deterioration $\Delta E=20$ eV. A similar estimation of the hexapole effects for the antisymmetric combination of two hexapoles in the first diffraction plane shows that the angular deflection introduced by correcting the geometric coefficient $A_{\gamma\alpha}$ is only in the order 10^{-3} mrad (corresponding to $\Delta E=2$ meV)¹⁶. The effects of the hexapole correcting the coefficient $C_{\gamma\gamma}$ can be neglected, as the introduced deflections are at least one order of magnitude smaller than the remaining coefficients $A_{\alpha\kappa}$, $A_{\kappa\kappa}$ and $B_{\delta\kappa}$.

The chromatic coefficients $A_{\gamma\kappa}$ and $B_{\beta\kappa}$ can be compensated by an opportune combination of hexapoles centered in two image planes. The geometric coefficients $A_{\gamma\alpha}$, $A_{\beta\delta}$ and $B_{\beta\gamma}$ can be corrected by an antisymmetric couple of hexapoles in the first diffraction plane; it is important to remark, however, that this last solution might be unpractical, as it demands that two hexapoles fit the limited drift space between the sectors. For this reason, it is convenient to discuss first the expected improvement due to the correction of the chromatic terms only, and then the fully corrected system.

Practically, the effects of aberrations are undetectable if the value Δx is smaller than the resolution limit of the detector (i.e. the pixel size resolution). Fig. 6.18 compares the lateral resolution of the uncorrected system (dotted line) to the detector resolution (red line; $\text{FoV}/500$). The contributions from the chromatic (blue line) and geometric (black line) aberrations are also shown separately. The lateral resolution is calculated at the sample surface. For $\text{FoV} > 15 \mu\text{m}$, the lateral resolution of the image is limited by the filter aberration ($\Delta x > \text{FoV}/500$). To avoid this, Δx has to be reduced below the detector resolution limit: for

¹⁵ Proportional to the coefficients $B\gamma^2$, see comment in section 6.3.2

¹⁶ The same geometric correction can be introduced by combining opportunely two hexapoles in the two diffraction planes. However, this solution is ineffective, due to the chromatic coefficients introduced.

small FoV the correction of the chromatic contribution only should be sufficient, while at larger FoV also the geometric contribution should be corrected.

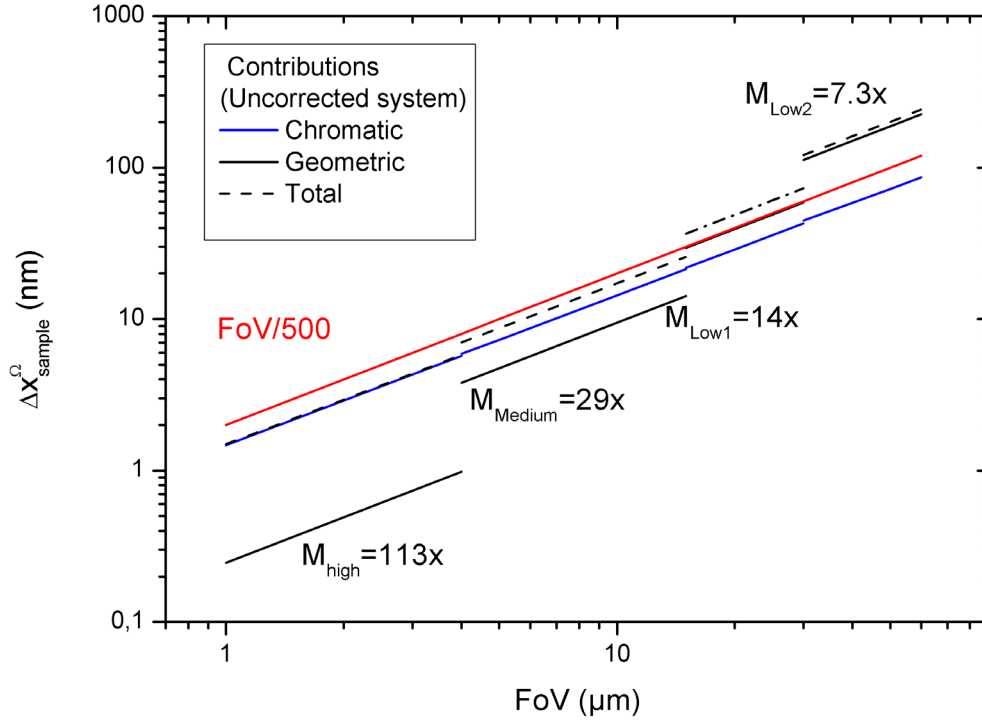


Fig. 6.18: Contributions to the overall lateral resolution (dotted line) of the uncorrected filtering system due to the chromatic (blue line) and geometric (red line) for different field of view, using $CA_a=11$ mrad.

($\Delta x > \Delta y$) At small FoV the resolution is completely limited by chromatic aberrations, while the geometrical ones are limiting the biggest FoV.

The correction of the chromatic terms $A_{\gamma\kappa}$ and $B_{\beta\kappa}$ clearly improves the lateral resolution (see Fig 6.19, also in this case $\Delta x > \Delta y$). The expected lateral resolution for the uncorrected system (dotted lines) is compared to the lateral resolution for the corrected (colored straight lines), depending on the CA size. The pixel size of the detector system is also shown (red and green lines represent the detector resolution FoV/500 and FoV/1000, respectively). The value Δx is calculated at the sample surface. As already pointed out, Δx should at least be smaller than FoV/500 ; however, $\Delta x < \text{FoV}/1000$ is desirable¹⁷.

¹⁷ This is the pixel size expected for the new detector systems.

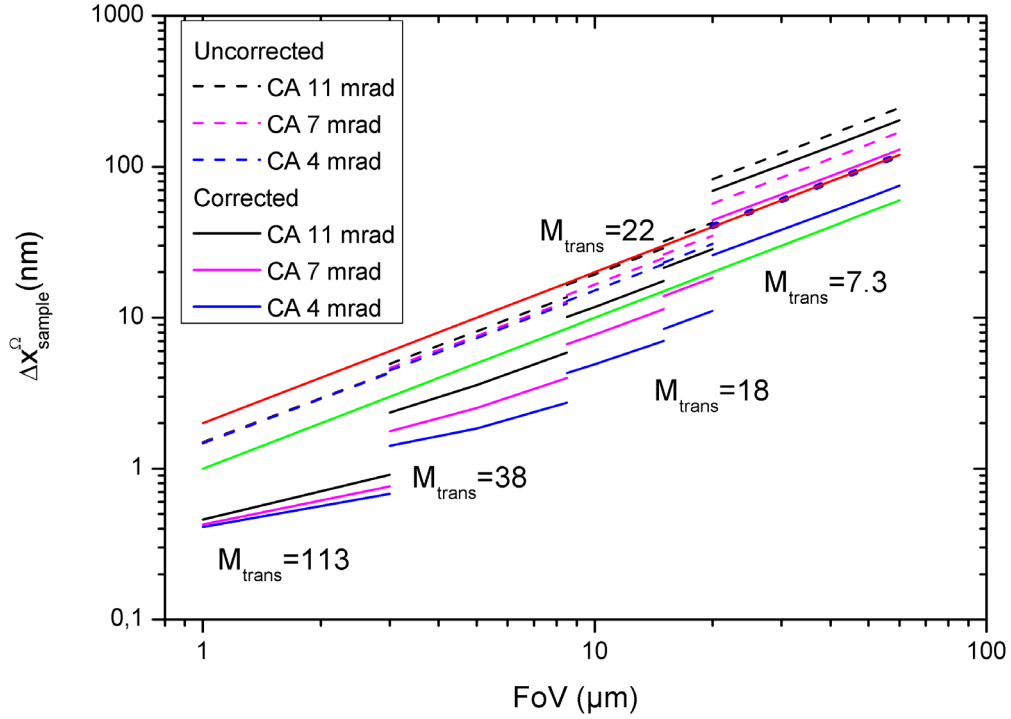


Fig. 6.19: Lateral resolution, at the sample surface, for the uncorrected (dotted lines) and the corrected system. The different colors refer to different CA size. The magnification of the transfer optics is indicated. M_{trans} . The red and green lines represent the resolution limit of the detector ($FoV/500$ and $FoV/1000$, respectively).

For high and medium magnifications, ($1 \mu m - 15 \mu m$ FoV), the correction of chromatic aberration coefficients improves the resolution below the $FoV/1000$ threshold, independently on the CA size. **For low magnifications** ($15 \mu m - 60 \mu m$ FoV), the resolution depends on the CA aperture size, which has to be reduced to maintain the value of $\Delta x < FoV/500$. Remarkably, the expected lateral resolution of the system Δx is lower than $1 nm$ ($FoV < 3 \mu m$). Moreover, using $CA_a = 4$ mrad, the lateral resolution is better than $FoV/800$, for all the FoV range.

The expected lateral resolution for the fully corrected system (also in this case $\Delta x > \Delta y$) is shown in Fig 6.20. The geometric aberrations $A_{\gamma\alpha}$, $A_{\beta\delta}$, $B_{\beta\gamma}$ and $B_{\alpha\delta}$ are compensated by introducing an antisymmetric couple of multipoles at the first diffraction plane inside the Ω -filter.

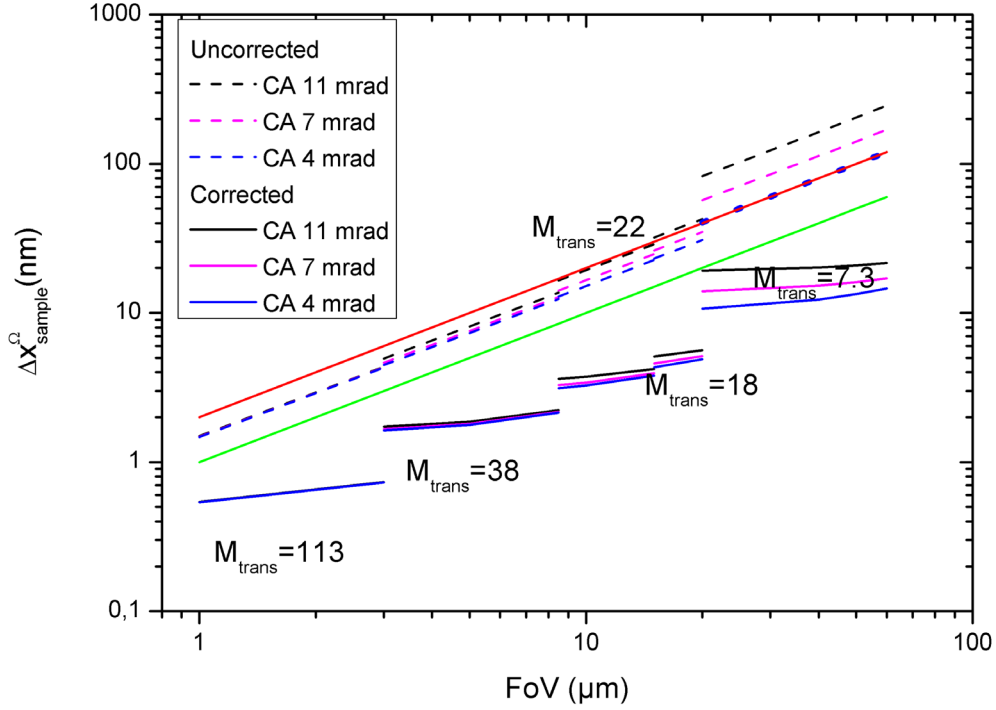


Fig. 6.20: Lateral resolution, at the sample surface for the uncorrected (dotted lines) and the corrected system (chromatic and geometric terms). The different colors refer to different CA size. The red and green lines represent the resolution limit of the detector (FoV/500 and FoV/1000, respectively).

As we can see, the resolution is below FoV/1000 for all FoV, independently from the CA size.

6.4.4 Hexapoles arrangement

Fig 2.21 shows one of the possible hexapole rearrangements realizing the corrections as described in the previous sections. The first multipole in the first image plane corrects the geometric term $C_{\gamma\gamma}$ to half of its value¹⁸. For $\text{FoV} > 9 \mu\text{m}$ the energy resolution is $\Delta E > 100 \text{ meV}$, and it is limited by the angular acceptance of the system. For FoV below $9 \mu\text{m}$ the corrected system has $\Delta E < 100 \text{ meV}$. The identical multipoles centered at the second and third image planes correct the chromatic terms $A_{\gamma\kappa}$ and $B_{\delta\kappa}$. This, together with the implementation of CA of different sizes (corresponding to 11 mrad, 7 mrad and 4 mrad of angular acceptance)

¹⁸ The effects of the others hexapoles on the energy resolution is negligible: $C_{\gamma\gamma}/2 \gg (L \cdot H_{AS}^{d1})_{x'}$, and $C_{\gamma\gamma}/2 \gg (H_0^{i2} + H_0^{i3})_{x'}$

yields in a lateral resolution of the SMART-2 microscope below the detector resolution $800/\text{FoV}$ for all FoV between $1\text{ }\mu\text{m}$ and $60\text{ }\mu\text{m}$; the expected lateral resolution $\Delta x < 1\text{ nm}$ (FoV $1\text{ }\mu\text{m}$). A pair of antisymmetric hexapoles in the first diffraction plane could correct the remaining geometric aberrations. This solution brings theoretically the resolution even far below the threshold of $\text{FoV}/1000$. However, the system should also fit the strict mechanical constraints set by the drift space between the sectors (37 mm).

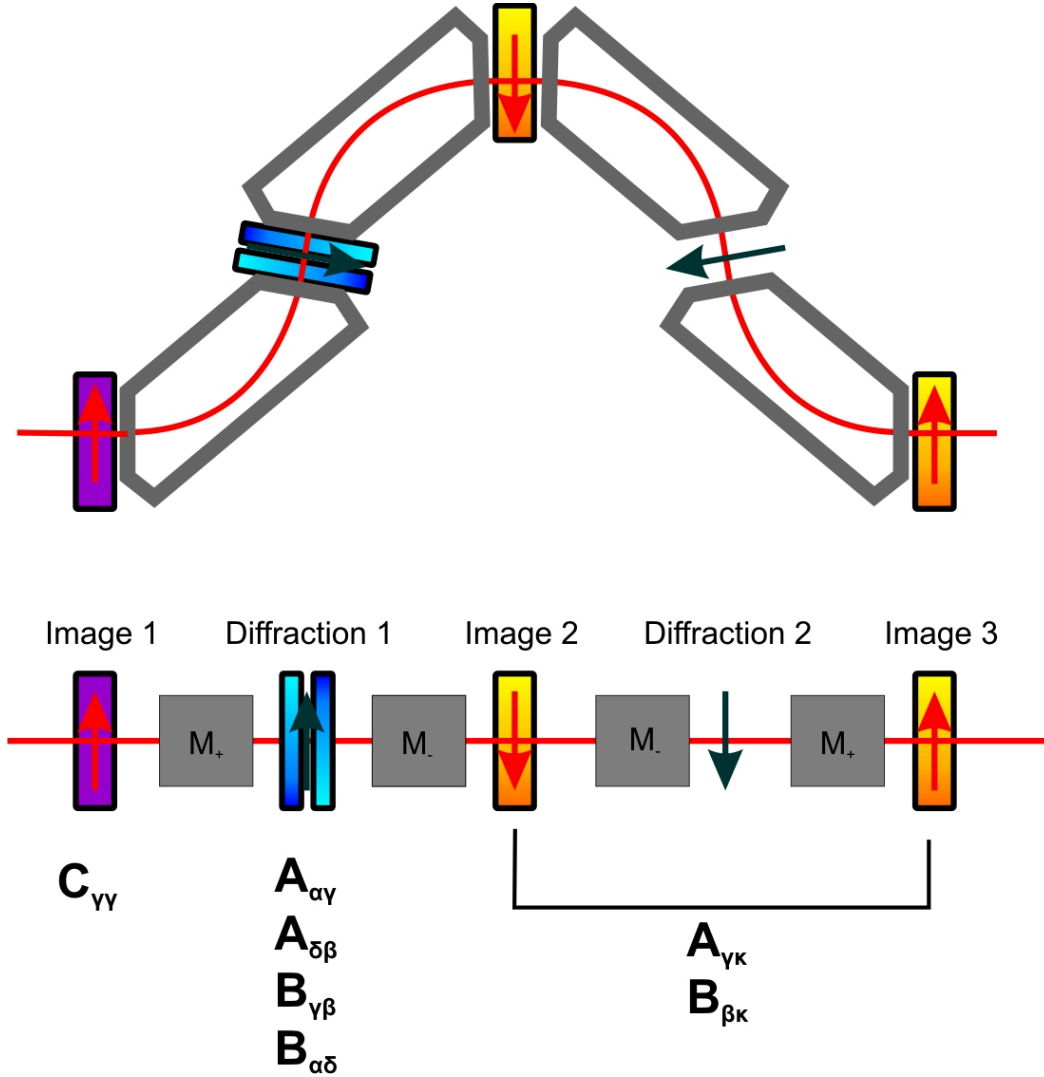


Fig. 6.21: Scheme of the hexapole combination that improves the energy and lateral resolution as discussed in the previous sections. The first hexapole (correction coefficient $B = 0.4\text{ mrad mm}^2$; multipole length 15 mm, $a_0 = 5\text{ mm}$, $V = 0.6\text{ V}$) correct the C_{YY} coefficient. The couple in the first image plane corrects the $A_{\gamma\kappa}$ and $B_{\delta\kappa}$ terms (correction coefficient $A = 2.85 \cdot 10^{-3}\text{ mrad}^{-1}$, multipole length 15 mm, $a_0 = 5\text{ mm}$ and $V = 200\text{ V}$). Additionally, an antisymmetric couple can be inserted in the first diffraction plane, to correct the geometric aberrations (for instance: $B = -3.82\text{ mrad mm}^{-2}$, multipole length 10mm, $L = 7,5\text{ mm}$ $a_0 = 5\text{ mm}$ and $V = 300\text{ V}$).

As an outlook, it should be mentioned that the energy resolution could be further improved by the introduction of two quadrupoles in one of drift spaces inside the Ω -filter. In fact, quadrupole fields have first order focusing properties only in one direction, while in the other the beam is defocused. A symmetric beam passing through a quadrupole (correctly oriented) is focused in the y direction and defocused in the x direction, i.e. $\delta \ll \gamma$. Consequently, an additional hexapole acting on this beam has a strong effect on the x direction (γ) and a small effect on the y (δ) direction. A second quadrupole, oriented opposite to the first one, is necessary to refocus the beam in the x direction and defocus it the y direction, restoring the initial symmetry of the beam (see Fig 6.22). In this way, the $C_{\gamma\gamma}$ coefficient could be corrected independently from the $C_{\delta\delta}$. However, this solution should be carefully evaluated, by determining the effects of this optical system on the image and diffraction beams in both xy coordinate. Moreover, such system has to fit the strong mechanical constraints set by the length of the drift space between the sectors.

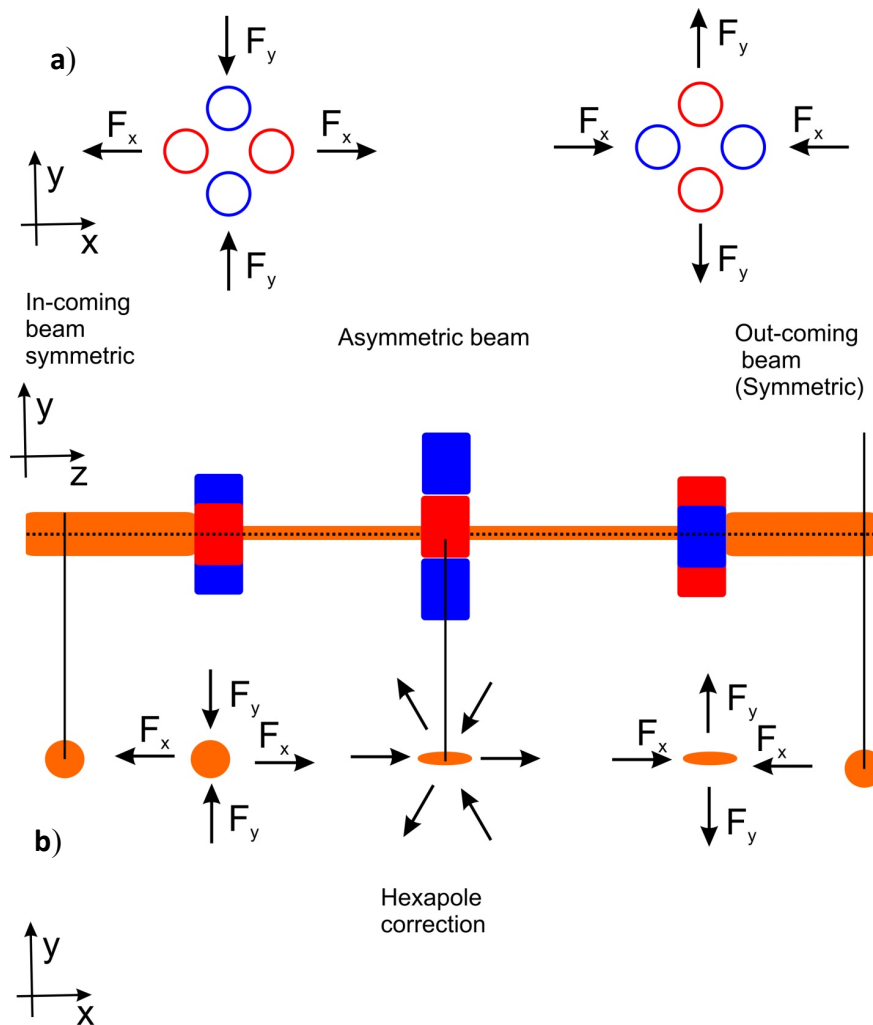


Fig. 6.22a) Electrostatic quadrupole: definition of its orientation and forces acting on a negatively charged beam passing through it. b) the representation of the action of a quadrupole/hexapole/quadrupole acting on an incoming symmetric electron beam. The action of the multipole is much stronger on the x coordinate $x \gg y$

6.5 Conclusions

In this chapter, two main topics were discussed: the adapting optical system and the strategy for second order aberrations correction optimized for an electrostatic omega filter.

This device, developed with electron optics simulations by Dr Marchetto and Dr. Rombolá on the basis of the SMART-1 magnetic energy filter, will be the first aberration corrected electrostatic filter optimized for a LEEM microscope.

The approach combined the matrix theoretical formalism (implemented in Wolfram Mathematica) with direct electron beam tracing simulations (using Lorentz-E 3D software) at different levels. This way we could:

- quantify optical parameters of realistic electrode arrangements
- verify theoretical expectations
- define construction requirements

The system fulfills all the mechanical and optical constraints and delivers the expected high energy (75 meV - 100 meV) and the lateral resolution.

The systematic approach was introduced to implement the hexapole correction inside the new Ω -filter without producing additional aberrations.

The correction of the chromatic image aberrations correction improves the lateral resolution below the value $\text{FoV}/1000$, which is much higher than currently available detectors resolution (130 μm for a 40mm detector).

Two possible strategies have been discussed to compensate the energy gradient in the image plane, resulting from the quadratic dependency of the outgoing angle on the x-position. This aberration cannot be corrected by simple combination of hexapole and produce an energy gradient which has a maximum value of $\Delta E = 250 \text{ meV}$ at the border of the image. The optimization of the lateral magnification in front of the filter limits this aberration effect, without influencing the lateral resolution. The expected energy resolution $\Delta E < 100 \text{ meV}$ between 1 μm to 3 μm FoV. For higher FoV, the energy resolution is set by the angular size of the beam.

7. Summary and Outlooks

This work presents two main topics related to Low Energy and Photo Emitted Electron Microscopy (LEEM/PEEM).

In the first part, the multi-method capabilities of the so-called SMART instrument are applied to study the preparation and properties of metal supported thin iron-oxide films, basing and continuing the previous work of *A. Sala* and *M. Lewandowsky* [52, 86].

Firstly, I focused on the nucleation and growth conditions for the α -Fe₂O₃ phase on different substrates, as well as on the surface modification induced by extra Fe deposition on α -Fe₂O₃ and Fe₃O₄ surfaces. On the Fe₃O₄ surface, Fe deposition at room temperature (RT) yields in a well ordered structure exhibiting a $(2\sqrt{3} \times 2\sqrt{3})R30^\circ$ reconstruction. The origin of the pattern might be associated with the distortion of the Fe atomic position at the surface. Additionally, the biphasic termination (i.e. characterized by satellite spots around the fundamental LEED spots) can be produced in a specific temperature range (700 K - 820 K) by excess of superficial Fe. Interestingly, Fe deposition at RT and subsequent annealing or directly at high temperature, leads to the same biphasic structure. In contrast, on the α -Fe₂O₃ phase terminated with the " $(\sqrt{3} \times \sqrt{3})R30^\circ$ biphasic reconstruction" (i.e. characterized by satellite spots surrounding also the $(\sqrt{3} \times \sqrt{3})R30^\circ$ oxide spots), the Fe deposition at RT produces a metastable " (1×1) biphasic structure" (i.e. only the (1×1) spots are visible and surrounded by satellite spots). This structure, unknown up to now, is stable under UHV annealing up to $T \approx 710$ K. The two α -Fe₂O₃ biphasic structures were discussed basing on the two main structural models suggested in the literature for the biphasic termination. However, the proposed models are based mainly on LEED measurements and should be also checked with other experimental methods.

Secondly, we studied systematically the interconversion of Fe₃O₄, γ -Fe₂O₃ and α -Fe₂O₃ phases. In particular, the structural transformation γ -Fe₂O₃ \rightarrow α -Fe₂O₃ and the "direct" oxidation Fe₃O₄ \rightarrow α -Fe₂O₃, (without identifiable intermediate phase) could be distinguished, thanks to the combination of structural, chemical and spatial sensitivity. The real time observation of the reactions outlined some interesting aspects of the phase transformation, such as the substrate influence on the thin film system. The analysis of the front velocity showed two transformation regimes, which were identified by the average reaction rate and the shape of the reaction front: fast and dendritically growing fronts on one hand, slow and

rather smooth on the other. The Arrhenius-like temperature dependence of the reaction rates allowed the determination of the effective activation energies for the transformation. However, not all the experimental observations could be fully explained. In particular, due to the low kinetic electron energy and concomitantly surface sensitivity, the available methods in the SMART can only probe the top most layers of the sample surface. Some of the assumptions made in the analysis, e.g. that the film was converted over the whole thickness should be verified by less surface sensitive methods like TEM or x-ray diffraction.

The interaction of supported Pt nanoparticles (NP) on Fe_3O_4 and $\alpha\text{-Fe}_2\text{O}_3$ surfaces was the topic of the last experimental section. Based on the previous studies, on the Fe_3O_4 support, I have extended the characterization of the system from previous results on the NPs encapsulation process, by studying the effects of O_2 pressure in real time XPS and of deposition temperature in SPA-LEED. On the biphasic terminated $\alpha\text{-Fe}_2\text{O}_3$ the encapsulation process follows a similar mechanism as already observed on the Fe_3O_4 surface. By direct comparison on a mixed film, we could find that the particles have slightly different surface areas on the two oxides, most likely because of the adhesion energy of Pt on the two different surfaces.

The identification of the encapsulated Pt NPs from dewetted areas of a $\text{Fe}_3\text{O}_4/\text{Pt}(111)$ film was the main motivation to develop a software simulating the LEEM imaging process. The software is meant to reproduce the image contrast features for mixed surfaces with objects of different composition and height. The comparison between the simulation prediction and the experimental system was not possible in the present work due to the lack of information on the complex part of the scattering amplitude. However, strategies to overcome these limitations in future applications to experimental systems are discussed.

The final part deals with the electron optical development of a fully electrostatic Omega-type filtering system, designed for a new LEEM/PEEM microscope. In the new system, both the energy filtering and the aberration correction are based on the optical principle of a magnetic Omega-filter, already successfully operating in the actual SMART prototype. Compared to the magnetic Omega-filter, the electrostatic system will have a better electric stability (due to voltage supplies floating on a common high voltage), and compare to existing hemispherical electrostatic filters, the Omega-type filter will have enhanced performances, in both energy and lateral resolution.

Appendix1:

Definition of variables

In the following: z denotes the coordinate along the (curved) optical axis of the Ω -filter; x and y are the horizontal and vertical displacements perpendicular to the optical axis, respectively. Both are functions of the starting coordinates $\alpha, \beta, \gamma, \delta$ and defined in the section 6.1 of the text. The positions at the first (object plane) and final image planes are named x_o and y_o , x'_o and y'_o the respective angles.

$$x_o = x_o(\alpha, \beta, \gamma, \delta, \kappa) \quad (\text{A1.2a})$$

$$y_o = y_o(\alpha, \beta, \gamma, \delta, \kappa) \quad (\text{A1.2b})$$

$$x'_o = x'_o(\alpha, \beta, \gamma, \delta, \kappa) \quad (\text{A1.2c})$$

$$y'_o = y'_o(\alpha, \beta, \gamma, \delta, \kappa) \quad (\text{A1.2d})$$

Symmetry of the system

Vertically (y direction) the filter has mirror symmetry. Consequently, the horizontal and the vertical image position are a symmetric and antisymmetric function of the variables β and δ , respectively. Rays starting at $\pm\delta_0$ have the same horizontal image point; the same is valid for the starting angle $\pm\beta_0$, both symmetries are independent from the horizontal starting angle α and position γ and from the energy κ .

$$x(\alpha, \beta, \gamma, \delta, \kappa) = x(\alpha, -\beta, \gamma, -\delta, \kappa)$$

$$y(\alpha, \beta, \gamma, \delta, \kappa) = -y(\alpha, -\beta, \gamma, -\delta, \kappa)$$

$$y(\alpha, 0, \gamma, 0, \kappa) = 0$$

Resolution expanded to the second order

Positions and angles at the final image plane can be expressed as Taylor series of the starting variable; for instance:

$$x_o(\alpha, \beta, \gamma, \delta, \kappa) = x_o^{(0)} + x_o^{(1)} + x_o^{(2)} + x_o^{(3)} + \dots$$

(0), (1), (2) etc. labels the order of the expansion in $\alpha, \beta, \gamma, \delta$ and κ .

The Taylor expansion for the function $f(x_i)$ ($i=[1,5]$ variables) is in the form:

$$\begin{aligned} f(x_1, x_2, x_3, x_4, x_5) &= f(0,0,0,0,0) + \sum_{i=1}^5 \frac{\partial}{\partial x_i} f(x_1, x_2, x_3, x_4, x_5) \cdot x_i \\ &+ \frac{1}{2!} \sum_{i=1}^5 \sum_{j=1}^5 \frac{\partial}{\partial x_i} \frac{\partial}{\partial x_j} f(x_1, x_2, x_3, x_4, x_5) \cdot x_i x_j \\ &+ \frac{1}{3!} \sum_{i=1}^5 \sum_{j=1}^5 \sum_{k=1}^5 \frac{\partial}{\partial x_i} \frac{\partial}{\partial x_j} \frac{\partial}{\partial x_k} f(x_1, x_2, x_3, x_4, x_5) \cdot x_i x_j x_k + \dots \end{aligned}$$

The exponent for the geometrical expansions $(\alpha, \beta, \gamma, \delta)$ (or their sum for mixed expansions) are called “**order**”, the exponent of κ is called “**degree**” and the sum of both is the “**rank**”.

First order

For all the four coordinates:

$$x_o^{(1)}(\alpha, \beta, \gamma, \delta, \kappa) = \textcolor{red}{A}_\alpha \cdot \alpha + \textcolor{orange}{A}_\beta \cdot \beta + A_\gamma \cdot \gamma + \textcolor{orange}{A}_\delta \cdot \delta + \textcolor{green}{A}_\kappa \cdot \kappa$$

$$y_o^{(1)}(\alpha, \beta, \gamma, \delta, \kappa) = \textcolor{orange}{B}_\alpha \cdot \alpha + \textcolor{red}{B}_\beta \cdot \beta + \textcolor{orange}{B}_\gamma \cdot \gamma + B_\delta \cdot \delta + \textcolor{blue}{B}_\kappa \cdot \kappa$$

$$x_s^{(1)}(\alpha, \beta, \gamma, \delta, \kappa) = C_\alpha \cdot \alpha + \textcolor{orange}{C}_\beta \cdot \beta + \textcolor{red}{C}_\gamma \cdot \gamma + \textcolor{orange}{C}_\delta \cdot \delta + C_\kappa \cdot \kappa$$

$$y_s^{(1)}(\alpha, \beta, \gamma, \delta, \kappa) = \textcolor{orange}{D}_\alpha \cdot \alpha + D_\beta \cdot \beta + \textcolor{orange}{D}_\gamma \cdot \gamma + \textcolor{red}{D}_\delta \cdot \delta + \textcolor{blue}{D}_\kappa \cdot \kappa$$

The **red colored** coefficients are zero because of the definition of the object and source image plane. As the system has no vertical dispersion, the **blue marked** coefficients are zero. A_κ equals zero in the case of a non-dispersive image plane. The **orange coefficients** are zero due to symmetry. Therefore:

$$\begin{pmatrix} x_o^{(1)} \\ y_o^{(1)} \\ x_s^{(1)} \\ y_s^{(1)} \end{pmatrix} = \begin{pmatrix} 0 & 0 & A_\gamma & 0 & 0 \\ 0 & 0 & 0 & B_\delta & 0 \\ C_\alpha & 0 & 0 & 0 & C_\kappa \\ 0 & D_\beta & 0 & 0 & 0 \end{pmatrix} \begin{pmatrix} \alpha \\ \beta \\ \gamma \\ \delta \\ \kappa \end{pmatrix}$$

$$x_o^{(1)}(\alpha, \beta, \gamma, \delta, \kappa) = A_\gamma \cdot \gamma$$

$$y_o^{(1)}(\alpha, \beta, \gamma, \delta, \kappa) = B_\delta \cdot \delta$$

$$x_s^{(1)}(\alpha, \beta, \gamma, \delta, \kappa) = C_\alpha \cdot \alpha + C_\kappa \cdot \kappa$$

$$y_s^{(1)}(\alpha, \beta, \gamma, \delta, \kappa) = D_\beta \cdot \beta$$

For the electrostatic Ω -filter, the coefficients A_γ B_β C_α and D_δ are 1; the coefficient C_κ is the angular dispersion and is $C_\kappa = 2 \text{ mrad/eV}$

Second order

$$\begin{aligned} x_o^{(2)}(\alpha, \beta, \gamma, \delta, \kappa) &= \frac{1}{2!} \\ &\cdot (A_{\alpha\alpha} \cdot \alpha^2 + A_{\alpha\beta} \cdot \alpha\beta + A_{\alpha\gamma} \cdot \alpha\gamma + A_{\alpha\delta} \cdot \alpha\delta + A_{\alpha\kappa} \cdot \alpha\kappa + A_{\beta\alpha} \cdot \beta\alpha + \dots) \\ &= \frac{1}{2!} \cdot \sum_{i=1}^5 \sum_{j=1}^5 A_{x_i x_j} \cdot x_i x_j \end{aligned}$$

with the partial derivations $A_{x_i x_j} = \frac{\partial}{\partial x_i} \frac{\partial}{\partial x_j} x_o(\alpha, \beta, \gamma, \delta, \kappa)$; $x_i \in \{\alpha, \beta, \gamma, \delta, \kappa\}$.

The Taylor series can be expressed in the matrix form:

$$\begin{aligned} x_o^{(2)}(\alpha, \beta, \gamma, \delta, \kappa) &= \frac{1}{2!} \cdot \begin{pmatrix} \alpha \\ \beta \\ \gamma \\ \delta \\ \kappa \end{pmatrix}^T \cdot \begin{pmatrix} A_{\alpha\alpha} & A_{\alpha\beta} & A_{\alpha\gamma} & A_{\alpha\delta} & A_{\alpha\kappa} \\ A_{\beta\alpha} & A_{\beta\beta} & A_{\beta\gamma} & A_{\beta\delta} & A_{\beta\kappa} \\ A_{\gamma\alpha} & A_{\gamma\beta} & A_{\gamma\gamma} & A_{\gamma\delta} & A_{\gamma\kappa} \\ A_{\delta\alpha} & A_{\delta\beta} & A_{\delta\gamma} & A_{\delta\delta} & A_{\delta\kappa} \\ A_{\kappa\alpha} & A_{\kappa\beta} & A_{\kappa\gamma} & A_{\kappa\delta} & A_{\kappa\kappa} \end{pmatrix} \cdot \begin{pmatrix} \alpha \\ \beta \\ \gamma \\ \delta \\ \kappa \end{pmatrix} \\ y_o^{(2)}(\alpha, \beta, \gamma, \delta, \kappa) &= \frac{1}{2!} \cdot \begin{pmatrix} \alpha \\ \beta \\ \gamma \\ \delta \\ \kappa \end{pmatrix}^T \cdot \begin{pmatrix} B_{\alpha\alpha} & B_{\alpha\beta} & B_{\alpha\gamma} & B_{\alpha\delta} & B_{\alpha\kappa} \\ B_{\beta\alpha} & B_{\beta\beta} & B_{\beta\gamma} & B_{\beta\delta} & B_{\beta\kappa} \\ B_{\gamma\alpha} & B_{\gamma\beta} & B_{\gamma\gamma} & B_{\gamma\delta} & B_{\gamma\kappa} \\ B_{\delta\alpha} & B_{\delta\beta} & B_{\delta\gamma} & B_{\delta\delta} & B_{\delta\kappa} \\ B_{\kappa\alpha} & B_{\kappa\beta} & B_{\kappa\gamma} & B_{\kappa\delta} & B_{\kappa\kappa} \end{pmatrix} \cdot \begin{pmatrix} \alpha \\ \beta \\ \gamma \\ \delta \\ \kappa \end{pmatrix} \end{aligned}$$

$$x_s^{(2)}(\alpha, \beta, \gamma, \delta, \kappa) = \frac{1}{2!} \cdot \begin{pmatrix} \alpha \\ \beta \\ \gamma \\ \delta \\ \kappa \end{pmatrix}^T \cdot \begin{pmatrix} C_{\alpha\alpha} & \textcolor{red}{A}_{\alpha\beta} & C_{\alpha\gamma} & \textcolor{red}{C}_{\alpha\delta} & C_{\alpha\kappa} \\ \textcolor{red}{C}_{\beta\alpha} & C_{\beta\beta} & \textcolor{red}{C}_{\beta\gamma} & \textcolor{orange}{C}_{\beta\delta} & \textcolor{red}{C}_{\beta\kappa} \\ \textcolor{orange}{C}_{\gamma\alpha} & \textcolor{red}{C}_{\gamma\beta} & C_{\gamma\gamma} & \textcolor{red}{C}_{\gamma\delta} & C_{\gamma\kappa} \\ \textcolor{red}{C}_{\delta\alpha} & \textcolor{orange}{C}_{\delta\beta} & \textcolor{red}{C}_{\delta\gamma} & C_{\delta\delta} & \textcolor{red}{C}_{\delta\kappa} \\ C_{\kappa\alpha} & \textcolor{red}{C}_{\kappa\beta} & C_{\kappa\gamma} & \textcolor{red}{C}_{\kappa\delta} & C_{\kappa\kappa} \end{pmatrix} \cdot \begin{pmatrix} \alpha \\ \beta \\ \gamma \\ \delta \\ \kappa \end{pmatrix}$$

$$y_s^{(2)}(\alpha, \beta, \gamma, \delta, \kappa) = \frac{1}{2!} \cdot \begin{pmatrix} \alpha \\ \beta \\ \gamma \\ \delta \\ \kappa \end{pmatrix}^T \cdot \begin{pmatrix} \textcolor{red}{D}_{\alpha\alpha} & D_{\alpha\beta} & \textcolor{red}{D}_{\alpha\gamma} & \textcolor{orange}{D}_{\alpha\delta} & \textcolor{red}{D}_{\alpha\kappa} \\ D_{\beta\alpha} & \textcolor{red}{D}_{\beta\beta} & \textcolor{orange}{D}_{\beta\gamma} & \textcolor{red}{D}_{\beta\delta} & D_{\beta\kappa} \\ \textcolor{red}{D}_{\gamma\alpha} & \textcolor{orange}{D}_{\gamma\beta} & \textcolor{red}{D}_{\gamma\gamma} & D_{\gamma\delta} & \textcolor{red}{D}_{\gamma\kappa} \\ \textcolor{orange}{D}_{\delta\alpha} & \textcolor{red}{D}_{\delta\beta} & D_{\delta\gamma} & \textcolor{red}{B}_{\delta\delta} & D_{\delta\kappa} \\ \textcolor{red}{D}_{\kappa\alpha} & D_{\kappa\beta} & \textcolor{red}{D}_{\kappa\gamma} & B_{\kappa\delta} & \textcolor{red}{D}_{\kappa\kappa} \end{pmatrix} \cdot \begin{pmatrix} \alpha \\ \beta \\ \gamma \\ \delta \\ \kappa \end{pmatrix}$$

The red marked coefficients are zero due to vertical symmetries outlined in 1.2: while the orange marked coefficient are zero due to the point symmetry of the filter. Moreover, the matrix is symmetric, due to fact that the derivation order is unimportant ($A_{x_i x_j} = A_{x_j x_i}$ as $\frac{\partial}{\partial x_i} \frac{\partial}{\partial x_j} x_o(\alpha, \beta, \gamma, \delta, \kappa) = \frac{\partial}{\partial x_j} \frac{\partial}{\partial x_i} x_o(\alpha, \beta, \gamma, \delta, \kappa)$).

Thus, the overall number of the coefficients reduces to $5+4+7+4 = 20$

$$x_o^{(2)}(\alpha, \beta, \gamma, \delta, \kappa) = \frac{1}{2!} \cdot \begin{pmatrix} \alpha \\ \beta \\ \gamma \\ \delta \\ \kappa \end{pmatrix}^T \cdot \begin{pmatrix} 0 & 0 & 2 \cdot A_{\alpha\gamma} & 0 & 2 \cdot A_{\alpha\kappa} \\ 0 & 0 & 0 & 2 \cdot A_{\beta\delta} & 0 \\ 0 & 0 & 0 & 0 & 2 \cdot A_{\gamma\kappa} \\ 0 & 0 & 0 & 0 & 0 \\ 0 & 0 & 0 & 0 & A_{\kappa\kappa} \end{pmatrix} \cdot \begin{pmatrix} \alpha \\ \beta \\ \gamma \\ \delta \\ \kappa \end{pmatrix}$$

$$y_o^{(2)}(\alpha, \beta, \gamma, \delta, \kappa) = \frac{1}{2!} \cdot \begin{pmatrix} \alpha \\ \beta \\ \gamma \\ \delta \\ \kappa \end{pmatrix}^T \cdot \begin{pmatrix} 0 & 0 & 0 & 2 \cdot B_{\alpha\delta} & 0 \\ 0 & 0 & 2 \cdot B_{\beta\gamma} & 0 & 2 \cdot B_{\beta\kappa} \\ 0 & 0 & 0 & 0 & 0 \\ 0 & 0 & 0 & 0 & 2 \cdot B_{\delta\kappa} \\ 0 & 0 & 0 & 0 & 0 \end{pmatrix} \cdot \begin{pmatrix} \alpha \\ \beta \\ \gamma \\ \delta \\ \kappa \end{pmatrix}$$

$$x_s^{(2)}(\alpha, \beta, \gamma, \delta, \kappa) = \frac{1}{2!} \cdot \begin{pmatrix} \alpha \\ \beta \\ \gamma \\ \delta \\ \kappa \end{pmatrix}^T \cdot \begin{pmatrix} C_{\alpha\alpha} & 0 & 0 & 0 & 2 \cdot C_{\alpha\kappa} \\ 0 & C_{\beta\beta} & 0 & 0 & 0 \\ 0 & 0 & C_{\gamma\gamma} & 0 & 2 \cdot C_{\gamma\kappa} \\ 0 & 0 & 0 & C_{\delta\delta} & 0 \\ 0 & 0 & 0 & 0 & C_{\kappa\kappa} \end{pmatrix} \cdot \begin{pmatrix} \alpha \\ \beta \\ \gamma \\ \delta \\ \kappa \end{pmatrix}$$

$$y_s^{(2)}(\alpha, \beta, \gamma, \delta, \kappa) = \frac{1}{2!} \cdot \begin{pmatrix} \alpha \\ \beta \\ \gamma \\ \delta \\ \kappa \end{pmatrix}^T \cdot \begin{pmatrix} 0 & 2 \cdot D_{\alpha\beta} & 0 & 0 & 0 \\ 0 & 0 & 0 & 0 & 2 \cdot D_{\beta\kappa} \\ 0 & 0 & 0 & 2 \cdot D_{\gamma\delta} & 0 \\ 0 & 0 & 0 & 0 & 2 \cdot D_{\delta\kappa} \\ 0 & 0 & 0 & 0 & 0 \end{pmatrix} \cdot \begin{pmatrix} \alpha \\ \beta \\ \gamma \\ \delta \\ \kappa \end{pmatrix}$$

Calculated aberration coefficient

The aberration coefficients for the electrostatic Ω -filter under development were explicitly obtained by direct electron ray tracing.

The procedure is described as follow:

- The passage through Ω -filter has been simulated for several electron beams: each electron beam has only two non-zero starting variables.
- The rays positions and angles at the initial and final image plane have been extrapolated from the calculated trajectories.
- The aberration coefficients are obtained from multiple fits on these data.

As an example, we treat explicitly the procedure for the non-zero combination of the starting variable α/γ .

$n=i$ electron beams are considered, starting at the initial image plane. Each beam starts from a position along the x axes ($x_i=\gamma_i$; $y_i=\delta_i=0$) with kinetic energy $E_k=E_0$ ($\kappa=0$); each beam is made up by $n=j$ rays, each one having a different starting angle in the x direction ($x'_j=\alpha_j$; $y'_j=\beta_j=0$).

After the filter, the simulated horizontal ray position at the final image plane is (power of α):

$$\begin{aligned} x_o(\alpha, \beta = 0, \gamma = \gamma_i, \delta = 0, \kappa=0) \\ = + A_{\alpha}^{(0)}(0, \gamma_i, 0, 0) + A_{\alpha}^{(1)}(0, \gamma_i, 0, 0) \cdot \alpha + A_{\alpha}^{(2)}(0, \gamma_i, 0, 0) \cdot \alpha^2 + A_{\alpha}^{(3)}(0, \gamma_i, 0, 0) \cdot \alpha^3 \end{aligned}$$

Where:

$$A_{\alpha}^{(0)}(0, \gamma_i, 0, 0) = A_{\gamma} \cdot \gamma_i + \frac{1}{6} A_{\gamma\gamma\gamma} \cdot \gamma_i^3$$

$$A_{\alpha}^{(1)}(0, \gamma_i, 0, 0) \cdot \alpha = (A_{\alpha\gamma} \cdot \gamma_i + \frac{1}{2} A_{\gamma\gamma\alpha} \cdot \gamma_i^2) \cdot \alpha$$

$$A_{\alpha}^{(2)}(0, \gamma_i, 0, 0) \cdot \alpha^2 = (\frac{1}{2} A_{\alpha\alpha} + \frac{1}{2} A_{\alpha\alpha\gamma} \cdot \gamma_i) \cdot \alpha^2$$

$$A_{\alpha}^{(3)}(0, \gamma_i, 0, 0) \cdot \alpha^3 = \frac{1}{6} A_{\alpha\alpha\alpha} \cdot \alpha^3$$

The polynomial fit x_0 vs α for fixed values of γ_i gives the values of the coefficients $A_\alpha^{(k)}(\gamma_i)$. The fit $A_\alpha^{(k)}(\gamma_i)$ vs γ gives explicitly the aberration coefficients.

For instance, the cubic fit of the coefficient $A_\alpha^{(0)}(0, \gamma_i, 0, 0) = A_\gamma \cdot \gamma_i + \frac{1}{6} A_{\gamma\gamma\gamma} \cdot \gamma_i^3$ vs γ gives the coefficients A_γ and $A_{\gamma\gamma\gamma}$.

Similarly:

- the quadratic fit of the coefficient $A_\alpha^{(1)}(0, \gamma_i, 0, 0) \cdot \alpha = (A_\alpha + A_{\alpha\gamma} \cdot \gamma_i + \frac{1}{2} A_{\gamma\gamma\alpha} \cdot \gamma_i^2)$ allows the determination of the coefficients A_α , $A_{\alpha\gamma}$, $A_{\gamma\gamma\alpha}$
- the linear fit of the coefficient $A_\alpha^{(2)}(0, \gamma_i, 0, 0) \cdot \alpha^2 = (\frac{1}{2} A_{\alpha\alpha\alpha} + \frac{1}{2} A_{\alpha\alpha\gamma} \cdot \gamma_i)$ gives the coefficients $A_{\alpha\alpha\alpha}$, $A_{\alpha\alpha\gamma}$

The same procedure applies to: the final vertical position y_0 , to the final angles x_s and y_s and to all the other possible combinations of stating variable.

All the aberration coefficients up to the third order were found independently; providing a test on the theoretical relationships between the coefficients given in [161, 162].

The second order coefficients calculated are summarized in table 1; these values refer to the electron passing energy $E_0=1$ keV. As the operating passing energy in the Ω - filter be $E_0=2$ keV, the chromatic coefficients will reduce by 1/2 (the coefficients linear in κ) and 1/4 (the quadratic ones).

$x_o^{(2)}$			$y_o^{(2)}$		
$A_{\gamma\alpha}$	$-5,73 \cdot 10^{-3}$	mr ad^{-1}	$B_{\alpha\delta}$	$4,06 \cdot 10^{-3}$	mr ad^{-1}
$A_{\delta\beta}$	$4,06 \cdot 10^{-3}$	mr ad^{-1}	$B_{\gamma\beta}$	$2,65 \cdot 10^{-3}$	mr ad^{-1}
$A_{\alpha\kappa}$	$1,45 \cdot 10^{-3}$	mm (mr $\text{ad}^{-1}\text{eV}^{-1}$)	$B_{\beta\kappa}$	$4,00 \cdot 10^{-3}$	mm (mr $\text{ad}^{-1}\text{eV}^{-1}$)
$A_{\kappa\kappa}$	$3,00 \cdot 10^{-3}$	mm eV $^{-2}$	$B_{\delta\kappa}$	$8,11 \cdot 10^{-3}$	eV $^{-1}$
$A_{\gamma\kappa}$	$-1,14 \cdot 10^{-2}$	eV $^{-1}$			

Table A1 1: Second order aberration coefficients affecting the lateral resolution. Their values were evaluated by direct electron ray tracing for the electrostatic Ω -filter under development. Passing energy $E_\Omega = 1 \text{ keV}$.

$x_o^{(2)}$			$y_o^{(2)}$		
$C_{\gamma\gamma}$	$-4,05 \cdot 10^{-1}$	mr ad mm^{-2}	$D_{\gamma\gamma}$	$1,60 \cdot 10^{-2}$	mr ad mm^{-2}
$C_{\delta\delta}$	$-8,00 \cdot 10^{-3}$	mr ad mm^{-2}	$D_{\alpha\beta}$	$1,30 \cdot 10^{-2}$	mr ad^{-1}
$C_{\alpha\alpha}$	$-2,87 \cdot 10^{-3}$	mr ad^{-1}	$D_{\beta\kappa}$	$8,11 \cdot 10^{-3}$	eV $^{-1}$
$C_{\beta\beta}$	$-1,33 \cdot 10^{-3}$	mr ad^{-1}	$D_{\delta\kappa}$	$3,81 \cdot 10^{-2}$	mr $\text{ad mm}^{-1}\text{eV}^{-1}$
$C_{\alpha\kappa}$	$-1,14 \cdot 10^{-2}$	eV $^{-1}$			
$C_{\kappa\kappa}$	$-2,50 \cdot 10^{-2}$	mr ad eV^{-2}			
$C_{\gamma\kappa}$	$-1,36 \cdot 10^{-1}$	mr $\text{ad mm}^{-1}\text{eV}^{-1}$			

Table A1 2: Second order aberration coefficients affecting the energy resolution. Their values were evaluated by direct electron ray tracing for the electrostatic Ω -filter under development. Passing energy $E_\Omega = 1 \text{ keV}$.

The dominating third order aberration for lateral resolution is $A_{\gamma\gamma\kappa} = 2,25 \cdot 10^{-3} \text{ mm}^{-1}\text{eV}^{-1}$.

Appendix 2

Two electrodes with aligned apertures at voltages V_1 and V_2 respectively, form an electrostatic lens. The common axis is the **optical axis**.

Referred to the principal plane (PP_1), the action of the electric field distribution of the lens on a charged particle travelling from the field free zone 1 ($V=V_1$) to the field free zone 2 ($V=V_2$), is (see Fig A2.1):

$$\begin{pmatrix} r \\ r' \end{pmatrix} = \begin{pmatrix} 1 & 0 \\ -\frac{1}{f_1} & \sqrt{\frac{E_1}{E_2}} \end{pmatrix}_{PP_1} \begin{pmatrix} r_0 \\ r'_0 \end{pmatrix}$$

where f_1 is called focal length, r_0 is the distance from the center of the aperture (z axis) at PP_1 , $\frac{\partial r}{\partial z} = r'_0$ is the particle direction, E_1 is the kinetic energy of the particle ($E_1=E_k=eV_1$) in the zone 1 and E_2 is the kinetic energy of the particle ($E_2=E_k=eV_2$) in the zone 2.

A particle travelling in the opposite direction, with kinetic energy $E_k=eV_2$, undergoes a different deflection referred to the principal plane PP_2 :

$$\begin{pmatrix} r \\ r' \end{pmatrix} = \begin{pmatrix} 1 & 0 \\ -\frac{1}{f_2} & \sqrt{\frac{E_2}{E_1}} \end{pmatrix}_{PP_2} \begin{pmatrix} r_0 \\ r'_0 \end{pmatrix}$$

and the general relation between the two focal lengths is [165, 166]:

$$f_2/f_1 = \sqrt{\frac{E_{fin}}{E_{in}}} = \sqrt{\frac{E_1}{E_2}}$$

In **thick** lenses the principal plane position PP_1 and PP_2 are different; if $PP_1 \approx PP_2$ (i.e. the PP distance is small compared to the focal length) the lens is “**thin**”.

As in light optics, the optical properties of a lens system are fully characterized by the behavior of special rays, the **principal rays**:

- the **α -ray**: $\begin{pmatrix} r_{obj} \\ r'_{obj} \end{pmatrix} = \begin{pmatrix} 0 \\ \alpha \end{pmatrix}$. that the plane with **α -rays** crossing the optical axes is an image plane for the system. The image plane position is given by the condition $b(r_{image}=0)$ and of course $\begin{pmatrix} r_{image} \\ r'_{image} \end{pmatrix} = \begin{pmatrix} 0 \\ \alpha' \end{pmatrix}$; the angular magnification of the system $M_\alpha = \alpha'/\alpha$.
- the **γ -ray**: $\begin{pmatrix} r_{obj} \\ r'_{obj} \end{pmatrix} = \begin{pmatrix} \gamma \\ 0 \end{pmatrix}$. The **γ -ray** defines a diffraction plane of the system each time it crosses the optical axes. At the image plane it is valid $\begin{pmatrix} r_{image} \\ r'_{image} \end{pmatrix} = \begin{pmatrix} \gamma' \\ 0 \end{pmatrix}$: the lateral magnification of the system $M_L = \gamma'/\gamma$.
- It can be shown [165] that : $M_L = \sqrt{\frac{E_1}{E_2}} \frac{1}{M_\alpha}$

Electrostatic lenses can be divided in two main groups: Immersion and Einzel lenses. When $V_1 \neq V_2$ the system is called **immersion lens**; if $V_1 = V_2$ the lens is called **Einzel lens**, at least three electrodes are necessary to have a finite focal length.

Einzel lenses are generally thin and symmetric lenses, i.e. the two principal planes coincide and are located at the geometrical center of the lens; as $V_1 = V_2$, $f_1 = f_2$ and the particle kinetic energy does not change ($E_{Kin} = E_{Kfin}$).

For immersion lenses, the principal plane positions differ and the optical center of the lens does not coincide with the geometrical one (their position is shifted towards the area with lower kinetic energy). The focal length is longer in the same direction.

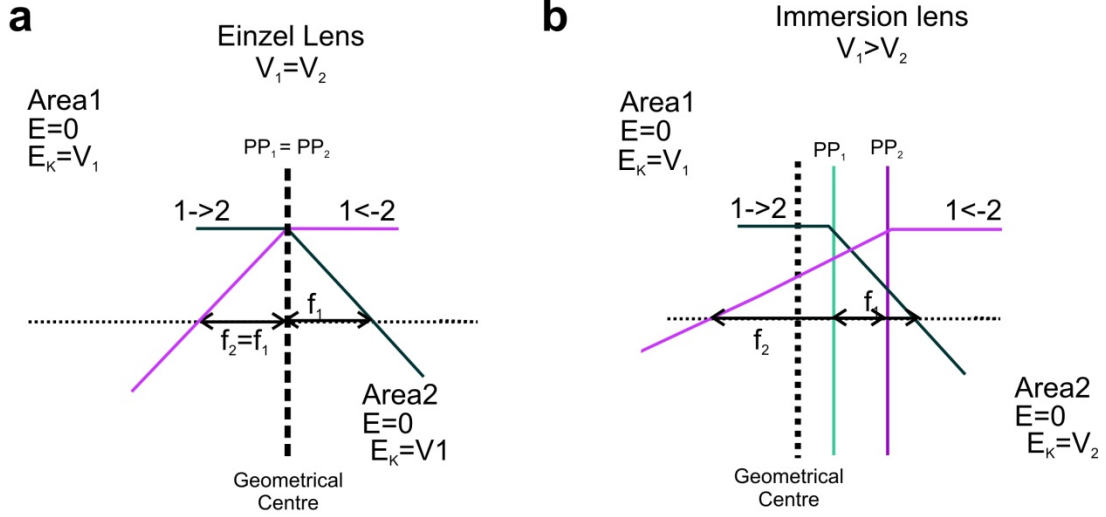


Fig A2 1: Principal plane positions for an (a) Einzel lens and (b) immersion lens. E denotes the electrostatic field in the two areas in front and behind the lens ($E=0$). E_k is the electron energy, while V is the potential of the electrodes in the two areas in front and behind the lens. It is adopted the convention $E_k=V$ as in [165]

Transfer matrix of a composed system

The transfer matrix of a composed lens system is the combination of the individual transfer matrices of each lens. The transfer matrix of a system composed by an immersion and an Einzel lens is:

$$\begin{aligned}
 \begin{pmatrix} r \\ r' \end{pmatrix} &= M \begin{pmatrix} r_{obj} \\ r'_{obj} \end{pmatrix} \\
 &= \begin{pmatrix} 1 & b \\ 0 & 1 \end{pmatrix}^{drift} \begin{pmatrix} 1 & 0 \\ -\frac{1}{f_{ein}} & 1 \end{pmatrix} \begin{pmatrix} 1 & c \\ 0 & 1 \end{pmatrix}_{||PP2}^{drift} \begin{pmatrix} 1 & 0 \\ -\frac{1}{f_{imm}} & \sqrt{\frac{V_1}{V_2}} \end{pmatrix}_{||PP1} \begin{pmatrix} 1 & a \\ 0 & 1 \end{pmatrix}^{drift} \begin{pmatrix} r_{obj} \\ r'_{obj} \end{pmatrix}
 \end{aligned}$$

Where a is the distance between object plane and PP_1 , c is the distance between the two lenses referred to their PP, M^{drift} denote the transfer matrix of a field free zone, the notation $(.)_{||PP}$ denotes on which principal plane the matrix is acting (see Fig. A2).

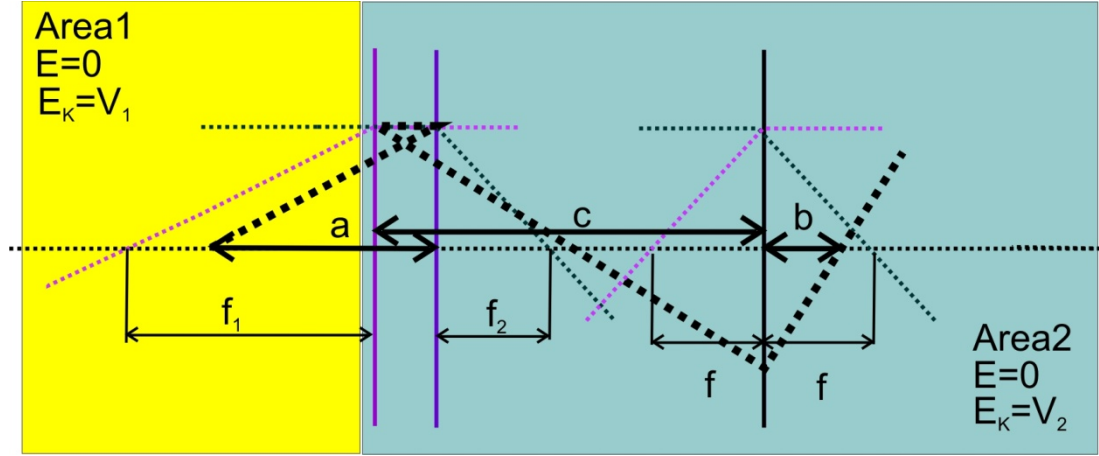


Fig. A2 2: Optical scheme for the combination of an immersion lens and Einzel lens. E_K indicates the kinetic energy of the electron ray. E indicates the electric field. $E_k=V$ as in [165]

Transfer matrices of Omega sectors

As a first approximation, the Ω -filter can be described as the composition of four dispersive lenses:

$$\begin{pmatrix} x \\ x' \\ \Delta E \end{pmatrix}_{exit} = M_+ M_- M_- M_+ \begin{pmatrix} x \\ x' \\ \Delta E \end{pmatrix}_{entrance}$$

Where:

$$M_+ = \begin{pmatrix} 0 & 0 & f & 0 & -f C_\kappa/4 \\ 0 & 0 & 0 & f & 0 \\ -1/f & 0 & 0 & 0 & -C_\kappa/4 \\ 0 & -1/f & 0 & 0 & 0 \\ 0 & 0 & 0 & 0 & 1 \end{pmatrix} = M_0 + D$$

$$M_- = \begin{pmatrix} 0 & 0 & f & 0 & f C_\kappa/4 \\ 0 & 0 & 0 & f & 0 \\ -1/f & 0 & 0 & 0 & C_\kappa/4 \\ 0 & -1/f & 0 & 0 & 0 \\ 0 & 0 & 0 & 0 & 1 \end{pmatrix} = M_0 - D$$

With:

$$M_0 = \begin{pmatrix} 0 & 0 & f & 0 & 0 \\ 0 & 0 & 0 & f & 0 \\ -1/f & 0 & 0 & 0 & 0 \\ 0 & -1/f & 0 & 0 & 0 \\ 0 & 0 & 0 & 0 & 1 \end{pmatrix} \text{ and } D = \begin{pmatrix} 0 & 0 & 0 & 0 & -f C_\kappa/4 \\ 0 & 0 & 0 & 0 & 0 \\ 0 & 0 & 0 & 0 & -C_\kappa/4 \\ 0 & 0 & 0 & 0 & 0 \\ 0 & 0 & 0 & 0 & 0 \end{pmatrix}$$

C_κ is the overall angular dispersion of the filter; i.e. $C_\kappa/4$ is the dispersion of one single sector.

Hexapole: 2nd order transfer matrix

If we consider the vector $V_0 = \begin{pmatrix} x_0 \\ y_0 \\ \alpha_0 \\ \beta_0 \\ E_0 \end{pmatrix}$ describing the ray position at the entrance of the

hexapole field, the action (at the second order) of the hexapole, given in [167], can be equivalently rewritten in the bilinear form matrix form:

$$\Delta V = \begin{pmatrix} \Delta x \\ \Delta y \\ \Delta \alpha \\ \Delta \beta \\ \Delta E \end{pmatrix} = \begin{pmatrix} V_0^T M_x^H V_0 \\ V_0^T M_y^H V_0 \\ V_0^T M_\alpha^H V_0 \\ V_0^T M_\beta^H V_0 \\ 0 \end{pmatrix}$$

Where M_i^H are 5x5 matrices:

$$M_x^H = -K \begin{pmatrix} t^2/2 & 0 & t^3/6 & 0 & 0 \\ 0 & -t^2/2 & 0 & -t^3/6 & 0 \\ t^3/6 & 0 & t^4/12 & 0 & 0 \\ 0 & -t^3/6 & 0 & -t^4/12 & 0 \\ 0 & 0 & 0 & 0 & 0 \end{pmatrix}$$

$$M_y^H = K \begin{pmatrix} 0 & t^2/2 & 0 & t^3/6 & 0 \\ t^2/2 & 0 & t^3/6 & 0 & 0 \\ 0 & t^3/6 & 0 & t^4/12 & 0 \\ t^3/6 & 0 & t^4/12 & 0 & 0 \\ 0 & 0 & 0 & 0 & 0 \end{pmatrix}$$

$$M_\alpha^H = -K \begin{pmatrix} t & 0 & t^2/2 & 0 & 0 \\ 0 & -t & 0 & -t^2/2 & 0 \\ t^2/2 & 0 & t^3/3 & 0 & 0 \\ 0 & -t^2/2 & 0 & -t^3/3 & 0 \\ 0 & 0 & 0 & 0 & 0 \end{pmatrix}$$

$$M_\beta^H = K \begin{pmatrix} 0 & t & 0 & t^2/2 & 0 \\ t & 0 & t^2/2 & 0 & 0 \\ 0 & t^2/2 & 0 & t^3/12 & 0 \\ t^2/2 & 0 & t^3/12 & 0 & 0 \\ 0 & 0 & 0 & 0 & 0 \end{pmatrix}$$

If we refer to the hexapole mid-plane coordinate system $V_m = \begin{pmatrix} x_m \\ y_m \\ \alpha_0 \\ \beta_0 \\ E_0 \end{pmatrix}$, the hexapole effect in the mid-plane can be written (as explicitly shown in Appendix 7) in the form:

$$\Delta V_m = \begin{pmatrix} \Delta x_m \\ \Delta y_m \\ \Delta \alpha \\ \Delta \beta \\ \Delta E \end{pmatrix} = \begin{pmatrix} V_m^T M_x^{Hm} V_m \\ V_m^T M_y^{Hm} V_m \\ V_m^T M_\alpha^{Hm} V_m \\ V_m^T M_\beta^{Hm} V_m \\ 0 \end{pmatrix}$$

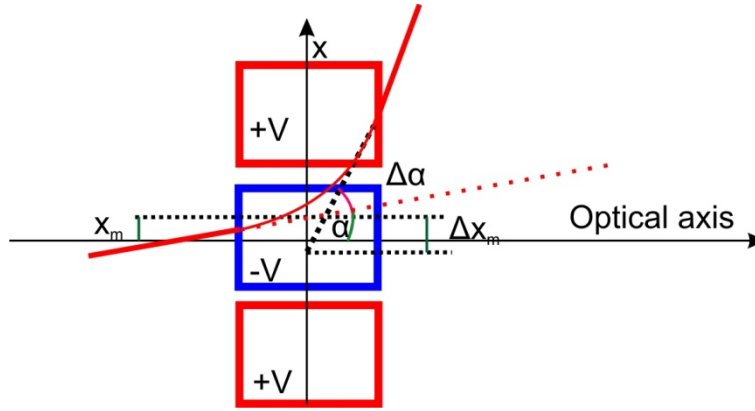


Fig. A2 1: Definition of the coordinate in the hexapole mid-plane reference system.

The matrices M_i^{Hm} have the simplified expression:

$$M_x^{Hm} = K \begin{pmatrix} 0 & 0 & t^3/12 & 0 & 0 \\ 0 & 0 & 0 & -t^3/12 & 0 \\ t^3/12 & 0 & 0 & 0 & 0 \\ 0 & -t^3/12 & 0 & 0 & 0 \\ 0 & 0 & 0 & 0 & 0 \end{pmatrix}$$

$$M_y^{Hm} = -K \begin{pmatrix} 0 & 0 & 0 & t^3/12 & 0 \\ 0 & 0 & t^3/12 & 0 & 0 \\ 0 & t^3/12 & 0 & 0 & 0 \\ t^3/12 & 0 & 0 & 0 & 0 \\ 0 & 0 & 0 & 0 & 0 \end{pmatrix}$$

$$M_\alpha^{Hm} = -K \begin{pmatrix} t & 0 & 0 & 0 & 0 \\ 0 & -t & 0 & 0 & 0 \\ 0 & 0 & t^3/12 & 0 & 0 \\ 0 & 0 & 0 & -t^3/12 & 0 \\ 0 & 0 & 0 & 0 & 0 \end{pmatrix}$$

$$M_\beta^{Hm} = K \begin{pmatrix} 0 & t & 0 & 0 & 0 \\ t & 0 & 0 & 0 & 0 \\ 0 & 0 & 0 & t^3/12 & 0 \\ 0 & 0 & t^3/12 & 0 & 0 \\ 0 & 0 & 0 & 0 & 0 \end{pmatrix}$$

Appendix 3

The optical properties of an Einzel lens and the immersion lens were calculated by direct electron ray tracing. Both lenses consist in three electrodes. The first and the third electrodes have voltages fixed by the boundary conditions; an external shielding around the lens electrode is also included in the model. In the **Einzel lens**, $V_{\text{bias}} = -18\text{kV}$ is applied to the first and third electrode, as well as to the external shielding; in the **immersion lens** the first electrode and shielding are set to $V_{\text{bias1}} = 0\text{ kV}$ while the third electrode and corresponding shielding have $V_{\text{bias2}} = -18\text{ kV}$. Passing through the lens the electrons are decelerate from $E_0 = 20\text{ keV}$ to $E_\Omega = 2\text{ keV}$. For both lenses, the voltage of the central electrode can vary in the range between 0 V and -20 kV.

Computation details

The calculations have been performed using Lorentz E software. The voltage and field distribution is computed applying the Boundary Element Method (BEM). In BEM, electric fields in every point of the whole space are directly calculated from the equivalent sources problem (i.e. charges distribution), applying integral Maxwell's equations. In this way, the boundary conditions are defined only at the surfaces of the electrodes. The results are intrinsically more accurate than for FEM (Finite Element Method) because the integration operation is computationally more stable than differentiation. Symmetric boundary conditions were applied on the xy and yz plane to enhance the speed of voltages calculation (only $\frac{1}{4}$ of the whole geometry was explicitly computed).

Evaluation procedure

The trajectory through the lens of two parallel electron beams (γ -rays), one for each side of the lens was calculated. Each beam is focused in one of the two **focal points** of the lens. **The principal planes positions** are the intersections between the initial trajectory (parallel) and the extrapolation of the linear trajectory in the field free zone after the lens. The **focal length** is the difference between the position of the focal point, i.e. the crossing of the γ -ray, with the optical axis, and the principal plane position.

Applying the procedure for both directions of the incoming beam, the two focal lengths were independently evaluated. Their ratio f_2/f_1 provides a test on the reliability of the simulation.

Theory predicts $f_2/f_1=1$ for the Einzel lens and $\frac{f_1}{f_2} = \sqrt{E_0/E_\Omega} = \sqrt{10}$ for the immersion lens.

Another test on the reliability of the simulation is the conservation of total energy along the whole optical path.

The calculation procedure can be summarized as follow:

- i. The voltage of the central electrode is set to a specific value.
- ii. A beam of parallel rays ($x(z) = x_{in}$), passes through the lens and it is focalized at the focal point z_f . The initial position of the beam sets is $y = -50$ mm for the “forward” direction, and $y = 70$ mm for the “backwards” direction; this guarantee that the starting is in the field free region. The beam have been considered in the paraxial approximation, i.e. the range has been limited to $x = \pm 0.6$ mm
- iii. the electron position $x(z_{plane})$ in the x-y planes perpendicular to the optical axes at $z = z_{plane}$ behind the lens (in the field free zone) is described as:

$$x(z) = x_{in} \cdot (z_{plane} - z_f)/f = x_{in} \cdot m(z).$$

$x(z)$ is obtain from the simulate trajectories on at least tree plane (z_{plane1} , z_{plane2} , z_{plane3}) and $m_i = (z_i - z_f)/f$ is obtained as the slope in the linear fit $x(z_i) = m_i \cdot x_{in}$

- iv. From the linear fit :

$$m(z) = A \cdot (z_{plane}) + B = 1/f \cdot (z_{plane}) - (z_f)/f$$

The **focus position** ($z_f = -B/A$) and the **focal length** ($f = 1/A$), are obtained for each beam directions ("forward" and "backwards")

- v. The corresponding **principal plane position** is found as $z_{pp} = z_f - f$

Einzel lens

The Einzel lens consists of three electrodes (thickness $t = 1$ mm, distance $s = 5$ mm); the first and third electrode aperture diameter is $D = 4$ mm, while in the central electrode (L1) $D = 5$ mm.

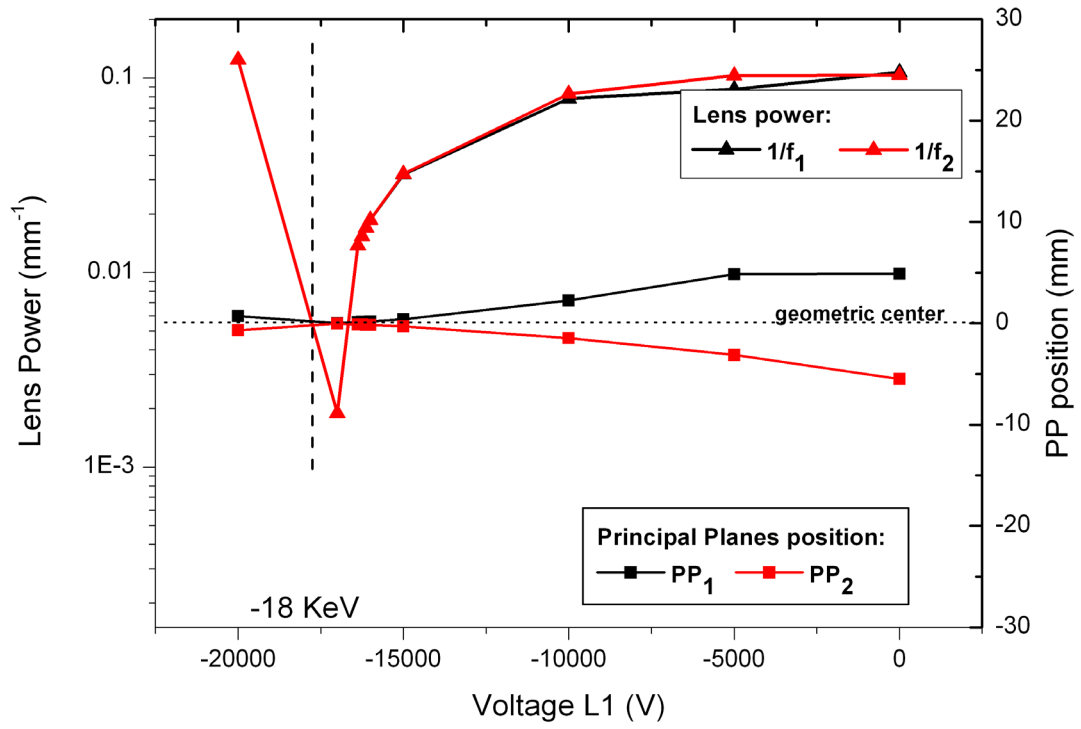


Fig A3 1: focal power and PP positions calculated for the Einzel lens in 1a by direct ray tracing calculation.

Focal lengths and PP positions have been calculated by electron ray tracing in both directions; the central electrode voltage V_{L1} varies in the range $[0 \text{ kV}, -20 \text{ kV}]$; all the other electrodes are set to $V_{\text{bias}} = -18 \text{ kV}$. The electron kinetic energy is $E_k = 2 \text{ keV}$.

Fig A3.1 shows that for $V > 10 \text{ kV}$, the lens can be considered as a thin lens ($PP_b \approx PP_f \approx 0$). The PP positions are symmetric with respect to the lens geometrical center. The focal length have an asymptotic behavior for $V_{L1} = -18 \text{ kV}$. If $V_{L1} = -18 \text{ kV}$, the beam is not focused (the focusing electric field strength is $E = 0 \text{ V/m}$): $f = \infty$.

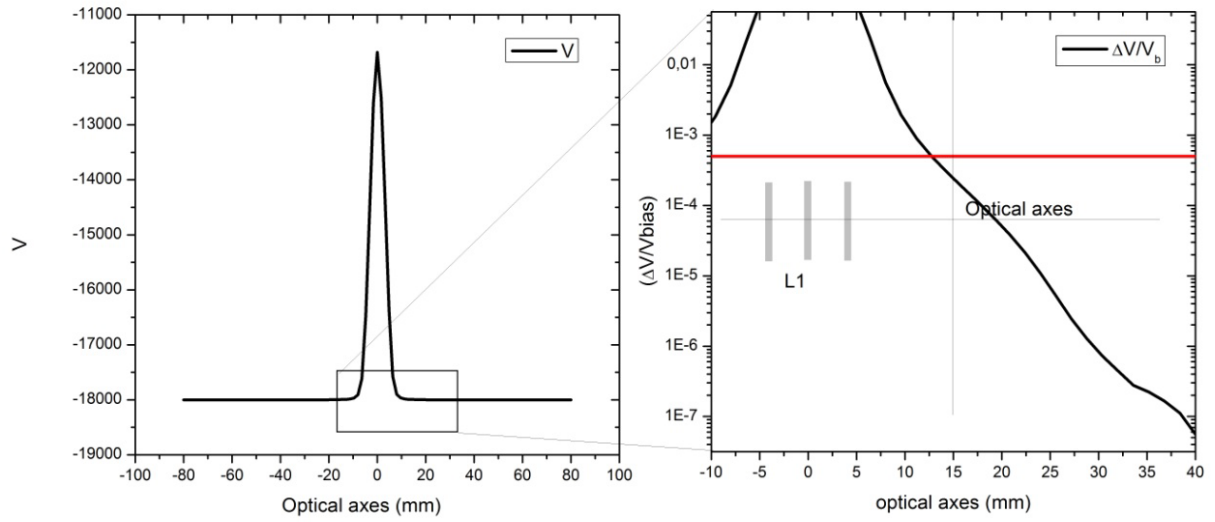


Fig A3 2: Evaluation of the lens extent along the optical axes. The deflecting field is considered as zero if the voltage $V \approx 0$.

Fig. A3.2 shows the profile $V(z)$ along the optical axes. As we can see from Fig A3.2, at 15 mm after the central electrode $V(z) \approx V_b$, and the electric field $E \approx 0$. This means that for $b > 15$ mm the influence of the electric field on the electron ray is negligible (“field free zone”).

Immersion lens

The first Immersion lens considered consists of three electrodes (thickness $t = 1$ mm, distance $s = 5$ mm, internal diameter $D = 10$ mm). The electron have $E_k = 20$ keV in the forward direction and $E_k = 2$ keV in the backward direction. ($E_{\text{tot}} = 20$ keV = const.)

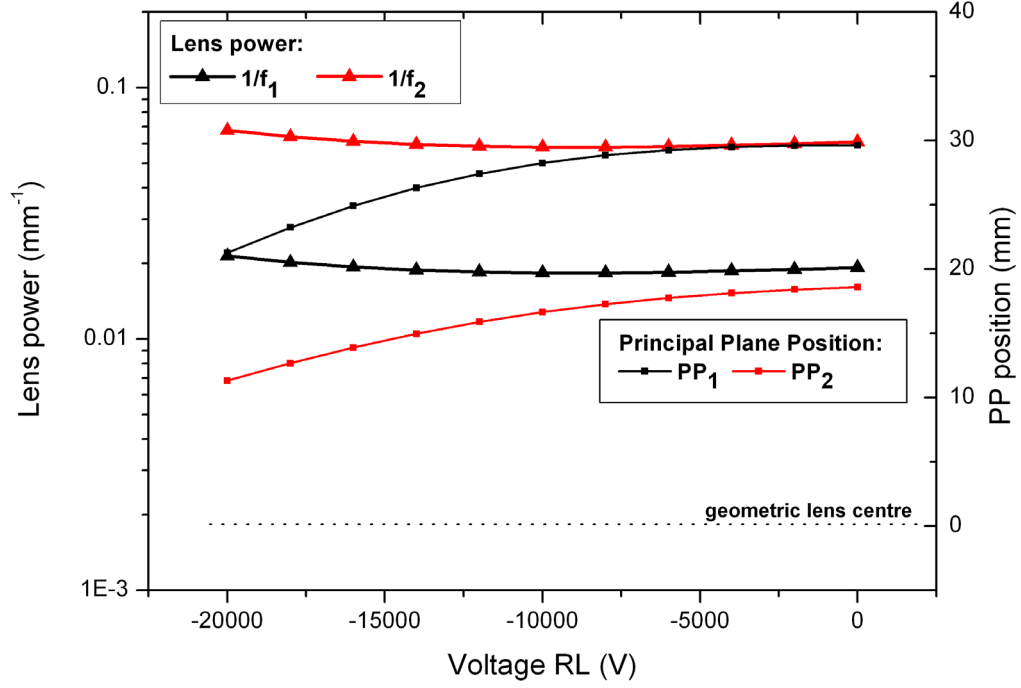


Fig A3 3: focal lengths and PP positions calculated for the immersion lens by direct ray tracing calculation

From Fig. A3 2 we see that:

- The immersion lens is a thick asymmetric lens ($PP_1 \neq PP_2$). The PP position is shifted behind the third electrode: the geometric and the optical centers do not coincide. The lower V_{RL} , the more the PP positions shift behind the third electrode.
- The focal lengths are related to the kinetic energy by the ratio $\frac{f_1}{f_2} = \sqrt{\frac{E_1}{E_2}} = \sqrt{10}$ (fast electron are less deflected than slow electrons), in our case the ratio of the kinetic energy before and after retarding is set to $\frac{E_1}{E_2} = 10$.
- The range of the focal length is strongly limited. No asymptotic behavior for the focal length is expected. In fact, for any value of V_{RL} an electrostatic field exists between the initial and the final electrode ($V_{bias1} \neq V_{bias2}$).

Two extreme situations can occur, when the voltage of the central electrode, V_{RL} , assume $V_{RL} = 0$ kV or $V_{RL} = -18$ kV. In the first case, the first electrode and RL are at the same voltage, i.e. the deflecting electric fields between these two electrodes is 0; the deflection occurs only between RL and the last electrode. In the second case there is an electric field only between

the first electrode and RL, as $V_{RL}=V_{bias2}$. For $V_{RL}<-18$ kV the lens is strongly decelerating the electrons, the electron beam is partially reflected.

For the **immersion lens**, the PPs shift and the focal length range depends on the lens geometries. Therefore, I have evaluated the effect of scaling the system:

- rescaling the whole geometry
- changing the electrodes distance
- changing the electrodes thickness
- changing the aperture diameter

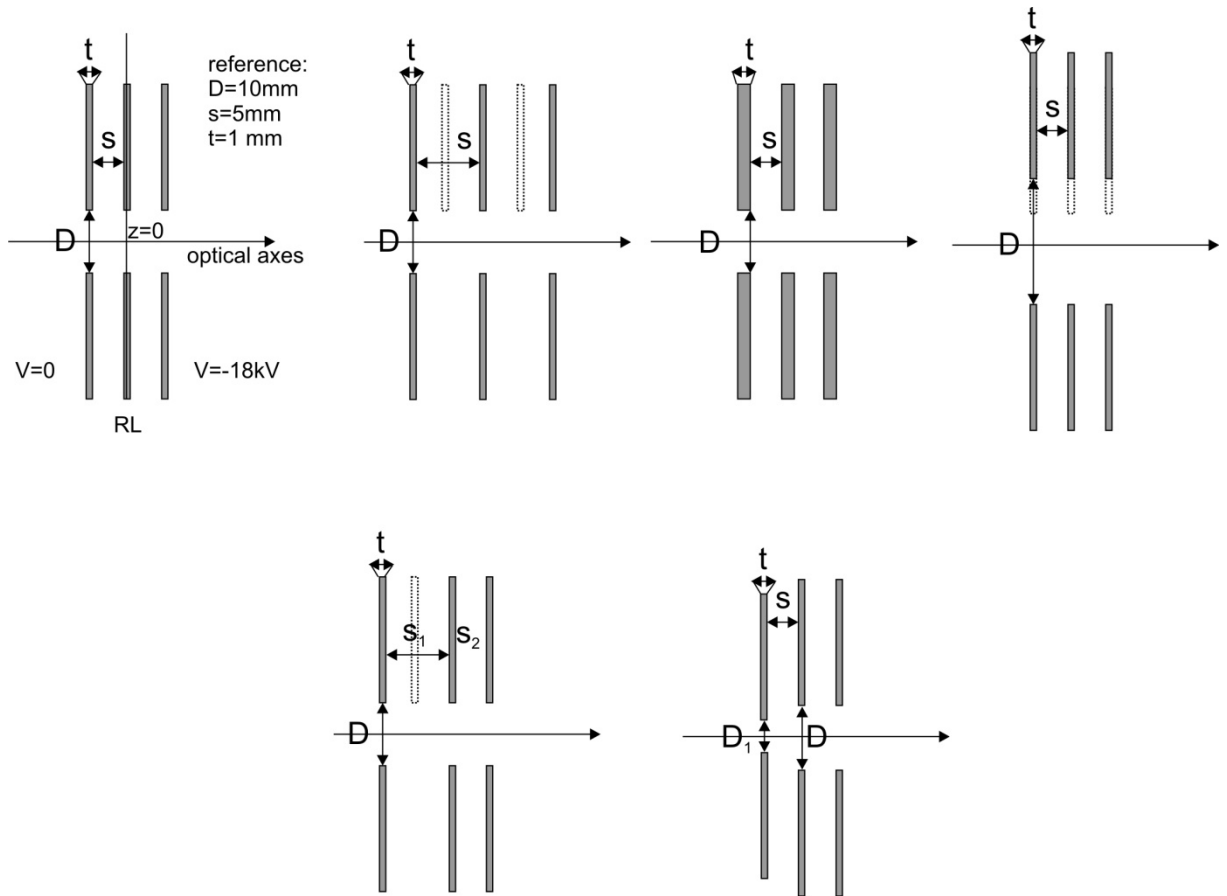


Fig A3 4: summary of the geometric modifications to the electrode distributions respect to the reference geometry $D = 10$ mm; $t/D = 0.1$; $s/D = 0.5$.

Immersion lens: shape optimization

The retarding system (RS) behavior is entirely described by two parameters: a and f_{RL} , the immersion lens focal length (in fact the focal length of the Einzel lens and distance between the immersion lens and the Einzel lens is set: $f_{L1}=1.4 a$). The value a depends mainly on the position of the first principal plane of RL, which varies with the voltage assigned to the central electrode.

Fig A3 5 summarizes the key results of the optimization analysis. The plot shows a portion of the (a, f_{RL}) plane. The colored area in the plane represents the conditions for a lens shorter than 200 mm satisfying the required angular magnification $M_a = 1/1.4$. The colors are associated to the value b (the distance from the image plane from the center of L1). The gray area represents the conditions $b < 0$ mm: the system has a virtual image behind L1. The blue area represents the conditions $b > 15$ mm: the image plane is the field free zone after L1.

The colored lines represents the value for a and f_{RL} obtained from the simulations of different lens geometries. Each point on the line corresponds to a voltage assigned to the central electrode, i.e. $V = 0, 10, 15, 20$ kV. Each of the four graphs sketches the effects of the rescaling of one of the construction parameters of the lens. The geometric changes refer to the “reference geometry” ($D = 10$ mm; $s/D = 0.5$; $t/D = 0.1$), arbitrarily chosen. Only lenses with curves, intercepting the blue area, can be implemented in the retarding system. From Fig A3 5, one sees that RL needs an aperture diameter in the range $[17.5, 20]$ mm.

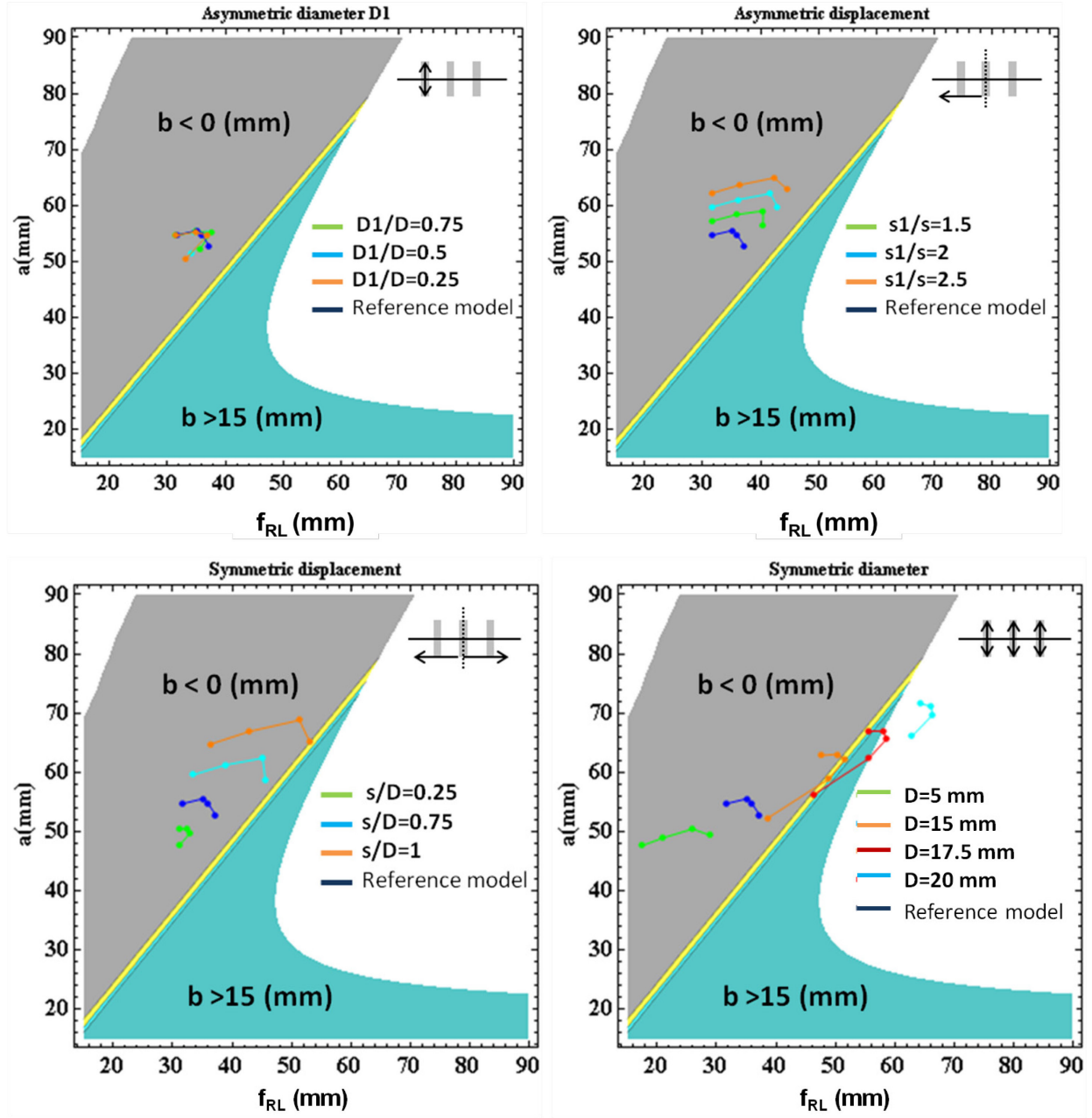


Fig A3 5: summary of the optical properties obtained for several kind of electrodes distributions. the colored areas correspond to lens systems shorter than 200 mm. The gray area indicates the conditions for virtual image (before L1); blue area indicates the conditions where the image plane is in the field free zone. The reference model corresponds to $D = 10\text{mm}$; $s/D = 0.5$; $b/D = 0.1$ (See Appendix 3).

The connection between the transfer optics to the retarding system is also an aperture (set to a bias voltage), and in principle acts as a part of the lens itself. Therefore, the influence of the shape of the **UHV sealing system** connection between the transfer and adaptive optics was investigated (See Fig A3 6 for the specific geometries).

In all the considered cases, the electrodes have an aperture diameter $D = 20$ mm, are spaced by $s = 5$ mm and have a thickness $b = 1$ mm. The sealing system consists in a tube with a diameter of 4 mm. The end of the tube can have different distances from the central electrode. Fig A3 10 summarizes the results of the analysis.

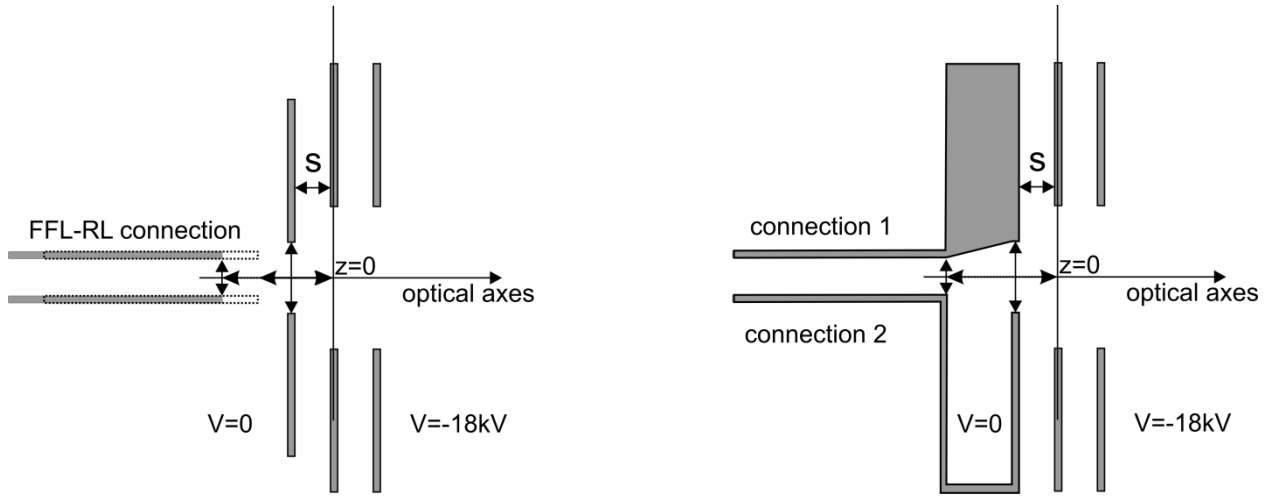


Fig A3 6: Schemes of possible optical setup for several kinds of mechanical connections between transfer optics and adapting optics..

Again, the blue area represents the values of a and f_{RL} satisfying three constraints: the system has a real image in the field free zone, the lens is shorter than 200 mm and $M_a = 1/1.4$.

In the first case (light blue curve), the tube ends at 10 mm from the central electrode and there is no connection. For the dark blue curve, the tube is 10 mm from the central electrode and it is connected directly to the first electrode (the shape of the connection is shown in Fig A3 6). Comparing the two curves, we see that the presence of the connection changes the properties of the lens. For the orange and the olive curves, the connection is 5 mm apart from the central electrode, but the type of connection is different: hence, the curves are not influenced by connection shape.

The green curve describes the situation when the central electrode is directly connected to the end of the sealing tube. We note that also in this case there is no significant change of the properties of the system. However, it minimized the spacing between the sealing and the central electrode and therefore this solution was implemented in the final system. This last geometry was implemented in the RS.

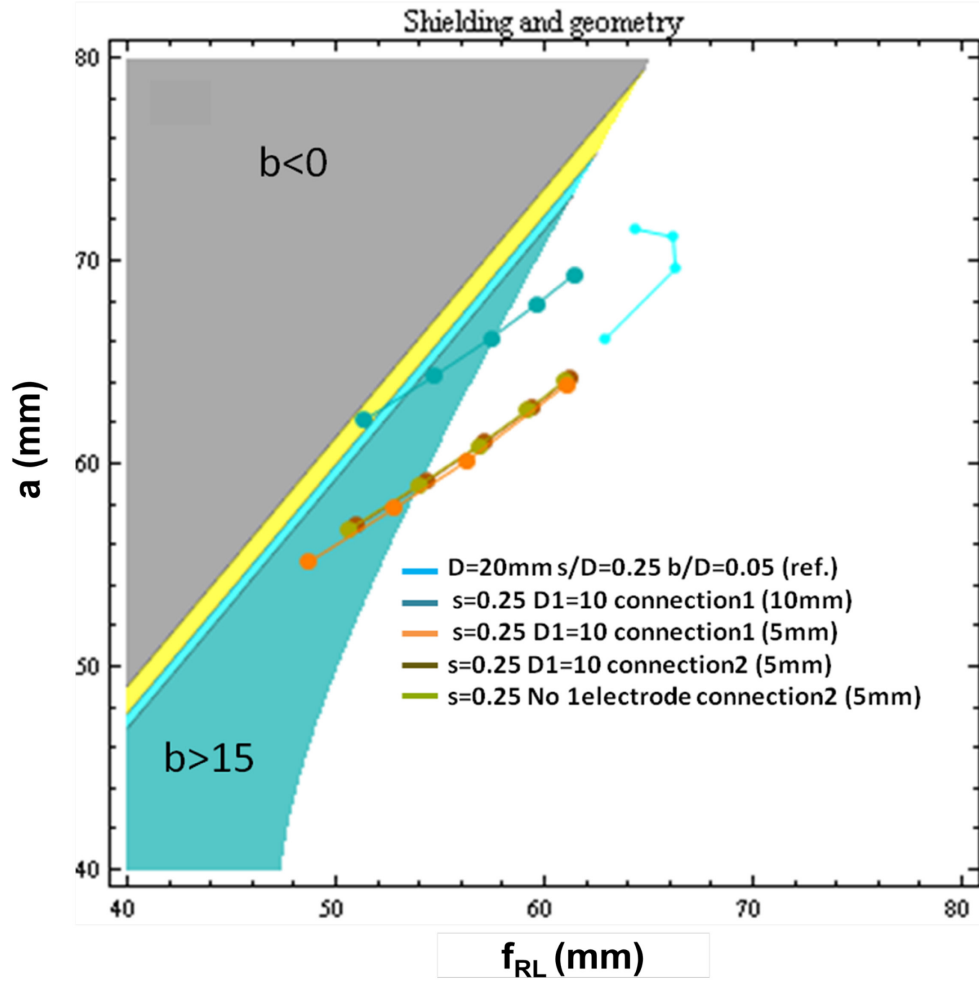


Fig A3 7: Summary of the characterization obtained for two kinds of possible UHV sealing connections (geometry indicated in Fig A3 4). The colored areas correspond to lens systems shorter than 200 mm. The gray area indicates the conditions for virtual image (before L1); the blue area marks the conditions where the image plane is in the field free zone.

Appendix 4

The maximum angular spread $\Delta\alpha$ is limited by the (contrast) aperture in the diffraction plane (also called back focal plane: BFP), centered on the optical axis. In the following image plane it is (Fig. A4.1):

$$\Delta\alpha = \Delta_{slit} \cdot \cos(\theta) / L,$$

where Δ_{slit} is the aperture width, θ is the tilt angle between the incoming ray and the optical axes and L is the distance between the BFP and the image plane.

The maximum angular spread occurs at $\theta = 0$, i.e. for rays imaged on the axes (α -rays). In the case of the energy filtering system, the angular spread of the beam after the Ω -filter corresponds to the energy spread of the beam. Therefore, rays imaged on the axes have the worst energy resolution.

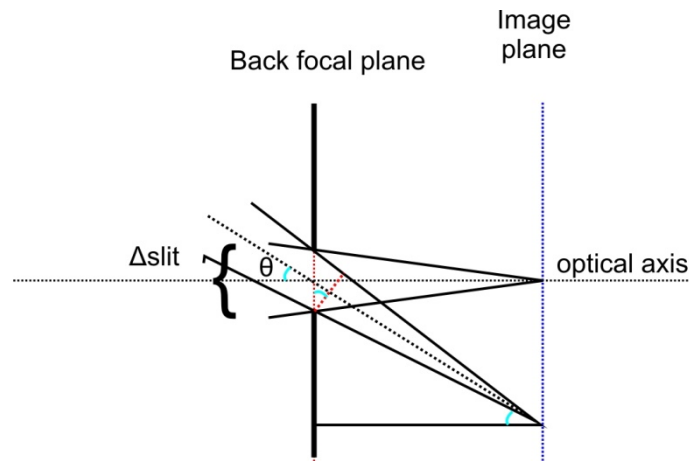


Fig.A4 1: geometrical relationship between the slit opening (in the diffraction plane) and the corresponding angular spread at the image plane.

A ray passing through an accelerating lens system AS ($E_{k1} < E_{k2}$), the general relation between the starting angle α_{obj} (which in this case the Ω -filter exit angle), L (the distance between the image and the diffraction plane) and x_{BF} (the position in the back focal plane of the lens) is:

$$x_{BF} = \alpha_{image} \cdot L = M_{\alpha} \cdot \alpha_{obj} \cdot L$$

This relation is easily found considering an **alpha ray** (i.e. the starting conditions are $(r, r')_0 = (0, \alpha)$ as defined in Appendix 2), but it is true for all other rays, as the position in the diffraction plane depends only on the starting angle α_{obj} .

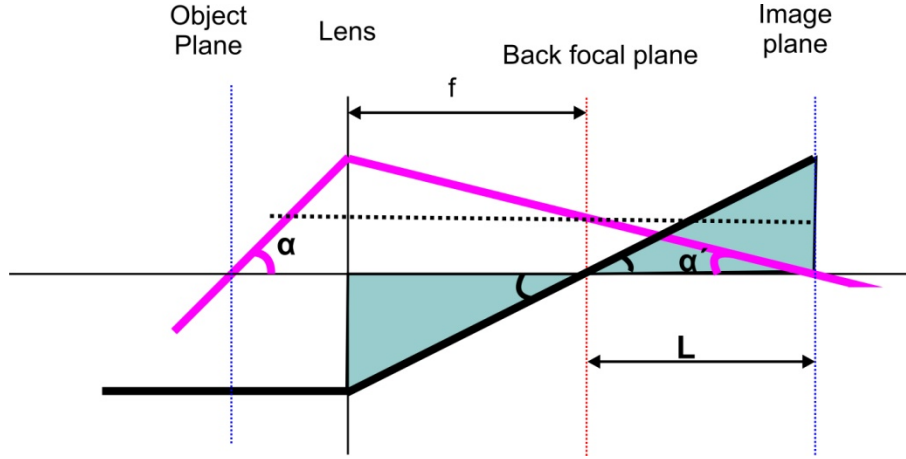


Fig.A4 2: Evaluation of the diffraction plane position as function of starting angle, L (distance between image and diffraction plane) and f_{AS} (focal power of the lens system). The light green triangles are similar.

If we consider a **gamma ray** (i.e. starting conditions $(r, r')_0 = (\gamma, 0)$), we find the relation:

$$\gamma_{image} / \gamma_{obj} = M_L = L / f_{AS} \rightarrow \sqrt{E_1 / E_2} \cdot 1 / M_\alpha = L / f_{AS}.$$

Where f_{AS} is the focal length of the total lens system (i.e. $1/f_{AS}$ is the outgoing angle for an incoming parallel beam) (see Fig.A4 2); γ_{obj} is the position at the Object plane. The relation is valid because the colored triangles in Fig A4 2 are similar.

From these relations, it follows:

$$x_{BF} = \alpha_{obj} \cdot \sqrt{E_1 / E_2} f_{AS}$$

We now consider the case of the accelerating system after the Ω - filter.

Given C_k as the angular dispersion of the Ω - filter:

$$\frac{\Delta \alpha_{image}}{\Delta E} = C_k$$

It follows that the linear dispersion in the BFP $C_{klinear}$ is:

$$C_{klinear} = \frac{\Delta x_{BF}}{\Delta E} = \frac{\Delta \alpha_{image}}{\Delta E} \cdot \sqrt{E_1 / E_2} f_{AS} = C_k \cdot \sqrt{E_1 / E_2} f = M_\alpha \cdot C_k \cdot (L);$$

The energy of the electron passing through a window through an aperture (size Δ_{slidt}) in the BFP of AS is therefore:

$$\Delta E = \frac{\Delta_{slidt} \sqrt{E_2 / E_1}}{C_k \cdot f_{AS}} = \frac{\Delta_{slidt}}{M_\alpha \cdot C_k \cdot (L)}$$

Appendix 5

Fig A5 1 shows the optical properties of the immersion lens AL ($E_{K1} = 2 \text{ keV}$; $E_{K2} = 20 \text{ keV}$).

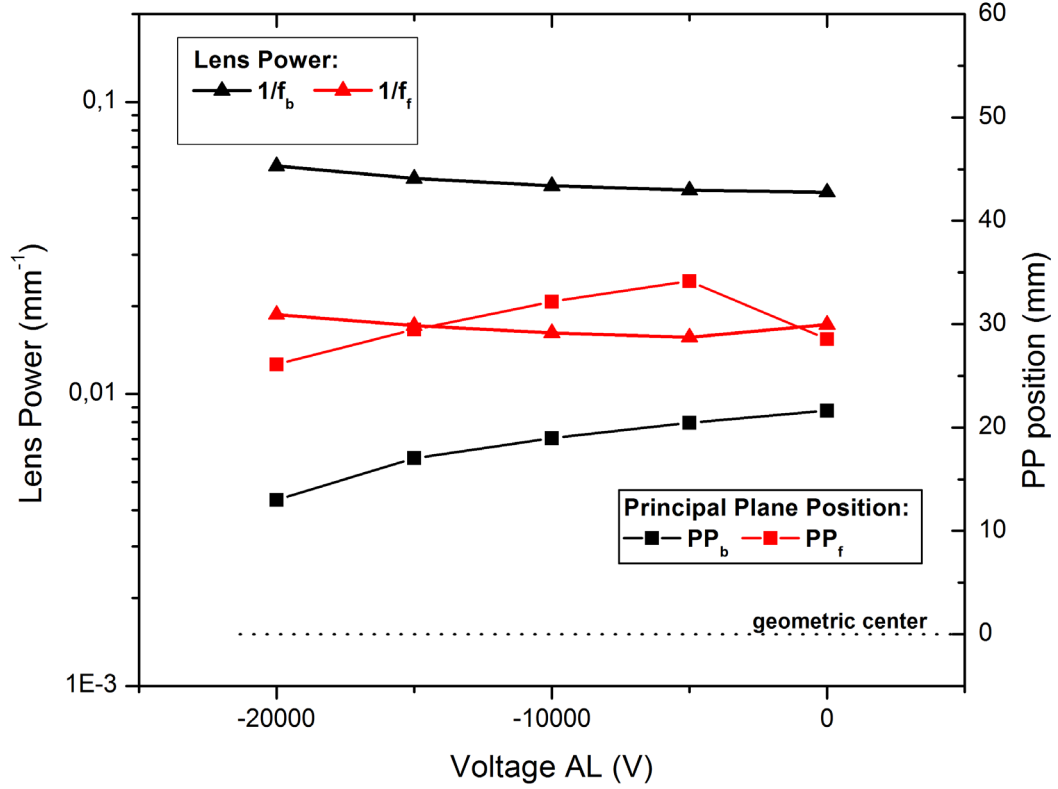


Fig. A5 1: Focal lengths and PP positions calculated for AL immersion lens (see text paragraph 1.2.2) by direct ray tracing calculation.

At $V_{AL} = -10 \text{ kV}$ the focal length is 61.84 mm. Assuming that the slit placed in the BF plane is $\Delta_{slit} = 3 \text{ }\mu\text{m}$ wide, the expected energy resolution expected for this value of the focal length is $\Delta E = 0.077 \text{ eV}$.

The system was simulated by ray tracing (image and diffraction rays) considering:

- one γ -ray (parallel)
- three image rays (α -rays) starting with initial angles 0.2 mrad, 0.15 mrad and 0.075 mrad; these angles correspond to $\Delta E = 0.1, 0.075, 0.0375 \text{ eV}$, respectively; the last value corresponds also to half of the expected angular dispersion for the whole image.

For each of these rays the crossing with the optical axes (diffraction or image plane position), outgoing angle (angular magnification), the ray position at the diffraction plane (Linear dispersion) and the lens length have been evaluated. The starting position have been varied in the range between 40 mm and 180 mm

Moreover, known the PP positions, the corrected value for a and b have been found, leading

to an independent determination of $M_L = \sqrt{E_1/E_2} \cdot 1/M_\alpha$.

Taking advantage from the lens equation $\sqrt{10}/b = 1/a - 1/f$ we provide an additional check on the simulation reliability.

The diffraction plane is at $d = -29.71$ mm after the lens, in the field free zone. The lens length reaches a minimum for $M_L = 0.5$ and increases again.

Appendix 6

The **projector system** consists in 2 lenses (P_2 and P_3) with adjustable focal length, between [4, 36] mm; the two magnetic lenses are separated by 98 mm. The round detector, 40 mm in diameter, is placed at the fixed image plane of P_3 ; its distance from P_3 is 172 mm. The wide focal range and the large lens-lens and lens-image plane distance, provide a large magnification range.

The magnification range, which depends on the distance between the image plane of AL image- and P_2 , has been evaluated using simple equations for a two lens systems. The required projector magnification lies in the range between $M_{\min} = 40$ and $M_{\max} = 60$; these values have been obtained according to the relation:

$$M_{tot} = M_{obj} \cdot M_{TO} \cdot M_{RS} \cdot M_{\Omega} \cdot M_{AL} \cdot M_{proj}$$

(where the total magnification range is $M_{tot} = [5 \cdot 10^2, 1 \cdot 10^5]$; the objective lens magnification is $M_{obj} = 18$; the transfer optics magnification range is $M_{TO} = [0.39, 42]$; the retarding system magnification is $M_{RS} = 4.43$, the filter magnification is $M_{\Omega} = 1$ and the accelerating system magnification is $M_{AL} = 0.56$). For AL image- P_2 distance between 5 mm and 7 mm the conditions on the projector magnification are always satisfied (Fig. A6.1).

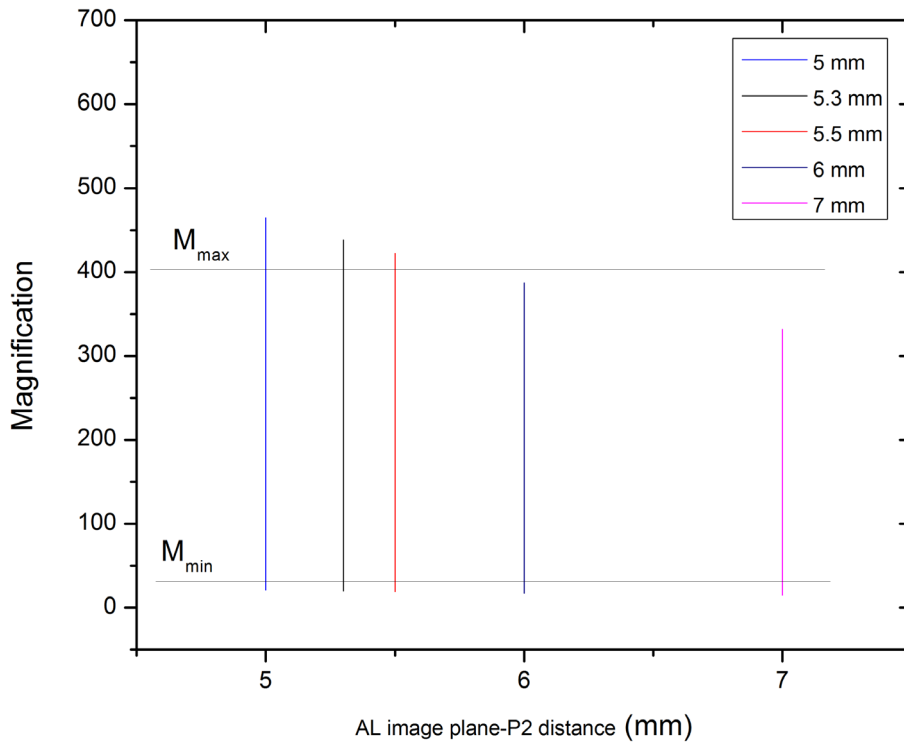


Fig. A6 1: expected magnification ranges for varying distances of AS- P_2

Also the diffraction planes (the plane of energy dispersion) needs to be magnified and projected on the screen. In this working modality, the so called "dispersive plane" mode, the microscope works as a standard non-imaging energy analyzer: in the "dispersive plane" the position on the horizontal axes is linearly related to energy.

E_0 , set by the objective lens voltage, corresponds to the central position; both the energy window $\pm\Delta E$ and the energy resolution σ_E depend on M_{Ld} which is the projector magnification of the **dispersive plane**:

$$\Delta E = \frac{1}{2} \left(\frac{\Delta_{Screen}}{M_{Ld}} \right) \cdot \frac{1}{C_{k_{linear}}} = \frac{1}{2} \left(\frac{40 \text{ mm}}{M_{Ld}} \right) \cdot \frac{1 \text{ eV}}{39.1 \mu\text{m}}$$

$$\sigma_E = \frac{2\Delta E}{\#_{pixel}} = 2\Delta E / 1024$$

Where $\#_{pixel}$ is the number of pixel of the revelator.

The optimal energy window $2\Delta E = 25 \text{ eV}$ is obtained for $M_{Ldproj} = 41$; the corresponding energy resolution $\sigma_E = 25 \text{ meV}$.

Taking in account the distance $L = 30.85 \text{ mm}$ between diffraction and image plane for the accelerating system considered, it is possible to show that the condition the $M_{Ldproj}=41$ is always satisfied for distances between AL image plane and P_2 distance lying the range considered above (i.e. 5 mm and 7 mm).

The expected magnification ranges at varied AL- P_2 distances are summarized in Table A6 1.

AL- P_2 (mm)	M_{min}	M_{max}	$f_{p2} (M_{min})$ (mm)	$f_{p3} (M_{min})$ (mm)	$f_{p2} (M_{max})$ (mm)	$f_{p3} (M_{max})$ (mm)
5	21	464	5,77	45	5,62	6,5
5,3	19,75	438	6,18	45	5,63	6,5
5,5	19	422	6,46	45	5,85	6,5
6	17,5	387	7,15	45	6,42	6,5
7	15	331	8,63	45	7,6	6,5

Table A6 1: Min-Max magnification ranges and corresponding f_{p3} and f_{p2} for various AL-image-plane- P_2 distances

Appendix 7

Theoretical approach

The potential distribution of an electrostatic hexapole is (the coordinate definition follows Fig A7 1):

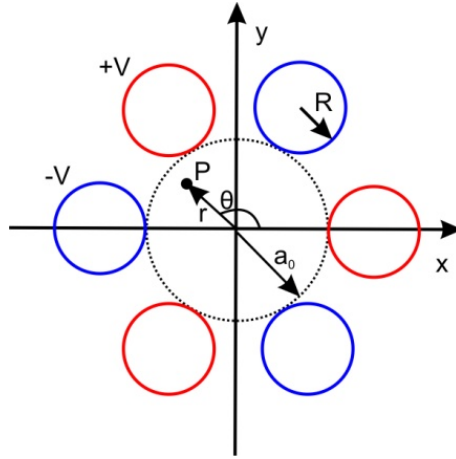


Fig. A7 1: Scheme of an hexapole, coordinate definition.

$$\varphi(x, y) = \frac{V}{a_0^3} (x^3 - 3xy^2) = k(x^3 - 3xy^2)$$

Where a_0 is the internal radius of the hexapole, and V is the electrodes voltage.

The deflection can be calculated by integration of the particle motion equation. The second order solutions for the particle trajectory at the exit of the hexapole can be written[167]:

Positions:

$$\frac{x_1^M}{a_0} = \frac{x_0}{a_0} + t \tan \alpha_0 - k \left(\left(\frac{1}{2} \left(\frac{x_0}{a_0} \right)^2 - \left(\frac{y_0}{a_0} \right)^2 \right) \left(\frac{t}{a_0} \right)^2 + \frac{1}{3} \left(\frac{x_0}{a_0} \alpha_0 - \frac{y_0}{a_0} \beta_0 \right) \left(\frac{t}{a_0} \right)^3 + \frac{1}{12} (\alpha_0^2 - \beta_0^2) \left(\frac{t}{a_0} \right)^4 \right)$$

$$\frac{y_1^M}{a_0} = \frac{y_0}{a_0} + t \tan \beta_0 + 2k \left(\frac{1}{2} \frac{x_0}{a_0} \frac{y_0}{a_0} \left(\frac{t}{a_0} \right)^2 + \frac{1}{6} \left(\frac{x_0}{a_0} \beta_0 + \frac{y_0}{a_0} \alpha_0 \right) \left(\frac{t}{a_0} \right)^3 + \frac{1}{12} \alpha_0 \beta_0 \left(\frac{t}{a_0} \right)^4 \right)$$

Angles:

$$\tan \alpha_1^M = \tan \alpha_0 - k \left(\left(\left(\frac{x_0}{a_0} \right)^2 - \left(\frac{y_0}{a_0} \right)^2 \right) \left(\frac{t}{a_0} \right) + \left(\frac{x_0}{a_0} \alpha_0 - \frac{y_0}{a_0} \beta_0 \right) \left(\frac{t}{a_0} \right)^2 + \frac{1}{3} (\alpha_0^2 - \beta_0^2) \left(\frac{t}{a_0} \right)^3 \right)$$

$$\tan \beta_1^M = \tan \beta_0 + 2k \left(\frac{x_0}{a_0} \frac{y_0}{a_0} \left(\frac{t}{a_0} \right) + \frac{1}{2} \left(\frac{x_0}{a_0} \beta_0 + \frac{y_0}{a_0} \alpha_0 \right) \left(\frac{t}{a_0} \right)^2 + \frac{1}{3} \alpha_0 \beta_0 \left(\frac{t}{a_0} \right)^3 \right)$$

Where $(x_0, y_0, \alpha_0, \beta_0)$ are the position and angles (respectively) at the entrance hexapole plane; $(x_1^M, y_1^M, \alpha_1^M, \beta_1^M)$ are the exit coordinate, $k = 3/2 \frac{V}{E_k}$, t is a parameter which describes the hexapole field extent (and it is different from the hexapole geometrical thickness).

The deviation from the unperturbed particle trajectory at the exit of the hexapole field is:

$$\Delta x = - \frac{k}{a_0^3} \left(\left(\frac{t^2}{2} (x_0^2 - y_0^2) \right) + \frac{t^3}{3} (x_0 \alpha_0 - y_0 \beta_0) + \frac{t^4}{12} (\alpha_0^2 - \beta_0^2) \right)$$

$$\Delta y = + \frac{2k}{a_0^3} \left(x_0 y_0 \frac{t^2}{2} + (x_0 \beta_0 + y_0 \alpha_0) \frac{t^3}{6} + \alpha_0 \beta_0 \frac{t^4}{12} \right)$$

$$\Delta \alpha = - \frac{k}{a_0^3} \left((x_0^2 - y_0^2) t + (x_0 \alpha_0 - y_0 \beta_0) t^2 + (\alpha_0^2 - \beta_0^2) \frac{t^3}{3} \right)$$

$$\Delta \beta = + 2 \frac{k}{a_0^3} \left(x_0 y_0 t + (x_0 \beta_0 + y_0 \alpha_0) \frac{t^2}{2} + \alpha_0 \beta_0 \frac{t^3}{3} \right)$$

These equations can be strongly simplified if, we refer to the hexapole mid-plane ones $(x^m, y^m, 0)$ (see Fig. A7 2). We assume the origin of the coordinate system at the center of the multipole field of extent t .

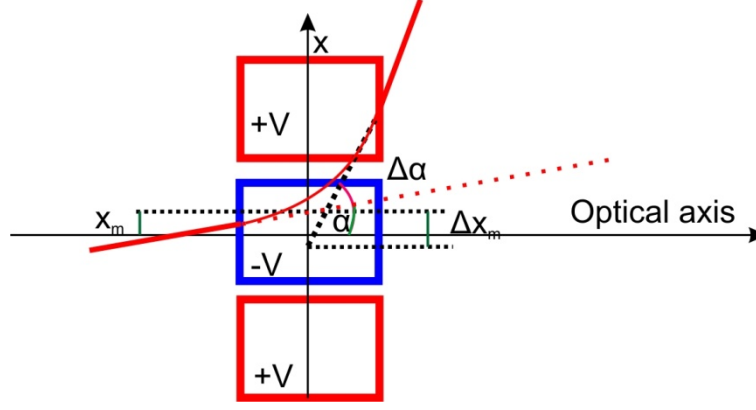


Fig. A7 2: Definition of the mid-plane coordinate system as projection on the central hexapole plane.

$x_0 = \left(x^m - \frac{t}{2}\alpha_0\right); y_0 = \left(y^m - \frac{t}{2}\beta_0\right)$ where α_0 and β_0 are the initial angles.

If we rewrite the exit conditions, we find that, at the exit,

$$x_1 = \left(x_m + \frac{t}{2}\alpha_0\right) + \Delta x; y_1 = \left(y_m + \frac{t}{2}\beta_0\right) + \Delta y; \alpha_1 = \alpha_0 + \Delta\alpha; \beta_1 = \beta_0 + \Delta\beta$$

If we project the effect of the multipole on the mid-plane, we can write:

$$x_1^m = \left(x_1 - \frac{t}{2}\alpha_1\right) = \left(x_m + \frac{t}{2}\alpha_0\right) + \Delta x - \frac{t}{2}(\alpha_0 + \Delta\alpha) = x_m + \left(\Delta x - \frac{t}{2}\Delta\alpha\right) = x_m + \Delta x^m$$

where Δx^m is the "effective action" of the multipole described in the mid-plane coordinate.

For the explicit calculation of Δx^m we find:

$$\begin{aligned} \Delta x^m &= -\frac{k}{a_0^3} \left[\left(\left(\frac{t^2}{2}(x_0^2 - y_0^2) \right) + \frac{t^3}{3}(x_0\alpha_0 - y_0\beta_0) \right. \right. \\ &\quad \left. \left. + \frac{t^4}{12}(\alpha_0^2 - \beta_0^2) \right) \right] - \frac{t}{2} \left[-\frac{k}{a_0^3} \left((x_0^2 - y_0^2)t + (x_0\alpha_0 - y_0\beta_0)t^2 \right. \right. \\ &\quad \left. \left. + (\alpha_0^2 - \beta_0^2)\frac{t^3}{3} \right) \right] = -\frac{k}{a_0^3} \left[\left(-\frac{t^3}{6}(x_0\alpha_0 - y_0\beta_0) - \frac{t^4}{12}(\alpha_0^2 - \beta_0^2) \right) \right] \\ &= -\frac{k}{a_0^3} \left[\left(-\frac{t^3}{6} \left(\left(x^m - \frac{t}{2}\alpha_0\right)\alpha_0 - \left(y^m - \frac{t}{2}\beta_0\right)\beta_0 \right) - \frac{t^4}{12}(\alpha_0^2 - \beta_0^2) \right) \right] \\ &= +\frac{k}{a_0^3} \frac{t^3}{6} (x^m\alpha_0 - y^m\beta_0) \end{aligned}$$

Similarly, we obtain:

$$\Delta y^m = -\frac{k}{a_0^3} \frac{t^3}{6} (x^m \beta_0 + y^m \alpha_0)$$

By substitution, we find:

$$\Delta \alpha = -\frac{k}{a_0^3} (t ((x^m)^2 - (y^m)^2) + \frac{t^3}{12} (\alpha_0^2 - \beta_0^2))$$

$$\Delta \beta = +2 \frac{k}{a_0^3} \left(x^m y^m t + \alpha_0 \beta_0 \frac{t^3}{12} \right);$$

For simplicity, we adopt the notation

$$K = \frac{k}{a_0^3} (\text{mm}^{-1}) \quad A = \frac{1}{6} K t^3 (\text{mrad}^{-1}) \quad B = -K t (\text{mrad mm}^{-2})$$

Hexapole simulation

The deflection coefficients were calculated by ray trajectories tracing using Lorentz-E. Several hexapole geometries were considered. The electrode voltages are: $V = 25, 50, 100, 500 \text{ V}$.

The deflection coefficients were evaluated directly, considering the electron ray deflections from the unperturbed coordinate, using electron beams with all possible combination of two non-zero starting variables (i.e. α_0 - x_0 , x_0 - y_0 , x_0 - β , α_0 - β_0 , α_0 - y_0 , y_0 - β_0). The starting positions varied in the range $x_0/y_0 = \pm 0.75 \text{ mm}$ (x and y respectively), the starting angles in the range α - $\beta = \pm 20 \text{ mrad}$ (xz and yz planes respectively). The beams originate from the field free zone ($z = +50 \text{ mm}$). The deflections were obtained by extrapolation of the electron positions on two planes in the field free zone after the hexapole ($z = -40 \text{ mm}$ and $z = -50 \text{ mm}$).

First the correctness of the equations referred to the mid-plane coordinates were tested, by projecting the measured ray deflections (angle and positions in both x and y directions) in the hexapole mid-plane and evaluating their dependency on mid-plane projection of the starting variables. This also gives the determination of the coefficients A and B defined above as function of several multipole geometries and voltages.

The value of K was found from the relationship $K = \sqrt{-\frac{B^3}{6A}}$. Fig A7 3 shows that K depends linearly on the electrode voltage. The deviation from linearity, observed for the smallest hexapole (green line), are attributed to the predominance of higher order effects. In fact, the (simulated) electron beam size is comparable with the internal radius of the multipole.

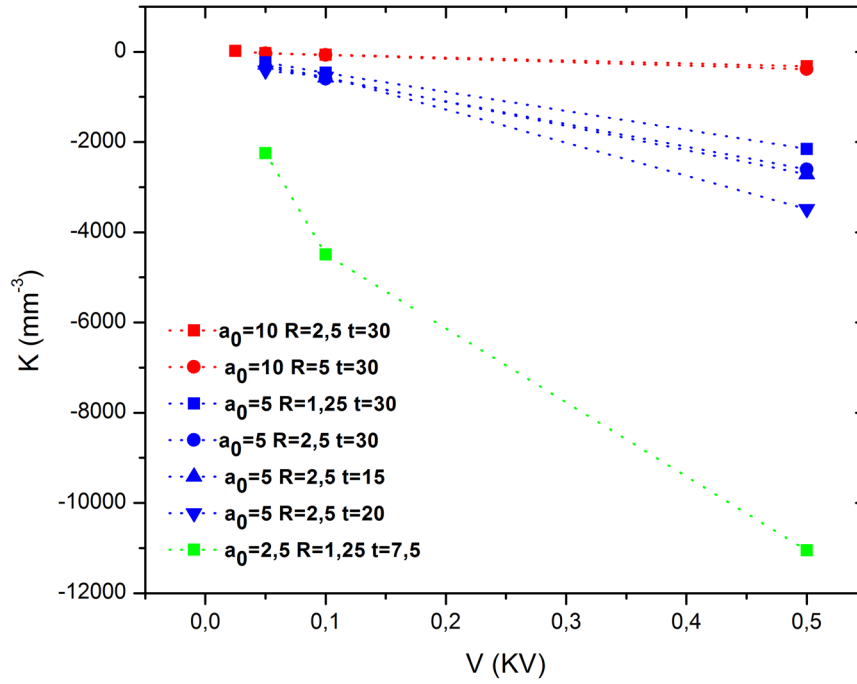


Fig. A7 3: Multipole strength K dependency on the hexapole electrode voltage. The geometries considered are indicated in the legend. Data set colors are associate to the internal diameter a_0 . The behavior of the smallest hexapole (green data sets) shows deviations from the linear dependency, which are assigned to higher order field effects

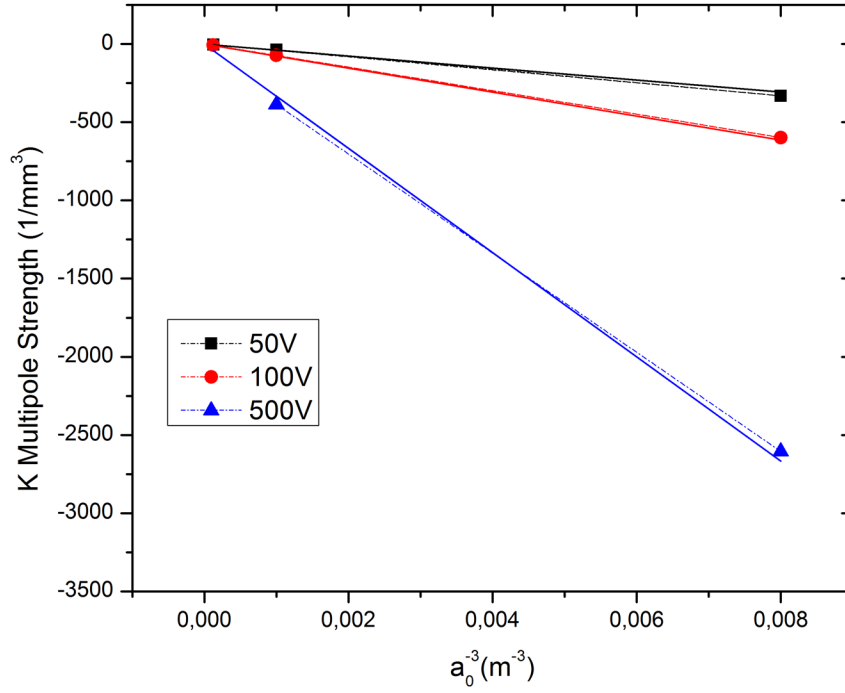


Fig. A7 4: K dependency on the internal hexapole radius (the hexapole thickness and the ratio R/a_0 were kept constant). The theoretical curves $K = \frac{3}{2} \frac{V}{a_0^3 \cdot E_k}$ have been superimposed, showing good agreement between the data and the theoretical curve

Fig A7 4 shows the K dependence on a_0^{-3} ; the theoretical curves $K = \frac{3}{2} \frac{V}{a_0^3 \cdot E_k}$ are superimposed. Small deviations from the theoretical relationship are observed for $V = 500$ V.

Fig A7 5 shows the correlation between the parameter t and the geometrical length of the multipole (in fact, t might depend on the fringe field effects,...). The value of t was obtained from the ratio $\sqrt{\frac{6A}{B}} = t$. The parameter t scales linearly with the geometrical length of the multipole; the deviation from the perfect linear correlation might arise from fringe field effects.

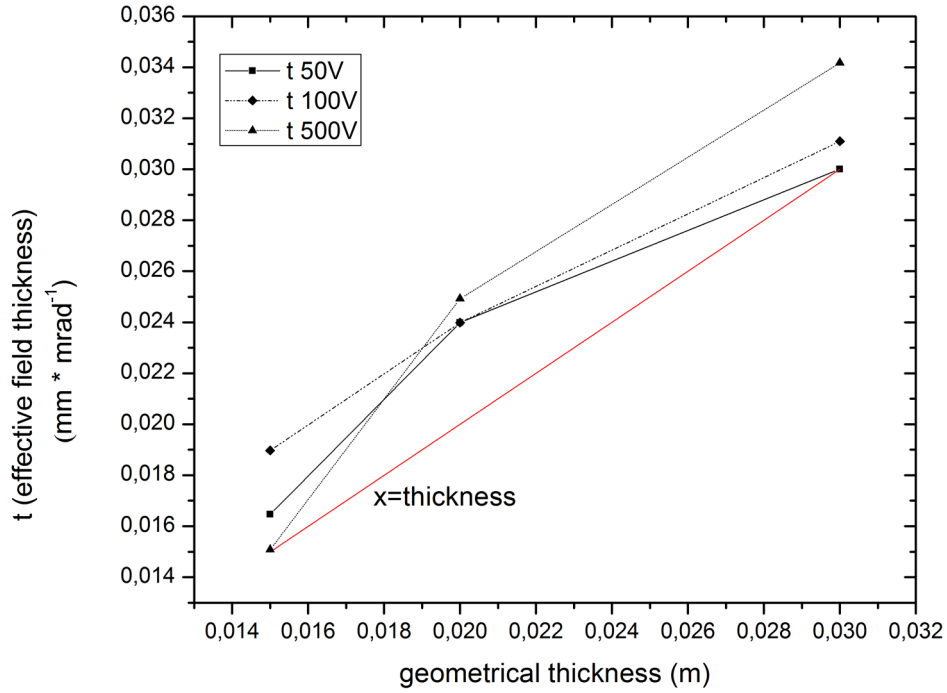


Fig. A7 0: Parameter t dependency on the geometrical thickness of the hexapole; a_0 and R were kept constant. The graph highlights the positive linear correlation between t and the hexapole thickness in m.

Deflection Coefficient

In the next section the four components for the hexapole contributions $H^P(+L, +K)$ are listed; the deflections coefficient $H^P(-L, +K)$ can be easily found from the listed contributions. The effects are calculated at the final image plane of the Ω -filter. P indicates the drift space containing one of the image or diffraction planes of the Ω filter.

As presented in the text, L is the distance from the central plane, while K is the Hexapole orientation. L is positive if the multipole shifted behind the relative image or diffraction plane along the electron optical path, and negative if shifted before it. $L=0$ if the hexapole is unshifted. The multipole voltage orientation is positive if $\Delta x^m \propto x^m$ is positive; K is negative if $\Delta x^m \propto -x^m$.

The P indexes indicate:

- $i1, i2, i3$ are the drift spaces containing the first, second or third image plane of the Ω -filter respectively.
- $d1$ and $d2$ are the drift spaces containing the first or the second diffraction plane of the Ω -filter.

To evaluate the order of magnitude for the contributions, we remember that:

- $t \approx 10^{-2} \text{ mm/mrad}$
- $f \approx 10^2 \text{ mm}/(10^3 \text{ mrad})$
- $L \approx 10 \text{ mm}/(10^3 \text{ mrad})$
- $A = \frac{1}{6} K t^3 \approx 10^{-4} \text{ mrad}^{-1} \quad B = -K t \approx \text{mrad mm}^{-2}$

First image plane

$$H_x^{i1}(+L, +K) = (A - 2BL^2)(\alpha\gamma - \beta\delta) - BL(\gamma^2 - \delta^2) + \left(\frac{3AL}{2} - BL^3\right)(\alpha^2 - \beta^2)$$

$$H_y^{i1}(+L, +K) = -(A - 2BL^2)(\beta\gamma + \alpha\delta) + 2BL \cdot \gamma\delta, -(3AL - 2BL^3)\alpha\beta$$

$$H_{x'}^{i1}(+L, +K) = B(\gamma^2 - \delta^2) + 2BL(\alpha\gamma - \beta\delta) - \left(\frac{A}{2} - BL^2\right)(\alpha^2 - \beta^2)$$

$$H_{y'}^{i1}(+L, +K) = -2B \cdot \gamma\delta - 2BL(\beta\gamma + \alpha\delta) + (A - 2BL^2)\alpha\beta$$

Second image plane

$$H_x^{i2}(+L, +K) = -(A - 2BL^2)(\alpha\gamma - \beta\delta) + BL(\gamma^2 - \delta^2) - \left(\frac{3AL}{2} + BL^3\right)(\alpha^2 - \beta^2) + 2C_k^*(A - 2BL^2)\gamma\kappa \\ + 2C_k^*(3AL - 2BL^3)\alpha\kappa - 2C_k^{*2}L(3A - 2BL^2)\kappa^2$$

$$H_y^{i2}(+L, +K) = (A - 2BL^2)(\beta\gamma + \alpha\delta) - 2BL \cdot \gamma\delta + (3AL - 2BL^3)\alpha\beta - 2C_k^*(A - 2BL^2)\delta\kappa - 2C_k^*L(3A \\ + 2BL^2)\beta\kappa$$

$$H_{x'}^{i2}(+L, +K) = -B(\gamma^2 - \delta^2) - 2BL(\alpha\gamma - \beta\delta) + \left(\frac{A}{2} - BL^2\right)(\alpha^2 - \beta^2) + 4BC_k^*L \cdot \gamma\kappa - 2C_k^*(A - 2BL^2)\alpha\kappa \\ + 2C_k^{*2}(A - 2BL^2)\kappa^2$$

$$H_{y'}^{i2}(+L, +K) = 2B \cdot \gamma\delta, +2BL(\beta\gamma + \alpha\delta) - (A - 2BL^2)\alpha\beta - 4BC_k^*L \cdot \delta\kappa + 2C_k^*(A - 2BL^2)\beta\kappa$$

Third image plane

$$H_x^{i3}(+L, +K) = (A - 2BL^2)(\alpha\gamma - \beta\delta) - BL(\gamma^2 - \delta^2) + \left(\frac{3AL}{2} - BL^3\right)(\alpha^2 - \beta^2) - 4C_k^*(A - 2BL^2)\gamma\kappa \\ - 4C_k^*L(3A - 2BL^2)\alpha\kappa + 8C_k^{*2}L(3A - 2BL^2)\kappa^2$$

$$H_y^{i3}(+L, +K) = -(A - 2BL^2)(\beta\gamma + \alpha\delta) + 2BL \cdot \gamma\delta - (3AL + 2BL^3)\alpha\beta + 4C_k^*(A - 2BL^2)\delta\kappa + 4C_k^*L(3A \\ - 2BL^2)\beta\kappa$$

$$H_{x'}^{i3}(+L, +K) = B(\gamma^2 - \delta^2) - 2BL(\alpha\gamma - \beta\delta) - \left(\frac{A}{2} - BL^2\right)(\alpha^2 - \beta^2) - 8BC_k^*L \cdot \gamma\kappa, +4C_k^*(A - 2BL^2)\alpha\kappa \\ - 8C_k^{*2}(A - 2BL^2)\kappa^2$$

$$H_{y'}^{i3}(+L, +K) = -2B \cdot \gamma\delta + 2BL(\beta\gamma + \alpha\delta) + (A - 2BL^2)\alpha\beta + 8BC_k^*L \cdot \delta\kappa - 4C_k^*(A - 2BL^2)\beta\kappa$$

First diffraction plane

$$H_x^{d1}(+L, +K) = \frac{(A - 2BL^2)}{2f}(\gamma^2 - \delta^2) + 2BfL(\alpha\gamma - \beta\delta) - Bf^3(\alpha^2 - \beta^2) + C_k^*(A - 2B(f + L)L) \cdot \gamma\kappa \\ + 2BC_k^*f^2(f + L)\alpha\kappa + \frac{1}{2}C_k^{*2}f(A - 2B(f + L)^2)\kappa^2$$

$$H_y^{d1}(+L, +K) = -\frac{(A - 2BL^2)}{f}\gamma\delta - 2BfL(\beta\gamma + \alpha\delta) + 2Bf^3 \cdot \alpha\beta - C_k^*(A - 2B(f + L)L) \cdot \delta\kappa - 2Bf^2(f \\ + L) \cdot \beta\kappa$$

$$H_x^{d1}(+L, +K) = -\frac{(A - 2BL^2)}{f}(\alpha\gamma - \beta\delta) + \frac{L(3A - 2BL^2)}{2f^3}(\gamma^2 - \delta^2) - BfL(\alpha^2 - \beta^2) \\ + C_k^*\frac{(A(f + 3L) - 2BL^2(f + L))}{f^2}\gamma\kappa - C_k^*(A - 2B(f + L)L)\alpha\kappa \\ + C_k^{*2}\frac{(A(2f + 3L) - 2B(f + L)^2L)}{2f}\kappa^2$$

$$H_y^{d1}(+L, +K) = \frac{(A - 2BL^2)}{f}(\beta\gamma + \alpha\delta) - \frac{(3AL - 2BL^3)\gamma\delta}{f^3} + 2BfL \cdot \alpha\beta - C_k^*\frac{(A(f + 3L) - 2BL^2(f + L))}{f^2}\delta\kappa \\ + C_k^*(A - 2B(f + L)L)\beta\kappa$$

Second diffraction plane

$$H_x^{d2}(+L, +K) = -\frac{(A - 2BL^2)}{2f}(\gamma^2 - \delta^2) - 2BfL(\alpha\gamma - \beta\delta) + Bf^3(\alpha^2 - \beta^2) - C_k^*(A - 2B(3f + L)L)\gamma\kappa \\ - 2BC_k^*f^2(3f + L)\alpha\kappa, -\frac{1}{2}C_k^{*2}f(A - 2B(3f + L)^2)\kappa^2$$

$$H_y^{d2}(+L, +K) = \frac{(A - 2BL^2)}{f}\gamma\delta + 2BfL(\beta\gamma + \alpha\delta) - 2Bf^3\alpha\beta + C_k^*(A - 2B(3f + L)L)\delta\kappa \\ + 2BC_k^*f^2(3f + L)\beta\kappa$$

$$H_x^{d2}(+L, +K) = \frac{(A - 2BL^2)}{f}(\alpha\gamma - \beta\delta) - \frac{L(3A + 2BL^2)}{2f^3}(\gamma^2 - \delta^2) + BfL(\alpha^2 - \beta^2) \\ - C_k^*\frac{(3A(f + L) - 2BL^2(3f + L))}{f^2}\gamma\kappa + C_k^*(A - 2B(3f + L)L)\alpha\kappa \\ - C_k^{*2}\frac{(3A(2f + L) - 2BL(L + 3f)^2)}{2f}\kappa^2$$

$$H_y^{d2}(+L, +K) = -\frac{(A - 2BL^2)(\beta\gamma + \alpha\delta)}{f} + \frac{L(3A - 2BL^2)\gamma\delta}{f^3} - 2BfL\alpha\beta + C_k^*\frac{(3A(f + L) - 2BL^2(L + 3f))}{f^2}\delta\kappa \\ - C_k^*(A - 2B(3f + L)L)\beta\kappa$$

References

- [1] R. Wichtendahl, R. Fink, H. Kuhlenbeck, D. Preikszas, H. Rose, R. Spehr, P. Hartel, W. Engel, R. Schlögl, H.-J. Freund, SMART: An aberration-corrected XPEEM/LEEM with energy filter, *Surface Review and Letters*, 5 (1998) 1249-1256.
- [2] R. Fink, M. Weiss, E. Umbach, D. Preikszas, H. Rose, R. Spehr, P. Hartel, W. Engel, R. Degenhardt, R. Wichtendahl, SMART: a planned ultrahigh-resolution spectromicroscope for BESSY II, *Journal of electron spectroscopy and related phenomena*, 84 (1997) 231-250.
- [3] T. Schmidt, U. Groh, R. Fink, E. Umbach, O. Schaff, W. Engel, B. Richter, H. Kuhlenbeck, R. Schlögl, H.-J. Freund, XPEEM with energy-filtering: advantages and first results from the SMART project, *Surface Review and Letters*, 9 (2002) 223-232.
- [4] R.M. Cornell, U. Schwertmann, Applications, in: *The Iron Oxides*, Wiley-VCH Verlag GmbH & Co. KGaA, 2004, pp. 509-524.
- [5] R.M. Cornell, U. Schwertmann, Environmental Significance, in: *The Iron Oxides*, Wiley-VCH Verlag GmbH & Co. KGaA, 2004, pp. 541-551.
- [6] A.S. Teja, P.-Y. Koh, Synthesis, properties, and applications of magnetic iron oxide nanoparticles, *Progress in Crystal Growth and Characterization of Materials*, 55 (2009) 22-45.
- [7] Q.A. Pankhurst, J. Connolly, S. Jones, J. Dobson, Applications of magnetic nanoparticles in biomedicine, *Journal of physics D: Applied physics*, 36 (2003) R167.
- [8] A. Sala, H. Marchetto, Z.-H. Qin, S. Shaikhutdinov, T. Schmidt, H.-J. Freund, Defects and inhomogeneities in Fe₃O₄ (111) thin film growth on Pt (111), *Physical Review B*, 86 (2012) 155430.
- [9] M. Lewandowski, Y. Sun, Z.-H. Qin, S. Shaikhutdinov, H.-J. Freund, Promotional effect of metal encapsulation on reactivity of iron oxide supported Pt catalysts, *Applied Catalysis A: General*, 391 (2011) 407-410.
- [10] S. Schauermann, N. Nilius, S. Shaikhutdinov, H.-J. Freund, Nanoparticles for Heterogeneous Catalysis: New Mechanistic Insights, *Accounts of Chemical Research*, 46 (2012) 1673-1681.
- [11] L. Freund, A criterion for arrest of a threading dislocation in a strained epitaxial layer due to an interface misfit dislocation in its path, *Journal of Applied Physics*, 68 (1990) 2073-2080.
- [12] H.-J. Freund, M. Bäumer, J. Libuda, T. Risse, G. Rupprechter, S. Shaikhutdinov, Preparation and characterization of model catalysts: from ultrahigh vacuum to in situ conditions at the atomic dimension, *Journal of Catalysis*, 216 (2003) 223-235.
- [13] M. Peter, S. Adamovsky, J.M. Flores Camacho, S. Schauermann, Energetics of elementary reaction steps relevant for CO oxidation: CO and O₂ adsorption on model Pd nanoparticles and Pd(111), *Faraday Discussions*, 162 (2013) 341-354.

- [14] U. Colombo, F. Gazzarrini, G. Lanzavecchia, G. Sironi, Magnetite Oxidation: A Proposed Mechanism, *Science*, 147 (1965) 1033.
- [15] U. Colombo, G. Fagherazzi, F. Gazzarrini, G. Lanzavecchia, G. Sironi, Mechanisms in the first stage of oxidation of magnetites, *Nature*, 202 (1964) 175-176.
- [16] K. Gallagher, Mechanism of oxidation of magnetite to gamma-Fe₂O₃, *Nature*, 217 (1968) 1118-1121.
- [17] W. Feitknecht, K.J. Gallagher, Mechanisms for the Oxidation of Fe₃O₄, *Nature*, 228 (1970) 548-549.
- [18] C. Schlueter, M. Lübke, A.M. Gigler, W. Moritz, Growth of iron oxides on Ag (111)—Reversible Fe₂O₃/Fe₃O₄ transformation, *Surface Science*, 605 (2011) 1986-1993.
- [19] Y. Zhou, X. Jin, Y. Mukovskii, I. Shvets, Kinetics of oxidation of low-index surfaces of magnetite, *Journal of Physics: Condensed Matter*, 16 (2004) 1.
- [20] M. Monti, B. Santos, A. Mascaraque, O. Rodríguez de la Fuente, M. Niño, T. Montes, A. Locatelli, K. McCarty, J. Marco, J. de la Figuera, Oxidation pathways in bicomponent ultrathin iron oxide films, *The Journal of Physical Chemistry C*, 116 (2012) 11539-11547.
- [21] S. Nie, E. Starodub, M. Monti, D.A. Siegel, L. Vergara, F. El Gabaly, N.C. Bartelt, J. de la Figuera, K.F. McCarty, Insight into Magnetite's Redox Catalysis from Observing Surface Morphology during Oxidation, *Journal of the American Chemical Society*, 135 (2013) 10091-10098.
- [22] W. Weiss, W. Ranke, Surface chemistry and catalysis on well-defined epitaxial iron-oxide layers, *Progress in Surface Science*, 70 (2002) 1-151.
- [23] S.M. Schramm, A.B. Pang, M.S. Altman, R.M. Tromp, A Contrast Transfer Function approach for image calculations in standard and aberration-corrected LEEM and PEEM, *Ultramicroscopy*, 115 (2012) 88-108.
- [24] A.B. Pang, A. Pavlovskaya, L. Däweritz, A. Locatelli, E. Bauer, M.S. Altman, LEEM image phase contrast of MnAs stripes, *Ultramicroscopy*, 130 (2013) 7-12.
- [25] M. Altman, W. Chung, C. Liu, LEEM phase contrast, *Surface Review and Letters*, 5 (1998) 1129-1141.
- [26] M. Henzler, LEED studies of surface imperfections, *Applications of surface science*, 11 (1982) 450-469.
- [27] H. Busch, M. Henzler, Quantitative evaluation of terrace width distributions from LEED measurements, *Surface Science*, 167 (1986) 534-548.
- [28] E.Z. Luo, J. Wollschläger, F. Wegner, M. Henzler, SPA-LEED studies of growth of Ag on Ag(111) at low temperatures, *Appl. Phys. A*, 60 (1995) 19-25.

- [29] M. Henzler, Measurement of surface defects by low-energy electron diffraction, *Appl. Phys. A*, 34 (1984) 205-214.
- [30] E. Bauer, LEEM basics, *Surface Review and Letters*, 5 (1998) 1275-1286.
- [31] E. Bauer, Low energy electron microscopy, *Reports on Progress in Physics*, 57 (1994) 895.
- [32] E. Bauer, Photoelectron spectromicroscopy: present and future, *Journal of Electron Spectroscopy and Related Phenomena*, 114 (2001) 975-987.
- [33] H. Marchetto, High-resolution spectro-microscopic investigations of organic thin film growth, in: *FB Physik, Frei Universität, Berlin*, 2006.
- [34] F. Genuzio, A. Sala, T. Schmidt, D. Menzel, H.-J. Freund, Interconversion of α -Fe₂O₃ and Fe₃O₄ Thin Films: Mechanisms, Morphology, and Evidence for Unexpected Substrate Participation, *The Journal of Physical Chemistry C*, (2014).
- [35] T. Schmidt, H. Marchetto, P.L. Lévesque, U. Groh, F. Maier, D. Preikszas, P. Hartel, R. Spehr, G. Lilienkamp, W. Engel, R. Fink, E. Bauer, H. Rose, E. Umbach, H.J. Freund, Double aberration correction in a low-energy electron microscope, *Ultramicroscopy*, 110 (2010) 1358-1361.
- [36] T. Schmidt, A. Sala, H. Marchetto, E. Umbach, H.-J. Freund, First experimental proof for aberration correction in XPEEM: Resolution, transmission enhancement, and limitation by space charge effects, *Ultramicroscopy*, 126 (2013) 23-32.
- [37] H.-J. Freund, M. Bäumer, H. Kuhlenbeck, Catalysis and surface science: What do we learn from studies of oxide-supported cluster model systems?, *Advances in Catalysis*, 45 (2000) 333-384.
- [38] J. Venables, G. Spiller, M. Hanbucken, Nucleation and growth of thin films, *Reports on Progress in Physics*, 47 (1984) 399.
- [39] K. Reichelt, Nucleation and growth of thin films, *Vacuum*, 38 (1988) 1083-1099.
- [40] G. Ketteler, W. Weiss, W. Ranke, R. Schlögl, Bulk and surface phases of iron oxides in an oxygen and water atmosphere at low pressure, *Physical Chemistry Chemical Physics*, 3 (2001) 1114-1122.
- [41] R.M. Cornell, U. Schwertmann, Thermodynamics of the Fe-O₂-H₂O System, in: *The Iron Oxides*, Wiley-VCH Verlag GmbH & Co. KGaA, 2004, pp. 185-199.
- [42] R.M. Cornell, U. Schwertmann, Crystal Structure, in: *The Iron Oxides*, Wiley-VCH Verlag GmbH & Co. KGaA, 2004, pp. 9-38.
- [43] R.M. Cornell, U. Schwertmann, Transformations, in: *The Iron Oxides*, Wiley-VCH Verlag GmbH & Co. KGaA, 2004, pp. 365-407.

- [44] H. Yanagihara, M. Hasegawa, E. Kita, Y. Wakabayashi, H. Sawa, K. Siratori, Iron Vacancy Ordered γ -Fe₂O₃(001) Epitaxial Films: The Crystal Structure and Electrical Resistivity, *Journal of the Physical Society of Japan*, 75 (2006) 054708.
- [45] P.B. Braun, A Superstructure in Spinel, *Nature*, 170 (1952) 1123-1123.
- [46] H. Takei, S. Chiba, Vacancy ordering in epitaxially-grown single crystals of γ -Fe₂O₃, *Journal of the Physical Society of Japan*, 21 (1966) 1255-1263.
- [47] G. Ketteler, W. Ranke, Heteroepitaxial Growth and Nucleation of Iron Oxide Films on Ru(0001), *The Journal of Physical Chemistry B*, 107 (2003) 4320-4333.
- [48] N. Condon, F. Leibsle, A. Lennie, P. Murray, D. Vaughan, G. Thornton, Biphasic ordering of iron oxide surfaces, *Physical review letters*, 75 (1995) 1961.
- [49] S.K. Shaikhutdinov, M. Ritter, X.-G. Wang, H. Over, W. Weiss, Defect structures on epitaxial Fe₃O₄(111) films, *Physical Review B*, 60 (1999) 11062.
- [50] R.J. Lad, V.E. Henrich, Structure of α -Fe₂O₃ single crystal surfaces following Ar⁺ion bombardment and annealing in O₂, *Surface science*, 193 (1988) 81-93.
- [51] W. Weiss, M. Ritter, Metal oxide heteroepitaxy: Stranski-Krastanov growth for iron oxides on Pt(111), *Physical Review B*, 59 (1999) 5201-5213.
- [52] A. Sala, Characterization of Iron oxide thin films as support for catalytically active nanoparticles, in: *Physic*, Freie Universität Berlin, Berlin, 2013.
- [53] T. Schmidt, Strukturelle Untersuchungen zur Homoepitaxie auf Pt(111), in: *Physics*, Hannover University, 1994.
- [54] R. Kunkel, B. Poelsema, L.K. Verheij, G. Comsa, Reentrant layer-by-layer growth during molecular-beam epitaxy of metal-on-metal substrates, *Physical Review Letters*, 65 (1990) 733-736.
- [55] Chapter 3 Theory of Solid State Reaction Kinetics, in: C.H. Bamford, C.F.H. Tipper (Eds.) *Comprehensive Chemical Kinetics*, Elsevier, 1980, pp. 41-113.
- [56] M.E. Brown, D. Dollimore, A.K. Galwey, *Reactions in the solid state*, Elsevier, 1980.
- [57] T. Luty, C.J. Eckhardt, General Theoretical Concepts for Solid State Reactions: Quantitative Formulation of the Reaction Cavity, Steric Compression, and Reaction-Induced Stress Using an Elastic Multipole Representation of Chemical Pressure, *Journal of the American Chemical Society*, 117 (1995) 2441-2452.
- [58] V. Raghavan, M. Cohen, Solid-State Phase Transformations, in: N.B. Hannay (Ed.) *Changes of State*, Springer US, 1975, pp. 67-127.
- [59] H. Schmalzried, *Chemical kinetics of solids*, VCH, Weinheim ; New York, 1995.

- [60] D. Hesse, H. Bethge, Solid state reactions for the epitaxial growth of spinel films, *Journal of Crystal Growth*, 65 (1983) 69-76.
- [61] D. Hesse, H. Sieber, P. Werner, R. Hillebrand, J. Heydenreich, Structure, Morphology, and Misfit Accommodation Mechanism of MgIn_2O_4 Films Grown on MgO (001) Substrates by Solid State Reaction, *Zeitschrift für Physikalische Chemie*, 187 (1994) 161-178.
- [62] C. Carter, Y. Simpson, Thin-Film Reactions, *Berichte der Bunsengesellschaft für physikalische Chemie*, 90 (1986) 676-680.
- [63] S. Mrowec, S. Marcinkiewicz, Defects and diffusion in solids: an introduction, Elsevier Amsterdam, 1980.
- [64] R.W. Balluffi, J.M. Bkakely, Special aspects of diffusion in thin films, *Thin Solid Films*, 25 (1975) 363-392.
- [65] M.A. Nicolet, Diffusion barriers in thin films, *Thin Solid Films*, 52 (1978) 415-443.
- [66] D. Gupta, P.S. Ho, Diffusion processes in thin films, *Thin Solid Films*, 72 (1980) 399-418.
- [67] R. Smoluchowski, Theory of Grain Boundary Diffusion, *Physical Review*, 87 (1952) 482-487.
- [68] V. Stubican, L. Carinci, Point Defects and Grain Boundary Diffusion in NiO and Fe_3O_4 , *Zeitschrift für Physikalische Chemie*, 207 (1998) 215-222.
- [69] H. Sieber, D. Hesse, P. Werner, S. Senz, Differences in the Defect Structures of the Reaction Fronts of Solid State Reactions within Interface-And Diffusion-Controlled Reaction Regimes, in: *DIFFUSION AND DEFECT DATA PART A DEFECT AND DIFFUSION FORUM*, SCI TECH PUBLICATIONS LTD, 1997, pp. 649-654.
- [70] D. Sun, S. Senz, D. Hesse, Crystallography, microstructure and morphology of $\text{Mg}_4\text{Nb}_2\text{O}_9/\text{MgO}$ and $\text{Mg}_4\text{Ta}_2\text{O}_9/\text{MgO}$ interfaces formed by topotaxial solid state reactions, *Journal of the European Ceramic Society*, 26 (2006) 3181-3190.
- [71] J.A. Thornton, D. Hoffman, Stress-related effects in thin films, *Thin solid films*, 171 (1989) 5-31.
- [72] I.N. Remediakis, N. Lopez, J.K. Nørskov, CO oxidation on gold nanoparticles: Theoretical studies, *Applied Catalysis A: General*, 291 (2005) 13-20.
- [73] N. Lopez, T.V.W. Janssens, B.S. Clausen, Y. Xu, M. Mavrikakis, T. Bligaard, J.K. Nørskov, On the origin of the catalytic activity of gold nanoparticles for low-temperature CO oxidation, *Journal of Catalysis*, 223 (2004) 232-235.
- [74] Q. Fu, T. Wagner, Interaction of nanostructured metal overlayers with oxide surfaces, *Surface Science Reports*, 62 (2007) 431-498.

- [75] A. Berkó, I. Ulrych, K. Prince, Encapsulation of Rh nanoparticles supported on TiO₂ (110)-(1×1) surface: XPS and STM studies, *The Journal of Physical Chemistry B*, 102 (1998) 3379-3386.
- [76] S. Tauster, S. Fung, R. Baker, J. Horsley, Strong interactions in supported-metal catalysts, *Science*, 211 (1981) 1121-1125.
- [77] S. Tauster, Strong metal-support interactions, *Accounts of Chemical Research*, 20 (1987) 389-394.
- [78] S. Tauster, S. Fung, Strong metal-support interactions: occurrence among the binary oxides of groups IIA–VB, *Journal of Catalysis*, 55 (1978) 29-35.
- [79] G. Graham, H.-W. Jen, W. Chun, R. McCabe, High-temperature-aging-induced encapsulation of metal particles by support materials: comparative results for Pt, Pd, and Rh on cerium–zirconium mixed oxides, *Journal of Catalysis*, 182 (1999) 228-233.
- [80] P. Meriaudeau, J. Dutel, M. Dufaux, C. Naccache, Further Investigation on Metal-Support Interaction: TiO₂, CeO₂, SiO₂ Supported Platinum Catalysts, *Studies in Surface Science and Catalysis*, 11 (1982) 95-104.
- [81] P. Bera, K. Patil, V. Jayaram, G. Subbanna, M. Hegde, Ionic Dispersion of Pt and Pd on CeO₂ by Combustion Method: Effect of Metal–Ceria Interaction on Catalytic Activities for NO Reduction and CO and Hydrocarbon Oxidation, *Journal of Catalysis*, 196 (2000) 293-301.
- [82] M.V. Ganduglia-Pirovano, A. Hofmann, J. Sauer, Oxygen vacancies in transition metal and rare earth oxides: Current state of understanding and remaining challenges, *Surface Science Reports*, 62 (2007) 219-270.
- [83] C. Hardacre, R.M. Ormerod, R.M. Lambert, Platinum-Promoted Catalysis by Ceria: A Study of Carbon Monoxide Oxidation over Pt (111)/CeO₂, *The Journal of Physical Chemistry*, 98 (1994) 10901-10905.
- [84] Y. Sun, M. Lewandowski, Z. Qin, S. Shaikhutdinov, H. Freund, Promotional effect of metal encapsulation on reactivity of iron oxide supported Pt catalysts.
- [85] M.G. Willinger, W. Zhang, O. Bondarchuk, S. Shaikhutdinov, H.-J. Freund, R. Schlögl, A Case of Strong Metal–Support Interactions: Combining Advanced Microscopy and Model Systems to Elucidate the Atomic Structure of Interfaces, *Angewandte Chemie International Edition*, 53 (2014) 5998-6001.
- [86] M. Lewandowsky, Scanning Tunneling Microscopy Study of Iron Oxide based Model Catalysts, in: *Prozesswissenschaften*, Technische Universität, Berlin, 2011.
- [87] S.K. Shaikhutdinov, W. Weiss, Oxygen pressure dependence of the α -Fe₂O₃(0001) surface structure, *Surface Science*, 432 (1999) L627-L634.
- [88] A. Barbieri, W. Weiss, M. Van Hove, G. Somorjai, Magnetite Fe₃O₄(111): surface structure by LEED crystallography and energetics, *Surface Science*, 302 (1994) 259-279.

- [89] X.-G. Wang, W. Weiss, S.K. Shaikhutdinov, M. Ritter, M. Petersen, F. Wagner, R. Schlögl, M. Scheffler, The hematite (α -Fe₂O₃)(0001) surface: evidence for domains of distinct chemistry, *Physical review letters*, 81 (1998) 1038.
- [90] M. Ritter, W. Ranke, W. Weiss, Growth and structure of ultrathin FeO films on Pt(111) studied by STM and LEED, *Physical Review B*, 57 (1998) 7240-7251.
- [91] Y. Tang, H. Qin, K. Wu, Q. Guo, J. Guo, The reduction and oxidation of Fe₂O₃(0001) surface investigated by scanning tunneling microscopy, *Surface Science*, 609 (2013) 67-72.
- [92] H. Qiu, V. Staemmler, H. Kuhlenbeck, E. Bauer, H.-J. Freund, Weak thermal reduction of biphasic Fe₂O₃(0001) films grown on Pt(111): Sub-surface Fe²⁺ formation, *Surface Science*, 641 (2015) 30-36.
- [93] C.H. Lanier, A.N. Chiamonti, L.D. Marks, K.R. Poeppelmeier, The Fe₃O₄ origin of the “Biphase” reconstruction on α -Fe₂O₃(0001), *Surface Science*, 603 (2009) 2574-2579.
- [94] N. Condon, F. Leibsle, T. Parker, A. Lennie, D. Vaughan, G. Thornton, Biphasic ordering on Fe₃O₄(111), *Physical Review B*, 55 (1997) 15885.
- [95] A. Kiejna, T. Pabisiak, Mixed Termination of Hematite (α -Fe₂O₃)(0001) Surface, *The Journal of Physical Chemistry C*, 117 (2013) 24339-24344.
- [96] Z. Qin, M. Lewandowski, Y. Sun, S. Shaikhutdinov, H. Freund, Morphology and CO adsorption on platinum supported on thin Fe₃O₄ (111) films, *Journal of Physics: Condensed Matter*, 21 (2009) 134019.
- [97] U. Colombo, F. Gazzarini, G. Lanzavecchia, *Mat. Sci. Eng.*, 2 (1967) 125-125.
- [98] U. Colombo, G. Fagherazzi, F. Gazzarini, G. Lanzavecchia, G. Sironi, *Nature*, 219 (1968) 1036-1036.
- [99] K.J. Gallagher, W. Feitknecht, U. Mannweiler, *Nature*, 217 (1968) 1118-1118.
- [100] J. Karunamuni, R.L. Kurtz, R.L. Stockbauer, Growth of iron oxide on Cu(001) at elevated temperature, *Surface Science*, 442 (1999) 223-238.
- [101] B. Luerßen, J. Janek, S. Günther, M. Kiskinova, R. Imbihl, Microspectroscopy at a moving reduction front in zirconia solid electrolyte, *Physical Chemistry Chemical Physics*, 4 (2002) 2673-2679.
- [102] H.H. Rotermund, S. Nettesheim, A. von Oertzen, G. Ertl, Observation of surface diffusion of adsorbates on metal surfaces by photoemission electron microscopy (PEEM), *Surface Science*, 275 (1992) L645-L649.
- [103] H. Marbach, G. Lilienkamp, H. Wei, S. Gunther, Y. Suchorski, R. Imbihl, Ordered phases in alkali redistribution during a catalytic surface reaction, *Physical Chemistry Chemical Physics*, 5 (2003) 2730-2735.

- [104] H. Marbach, S. Günther, B. Luerssen, L. Gregoratti, M. Kiskinova, R. Imbihl, Selforganization of alkali metal on a catalytic metal surface, *Catalysis letters*, 83 (2002) 161-164.
- [105] S. Günther, T.O. Menteş, M.A. Niño, A. Locatelli, S. Böcklein, J. Wintterlin, Desorption kinetics from a surface derived from direct imaging of the adsorbate layer, *Nat Commun*, 5 (2014).
- [106] S. Nettesheim, A. Von Oertzen, H. Rotermund, G. Ertl, Reaction diffusion patterns in the catalytic CO-oxidation on Pt (110): Front propagation and spiral waves, *The Journal of chemical physics*, 98 (1993) 9977-9985.
- [107] R. Röttger, H. Schmalzried, Chemical kinetics at solid/solid interfaces, *Solid State Ionics*, 150 (2002) 131-141.
- [108] G.S. Rohrer, Influence of interface anisotropy on grain growth and coarsening, *Annu. Rev. Mater. Res.*, 35 (2005) 99-126.
- [109] W. Jo, D.-Y. Kim, N.-M. Hwang, Effect of Interface Structure on the Microstructural Evolution of Ceramics, *Journal of the American Ceramic Society*, 89 (2006) 2369-2380.
- [110] S.Y. Chung, S.J.L. Kang, Effect of dislocations on grain growth in strontium titanate, *Journal of the American Ceramic Society*, 83 (2000) 2828-2832.
- [111] R. Benedek, D. Seidman, C. Woodward, The effect of misfit on heterophase interface energies, *Journal of Physics: Condensed Matter*, 14 (2002) 2877.
- [112] D. Hesse, P. Werner, R. Mattheis, J. Heydenreich, Interfacial reaction barriers during thin-film solid-state reactions: The crystallographic origin of kinetic barriers at the NiS₂/Si(111) interface, *Appl. Phys. A*, 57 (1993) 415-425.
- [113] X.-S. Yang, S. Sun, X.-L. Wu, E. Ma, T.-Y. Zhang, Dissecting the Mechanism of Martensitic Transformation via Atomic-Scale Observations, *Sci. Rep.*, 4 (2014).
- [114] P.S. Sidhu, R.J. Gilkes, A.M. Posner, Mechanism of the low temperature oxidation of synthetic magnetites, *Journal of Inorganic and Nuclear Chemistry*, 39 (1977) 1953-1958.
- [115] S. Kachi, K. Momiyama, S. Shimizu, An Electron Diffraction Study and a Theory of the Transformation from γ -Fe₂O₃ to α -Fe₂O₃, *Journal of the Physical Society of Japan*, 18 (1963) 106-116.
- [116] G.C. Bye, G.T. Simpkin, Influence of Cr and Fe on Formation of α -Al₂O₃ from γ -Al₂O₃, *Journal of the American Ceramic Society*, 57 (1974) 367-371.
- [117] R.B. Bagwell, G.L. Messing, P.R. Howell, The formation of α -Al₂O₃ from θ -Al₂O₃: The relevance of a “critical size” and: Diffusional nucleation or “synchro-shear”?, *Journal of Materials Science*, 36 (2001) 1833-1841.
- [118] Y. Watanabe, K. Ishii, Geometrical consideration of the crystallography of the transformation from α -Fe₂O₃ to Fe₃O₄, *physica status solidi (a)*, 150 (1995) 673-686.

- [119] R.M. Cornell, U. Schwertmann, Characterization, in: *The Iron Oxides*, Wiley-VCH Verlag GmbH & Co. KGaA, 2004, pp. 139-183.
- [120] F. Millot, J. Lorin, B. Klossa, Y. Niu, J. Tarento, Oxygen self-diffusion in Fe₃O₄: An experimental example of interactions between defects, *Berichte der Bunsen-Gesellschaft*, 101 (1997) 1351-1354.
- [121] K.D. Becker, V. von Wurmb, F.J. Litterst, Disorder and diffusional motion of cations in magnetite, Fe₃- δ O₄, studied by Mössbauer spectroscopy at high temperatures, *Journal of Physics and Chemistry of Solids*, 54 (1993) 923-935.
- [122] M. Bowker, G. Hutchings, P.R. Davies, D. Edwards, R. Davies, S. Shaikhutdinov, H.-J. Freund, Surface structure of γ -Fe₂O₃(111), *Surface Science*, 606 (2012) 1594-1599.
- [123] D.I. Jerdev, B.E. Koel, Fe deposition on Pt (111): a route to Fe-containing Pt-Fe alloy surfaces, *Surface science*, 513 (2002) L391-L396.
- [124] H. Okamoto, Fe-Pt (iron-platinum), *J Phs Eqil and Diff*, 25 (2004) 395-395.
- [125] Y. Watanabe, K. Ishii, Geometrical Consideration of the Crystallography of the Transformation from α -Fe₂O₃ to Fe₃O₄, *Physica status solidi (a)*, (1995) 673-686.
- [126] N.L. Peterson, W.-K. Chen, D. Wolf, Correlation and isotope effects for cation diffusion in magnetite, *Journal of Physics and Chemistry of Solids*, 41 (1980) 709-719.
- [127] Y. Oishi, W. Kingery, Self-Diffusion of Oxygen in Single Crystal and Polycrystalline Aluminum Oxide, *The Journal of Chemical Physics*, 33 (1960) 480-486.
- [128] M. Jiang, K. Oikawa, T. Ikeshoji, Molecular-dynamic simulations of martensitic transformation of cobalt, *Metall and Mat Trans A*, 36 (2005) 2307-2314.
- [129] A. Atkinson, R. Taylor, Diffusion of ⁵⁵Fe in Fe₂O₃ single crystals, *Journal of Physics and Chemistry of Solids*, 46 (1985) 469-475.
- [130] T.-Y. Lee, S. Sarbach, K. Kuhnke, K. Kern, Growth and surface alloying of Fe on Pt(111), *Surface Science*, 600 (2006) 3266-3273.
- [131] A.G. Crouch, J. Robertson, Creep and oxygen diffusion in magnetite, *Acta Metallurgica et Materialia*, 38 (1990) 2567-2572.
- [132] K.P.R. Reddy, A.R. Cooper, Oxygen Diffusion in MgO and α -Fe₂O₃, *Journal of the American Ceramic Society*, 66 (1983) 664-666.
- [133] D. Santos-Carballal, A. Roldan, R. Grau-Crespo, N.H. de Leeuw, A DFT study of the structures, stabilities and redox behaviour of the major surfaces of magnetite Fe₃O₄, *Physical Chemistry Chemical Physics*, (2014).
- [134] M. Bott, T. Michely, G. Comsa, The homoepitaxial growth of Pt on Pt (111) studied with STM, *Surface science*, 272 (1992) 161-166.

- [135] E. Cox, M. Li, P.-W. Chung, C. Ghosh, T. Rahman, C.J. Jenks, J.W. Evans, P.A. Thiel, Temperature dependence of island growth shapes during submonolayer deposition of Ag on Ag (111), *Physical Review B*, 71 (2005) 115414.
- [136] H. Brune, H. Röder, K. Bromann, K. Kern, J. Jacobsen, P. Stoltze, K. Jacobsen, N. Jens, Anisotropic corner diffusion as origin for dendritic growth on hexagonal substrates, *Surface science*, 349 (1996) L115-L122.
- [137] H. Brune, H. Röder, K. Bromann, K. Kern, Kinetic processes in metal epitaxy studied with variable temperature STM: Ag/Pt (111), *Thin Solid Films*, 264 (1995) 230-235.
- [138] T.t. Witten, L. Sander, Diffusion-limited aggregation, *Physical Review B*, 27 (1983) 5686.
- [139] T. Witten Jr, L.M. Sander, Diffusion-limited aggregation, a kinetic critical phenomenon, *Physical review letters*, 47 (1981) 1400.
- [140] S. Bharathi, D. Nataraj, K. Senthil, M. Yoshitake, Shape-controlled synthesis of α -Fe₂O₃ nanostructures: engineering their surface properties for improved photocatalytic degradation efficiency, *J Nanopart Res*, 15 (2012) 1-13.
- [141] M. Cao, T. Liu, S. Gao, G. Sun, X. Wu, C. Hu, Z.L. Wang, Single-Crystal Dendritic Micro-Pines of Magnetic α -Fe₂O₃: Large-Scale Synthesis, Formation Mechanism, and Properties, *Angewandte Chemie International Edition*, 44 (2005) 4197-4201.
- [142] L. Giordano, M. Lewandowski, I. Groot, Y.-N. Sun, J. Goniakowski, C. Noguera, S. Shaikhutdinov, G. Pacchioni, H.-J. Freund, Oxygen-Induced Transformations of an FeO (111) Film on Pt (111): A Combined DFT and STM Study, *The Journal of Physical Chemistry C*, 114 (2010) 21504-21509.
- [143] O. Dulub, W. Hebenstreit, U. Diebold, Imaging cluster surfaces with atomic resolution: the strong metal-support interaction state of Pt supported on TiO₂ (110), *Physical Review Letters*, 84 (2000) 3646.
- [144] M. Henzler, Texture of surfaces cleaned by ion bombardment and annealing, *Surface Science*, 22 (1970) 12-18.
- [145] S. Hüfner, G.K. Wertheim, J.H. Wernick, XPS core line asymmetries in metals, *Solid State Communications*, 17 (1975) 417-422.
- [146] A.K.-V. Alexander V. Naumkin, Stephen W. Gaarenstroom, and Cedric J. Powell NIST X-ray Photoelectron Spectroscopy Database in, 2006.
- [147] N. Barrett, C. Guillot, J.C. Bertolini, J. Massardier, B.C. Khanra, Bulk and surface core level binding energies in the Pt₈₀Fe₂₀(111) alloy, *Surface Science*, 260 (1992) L11-L16.
- [148] H.P. Sun, X.P. Pan, G.W. Graham, H.-W. Jen, R.W. McCabe, S. Thevuthasan, C.H.F. Peden, Partial encapsulation of Pd particles by reduced ceria-zirconia, *Applied Physics Letters*, 87 (2005) 201915.

- [149] J.-M. Pan, T.E. Madey, The encapsulation of Fe on TiO₂ (110), *Catalysis Letters*, 20 (1993) 269-274.
- [150] Q. Fu, T. Wagner, S. Olliges, H.-D. Carstanjen, Metal-oxide interfacial reactions: Encapsulation of Pd on TiO₂ (110), *The Journal of Physical Chemistry B*, 109 (2005) 944-951.
- [151] Y. Gao, Y. Liang, S.A. Chambers, Thermal stability and the role of oxygen vacancy defects in strong metal support interaction — Pt on Nb-doped TiO₂(100), *Surface Science*, 365 (1996) 638-648.
- [152] S.J. Tauster, S.C. Fung, R.L. Garten, Strong metal-support interactions. Group 8 noble metals supported on titanium dioxide, *Journal of the American Chemical Society*, 100 (1978) 170-175.
- [153] A. Pang, T. Müller, M. Altman, E. Bauer, Fourier optics of image formation in LEEM, *Journal of Physics: Condensed Matter*, 21 (2009) 314006.
- [154] S. Kennedy, N. Schofield, D. Paganin, D. Jesson, Wave optical treatment of surface step contrast in low-energy electron microscopy, *Surface Review and Letters*, 16 (2009) 855-867.
- [155] M.S. Altman, Trends in low energy electron microscopy, *Journal of Physics: Condensed Matter*, 22 (2010) 084017.
- [156] S. Schramm, A. Pang, M. Altman, R. Tromp, A Contrast Transfer Function approach for image calculations in standard and aberration-corrected LEEM and PEEM, *Ultramicroscopy*, 115 (2012) 88-108.
- [157] T.R. Bollmann, R. van Gastel, H.J. Zandvliet, B. Poelsema, Quantum size effects on surfaces without a projected bandgap: Pb/Ni (111), *New Journal of Physics*, 13 (2011) 103025.
- [158] M.S. Altman, Low energy electron microscopy of quantum well resonances in Ag films on W(110), *Journal of Physics: Condensed Matter*, 17 (2005) S1305.
- [159] W.F. Chung, Y.J. Feng, H.C. Poon, C.T. Chan, S.Y. Tong, M.S. Altman, Layer Spacings in Coherently Strained Epitaxial Metal Films, *Physical Review Letters*, 90 (2003) 216105.
- [160] Lorentz, in.
- [161] S. Lanio, H. Rose, D. Krah, Test and improved design of a corrected imaging magnetic energy filter, *Optik*, 73 (1986) 56-68.
- [162] H. Rose, D. Krah, Electron optics of imaging energy filters, in: *Energy-filtering transmission electron microscopy*, Springer, 1995, pp. 43-149.
- [163] H. Rose, *Geometrical charged-particle optics*, Springer, 2009.
- [164] S. Lanio, H. Rose, Omega-type electron energy filter, in, *Google Patents*, 1988.

- [165] H. Liebl, *Applied charged particle optics*, Springer, 2008.
- [166] P.W. Hawkes, E. Kasper, *Principles of electron optics*, Academic Press, 1996.
- [167] S. Taya, H. Matsuda, A third-order transfer matrix of an electrostatic hexapole lens, *International Journal of Mass Spectrometry and Ion Physics*, 9 (1972) 235-245.

Acknowledgments

I would like to thank many people, without whom this work would not exist.

First of all, I would like to thank Prof. H.J. Freund, Dr. T. Schmidt and Prof. Dr. D. Menzel for giving me the opportunity of learning and working with them, as well as Prof. Dr. N. Koch, for accepting to be my supervisor. I am grateful to the members of my research group, for their assistance during this time: Marcel Springer, Hagen Klemm, Gina Peschel, Alexander Fuhrich, Dr. Ewa Madej, Dr. Mauricio Prieto. A particular thanks goes to Dr. Alessandro Sala and Dr. Helder Marchetto, for their fundamental help and support.

I would like to thank my family for encouraging me in every possible way: my mother Mariliana, my father Aldo, my “little” brother Marco, my aunt and uncle Adriana and Loris, my cousin Erika and her family and my grandmother Lina. I would also like to thank all my friends spread around the world, and an incredible number of people, whom I had the luck and the pleasure to meet during all these years.

Finally, I would like to thank Enrico.